Friedrich-Alexander-Universität
Faculty of Engineering

Dissertation

2024

Andrés Felipe Betancourt Payán

Characterization and Correction of Ionospheric Signals in Low-Frequency Synthetic Aperture Radar Systems

Charakterisierung und Korrektur von Ionosphärischen Signalen in Niederfrequenten Radarsystemen mit Synthetischer Apertur

Characterization and Correction of Ionospheric Signals in Low-Frequency Synthetic Aperture Radar Systems

Charakterisierung und Korrektur von Ionosphärischen Signalen in Niederfrequenten Radarsystemen mit Synthetischer Apertur

Der Technischen Fakultät
der Friedrich-Alexander-Universität
Erlangen-Nürnberg
zur
Erlangung des Doktorgrades Dr. -Ing.
vorgelegt von

Andrés Felipe Betancourt Páyan
aus Armenia (Quindío)
Kolumbien

Als Dissertation genehmigt
von der Technischen Fakultät
der Friedrich-Alexander-Universität Erlangen-Nürnberg

Tag der mündlichen Prüfung:	04. Juli 2025
Gutachter:	Prof. Dr. -Ing. Gerhard Krieger
	Prof. Dr. Franz J. Meyer
	Prof. Dr. Marc Stamminger

Abstract

Low-frequency Synthetic Aperture Radar (SAR) plays an essential role in efficiently monitoring geophysical observables such as forest biomass or the state of ice sheets. The penetration capability of the incident electromagnetic waves into volume scatterers allows vertical structure characterization and the detection of non-superficial targets. The principle was demonstrated with L-band ($\lambda \sim 21\,\mathrm{cm}$) missions and currently the European Space Agency (ESA) is preparing for the launch of the first time in space P-band ($\lambda \sim 69\,\mathrm{cm}$) SAR mission called Biomass. As a primary objective, Biomass aims to estimate the global forest above-ground biomass at high spatial resolution and extensive coverage. The presence of the ionosphere will challenge this task since its dispersive and anisotropic nature introduces distortions in the transmitted and received signals, lowering the quality of the products and leading to the misinterpretation of the data. The amount of distortions depends on the Total Electron Content (TEC) experienced by the radar waves on their two-way path, and they range from time delays and phase errors to a rotation of the polarization plane and changes in the radar cross section known as scintillation. The TEC is a dynamic parameter that varies in time and space so that TEC distributions leave 2-D distortion maps in the images. For the ionospheric calibration processing step, state-of-the-art algorithms were adapted during the development of this thesis, and new ones were further developed for the preparation for the mission. In the absence of spaceborne P-band data, all this work was carried out based on simulations and L-band images from ALOS-PALSAR.

This thesis deals with the entire life cycle of the ionospheric signal from the generation, the injection into simulated data, the estimation and correction of data, and finally, the possibility of extracting geophysical parameters from the ionospheric signatures. Accurate but also efficient injection of ionospheric disturbances is a crucial step to develop estimation and correction algorithms in a simulation framework. The ionospheric calibration is divided into two steps: A visualization step, where the TEC is estimated via a distortion map (i.e., defocusing due to phase errors or Faraday rotation across the polarimetric channels), and a correction step, where the inverted TEC is used to compensate the original distortions. In this thesis, several calibration approaches are proposed for different data configurations (quad-pol, single-pol or interferometric stacks), and their performance is assessed and compared with each other for different scenarios. The product of the visualization step is unique in the sense that no other ionospheric sensing technology provides such a high resolution and wide coverage of 2-D maps of the ionosphere as SAR does, making it highly attractive to the community that studies small-scale TEC irregularities. For this reason, effort was put into the characterization of residual maps. Finally, as a use case of the exploitation of the ionospheric signature, the capability of estimating the location of the ionospheric irregularities based on scintillation patterns in an ALOS-2/PALSAR-2 dataset is shown.

The algorithms developed during this thesis are designed explicitly for P-band SAR data in the Biomass framework. The techniques will be helpful in the commissioning and opera-

tional phases of the mission. However, the knowledge and contributions go beyond Biomass. They are worth revisiting with other new L-band systems such as the NASA-ISRO Synthetic Aperture Radar (NISAR) and the development of even lower-frequency radar remote sensing approaches such as the Earth orbiting radar sounder.

Zusammenfassung

Synthetic Aperture Radar (SAR) Systeme in niedrigen Frequenzen nehmen eine Schlüsselrolle bei der effizienten Überwachung geophysikalischer Messgrößen wie der Biomasse von Wäldern oder dem Zustand von Eisschilden und Gletschern ein. Die Fähigkeit der elektromagnetischen Wellen, in semitransparente Volumina einzudringen, ermöglicht die Charakterisierung derer vertikalen Struktur und die Erkennung von nicht oberflächlichen Zielen. Das Prinzip wurde mit L-Band ($\lambda \sim 21\,\mathrm{cm}$) Missionen demonstriert, und derzeit bereitet die Europäische Weltraumorganisation (ESA) den Start der ersten raumgestützten SAR-Mission im P-Band ($\lambda \sim 69\,\mathrm{cm}$) mit dem Namen Biomass vor. Das Hauptziel von Biomass ist die Schätzung der weltweiten „above-ground" Biomasse der Wälder mit hoher räumlicher Auflösung und großer Abdeckung. Die Ionosphäre stellt eine Herausforderung für diese Aufgabe dar, da die dispersive und anisotrope Natur der Ionosphäre Verzerrungen in den gesendeten und empfangenen Signalen verursacht, die die Qualität der Produkte beeinträchtigen und zu einer Fehlinterpretation der Daten führen. Das Ausmaß der Verzerrungen hängt vom akkumulierten Elektronengehalt (TEC) der Ionosphäre ab, den die Radarwellen auf ihrem Hin- und Rückweg durchlaufen. Die Effekte der Ionosphäre zeigen sich als Zeitverzögerungen und Phasenfehler, Drehung der Polarisationsebene, sowie Veränderungen des Radarquerschnitts, die Szintillationen genannt werden. Der TEC ist ein dynamischer Parameter, der sich zeitlich und räumlich verändert, so dass die TEC-Verteilungen 2-D-Verzerrungseffekte in den Bildern hinterlassen. Für die Ionosphärenkalibrierung wurden in dieser Arbeit state-of-the-art Algorithmen angepasst und neue Algorithmen für die Vorbereitung der Biomass Mission entwickelt. Da es bis zum Start der Biomass Mission keine raumgestützten P-Band SAR Daten gibt, wurden die Arbeiten in dieser Dissertation auf der Grundlage von Simulationen und L-Band-Bildern der ALOS-PALSAR Mission durchgeführt.

Diese Arbeit befasst sich mit allen relevanten Aspekten des ionosphärischen SAR-Signals, von der Erzeugung, über die Injektion in simulierte Daten, die Schätzung und Korrektur von Daten, bis hin zur Möglichkeit, geophysikalische Parameter aus den ionosphärischen Signaturen zu extrahieren. Die genaue, aber auch effiziente Injektion ionosphärischer Störungen im Rahmen von Simulationen ist ein entscheidender Schritt zur Entwicklung von Schätz- und Korrekturalgorithmen. Die ionosphärische Kalibrierung ist in zwei Schritte unterteilt: Einen Visualisierungsschritt, bei dem der TEC über eine generierte Karte von Verzerrungsfehlern geschätzt wird (d. h. Defokussierung aufgrund von Phasenfehlern oder Faraday-Rotation zwischen den polarimetrischen Kanälen), und einen Korrekturschritt, bei dem der invertierte TEC verwendet wird, um die ursprünglichen Verzerrungen zu kompensieren. In dieser Arbeit werden mehrere Kalibrierungsansätze für verschiedene Datenkonfigurationen (Quad-Pol, Single-Pol, oder interferometrische Datensätze) vorgeschlagen, deren Performanz bewertet und für verschiedene Szenarien

miteinander verglichen wird. Das generierte Produkt aus dem Visualisierungsschritt ist als einzigartig anzusehen, da keine andere ionosphärische Sensortechnologie eine so hohe Auflösung und breite Abdeckung zur 2-D-Kartierung der Ionosphäre bietet wie SAR. Dies macht die entwickelte Technik relevant zur Erforschung von kleinskaligen TEC-Irregularitäten. Aus diesem Grund wurde zusätzlich Fokus auf die Charakterisierung von residuellen Signaturen der Phase und Faraday-Rotation gelegt. Schließlich wird als ein potentieller Anwendungsfall die Nutzung der ionosphärischen Signatur zur Schätzung der Höhe der ionosphärischen Unregelmäßigkeiten auf der Grundlage von Szintillationsmustern in einem ALOS-2/PALSAR-2-Datensatz gezeigt.

Die in dieser Arbeit entwickelten Algorithmen sind explizit für P-Band SAR-Daten im Rahmen von Biomass konzipiert. Die Techniken werden in der „Commissioning Phase“ und während der nominellen Mission hilfreich sein. Die Erkenntnisse und Beiträge gehen jedoch über Biomass hinaus. Sie haben hohes Potential, im Rahmen neuer L-Band-Systeme wie dem NASA-ISRO Synthetic Aperture Radar (NISAR) angewendet zu werden, sowie auf zukünftige Radar-Sounder Missionen angepasst zu werden.

Contents

List of Figures

List of Tables

List of Acronyms and Abbreviations

AGB	Above Ground Biomass
ALOS	Advanced Land Observing Satellite
BEEPS	Biomass End-to-End Performance Simulator
CME	Coronal Mass Ejection
DoY	Day of the Year
DEM	Digital Elevation Model
DLR	German Aerospace Center
ECEF	Earth-Centered, Earth-Fixed
ESA	European Space Agency
EUV	Extreme Ultraviolet
FR	Faraday Rotation
GNSS	Global Navigation Satellite System
GPP	Ground Processor Prototype
GPS	Global Positioning System
IGR	International Geomagnetic Reference Field
IONEX	IONosphere maps EXchange
IRF	Impulse Response Function
IRI	International Reference Ionosphere
ISLR	Integrated Sidelobe Ratio
MAM	Multiple Aperture MapDrift
MDA	MapDrift Autofocus
MSFR	Multi-Squint Faraday Rotation
MoCo	Motion Compensation
MPS	Multiple Phase Screen
NED	North, East, Down
NISAR	NASA-ISRO Synthetic Aperture Radar
LOS	Line Of Sight
LS	Least Squares
LU	Lower-Upper decomposition
PALSAR	Phased Array L-band Synthetic Aperture Radar
PCA	Phase Curvature Autofocus
PGA	Phase Gradient Autofocus
PSD	Power Spectral Density
PSLR	Peak-to-Sidelobe Ratio
QPE	Quadratic Phase Error

RCS	Radar Cross Section
RDA	Research and Development in Aerospace GmbH
ROSE-L	Radar Observing System for Europe in L-band
SAA	South Atlantic Anomaly
SADI	Sub-Apertures for Disturbance Injection
SAR	Synthetic Aperture Radar
SAOCOM	Satélite Argentino de Observación COn Microondas, Spanish for Argentine Microwaves Observation Satellite
SLC	Single-Look Complex
STFT	Short-Time Fourier Transform
iSTFT	Inverse Short-Time Fourier Transform
TEC	Total Electron Content
TECU	TEC Unit
RMS	Root-Mean-Square
SNR	Signal-to-Noise Ratio
STEC	Slant TEC
STECU	Slant TEC Unit
UPC	Universitat Politècnica de Catalunya
UT	Universal Time
UV	Ultraviolet
VHF	Very High Frequency
VTEC	Vertical Total Electron Content
WBMOD	Wideband Ionospheric Scintillation Model
WLS	Weighted Least Squares

List of Constants

c_0	Speed of light in vaccum $299792458\,\mathrm{m/s}$
$\mathrm{m_e}$	Electron mass $9.1093837139 \cdot 10^{-31}\,\mathrm{kg}$
$\mathrm{r_e}$	Classical electron radius $2.8179403227 \cdot 10^{-15}\,\mathrm{m}$
$\mathrm{q_e}$	Electron charge $1.60217663 \cdot 10^{-19}\,\mathrm{C}$
ζ	$\frac{\mathrm{q_e^2}}{8 \cdot \pi^2 \cdot \epsilon_0 \cdot \mathrm{m_e}} \approx 40.31\,\mathrm{m^3/s^2}$
ϵ_0	Vacuum permittivity $8.8541878188 \cdot 10^{-12}\,\mathrm{C^2 \cdot kg^1 \cdot m^3 \cdot s^2}$

Mathematical Notations and Functions

$\sec$	Secant function
$\sin$	Sine function
sinc	Sinc function
$\cos$	Cosine function
$\exp$	Exponential function
j	$\sqrt{-1}$ Imaginary constant
Li_2	Euler dilogarithm
rec	Rectangle function
$^{\mathrm{T}}$	Transpose
$\Phi_{\ldots}$	PSD of . . .
$\circ$	Hadamard elementwise product
$\langle\cdot\rangle$	Spatial average

Latin Symbols

a		Anisotropy along $\hat{\kappa}_x$
$\mathcal{A}$		Replicas or aliasing
b		Anisotropy along $\hat{\kappa}_y$
B_{a}	Hz	Doppler bandwidth
B_{r}	Hz	Range bandwidth
$\vec{B}$	T	Geomagnetic field vector
$\vec{B}_{\mathrm{p}}$	T	Geomagnetic field vector projected onto ionospheric plane along $\hat{k}$
$\mathbf{C}$		Correlation matrix
$\hat{\mathbf{C}}$		Complementary matrix (Section 3.1.2)
$C_k L$		Vertically integrated strength of turbulence at the 1-km scale
$\vec{E}$		Jones vector

f	Hz	Frequency
f_0	Hz	Carrier frequency
f_a	Hz	Doppler frequency
f_p	Hz	Plasma frequency
H_az		Matched filter for azimuth compression in range-Doppler domain
h_rg		Matched filter for range compression
h_sat	m	Satellite orbit height
h_iono	m	Ionospheric irregularities height
$\mathbf{I}$		Identity matrix
K_a	s^{-2}	Azimuth Doppler rate
K_r	s^{-2}	Chirp rate
k	1/m	Carrier wavenumber
$\hat{k}$		Unitary LOS vector
$\hat{k}_\mathrm{bc}$		Unitary LOS vector at the center of the beam
$\mathbf{L}$		Linear transformation matrix
L		Linear interpolation operator (Section 6.1)
L_a	m	Antenna length
L_sa	m	Synthetic apeture length
$L_\mathrm{sa,iono}$	m	Synthetic apeture length projected at ionospheric height
$\mathbf{M}$		Measured scattering matrix
$\hat{n}$		Normal to ionospheric plane
N_e	m^{-3}	Electron density
N_i	m^{-3}	Ion density
p		Phase spectral index
p_sat	[m, m, m]	Satellite position
R_0	m	Range of closest approach
R_iono	m	Range from the satellite to the ionosphere
$\mathbf{S}$		Scattering matrix
s_rc		Range compresssed signal
s_rx		Received complex signal
s_tx		Transmitted pulse
t_a	s	Azimuth slow time
v_g	m/s	Group velocity
v_p	m/s	Phase velocity
v_sat	m/s	Satellite velocity
$\hat{v}_\mathrm{sat}$		Direction of the satellite motion
$\vec{v}_\mathrm{sat}$	m/s	Satellite velocity vector
x	m	Azimuth coordinate
$\mathbf{W}$		Diagonal weight matrix

Greek Symbols

β_a	rad	Squint angle
γ		Coherence
Δa	pixel	Shift between sub-looks
Δt	s	Time delay
Δl	m	Increase in slant range
Δr	m	Interferometric range change
Δx	m	Squint horizontal displacement
Θ	rad	Geographic longitude
θ	rad	Incidence angle onto the ionospheric plane or onto the ground
$\vec{\kappa}_x$	m^{-1}	Transversal wavenumber vector in the geomagnetic North direction
$\vec{\kappa}_y$	m^{-1}	Transversal wavenumber vector in the geomagnetic East direction
κ_0	m^{-1}	Irregularity outer scale wavenumber
$\vec{\kappa}_\perp$	m^{-1}	Transversal wavenumber vector
Λ	rad	Geographic latitude
λ	m	Wavelength
μ		Refractive index
$\sigma_{\dots}$		Standard deviation or uncertainty of . . .
$\sigma^2_{\dots}$		Variance of . . .
υ	rad	Angle between the velocity vector and geomagnetic North direction (horizontal plane)
ϕ	rad	Phase delay (or advance)
$\ddot{\phi}$	$\mathrm{rad/s}^2$	Second derivative of phase error
ϕ_Q	rad	Quadratic phase history
φ	rad	Angle between the x direction and the horizontal projection of $\hat{k}$
ψ	rad	Signal phase (Section 2.1)
		Magnetic inclination
Ω	rad	Faraday rotation angle

To the kids who believe that science isn't meant for them because of where they come from or how they look.

Acknowledgments

The pages of this thesis only reflect part of the technicalities learned in the past five years at the Microwaves and Radar Institute of the German Aerospace Center (DLR-HR). The process was challenging, but it also taught me about myself and made me eager to become a better student, colleague and scientist. I am forever thankful to my supervisor, Marc Rodriguez-Cassola, for leading me in the process and never doubting me. Thanks for the technical advice, the discussion, the good criticism, for pushing me to do what I could not imagine, and for standing on my side when I needed visibility or the situations were unfavorable for me. I would also like to extend my gratitude to Prof. Gerhard Krieger for supporting my initiatives and being the fundamental gear I needed for the completion of this thesis. Likewise, I thank Prof. Alberto Moreira for giving me the extraordinary opportunity to carry out my thesis in this stimulating environment and always guiding me when important decisions had to be taken. Additionally, I am indebted to my unofficial mentor, Pau Prats-Iraola. Thanks for taking the time to discuss and review my work when it did not seem possible and for helping me have a broader perspective every time I needed a little push. Finally, I would like to thank Kostas Papathanassiou, Jun Su Kim and Adriano Camps (together with the RDA team) for the discussions, teachings and revisions that helped me complete this work.

I will not forget the bad parts (the sleepless nights, the anxiety, the frustration...), and if anything, I take with me that if I do not get my things done, no one else will. I will not forget the good parts either: the collaborations with my colleagues, the side activities that became traditions and being there for each other when we needed it the most. From the beginning to the end, I am grateful I was accompanied by my friends in the SAR Missions group: Eduardo, Dominik, Andi, Jalal, Mai, Reuben and Maria. The collaborations beyond the PhD were infinitely fruitful, and the (emotional) support made it feel as if the thesis was a piece of teamwork. I cannot list them all, but I thank everyone who was there for the most memorable moments: the conferences (and the conference parties), the dinners, the hikes, the sledding days, our annual ice skating evenings, and the dance nights!

I thank my parents, Pilar and Harol, as well as my brother Camilo, for teaching me that even when the world falls apart, literally, there is always a way forward. It seems that there is a scientist prototype out there, but with their help, being brown, immigrant and queer was never an impediment. That is why my multiple international host families also deserve mention: the Turza family in Austria, the Razak family in Malaysia and the Trautmann family

in Germany. My last words go to Eduardo Goulart for being my companion, my shelter and the best cheerleader. Thank you for making me more than *another PhD candidate* and close this chapter with a raised chin and looking ahead.

1 Introduction

1.1 Motivation and State of the Art

Monitoring the changes in the Earth system at a global scale is an ambitious yet necessary task to deal with the biggest challenge of the 21st century: Fighting climate change. The most fundamental aspect is understanding the carbon cycle, considering the carbon exchange processes between the atmosphere, land, and ocean. Spaceborne remote sensing technologies can efficiently facilitate this task with periodic observations and wide coverage. A particular aspect of interest is the net carbon balance of the land use and the carbon sink characteristic of the forests. Synthetic Aperture Radar (SAR) has shown to be the best candidate to achieve this task; as a high-resolution active sensor (it illuminates a region of interest and measures echoes), it is capable of measuring 2-D maps of complex reflectivity that with appropriate interferometric and polarimetric processing, can be translated into forest parameters such as tree vertical structure and Above Ground Biomass (AGB) [20]. In addition, SAR is capable of monitoring other global warming indicators, such as the state of ice terrains covered by permafrost and glaciers [89, 100, 105].

SAR allows for (almost) all-weather observations in the absence of Sun illumination, and the measurement requirements can be achieved by adapting the carrier frequency and bandwidth of the system. On the one hand, while high frequencies offer very high resolution and interferometric sensitivity, they present high temporal decorrelation in forested areas and do not fully exploit the penetration capability of radar. On the other hand, experiments with low-frequency systems demonstrated the possibility of penetrating dense tree canopies to the ground and low decorrelation, beneficial for interferometric and differential interferometric processing [46]. The capabilities of spaceborne low-frequency SAR have been proven with

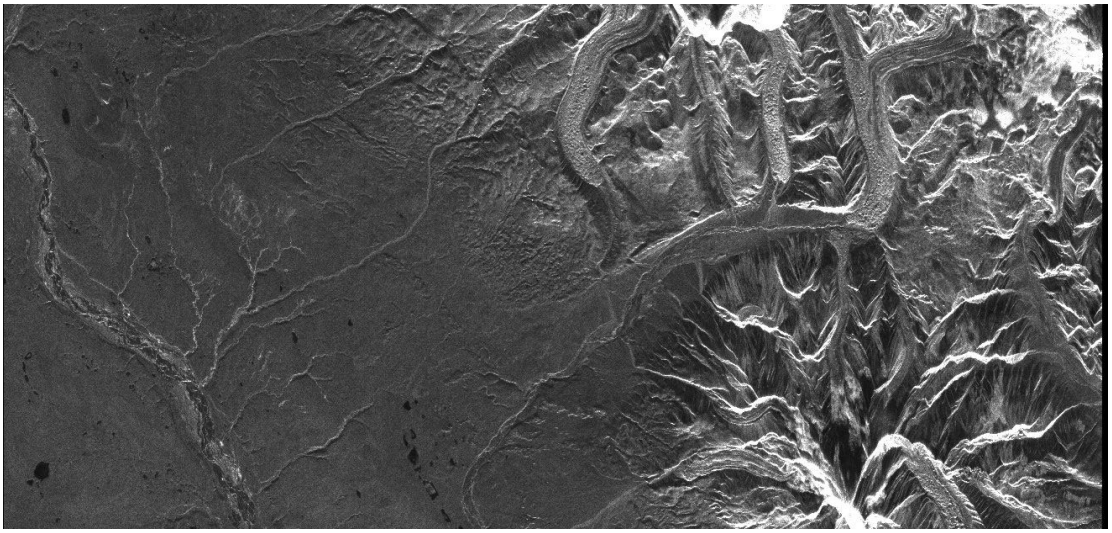

Figure 1.1: ALOS-PALSAR acquisition over a glacier in Alaska ALPSRP063051250. The along-track direction is horizontal and the satellite is observing from the top of the figure. The acquisition is made in strip-map mode and the polarization is HH.

several L-band missions (e.g., ALOS-PALSAR [87] and ALOS-2/PALSAR-2 or SAOCOM [37]). More missions are currently in preparation for launch (e.g., NISAR [58]) or in an early development stage (e.g., ROSE-L [27]). As an example, Figure 1.1 shows an acquisition of the ALOS-PALSAR instrument of glacier tongues next to the Copper River in Alaska; it shows glaciers with the characteristic ice displacement features on the right, which then melt and flow through the forest into the main river. The ESA Biomass Earth Explorer will be the first spaceborne mission operating a fully polarimetric P-band SAR to observe such processes. The challenges are enormous in many aspects, one of them being the impact of the ionosphere on the data.

At low frequencies (L and P band), the troposphere is considered transparent, and the propagation distortions are considered to come from the ionosphere (the upper part of the Earth's atmosphere made of ionized plasma). The ionosphere has a *dispersive* nature, meaning that its index of refraction is frequency dependent and at L and P bands introduces considerable time delays and phase errors [112, 110]; these undesired effects are seen as geolocation errors and defocusing apart of interferometric decorrelation [10]. At these bands, the absorption is considered negligible. The anisotropic property of the ionosphere also causes the power to be redistributed in different polarimetric channels, a phenomenon known as Faraday Rotation (FR), which affects the quality of the products derived from the polarimetry [28]. Without a dedicated ionospheric calibration step, the data will remain distorted, leading to incorrect interpretations of the results. In [3], an analysis of the expected impact of the low-latitude ionosphere in the frame of the Biomass mission was developed. It was determined that spatial gradients and scintillations are expected to degrade the quality of the

data significantly.

The ionospheric disturbances are known to other technical and scientific applications that range from the Global Positioning System (GPS) [8, 30] to radio astronomy [17, 18], and due to their interaction with the space weather and Earth's interior, they wake the interest of a broad scientific community. Different systems have been developed for sensing the ionosphere locally with ionosondes or at a global scale with a network of Global Navigation Satellite System (GNSS) receivers [77, 49], among others. Even though the number of stations is increasing, the availability is still limited and the uneven distribution hinders the observation of small-scale characteristics. In this sense, SAR unlocks new ways to extract information about the state of the ionosphere as it scans the target area. The ionospheric calibration involves an imaging step in which the disturbances can be inverted into an ionospheric map, whose resolution and characteristics will depend on the technique used. In L-band systems, it was proven that the spatial resolution of the ionospheric maps can be brought down to the kilometer scale [76] based on FR estimations, allowing for an unprecedented imaging of the small-scale ionospheric irregularities characteristic of the polar areas. At low latitudes, effort has been put into the mitigation of intensity scintillations; for example, in [88], frequency domain filtering is used to mitigate the intensity stripes characteristic of low-latitude scintillation. However, even though the FR-baed techniques have proven to give good results in correcting polarimetric and phase distortions at high latitudes [62], there is still the need for consolidated calibration algorithms that also work well at mid and low latitudes.

The ionospheric disturbance maps obtained during the correction can be used to invert geophysical parameters, and the results complement those of other ionospheric sensing techniques. This principle has been extensively applied to L-band images from the ALOS satellites. Gomba et al. [42] fit the spectrum of the differential phase recovered after interferometric calibration to estimate the turbulent characteristics of the ionosphere at high latitudes. Jui et al. [51] use the intensity scintillation signature to extract turbulent parameters of the low-latitude ionosphere. Finally, in [91] and [61], synergy examples between SAR and ground-based observations of the ionosphere were shown. Because of the high phase sensitivity of SAR and the relatively large range bandwidth, ionospheric effects have also been observed and calibrated in Sentinel-1 (C-band) interferometric products. The impact on the images and the algorithms must be revisited for the P-band case to adapt the correction and assess new ways of extracting information. To this end, first of all, it is necessary to improve the simulation chain with accurate ionospheric injection methods.

The SAR principle works by coherently adding different looks to a target as a moving platform passes next to it. In the current literature, the *beam-center* approximation is a common assumption. The ionospheric effects are considered according to what the radar beam sees in its zero-Doppler (center of the beam for a non-squinted geometry) direction. However, the variability inside the beam is neglected. An established method for the injection, estimation and correction of ionospheric disturbances is *semi-focusing* the image to the height of where the disturbances take place [62]. Then, beam-center ionospheric injection intro-

duces the ionospheric disturbances with a simple averaging filter, lowering the capability of accounting for small-scale irregularities without considering the impact of pointing angle variability. These kinds of errors are non-negligible in a system such as Biomass. Multi-squint [78, 99, 86] introduces different ways to exploit the separation of the different looks represented by squinted views of the synthetic aperture acquisition to correct phase distortions. Multi-squint techniques in the ionospheric domain cannot be adequately assessed without aperture-dependent disturbance injection.

Squinted-look separation has also been used for the estimation of other geophysical parameters, such as the location of ionospheric irregularities by means of the FR parallax [62] and by the combination with azimuth sub-apertures at low-latitudes [60]. Squinted-look separation has definitely been shown to be a powerful technique for extracting the ionospheric signature from the SAR data, and further applications will be investigated in the development of this thesis.

1.2 Objectives and Organization of this Thesis

This thesis deals with different kinds of disturbances in low-frequency radar imaging due to trans-ionospheric propagation, as well as the exploitation of the 2-D high resolution offered by SAR to extract geophysical information. Understanding the effects and the development of simulation and calibration algorithms unlocks the possibility of further developing operational low-frequency SAR and future low-frequency radar remote sensing missions such as an Earth-orbiting radar sounder. Parallel to the ionospheric compensation point of view, high-resolution ionospheric mapping allows putting the research focus on small-scale irregularities, a significant challenge to the community with current ionospheric sensing systems.

In this work, the entire life cycle of the ionospheric signal present in low-frequency SAR is presented as follows:

1. *Simulation*: It is necessary to develop accurate simulation tools within a level of complexity that keeps the implementation efficient to understand the impact of the ionosphere in radar images as well as to implement functional correction algorithms. At this step, an accurate ionospheric injection into simulated data is necessary to develop algorithms that are directly scalable to real scenarios.

2. *Calibration*: Up to now, algorithms for compensation in L-band SAR systems (like ALOS, ALOS-2, SAOCOM...) are available, but with the coming Biomass mission (P band), they must be adapted and further developed. Apart from the FR-based approaches, complementary autofocus algorithms that directly correct for phase errors and defocusing are needed. The cooperation of different calibration approaches compensates for the independent limitations in challenging scenarios.

3. *Error characterization*: Even though multiple methods for ionospheric correction have been proposed, there has not been much effort to characterize the residual errors of the

disturbance maps or the impact of the residuals in the SAR images after correction. This characterization is necessary for the appropriate interpretation of the corrected data.

4. *Extraction of parameters*: The fact that the ionosphere leaves a footprint in radar images should be seen as an opportunity to extract geophysical information from the disturbance maps that serve the scientific community. In this work, we focus on the intensity scintillations to estimate the location of the ionospheric irregularities. This information will also be necessary for the appropriate correction of the disturbed data.

In the preparation of the Biomass mission, the Microwaves and Radar Institute of the German Aerospace Center (DLR) has developed the Biomass End-to-End Performance Simulator (BEEPS) [90] and the Ground Processor Prototype (GPP) [79]. These tools were used, and contributions to them were made during this thesis. BEEPS simulates acquisitions with the entire Biomass system, accounting for the propagation of the orbit and exact observation geometry, the instrument and the injection of the ionosphere. In the absence of spaceborne P-band images, BEEPS also simulates the complex reflectivity of forest scenarios. Reverse processing is used in BEEPS to simulate raw data with the Biomass parameters and system and ionospheric disturbances. The contributions to BEEPS related to this work focused on the generation of ionospheric scenarios in cooperation with the Universitat Politècnica de Catalunya (UPC) and Research and Development in Aerospace GmbH (RDA) [22] and the injection of the ionospheric disturbances in the data. The GPP is a prototype of the operational processor, where the image formation and calibration algorithms are developed and tested. The contributions to the GPP related to this work were in the field of the ionospheric calibration step.

This thesis is organized as follows:

- Chapter 2 serves as a short introduction to the basics of SAR remote sensing, focusing on the aspects needed to follow the rest of the thesis. It goes from the acquisition geometry to the image focusing (compression), passing by an explanation of the SAR signal model. Since we are going to speak about the polarimetric cross-talk introduced by the ionosphere, some short definitions of polarimetry will be necessary, too.
- Chapter 3 focuses on the description of the ionosphere and the role it plays in radar remote sensing. Here, a detailed explanation of the different kinds of disturbances can be found, as well as the most relevant state-of-the-art methods for their correction.
- Chapter 4 focuses on the simulation of SAR data and the injection of ionospheric disturbances. An aperture-dependent method for disturbance injection by sub-apertures is proposed. This method drops many of the assumptions and constraints imposed on current beam-centered approaches available in the literature while still being efficiently implemented and parallelized.

- Chapter 5 introduces three calibration approaches developed during this work: One based on the estimation of the FR, one MapDrift Autofocus (MDA) and one interferometric autofocus. The principle, simulated results and a discussion of their limitations are presented for each of them.
- Chapter 6 deals with the error characterization of the FR-based calibration and the MDA previously presented in Chapter 5 for correcting the disturbances caused by small-scale ionospheric irregularities. It shows that it is possible to characterize performance limits and the structure of the residual disturbance maps by analyzing the Power Spectral Density (PSD) function of the ionospheric irregularities and the frequency response of the linear operations carried out by the calibration filters.
- Chapter 7 presents how a maximum contrast autofocus of ionospheric intensity scintillations can be used to estimate the irregularity height. The case is made on an L-band ALOS-2/PALSAR-2 image close to the Equator. The method is complemented with a geometric approach that uses feature tracking of the intensity scintillation in azimuth sub-looks to validate the findings.
- Chapter 8 closes this thesis with a summary and highlight of the contributions and an outlook of future work.

1.3 Publications in the Frame of the Cumulative Thesis

The following publications form the basis of the cumulative thesis and were developed with the author as the primary contributor. The publications are attached in the Appendix at the end of the thesis. In the following, the contributions of the different authors to each of the publications are listed based on the CRediT-System (Contributor Roles Taxonomy).

Pub1 *Aperture-Dependent Injection of Ionospheric Perturbations into Simulated SAR Data.* This publication is a result of the collaboration with the DLR colleagues listed in the paper, with the author of this thesis as the primary contributor. The co-authors had a supervision role, providing the resources and a critical review of the manuscript. In addition, Marc Rodriguez-Cassola contributed to the main conceptualization of the paper and the methodology. The author of this thesis carried out the following roles: Conceptualization, data curation, formal analysis, investigation, methodology, software development, validation, visualization and writing - original draft and editing.

Pub2 *An Autofocus Algorithm for the Recovery of Ionospheric Signatures in the Biomass Mission.* This publication is a result of the collaboration with the DLR colleagues listed in the paper, with the author of this thesis as the primary contributor. The co-authors had a supervision role, providing the resources and a critical review of the manuscript. Marc Rodriguez-Cassola and Pau Prats-Iraola conceptualized the problem and gave initial indications regarding the methodology. The author of this thesis carried out

the following roles: Data curation, formal analysis, investigation, contributions to the methodology, software development, validation, visualization and writing - original draft and editing.

Pub3 *Towards and Interferometric Autofocus for the Estimation of Ionospheric Signatures in Biomass.* This publication is a result of the collaboration with the DLR colleagues listed in the paper, with the author of this thesis as the primary contributor. The co-authors had a supervision role, providing the resources and a critical review of the manuscript. Marc Rodriguez-Cassola and Pau Prats-Iraola facilitated the simulation environment used in the software development. The author of this thesis carried out the following roles: Conceptualization, data curation, formal analysis, investigation, methodology, software development, validation, visualization and writing - original draft and editing.

Pub4 *Analysis of the Retrieval Performance of 2-D Ionospheric Irregularity Maps in the Biomass Mission.* This publication is a result of the collaboration with the DLR colleagues listed in the paper, with the author of this thesis as the primary contributor. The co-authors had a supervision role, providing resources based on existing published and unpublished works and a critical review of the manuscript. Marc Rodriguez-Cassola and Pau Prats-Iarola contributed to the conceptualization of the paper. The author of this thesis carried out the following roles: Data curation, formal analysis, investigation, methodology, software development, validation, visualization and writing - original draft and editing.

Pub5 *Estimating the Ionospheric Height from Amplitude Scintillation Signatures in SAR Images.* This publication is a result of the collaboration with the DLR colleagues listed in the paper, with the author of this thesis as the primary contributor. The co-authors had a supervision role, providing the resources and a critical review of the manuscript. In addition, Jun Su Kim and Konstantinos Papathanassiou conceptualized the main problem based on observations of real data. Marc Rodriguez-Cassola facilitated the simulation tools used in the software development. The author of this thesis carried out the following roles: Data curation, formal analysis, investigation, methodology, software development, validation, visualization and writing - original draft and editing.

2
SAR Remote Sensing

The discovery of the Synthetic Aperture Radar (SAR) principle by Carl Wiley in the 1950s [108] for the generation of high-resolution remote sensing images allowed the development of dedicated satellites for military and civil applications. In this chapter, we proceed to summarize the most relevant aspects and parameters of SAR required to follow this thesis. In Section 2.1, we introduce the SAR principle and acquisition geometry. In Section 2.2, the signal model and compression for image formation are explained. Here, we also look for the resolution and performance relations based on the analysis of the impulse response function. Finally, Sections 2.3 and 2.4 highlight the interferometric and polarimetric definitions needed to follow this thesis.

2.1 Synthetic Aperture Radar Imaging

SAR is an active sensor on a moving platform that illuminates a scene with electromagnetic waves and measures the delays and complex reflectivity of the returned echoes. The aperture synthesis accomplishes high along-track resolution by exploiting the relative motion between a fast-moving platform (a satellite in the spaceborne case) and the targeted scene. As depicted in Figure 2.1, a target is illuminated by a moving antenna that displaces with a velocity $\vec{v}_{\mathrm{sat}}$ in the azimuth direction; note that this is a simplified linear track representation and an effective velocity v should account for the curved satellite trajectory and the relative motion between the satellite and the target. The transmitted pulse has duration τ. The radar coordinates of the target are azimuth and slant range: the along-track position and the range (distance) from the satellite track. Note that in this representation and along this thesis, the acquisitions are

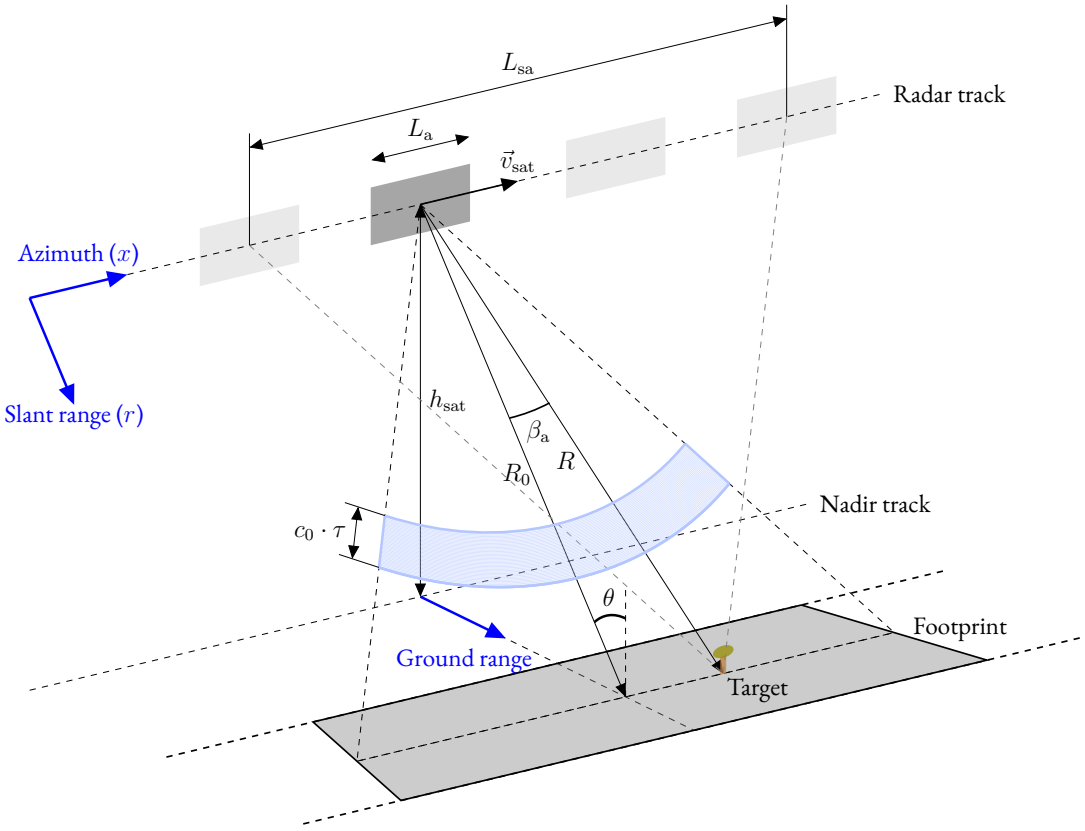

Figure 2.1: Simplified SAR geometry.

considered at zero Doppler (the pointing of the antenna beam center is perpendicular to the satellite motion).

The platform moves at an altitude h_{sat} above the ground and the acquisition is done with a side-looking geometry to avoid echo return ambiguity from both sides. The acquisition is composed of the targets covered by the sliding footprint and the incidence angle of a specific target θ is the one between the direct look at the moment of closest approach and the local vertical. All the targets along a closest approach distance R_0 form a *range bin* in the radar coordinates and the actual distance between the satellite and the target at a given time is R. From the center of the beam, β_{a} is the squint angle to the target, which varies with the satellite motion. The high resolution is obtained by the combination of the different *looks* of the target across the approximate angles

$$\beta_{\text{a}} \in \left[-\frac{\lambda}{2 \cdot L_{\text{a}}}, \frac{\lambda}{2 \cdot L_{\text{a}}} \right] , \tag{2.1}$$

where λ is the carrier wavelength and L_{a} is the azimuth antenna length. The range variation as the satellite moves along azimuth corresponds to a Doppler frequency shift, related to the

instantaneous squint angle as

$$f_{\mathrm{a}}\left(t_{\mathrm{a}}\right) = \frac{2 \cdot v \cdot \sin \beta_{\mathrm{a}}\left(t_{\mathrm{a}}\right)}{\lambda}\,, \tag{2.2}$$

where t_{a} is the azimuth *slow time*. For a target at R_0, the synthetic aperture length is approximately

$$L_{\mathrm{sa}} \approx R_0 \cdot \frac{\lambda}{L_{\mathrm{a}}} \tag{2.3}$$

which corresponds to a synthetic aperture time

$$T_{\mathrm{a}} \approx \frac{L_{\mathrm{sa}}}{v}\,. \tag{2.4}$$

2.2 SAR Signal Model, Compression and Resolution

In SAR imaging, the transmitted pulses s_{tx} are usually *chirps*: Waveforms with quadratic phase modulation

$$s_{\mathrm{tx}}(t) = \mathrm{rect}\left(\frac{t}{\tau}\right) \cdot \exp\left(j \cdot 2 \cdot \pi \cdot f_0 \cdot t + j \cdot \pi \cdot K_r \cdot t^2\right)\,, \tag{2.5}$$

where t is the *fast time* in range, the rect function limits the pulse to the duration τ, f_0 is the carrier frequency and K_r is the chirp rate. Note that the range bandwidth of the transmitted pulse is given by

$$B_{\mathrm{r}} = K_r \cdot \tau\,. \tag{2.6}$$

The phase of the signal is

$$\psi = 2 \cdot \pi \cdot f_0 \cdot t + \pi \cdot K_r \cdot t^2\,, \tag{2.7}$$

and the corresponding instantaneous frequency

$$f(t) = \frac{1}{2 \cdot \pi}\frac{\mathrm{d}\psi}{\mathrm{d}t} = f_0 + K_r \cdot t\,. \tag{2.8}$$

The echo from a point-like scatterer at slant distance R_0 returns after 2-way propagation time

$$t_0 = \frac{2 \cdot R_0}{c_0}\,, \tag{2.9}$$

where c_0 is the speed of light assuming vacuum. Ignoring attenuation during propagation and the measured amplitude of the target, the received signal after coherent demodulation is

$$s_{\mathrm{rx}}(t) = \mathrm{rect}\left(\frac{t - t_0}{\tau}\right) \cdot \exp\left(-j \cdot 2 \cdot \pi \cdot f_0 \cdot t_0 - j \cdot \pi \cdot K_r \cdot (t - t_0)^2\right) + n(t)\,, \quad (2.10)$$

where $n(t)$ is additive noise.

Range Dimension

The high resolution in the slant range dimension is obtained by compressing the received signal with a matched filter [73] whose impulse response is the inverted complex conjugate of the quadratic component of the transmitted chirp

$$h_{\mathrm{rg}}(t) = \mathrm{rect}\left(\frac{t}{\tau}\right) \exp\left(-j \cdot \pi \cdot K_r \cdot t^2\right)\,. \quad (2.11)$$

The matched filter can be applied in the frequency domain and maximizes the Signal-to-Noise Ratio (SNR) of the output in the case of uncorrelated white noise while locating the scatterer at the correct slant range R_0. The compressed received signal is approximately (without a scaling constant)

$$s_{\mathrm{rg}}(t) \approx \mathrm{sinc}\left(B_{\mathrm{r}} \cdot t\right)\,, \quad (2.12)$$

where sinc is the cardinal sine function. The distance between the maximum and the first null of $|s_{rg}(t)|^2$ gives the slant range resolution

$$\delta r_g \approx \frac{c_0}{2 \cdot B_{\mathrm{r}}}\,, \quad (2.13)$$

which can be transformed into ground range with the sine of θ.

Azimuth Dimension

From Figure 2.1, it is possible to see that the *range history* of the satellite motion is approximately [26]

$$R = \sqrt{R_0^2 + x^2} \approx R_0 + \frac{(v \cdot t_{\mathrm{a}})^2}{2 \cdot R_0}\,, \quad (2.14)$$

where t_{a} is the azimuth *slow time*. The corresponding received phase history at the carrier frequency is

$$\psi(t_{\mathrm{a}}) = \frac{4 \cdot \pi \cdot R_0}{\lambda} + \frac{2 \cdot \pi \cdot (v \cdot t_{\mathrm{a}})^2}{\lambda \cdot R_0}\,, \quad (2.15)$$

which also shows a quadratic behavior. Similar to (2.8), from the instantaneous azimuth frequency, it is possible to define the Doppler rate K_{a}

$$K_{\mathrm{a}} = \frac{2 \cdot v^2}{\lambda \cdot R_0} \,. \tag{2.16}$$

The received echoes can be processed in azimuth with a matched filter in the range-Doppler domain with the hyperbolic phase function [70]

$$H_{\mathrm{az}}(R_0, f_{\mathrm{a}}, v) = \exp\left(-j \cdot \frac{4 \cdot \pi}{\lambda} \cdot R_0 \cdot \sqrt{1 - \left(\frac{\lambda \cdot f_{\mathrm{a}}}{2 \cdot v}\right)^2}\right) \,, \tag{2.17}$$

where for non-squinted acquisitions, the Doppler frequency vector is limited by the Pulse Repetition Frequency (PRF)

$$-\frac{PRF}{2} \leq f_{\mathrm{a}} \leq \frac{PRF}{2} \,. \tag{2.18}$$

It can be shown that the result of the compression is approximately

$$s_{\mathrm{az}}(t_{\mathrm{a}}) \approx \mathrm{sinc}\left(B_a \cdot t_{\mathrm{a}}\right) \,, \tag{2.19}$$

where the Doppler bandwidth is given by

$$B_{\mathrm{a}} = \frac{2 \cdot v}{L_{\mathrm{a}}} \,. \tag{2.20}$$

Finally, the azimuth resolution achieved by the azimuth compression is

$$\delta r_a \approx \frac{L_{\mathrm{a}}}{2} \,. \tag{2.21}$$

Note that the azimuth resolution is independent of the range and only limited by the antenna size in a Single Look Complex (SLC) image. However, *multi-looking* (averaging) is commonly applied to reduce the effect of noise and *speckle* in the images. Speckle is an effect of the coherent superposition of multiple targets within a resolution cell, giving a grainy texture to the images. The Doppler bandwidth is also the minimum sampling frequency in azimuth for non-aliased acquisitions within the main lobe. In practice, the transmission and receiving of the echoes occur at a higher PRF with an oversampling factor osf.

System performance

From (2.12) and (2.19), the Impulse Response Function (IRF) of an ideal point target takes the form

$$I(\mathrm{r}, x) \approx \mathrm{sinc}\left(\frac{2 \cdot B_{\mathrm{r}}}{c_0} \cdot (r - R_0)\right) \cdot \mathrm{sinc}\left(\frac{2}{L_{\mathrm{a}}} \cdot (x - x_0)\right) \,. \tag{2.22}$$

Note that in (2.22), the target is seen as a 2-D sinc placed in the radar coordinates (R_0, x_0). The half-power widths in slant range and azimuth determine the resolution. However, the IRF also presents sidelobes that might lower the image quality and make it difficult to detect weak scatterers. Two important performance metrics to characterize the focusing of the processed images are the Peak-to-Sidelobe Ratio (PSLR) and the Integrated Sidelobe Ratio (ISLR) of point targets. In a real system, these targets can be, for example, corner reflectors or transponders. The PSLR is the ratio in intensity between the highest sidelobe and the main lobe. The highest sidelobe pair is usually the first. The ISLR is the ratio between integrated energy outside the main lobe and the energy of the main lobe.

As it will be seen in Section 3.3, propagation phase errors degrade the matched filter output, having a direct impact on these two parameters. In addition, the broadening of the main lobe produces a loss of spatial resolution. If the targets are not point-like but distributed (they extend over several resolution cells), then the direct effect is a loss of contrast and resolution. Non-vacuum propagation also affects the echo arrival time in (2.9), which, if not compensated, is seen as a geolocation error.

2.3 Interferometry

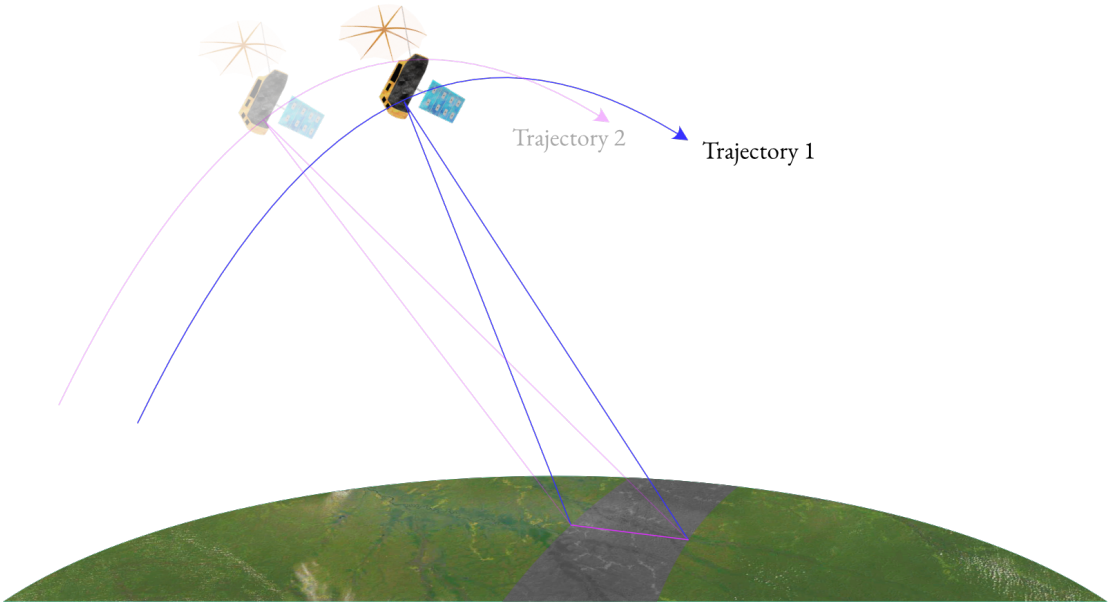

Figure 2.2: InSAR with spatial baseline.

SAR Interferometry (InSAR) is a well-established technique that exploits the phase difference between two SAR acquisitions to resolve several geophysical parameters and phenomena, such as terrain topography, deformation and displacement [71]. The *baselines* between

the acquisitions can be temporal, spatial or both. Figure 2.2 depicts the use of InSAR from two parallel tracks with a monostatic system such as Biomass. The temporal baselines are acquired by repeatpass interferometry; Differential Interferometric SAR (DInSAR) enables new ways for ice and permafrost monitoring [53, 93], and is sensitive to terrain deformation such as subsidence [36, 102, 13].

In traditional SAR, the image is projected into the azimuth-slant range plane, and the information in the normal coordinate is lost. Spatial baselines are acquired by slightly changing the acquisition geometry (either with a companion satellite or a slightly different orbit path), enabling the resolution of this last component and the generation of Digital Elevation Models (DEMs). Spatial baselines also allow to resolve vertical structures of forest [101] and ice sheets [33] by means of tomography. If the geometry is changed just slightly with a parallel track, then it is reasonable to assume that the complex reflectivity of one fixed target remains the same and the phase difference between the acquisitions is

$$\Delta\psi = \frac{4 \cdot \pi}{\lambda} \cdot \Delta r \,, \tag{2.23}$$

where Δr is the range difference. Then $\Delta\psi$, h_{sat} and the perpendicular baseline can be used to resolve for the vertical coordinate of the targets [85].

InSAR and DInSAR exploit the phase difference between two or more acquisitions. Apart from the phase wrapping (ambiguous phase measurements when Δr is larger than half the wavelength), the coherence between the acquisitions needs to be sufficient to ensure that the measured phase $\Delta\psi$ fully represents Δr as in (2.23). The complex coherence in a pair of SAR images is given by [104]

$$\gamma = \frac{\langle s_1 \cdot s_2^* \rangle}{\sqrt{\langle s_1 \cdot s_1^* \rangle \cdot \langle s_2 \cdot s_2^* \rangle}} \,, \tag{2.24}$$

where s_1 and s_2 are the primary and secondary SAR acquisitions and * is the complex conjugate operator. $\langle \cdot \rangle$ is the spatial average over a moving window. The absolute value ranges from 0 to 1 and gives the degree of coherence (1 for full correlation), and the phase is an estimate of the phase difference between the acquisitions. Many factors affect the complex correlation; here, we highlight the most important for this thesis:

$$\gamma = \gamma_{SNR} \cdot \gamma_{\text{vol}} \cdot \gamma_{\text{temp}} \tag{2.25}$$

- γ_{SNR} is the decorrelation due to additive white noise. It depends on the SAR system's power and sensitivity as well as the strength of the scatterers in the scene. Regions with low backscattering are more affected by this kind of decorrelation.
- γ_{vol} is the volumetric decorrelation that occurs during the interaction with vertically separated scatterers inside volumetric targets such as ice or forest. It can be used to estimate the vertical profile of volume scatterers.

- γ_{temp} is the decorrelation caused by temporal changes between the interferometric SAR image acquisitions. These changes can reflect variations in the scatterer properties and their displacement or changes in the propagation medium. In this thesis, we will consider frequencies so low that can penetrate the forest canopy and detect elements that do not change much, such as the tree trunks and the ground. Then, the main temporal changes to be considered are given by changes in the refractive index inside the propagating atmosphere and ionosphere.

2.4 Polarimetry

The electric and magnetic fields that compose a plane electromagnetic wave are placed on a plane perpendicular to the propagation direction $\hat{z}$, with each of the fields described by two waves in the $\hat{x}$ and $\hat{y}$ coordinates. At a certain point, a representation of the electric field vector of a monochromatic, uniform plane wave with a constant polarization is given by the *Jones vector* [45]

$$\vec{E}_0 = \begin{pmatrix} E_{0,x} \cdot \exp(j \cdot \delta_x) \\ E_{0,y} \cdot \exp(j \cdot \delta_y) \end{pmatrix} , \tag{2.26}$$

where $E_{0,x}$ and $E_{0,y}$ are the amplitudes of the waves in each coordinate and δ_x and δ_y are their phases. In SAR remote sensing, the orthogonal coordinates are set to be one parallel to the ground (H) and the other (V) perpendicular to H and the propagation direction.

The incident wave $\vec{E}^i = (E^i_{\text{H}},\ E^i_{\text{V}})^{\text{T}}$ interacts with the scatterers and part of it is reradiated into space. In a monostatic system, the one to be considered in this thesis, we account for the part of the scattered wave that follows the same path back to the sensor. It is measured as $\vec{E}^s = (E^s_{\text{H}},\ E^s_{\text{V}})^{\text{T}}$ and the interaction with the scatterers is described by the *scattering matrix* $\mathbf{S}$. Then,

$$\vec{E}^s = \frac{\exp\left(-j \cdot k \cdot R\right)}{R} \cdot \mathbf{S} \cdot \vec{E}^i \, , \tag{2.27}$$

where

$$k = \frac{2 \cdot \pi}{\lambda} \tag{2.28}$$

is the wavenumber of the illuminating wave, $1/R$ accounts for the free space attenuation that occurs during the propagation from the target, and the exponential term is the phase delay that occurs between the scatterer and the receiver antenna.

The components of the scattering matrix

$$\mathbf{S} = \begin{pmatrix} S_{\text{HH}} & S_{\text{HV}} \\ S_{\text{VH}} & S_{\text{VV}} \end{pmatrix} \tag{2.29}$$

are complex amplitudes that describe the interaction of the electromagnetic wave with the scatterers and allow us to infer their properties. The first column corresponds to the wave transmitted in the H channel and received by both the H and V channels. The second column corresponds to the wave transmitted in the V channel. The elements in the main diagonal are called *co-pol terms* and the ones in the off-diagonal are called *cross-pol terms*. In a monostatic system, in the absence of distortions, $S_{\mathrm{HV}} = S_{\mathrm{VH}}$. *Polarimetric cross-talk* occurs when, either during the propagation or inside the system, energy is transferred from one polarimetric channel to another; if uncorrected, it leads to misinterpretation of the scattering properties and mechanisms in the targets.

3

The Ionosphere in Radar Remote Sensing

This chapter presents an overview of the ionospheric descriptions focusing on the relevant characteristics for radar remote sensing. Section 3.1 starts describing the ionosphere, including its geographic and temporal variations. Section 3.2 focuses on the change in refractive index in an ionized medium, and Section 3.3 focuses on all the disturbances present in radar remote sensing due to the dispersive nature of the ionosphere. It also discusses the impact in SAR with simulated and real examples. Section 3.4 highlights the most relevant state-of-the-art ionospheric correction approaches developed for SAR.

3.1 The Ionosphere

The ionosphere is the region that covers the upper part of the atmosphere starting at around 90 km height, where Ultraviolet (UV) and Extrem Ultraviolet (EUV) solar radiation have enough energy to produce ionized plasma out of the atmospheric particles [56]. The plasma remains quasi-neutral with the free ion and electron density nearly equal, $N_i \approx N_e$. To follow the traditional convention, we will refer to free electron density and electron content in this work; note that the heavier ions will interact with even longer frequencies. As it will be described in Section 3.2, the free electron concentrations are such that the changes in the propagation properties affect the trans-ionospheric propagation of radio waves and introduce distortions in the SAR measurements, especially in the lower-frequency range [112].

Figure 3.1 shows the layered representation of two free electron density distributions (one at day and one at night). Note the difference in the range of values between day and night and that during the day, the upper F-layer is divided into F1 and F2. The height of maximum

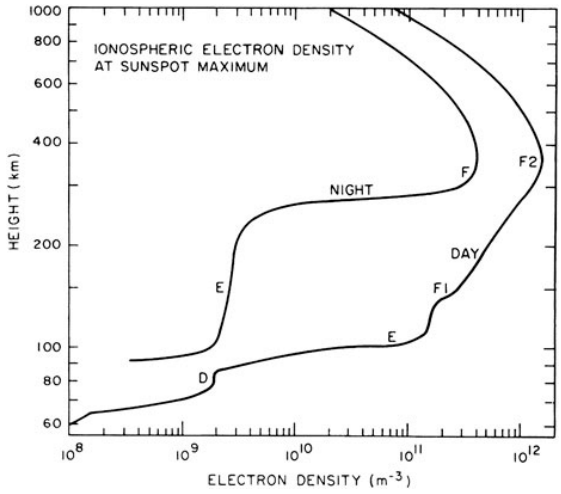

Figure 3.1: Idealized vertical electron density distribution in the Earth's ionosphere. The values are typical for a mid-latitude in times of solar maximum [103].

ionization is located in the F (or F2) layer, usually between 250 and 400 km. The primary source of plasma generation is solar illumination, which causes free electron excitation, and the global distribution varies during the day with geomagnetic latitude, time of the year and the sunspot cycle [103]. The total change in the radio waves measured in SAR is a result of the Total Electron Content (TEC) experienced by the waves on their way through the ionosphere,

$$TEC = \int_L N_\mathrm{e}\,\mathrm{d}l\,, \tag{3.1}$$

where l is the integration path length. The usual unit is called TEC Unit (TECU) and is defined as $\mathrm{TECU} = 10^{16}\,\mathrm{el/m^2}$. The integral of the electron density curves shown in Figure 3.1 from the ground to the outer boundaries of the ionosphere corresponds to the Vertical TEC (VTEC). In the case of SAR, the contribution from the orbit height upwards must be discounted and the vertical electron content has to be adapted to the side-looking geometry in what is referred to as Slant TEC ($STEC$). In this thesis, the mapping is done with the cosine of the incidence angle of the radar beam into the ionosphere. For the frequency ranges considered in this work, L and P band, the ray bending inside the ionospheric volume can be neglected.

Before going deeper into the description of the different regions of the ionosphere, we should comment on the Earth's magnetic field due to its importance in the definition of the different ionospheric regions, and later in Section 3.3, the impact of the ionosphere due to Faraday rotation (FR). In a first approximation, the Earth's magnetic field can be described as a dipole with the poles shifted from the Earth's rotation axis, causing the geomagnetic Equator to be tilted with respect to the geographic Equator, see Figure 3.2. The magnetization

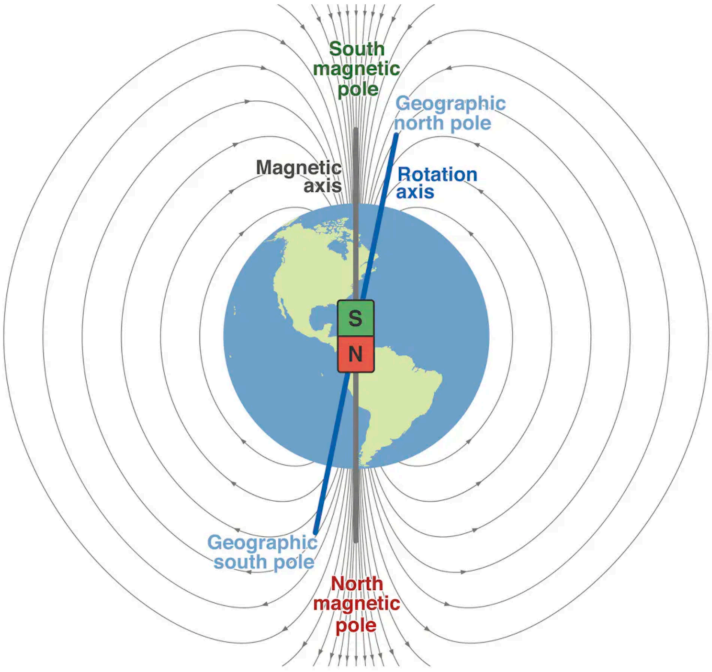

Figure 3.2: Idealized Earth's geomagnetic dipole [25].

comes mainly from the conducting and fluid outer core of the Earth, together with remaining contributions from the Earth's crust, electric currents in the atmosphere and the interaction with solar phenomena [113, 56]. For the development of this thesis, we refer to the International Geomagnetic Reference Field (IGRF) [4], which fits empirical spherical harmonic coefficients to describe the geomagnetic field and its temporal variation. The IGRF calculates the geomagnetic field vector in a local North, East, Down (*NED*) reference frame from which the magnetic inclination (angle between the geomagnetic field vector and its projection onto the horizontal plane, positive downwards) and declination (angle of between the North direction and the projection of the geomagnetic field onto the local horizontal plane, positive eastwards) can be calculated. These two angles are shown in Figure 3.3, where the following two features are highlighted:

1. The geomagnetic Equator follows the 0° inclination line, and the contours describe the geomagnetic latitudes, except for the distortions caused by the South Atlantic Anomaly (SAA). The field is horizontal at the geomagnetic Equator, responsible for the Appleton anomaly (see Section 3.1.1) and the low FR impact on the images. The field gets steeper towards the poles.

2. Knowing the local magnetic orientation will be essential for the characterization of the turbulent component of the ionosphere (see Section 3.1.2) since electron density irregularities will tend to align with the geomagnetic field that points towards the poles.

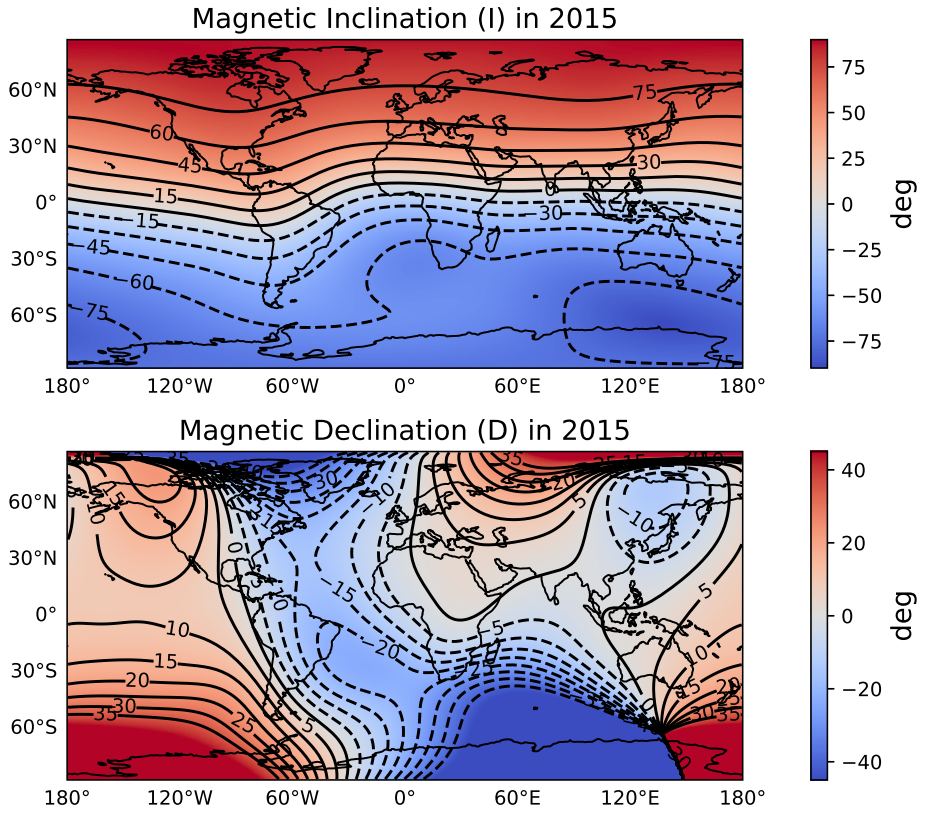

Figure 3.3: Global magnetic inclination (top) and declination (bottom) angles for the year 2015 extracted from the IGRF model at 300 km height.

Around the geomagnetic Equator, three regions will be used to characterize the spatial distribution of the background ionosphere: The low-latitude region (up to $\pm 20°$), the mid-latitude region (between $\pm 20°$ and $\pm 60°$) and the high-latitude region (above $\pm 60°$). The mid-latitude is relatively calm compared to the high and low-latitude regions, which are highly active due to Sun interaction. In the auroral regions, electron precipitation is also a cause of ionospheric activity. Considering the impact in SAR images, these two regions present high activity in terms of irregularities that introduce fast-changing distortions that are challenging to correct.

3.1.1 Background Component

In this thesis, the *background ionosphere* corresponds to large spatial-scale VTEC variations. This component is mainly driven by solar activity and illumination, as well as the geomagnetic field of the Earth. Figure 3.4 shows a series of global VTEC maps that well represent the temporal and spatial characteristic variations of the background ionosphere. The maps are obtained from the IONosphere map EXchange (IONEX) products, derived from global

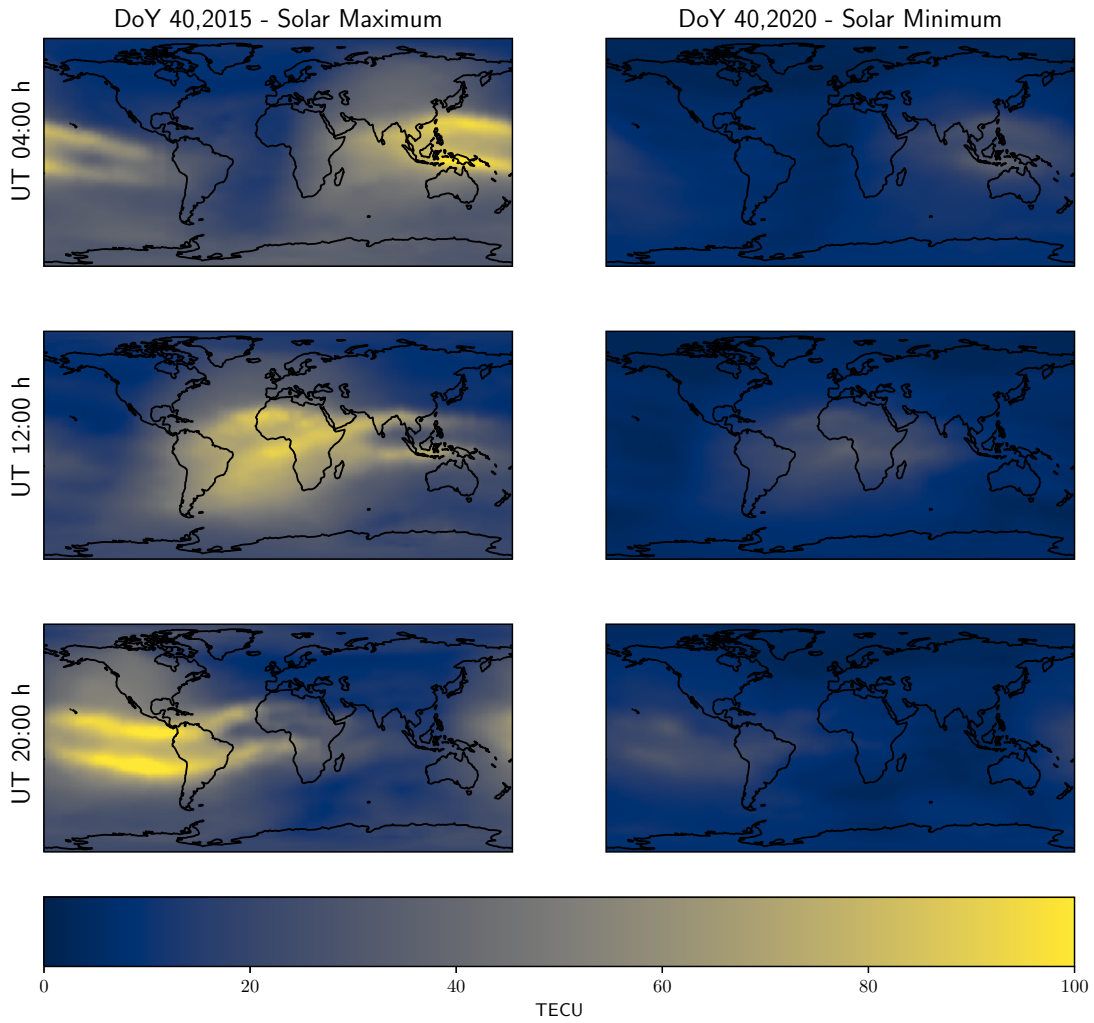

Figure 3.4: Global VTEC maps at different UT, extracted from the IONEX database. The plots in the left column show the 40th DoY for 2015, around the peak of a solar maximum. The plots in the right column show the TEC for the same day in 2020 at the low of a solar minimum.

GNSS data [92]. For a given Day of the Year (DoY), from top to bottom, global VTEC maps are shown at different Universal Times (UT); the left column corresponds to observations taken in 2015 and the right column to 2020. The IONEX products can provide global and periodic VTEC maps at a coarse spatial and temporal resolution (5° in longitude, 2.5° in latitude and every 2 hours).

The first thing to notice is the overall difference in VTEC levels in the left and right column plots. 2015 was a year of solar maximum, characterized by high solar activity, opposite to 2020, which was the low of a solar minimum. The amount of solar activity oscillates in an approximately 11-year cycle. It is characterized by the appearance of sunspots, which are lower-temperature transient patches in the Sun surface related to significant magnetic activity. From sunspot-concentrated areas, solar flares and Coronal Mass Ejections (CMEs) emit radiation that may reach the Earth's magnetosphere as X-ray, UV, EUV and plasma in the form of solar wind [113]. Following the discussion of Figure 3.4, in the left column, it is evident that the electron concentrations travel westwards with the solar illumination, leaving two tails that fade into the evening side eastwards. They follow a path along the geomagnetic Equator with two almost symmetric crests on both sides at around $\pm 15^\circ$ geomagnetic latitude. This is known as equatorial ionization anomaly or *Appleton anomaly* and is caused by the fountain effect that arises from the up-drift of the equatorial plasma and its descent following along the magnetic field lines [6, 7]. More detailed observation also reveals slightly larger TEC values in the southern hemisphere, related to the steeper Sun incidence angle in the Summer (the data were recorded in February).

Numerous models exist for the description of the background ionosphere, both theoretical and empirical. In this work, we are primarily interested in two parameters: The integrated satellite-to-ground TEC and the height of maximum ionization. This second parameter will be used to approximate the ionospheric injection and correction in the simulated data. Both parameters will be extracted from the International Reference Ionosphere (IRI) [15] and the NeQuick Model [72].

3.1.2 Turbulent Component

On top of the background ionosphere, instabilities produce different sorts of irregularities covering different scale sizes and shapes through complex processes. In the radar remote sensing literature, these are often referred to as *scintillation*, as in some instances, we will do as well in this text. However, we want to emphasize that the scintillation is an effect visible in the images as a product of radio wave propagation through (and beyond) an irregular medium, not the irregularities themselves. By definition, scintillation refers to fast changes in phase and incident angle in the received waves and the intensity changes that occur due to the interaction of the wavefront with a phase-modulating interface [84]. In the examples shown in this thesis, the fast changes in phase will produce a defocusing of the SAR images and, in some cases, a signature in the perceived Radar Cross Section (RCS) of the scatterers in the scene.

In the following, we will comment on the irregularities found in two regions (low and high latitudes) because they are most observed in previous works with L-band SAR and can be used to validate the contributions of this thesis. At mid-latitudes, the ionosphere shows a milder turbulent characteristic [1]. We will also comment on the Power Spectral Density (PSD) model used in this thesis to simulate ionospheric irregularities.

Equatorial Scintillation

Spread-F is a cause for ionospheric scintillation in the post-sunset equatorial region. When the ionization due to solar illumination stops and recombination in the lower part of the ionosphere starts in the evening, a vertical steep gradient is formed with higher plasma density on the top. The interaction of Rayleigh-Taylor-like instabilities in the transition area at the bottom part of the F-layer with the geomagnetic field causes vertical plasma drifts that develop into depleted bubbles with the associated changes in electron density and refractive indexes. These bubbles quickly align and stretch along the geomagnetic field lines [1, 56, 74], and the large density gradients at the edges lead to smaller scale irregularities.

The signature of this kind of irregularities in the SAR images will be fast phase errors that introduce defocusing and an intensity scintillation pattern. The intensity scintillation is already observed in ALOS/PALSAR and ALOS-2/PALSAR-2 L-band images [97, 88, 61] and also expected for Biomass.

High-latitude Scintillation

Energetic solar particles can enter the atmosphere at the poles due to the interconnection between the solar and Earth's magnetic fields. This particle precipitation is an important source of neutral particle ionization at the F-layer of the ionosphere, producing long-lasting irregularities of the 10-km scale that travel far away from their origination location [57]. These large structures might turn unstable and develop into smaller-scale irregularities. More energetic precipitation can also ionize the E-layer and might produce aurora visible with the naked eye, but this kind of instability fades faster [91]. High-latitude irregularities are also well known from L- and C-band SAR images and interferograms [62, 39, 91].

Modelling

Observations have shown that the ionospheric irregularities that are primarily responsible for causing scintillation are found in a narrow region of the ionosphere, leading to the common *thin layer* approximation [14]. This approximation is widely used and leads to the phase screen theory [82, 83]. This theory is based on the principle that it is possible to compress the ionospheric volume to a shell, neglecting diffraction effects inside so that the impact on a wavefront emerging from the ionospheric layer is solely a phase modulation, that is known as a *phase screen*, corresponding to the electron density irregularities [64]. This phase screen

model can, in general, be extended to a Multiple Phase Screen (MPS) description. Unless stated otherwise, in this work, we stick to the thin layer approximation but with two remarks: (i) In the literature, it is often stated that this layer is located at the height of maximum ionization; instead, we generalize to the term *irregularity height* and, (ii) the layer forms a continuous shell that in general can continuously change altitude. The first remark gives space to the center of gravity of the irregularities to be located at a height other than the one of maximum ionization, which seems reasonable given that both spread-F and auroral scintillation occur due to processes in the vertical axis. It also leaves space to account for the effect of irregularities that occur in the E-layer instead of the usual F-layer. The second remark is consistent with the electron density profiles from the NeQuick model and the hmF2 [1] parameter from the IRI model analyzed during this work [22]. For simplicity and coherence with the references in the literature, we might also refer to it as *ionospheric plane* when speaking of a fixed altitude ionospheric layer.

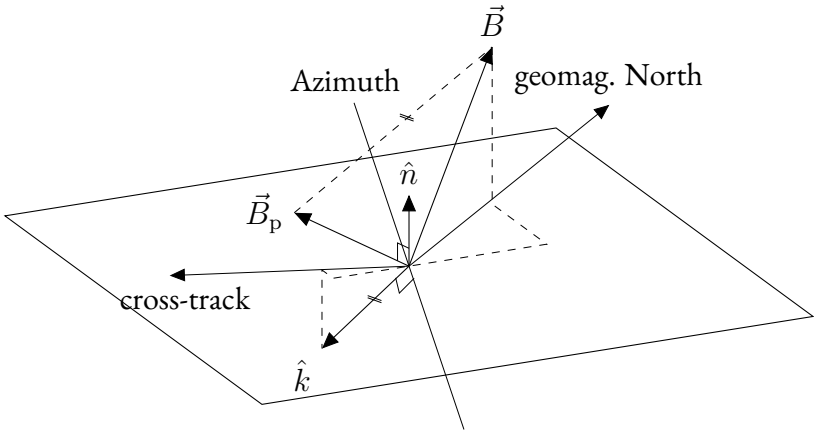

Figure 3.5: Geomagnetic field in SAR image geometry. The geomagnetic field vector $\vec{B}$ is projected along the propagation vector $\hat{k}$ on the horizontal ionospheric layer (with normal vector $\hat{n}$). The satellite velocity vector is along the azimuth line, and the direction determines a right or left-looking geometry for a fixed $\vec{k}$. The cross-track direction is the $\hat{k}$ projection in the horizontal. Note the marked parallel directions (adapted from [61]).

Observations have also shown that the horizontal spatial correlation of equatorial ionospheric irregularities in this thin layer can be described with a PSD function that follows a power law [111]. Consequently, realizations of the wavefront modulation can directly be generated with a phase screen realization. For detailed explanations regarding the nature of the phase screen and the generation of random irregularity fields whose spatial correlation is defined by a given PSD function, the reader should refer to [84, 64].

The only thing we should highlight at this discussion stage is an adaptation of the PSD expressions found in the literature to the SAR image geometry. In particular, we want to adjust the anisotropy relations from the geomagnetic North-East coordinate frame usually

[1] Density-peak height in the F2-layer.

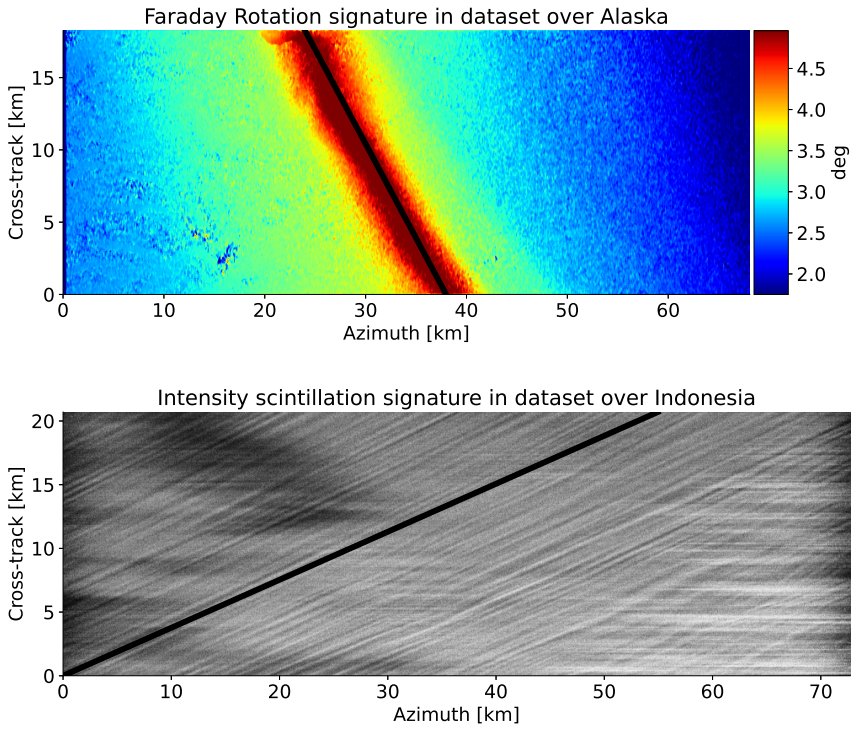

Figure 3.6: Ionospheric signature in ALOS/PALSAR datasets. The FR signature is visible over the dataset in Alaska, ALPSRP063051250 (top). Over the dataset in Indonesia, an intensity scintillation signature is observed, ALOS2050060000 (bottom). The corresponding projected geomagnetic field lines are plotted in black.

found in the literature [81, 23] to the azimuth and cross-track reference frame of the SAR acquisitions. This reconfiguration simplifies the projection of the geomagnetic field onto the image plane and the processing of the ionospheric signatures that correspond to the turbulent component of the ionosphere. Figure 3.5 shows the projection $\vec{B}_{\mathrm{p}}$ of the geomagnetic field $\vec{B}$ onto the ionospheric plane geometry along the line of sight (LOS) vector $\hat{k}$ as seen from the satellite

$$\vec{B}_{\mathrm{p}} = \vec{B} - \frac{\hat{n} \cdot \vec{B}}{\hat{n} \cdot \hat{k}} \hat{k} \,, \tag{3.2}$$

where $\hat{n}$ is the vector perpendicular to the ionospheric plane (positive upwards). Figure 3.6 shows examples of the directionality of the ionospheric signature in two ALOS/PALSAR datasets together with the geomagnetic field projection according to (3.2).

The ionospheric phase screen is generated by filtering Gaussian noise in the frequency domain with the PSD given by Rino [23]

$$\Phi_\phi(\kappa_x, \kappa_y) = \frac{\lambda^2 \cdot \mathrm{r_e^2} \cdot \sec^2\theta \cdot ab \cdot \left(\frac{2\cdot\pi}{1000}\right)^{p+1} \cdot C_k L}{\left(\kappa_0^2 + A \cdot \kappa_x^2 + B \cdot \kappa_x \cdot \kappa_y + C \cdot \kappa_y^2\right)^{\frac{p+1}{2}}}, \tag{3.3}$$

where κ_x and κ_y are the transversal wavenumbers in the geomagnetic North and East directions, λ is the carrier wavelength, $\mathrm{r_e}$ is the classical electron radius, θ is the incidence angle onto the ionospheric plane, ab is the anisotropy ratio (more precisely, it represents $a : b$), p is the phase spectral index, $C_k L$ is the vertically integrated strength of turbulence at the 1-km scale, κ_0 is the irregularity outer scale wavenumber and the A, B and C coefficients relate the anisotropy in the principal axis of the irregularity and the view of the ionospheric plane from the LOS.

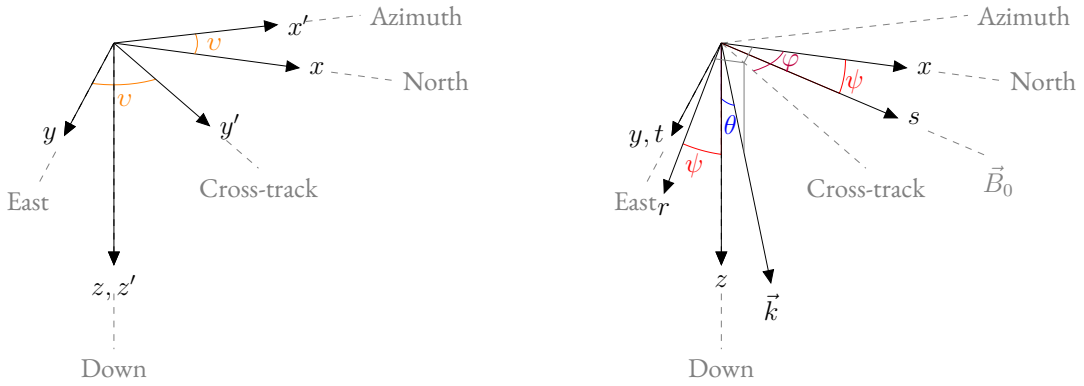

Figure 3.7: Scintillation reference frames. $(x,\ y,\ z)$ is aligned to the geomagnetic North, East and Down coordinates. $(s,\ t,\ r)$ is aligned with the ionospheric irregularities principal axis. $(x',\ y',\ z')$ is aligned to the azimuth, cross-track and down directions. ψ is the magnetic inclination, θ is the incidence angle of the wave vector $\vec{k}$ onto the horizontal, υ is the angle between the satellite velocity vector and the geomagnetic North, and φ is the magnetic heading of the beam. $\mathbf{R}_2$ is represented in the left panel and $\mathbf{R}_1$ in the right panel.

From [81], to calculate the A, B and C coefficients, it is first necessary to express the 2-D autocorrelation by rotating the coordinate system from the $(x,\ y,\ z)$ reference frame to the frame given by the irregularity principal axis $(s,\ t,\ r)$ (see the right panel in Figure 3.7) with the rotation matrix

$$\mathbf{R_1} = \begin{pmatrix} \cos\psi & 0 & \sin\psi \\ 0 & 1 & 0 \\ -\sin\psi & 0 & \cos\psi \end{pmatrix}, \tag{3.4}$$

ψ being the magnetic inclination angle. In this work, we will disregard the anisotropy along the second principal axis b by setting it to 1 (as is usually valid for equatorial irregularities). The correlation matrix, including anisotropy, is defined as

$$\mathbf{C} = \mathbf{R_1}^T \cdot \begin{pmatrix} \frac{1}{a^2} & 0 & 0 \\ 0 & 1 & 0 \\ 0 & 0 & 1 \end{pmatrix} \cdot \mathbf{R_1}\,, \tag{3.5}$$

from where a $\hat{\mathbf{C}}$-matrix that uses the anisotropy relation in the Frequency domain (same as the PSD function) can be obtained by inverting $1/a^2$. The coefficients of $\hat{\mathbf{C}}$ are used in the definition of the A, B and C coefficients with

$$A = \hat{C}_{11} + \hat{C}_{33} \cdot \tan^2\theta \cdot \cos^2\varphi - 2 \cdot \hat{C}_{13} \cdot \tan\theta \cdot \cos\varphi\,, \tag{3.6a}$$

$$B = 2 \cdot \left[\hat{C}_{12} + \hat{C}_{33} \cdot \tan^2\theta \cdot \sin\varphi \cdot \cos\varphi - \tan\theta \left(\hat{C}_{13} \cdot \sin\varphi + \hat{C}_{23} \cdot \cos\varphi\right)\right]\,, \tag{3.6b}$$

$$C = \hat{C}_{22} + \hat{C}_{33} \cdot \tan^2\theta \cdot \sin^2\varphi - 2 \cdot \hat{C}_{23} \cdot \tan\theta \cdot \sin\varphi\,, \tag{3.6c}$$

where φ is the magnetic heading (the angle between the x direction and the horizontal projection of $\hat{k}$). In this work, instead of working with a frame aligned to the magnetic field, we move to a reference frame aligned to the image to generate ionospheric phase screens. For that, we add another rotation $\mathbf{R_2}$ to $\mathbf{R_1}$ to move from the image frame $(x'\,, y'\,, z')$ to the $(x,\, y,\, z)$ reference frame. $\mathbf{R_2}$ is a rotation υ around the vertical axis z (see the left panel in Figure 3.7) that moves from the azimuth and cross-track coordinates to the geomagnetic North-East frame

$$\mathbf{R_2} = \begin{pmatrix} \cos\upsilon & \sin\upsilon & 0 \\ -\sin\upsilon & \cos\upsilon & 0 \\ 0 & 0 & 1 \end{pmatrix} \tag{3.7}$$

so that the final rotation used for the calculation of the correlation matrix is $\mathbf{R} = \mathbf{R_1} \cdot \mathbf{R_2}$

$$\mathbf{R} = \begin{pmatrix} \cos\psi \cdot \cos\upsilon & \sin\upsilon \cdot \cos\psi & \sin\psi \\ -\sin\upsilon & \cos\upsilon & 0 \\ -\sin\psi \cdot \cos\upsilon & -\sin\psi \cdot \sin\upsilon & \cos\psi \end{pmatrix} \tag{3.8}$$

Applying 3.5 again, the coefficients of the correlation matrix $\mathbf{C}$ are

$$C_{11} = \sin^2\psi \cdot \cos^2\upsilon + \sin^2\upsilon + \frac{\cos^2\psi \cdot \cos^2\upsilon}{a^2} \tag{3.9a}$$

$$C_{22} = \sin^2\psi \cdot \sin^2\upsilon + \cos^2\upsilon + \frac{\sin^2\upsilon \cdot \cos^2\psi}{a^2} \tag{3.9b}$$

$$C_{33} = \cos^2\psi + \frac{\sin^2\psi}{a^2} \tag{3.9c}$$

$$C_{12} = C_{21} = \sin^2\psi \cdot \sin\upsilon \cdot \cos\upsilon - \sin\upsilon \cdot \cos\upsilon + \frac{\sin\upsilon \cdot \cos^2\psi \cdot \cos\upsilon}{a^2} \tag{3.9d}$$

$$C_{13} = C_{31} = -\sin\psi \cdot \cos\psi \cdot \cos\upsilon + \frac{\sin\psi \cdot \cos\psi \cdot \cos\upsilon}{a^2} \tag{3.9e}$$

$$C_{23} = C_{32} = -\sin\psi \cdot \sin\upsilon \cdot \cos\psi + \frac{\sin\psi \cdot \sin\upsilon \cdot \cos\psi}{a^2} \tag{3.9f}$$

and $\hat{\mathbf{C}}$ can also be plugged in (3.6) for the calculation of A, B and C. Note that with this configuration, for non-squinted acquisitions, the magnetic heading angle φ is fixed to $\frac{\pi}{2}$ for right-looking acquisitions and $-\frac{\pi}{2}$ to left-looking ones. The scintillation parameters in (3.3) can, in general, be approximated from the Wideband Ionospheric Scintillation Model (WBMOD) [94]. Figure 3.8 shows two examples of phase screens generated to test that this approach is compatible with the observations in Figure 3.6. Note the consistency in the orientation and alignment with the geomagnetic field projection.

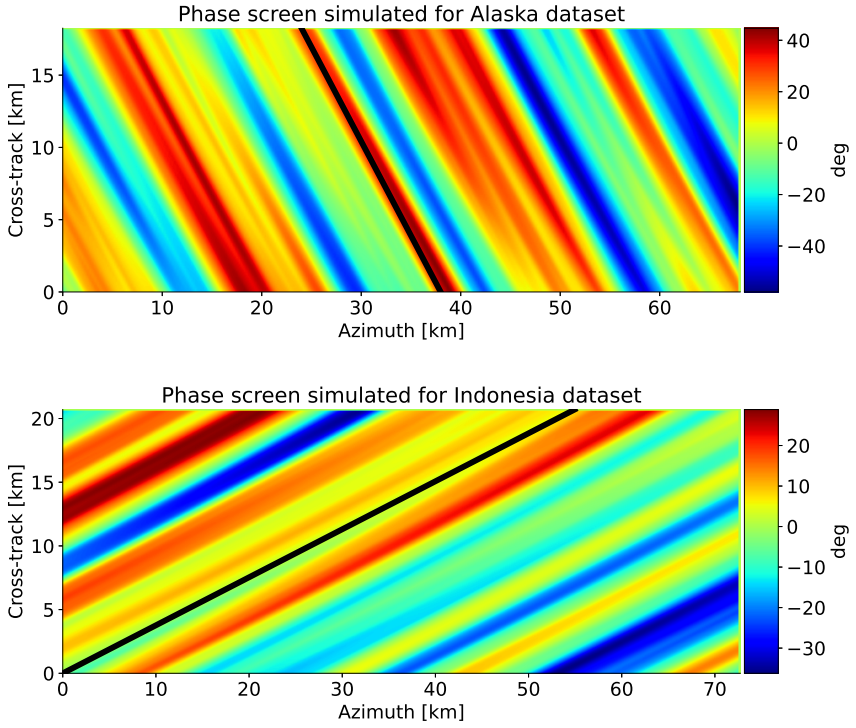

Figure 3.8: Simulated phase screens following the orientation of the geomagnetic field (highlighted in black) as in Figure 3.6.

3.2 Ionospheric Refractive Index

Trans-ionospheric propagation of radio waves is ruled by the *dispersive* and *anisotropic* refractive index of the ionized medium. In this work, we will neglect wave absorption through the ionosphere. From the Appleton relation [28], ignoring the effect of the magnetic field, the local refractive index of the ionized medium for a wave with frequency f becomes

$$\mu^2 = 1 - \frac{f_{\mathrm{p}}^2}{f^2}, \tag{3.10}$$

with the *plasma frequency*, the critical frequency at which propagation cannot take place, given by

$$f_{\mathrm{p}} = \frac{\mathrm{q_e}}{2 \cdot \pi} \cdot \sqrt{\frac{N_{\mathrm{e}}}{\epsilon_0 \cdot \mathrm{m_e}}}. \tag{3.11}$$

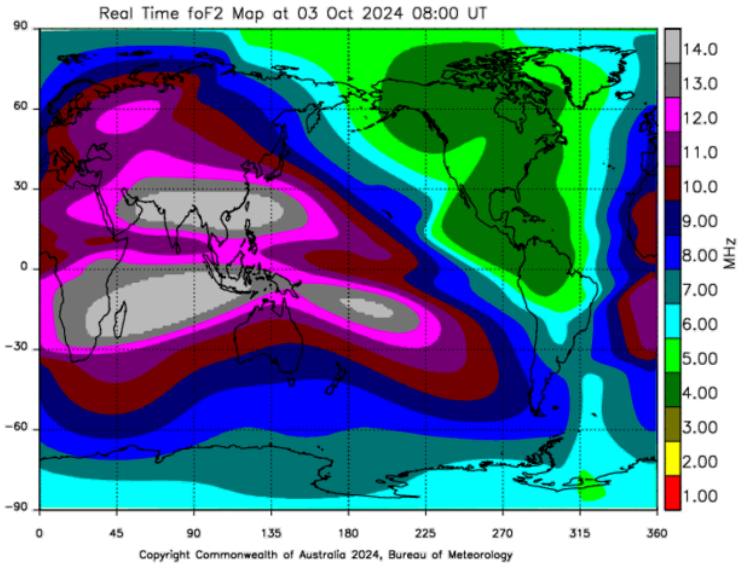

Figure 3.9: Global critical frequency at the F2 layer (foF2) extracted from ionograms. Source: *https://www.sws.bom.gov.au/HF_Systems/6/5*

In (3.11), $\mathrm{q_e}$ is the electron charge, ϵ_0 is the vacuum permittivity, and $\mathrm{m_e}$ is the electron mass. From (3.10), apart from the electron density, we highlight the dependency on the frequency of the propagating wave that makes the medium dispersive. Lower frequencies are more affected; however, L and P-band radar systems are far above the critical frequency. In 2024, a year of solar maximum, Figure 3.9 shows an example of the global critical frequency in the F2 layer (foF2); note that the values are below 20 MHz. With this high-frequency approximation, (3.10) becomes

$$\mu \approx 1 - \frac{1}{2} \cdot \frac{\mathrm{q_e^2} \cdot N_\mathrm{e}}{4 \cdot \pi^2 \cdot \epsilon_0 \cdot \mathrm{m_e} \cdot f^2} = 1 - \zeta \cdot \frac{N_\mathrm{e}}{f^2}\,, \tag{3.12}$$

with $\zeta = \frac{\mathrm{q_e^2}}{8 \cdot \pi^2 \cdot \epsilon_0 \cdot \mathrm{m_e}} \approx 40.31\,\mathrm{m^3/s^2}$.

3.3 Impact on SAR Remote Sensing

Group velocity

The expression of the group velocity (including the high-frequency approximations) is [28]

$$v_g \approx c_0 \cdot \left(1 - \zeta \cdot \frac{N_\mathrm{e}}{f^2}\right)\,, \tag{3.13}$$

indicating that the pulse velocity is slower than in the vacuum and the echoes are delayed. This effect introduces errors in the ranging and coregistration. The 1-way time delay is

$$\Delta t = \int_L \frac{\mathrm{d}l}{c_0 \cdot \left(1 - \zeta \cdot \frac{N_\mathrm{e}}{f^2}\right)} - \int_L \frac{\mathrm{d}l}{c_0} \approx \zeta \cdot \frac{STEC}{c_0 \cdot f^2} \tag{3.14}$$

and the increase in slant range is given by

$$\Delta l = c_0 \cdot \Delta t = \frac{\zeta \cdot STEC}{f^2}\,. \tag{3.15}$$

Phase velocity

The phase velocity v_p is given by [28]

$$v_p = \frac{c_0}{\mu} = \frac{c_0}{1 - \zeta \cdot \frac{N_\mathrm{e}}{f^2}}\,, \tag{3.16}$$

and the 2-way phase difference with respect to propagation in free space is

$$\phi = 2 \cdot \frac{2 \cdot \pi \cdot f}{c_0} \int_L \left(\frac{1}{v_p} - \frac{1}{c_0}\right) \mathrm{d}l = -\frac{4 \cdot \pi}{c_0 \cdot f} \cdot \zeta \cdot STEC\,. \tag{3.17}$$

When translating this into a band-limited chirp signal, two direct effects are the displacement and spread of the impulse response in range. If we perform a Taylor expansion of (3.17) around the carrier frequency f_0 we obtain

$$\phi(f - f_0) \approx \frac{4 \cdot \pi \cdot \zeta \cdot STEC}{c_0} \cdot \left(-\frac{1}{f_0} + \frac{(f - f_0)}{f_0^2} - \frac{(f - f_0)^2}{f_0^3}\right)\,, \tag{3.18}$$

where the second term in the expansion is responsible for the range displacement, while the third term introduces an error in the chirp rate of the received echo, causing range defocusing and loss of resolution.

A limit for the allowed phase error at the edges of the chirp is set to π [10] so that if the range bandwidth B_r and the carrier frequency f_0 are design parameters, they require that

$$B_r^2 < \frac{f_0^3 \cdot c_0}{\zeta \cdot STEC} \tag{3.19}$$

to avoid range defocusing. ALOS-2/PALSAR-2 allows an irrealistic $STEC$ of up to 238 TECU in its wider bandwidth mode (80 MHz) and Biomass of up to 1700 TECU.

The negative sign in (3.17) indicates that the phase is advanced because it travels faster than the speed of light. Table 3.1 shows some values for phase and slant range errors introduced by a 10 Slant TECU (STECU) ionosphere in ALOS-2/PALSAR-2 and Biomass.

Effect	L band (1270 MHz)	P band (435 MHz)
Range delay	2.5 m	21 m
Phase advance	21.17 cycles	61.82 cycles

Table 3.1: Representative delays (phase and slant range) for a 10-STECU ionosphere in different radar remote sensing systems.

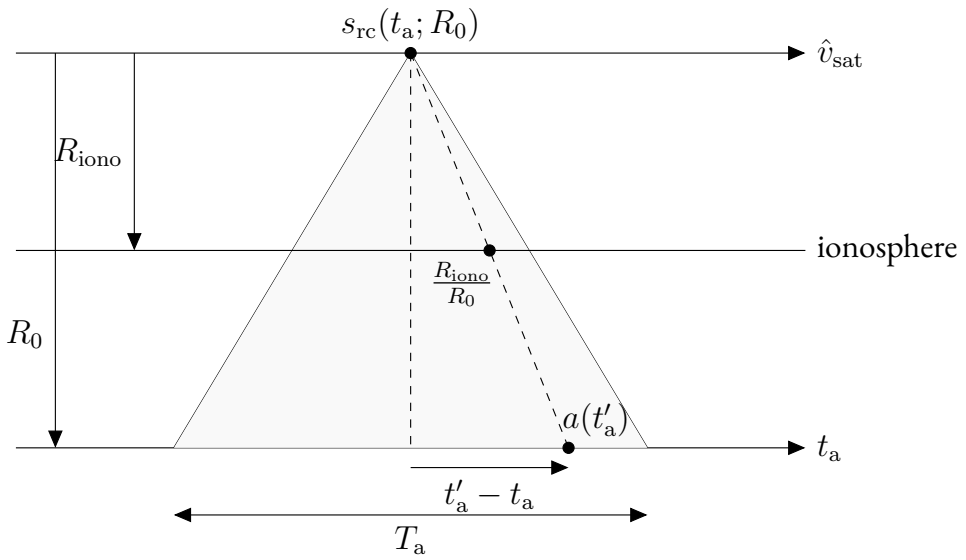

Figure 3.10: Simplified slant observation geometry with ionospheric layer. The range compressed signal at an azimuth position is composed of the sum of the complex reflectivity of the $a(t'_{\mathrm{a}})$ inside the beam modulated with the range history and the phase advance in the ionospheric layer.

Figure 3.10 shows a simplified version of the slant observation geometry for a given range bin at R_0 and the ionospheric layer between the satellite trajectory (top) and the ground. The radar beam illuminates all the targets compressed inside a synthetic aperture time T_a at slow times t'_a, and a portion of the ionosphere at a slant distance R_iono. Figure 3.10 represents a flat Earth and rectilinear trajectory for illustration purposes. However, in the simulations shown in this work, we account for the exact geometry with the Earth's ellipsoid and satellite orbit. The azimuth signal model for range compressed data is described in (3.20): For a given satellite position at time t_a the range compressed data are composed by the complex reflectivity of all the targets $a(t'_\mathrm{a})$ inside the beam (represented with a rectangular function) and the closest approach phase convolved with the quadratic component of the phase history modulated with the azimuth chirp rate K_a. In addition, the last term in the integral represents the phase-modulating ionosphere $\phi_\mathrm{iono}(t_\mathrm{a})$ with the azimuth time coordinate being reduced by approximately $\frac{R_\mathrm{iono}}{R_0}$,

$$s_\mathrm{rc}(t_\mathrm{a}; R_0) = \int a\left(t'_\mathrm{a}\right) \cdot \mathrm{rect}\left(\frac{t'_\mathrm{a} - t_\mathrm{a}}{T_\mathrm{a}}\right) \cdot \exp\left(-\frac{4 \cdot j \cdot \pi}{\lambda} \cdot R_0\right) \cdot \exp\left(j \cdot \pi \cdot K_\mathrm{a} \cdot \left(t'_\mathrm{a} - t_\mathrm{a}\right)^2\right) \cdot \exp\left(j \cdot \phi_\mathrm{iono}\left(\frac{R_\mathrm{iono}}{R_0}\left(t'_\mathrm{a} - t_\mathrm{a}\right)\right)\right) \mathrm{d}t'_\mathrm{a}\,, \tag{3.20}$$

From here, we interpret that both in the range-compressed and azimuth-compressed data, the phase signature of the ionosphere will be convolved with the synthetic aperture length projected on the ionospheric layer. The implications of this will be thoroughly discussed in the following Chapters. For now, let us describe the direct impact of a spatially changing ionosphere in SAR remote sensing:

1. The multiplication with a linear increase in TEC across the synthetic aperture translates into *azimuth shifts* of the focused targets. These shifts are mostly examined as coregistration errors in interferometric pairs [39, 42]. Figure 3.11 shows an example of blockwise azimuth shifts from a differential turbulent ionosphere simulated for Biomass.

2. In the presence of small-scale ionospheric irregularities (with a size comparable to or smaller than the synthetic aperture length projected on the ionospheric layer), after azimuth compression, the response of targets on the ground will be defocused as seen in Figure 3.12. Note the worsening of the main lobe and the rise of side lobes, which translates into loss of contrast and resolution. In addition, the phase errors introduce decorrelation and phase screens in interferometric pairs that add to the non-dispersive phase components (such as deformation) [11, 62, 44].

Correction approaches for these high-frequency phase errors will be discussed in Chapters 5 and 6.

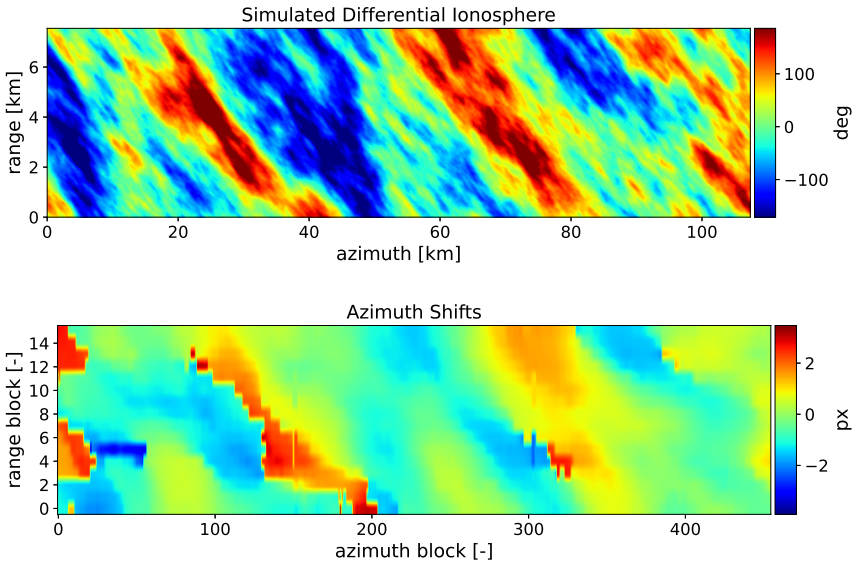

Figure 3.11: Simulated azimuth shifts in an interferometric pair (Biomass). Differential ionosphere (top) and azimuth coregistration error map (bottom).

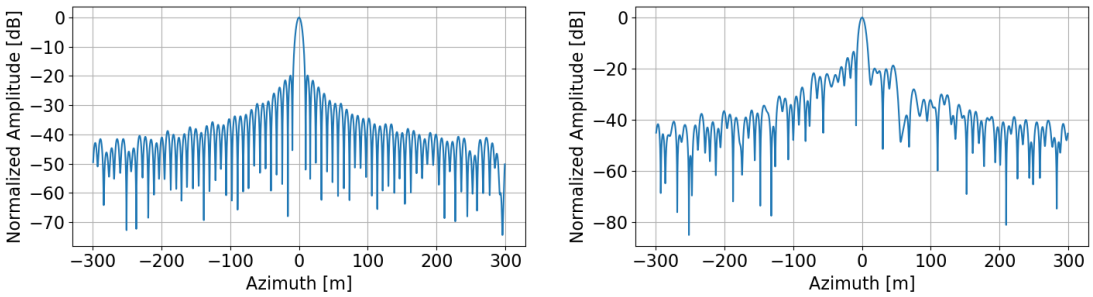

Figure 3.12: Impulse response of a simulated point target in the presence of a turbulent ionosphere (Biomass). Nominal case (left) and with turbulent ionosphere (right).

Faraday rotation

The Faraday Rotation (FR) is an effect of the double-valued refractive index of the ionosphere, a product of the magnetic field-induced anisotropy [28]. A linearly polarized wave traveling through the ionosphere can be decomposed into two circularly polarized waves rotating in opposite senses, each with a different velocity. With the high-frequency approximation, the refractive index for left- and right-handed circularly polarized waves becomes

$$\mu_{\mathrm{L,R}} \approx 1 - \frac{1}{2} \cdot \frac{f_p^2}{f^2} \left(1 \mp \frac{f_{\mathrm{B}}}{f} \right) , \tag{3.21}$$

with the *cyclotron frequency*

$$f_{\mathrm{B}} = \frac{\mathrm{q_e} \cdot \vec{B} \cdot \hat{k}}{2 \cdot \pi \cdot \mathrm{m_e}} . \tag{3.22}$$

When the circularly polarized waves recombine after traversing the ionosphere, they carry a phase mismatch provoking a polarization plane rotation, i.e.

$$\mathbf{R_\Omega} = \begin{pmatrix} \cos\Omega & \sin\Omega \\ -\sin\Omega & \cos\Omega \end{pmatrix} .$$

The one way FR [69, 109] is given by

$$\Omega = \zeta \cdot \frac{\mathrm{q_e}}{c_0 \cdot \mathrm{m_e}} \cdot \frac{\vec{B} \cdot \hat{k}}{f^2} \cdot STEC \tag{3.23}$$

where the term $\vec{B} \cdot \hat{k}$ is the signed projection of the magnetic field vector on the LOS. Note that in two-way propagation, for a given scattering matrix $\mathbf{S}$, the FR accumulates in the *measured scattering matrix* [35]

$$\mathbf{M} = \begin{pmatrix} M_{\mathrm{HH}} & M_{\mathrm{HV}} \\ M_{\mathrm{VH}} & M_{\mathrm{VV}} \end{pmatrix} = \begin{pmatrix} \cos\Omega & \sin\Omega \\ -\sin\Omega & \cos\Omega \end{pmatrix} \begin{pmatrix} S_{\mathrm{HH}} & S_{\mathrm{HV}} \\ S_{\mathrm{VH}} & S_{\mathrm{VV}} \end{pmatrix} \begin{pmatrix} \cos\Omega & \sin\Omega \\ -\sin\Omega & \cos\Omega \end{pmatrix} . \tag{3.24}$$

$\mathbf{M}$ can be simplified with the backscatter reciprocity principle on the cross-pol terms of the scattering matrix ($S_{\mathrm{VH}} = S_{\mathrm{HV}}$):

$$M_{\mathrm{HH}} = S_{\mathrm{HH}} \cdot \cos^2\Omega - S_{\mathrm{VV}} \cdot \sin^2\Omega , \tag{3.25a}$$
$$M_{\mathrm{HV}} = S_{\mathrm{HV}} + (S_{\mathrm{HH}} + S_{\mathrm{VV}}) \cdot \sin\Omega \cdot \cos\Omega , \tag{3.25b}$$
$$M_{\mathrm{VH}} = S_{\mathrm{HV}} - (S_{\mathrm{HH}} + S_{\mathrm{VV}}) \cdot \sin\Omega \cdot \cos\Omega , \tag{3.25c}$$
$$M_{\mathrm{VV}} = S_{\mathrm{VV}} \cdot \cos^2\Omega - S_{\mathrm{HH}} \cdot \sin^2\Omega . \tag{3.25d}$$

Note that in the presence of FR, $M_{\mathrm{VH}} \neq M_{\mathrm{HV}}$. This feature is exploited in SAR for FR angle estimation and correction. There are different estimators for the FR from quad-pol data; in this work, we will focus on the *Bickel and Bates estimator* due to the proven good performance in error variance [59]. This estimator is based on the relative phase between the cross-polar channels (Right-Left and Left-Right) when transforming the measured scattering matrix into a circular basis with

$$\mathbf{M_C} = \frac{1}{2} \cdot \begin{pmatrix} -i & 1 \\ 1 & -i \end{pmatrix} \cdot \begin{pmatrix} M_{\mathrm{HH}} & M_{\mathrm{HV}} \\ M_{\mathrm{VH}} & M_{\mathrm{VV}} \end{pmatrix} \cdot \begin{pmatrix} 1 & i \\ i & 1 \end{pmatrix} \tag{3.26}$$

so that

$$M_{\mathrm{LR}} = M_{\mathrm{HH}} - i \cdot M_{\mathrm{HV}} + i \cdot M_{\mathrm{VH}} + M_{\mathrm{VV}} = (S_{\mathrm{HH}} + S_{\mathrm{VV}}) \exp(-i \cdot 2 \cdot \Omega) \tag{3.27a}$$
$$M_{\mathrm{RL}} = M_{\mathrm{HH}} + i \cdot M_{\mathrm{HV}} - i \cdot M_{\mathrm{VH}} + M_{\mathrm{VV}} = (S_{\mathrm{HH}} + S_{\mathrm{VV}}) \exp(i \cdot 2 \cdot \Omega)\ , \tag{3.27b}$$

and finally the estimated FR angle is $\Omega = -\frac{1}{4} \arg(M_{\mathrm{LR}} \cdot M_{\mathrm{RL}}^*)$. In Pub4, we conduct a deeper analysis of the sensitivity and resolution of the estimation.

Intensity Scintillation

An effect of the irregular phase modulation within the ionospheric layer is the appearance of intensity scintillation in the SAR images. This kind of scintillation is seen as high-frequency changes in the RCS of the targets in the scene, and their presence is well known in ALOS/PALSAR and ALOS-2/PALSAR-2 images close to the Equator [97, 88].

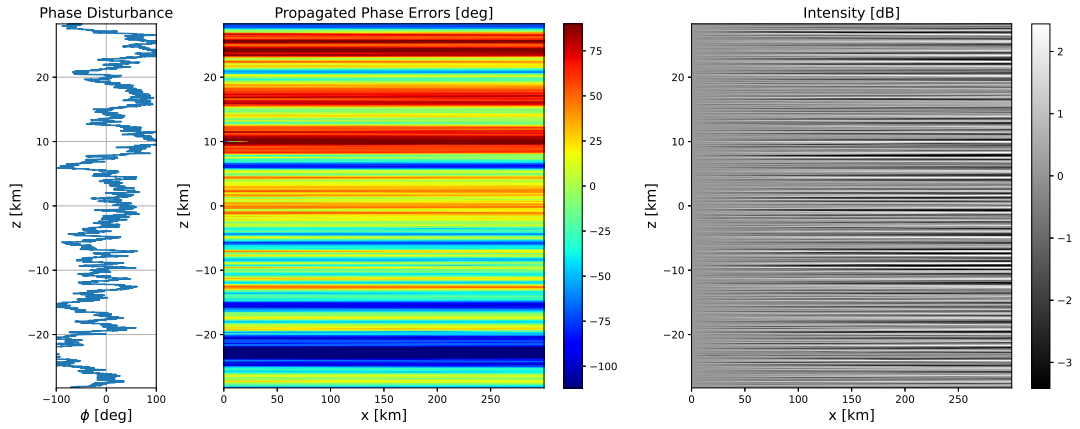

Figure 3.13: Simulated one-way intensity scintillation. The modulating phase screen generated with a power-law (left) produces a phase error (middle) and intensity scintillation (right) that propagates in free space. The propagation direction is x. Assume a monochromatic plane incident wavefront.

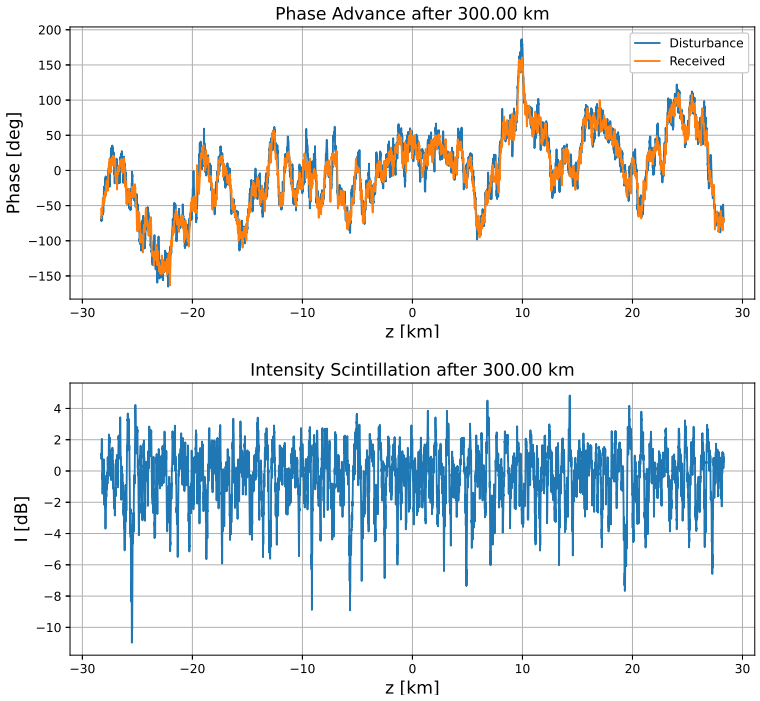

Figure 3.14: Simulated phase error (top) and intensity scintillation (bottom) after 1-way propagation.

As described in [18], an irregular phase screen might act as a diffraction grating that splits an incident wavefront into different spectra that interact constructively and destructively as they propagate in free space. We will use the *split-spectrum* solution for wave propagation in free space after passing by a turbulent medium [98] to simulate the development of such scintillations. To dive into the simulation details, the reader might refer to [84, 64]. As an example, Figure 3.13 shows the one-way development of the intensity of a monochromatic wavefront (P band = 435 MHz) after passing through a 1-D phase-modulating screen (as it is assumed to be the case of the ionosphere) to the ground [2]. The interaction of the diffracted spectra can be appreciated in the development of the phase of the wavefront and the change in intensity. The statistics of the intensity profiles in tend to stabilize for large distances in the propagation direction.

We stop to analyze the received phase disturbance on the ground. As shown in Figure 3.14, the interaction of the spectra acts as an averaging filter that damps some high-frequency components of the phase screen (note the negative bump at around 10 km^{-1}). This effect will be disregarded in this work, and it will be assumed that the phase disturbance will only be a phase advance, as described previously. The validity of this assumption can also be justified by looking at the PSD of the simulated and received phase error at the top of Figure 3.15,

[2] This analysis can directly be extended to the return propagation and 2-dimensional ionospheric irregularities

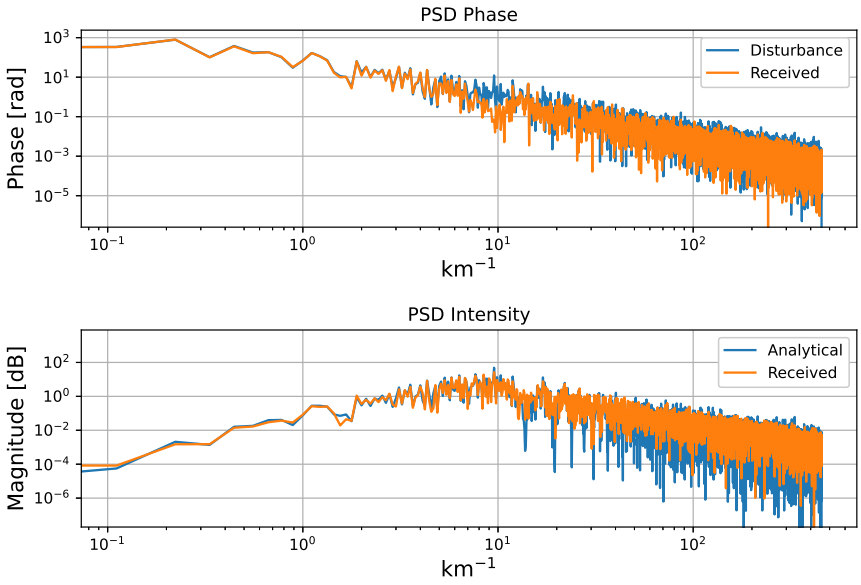

Figure 3.15: Simulated PSD of one-way phase error and intensity scintillation after passing a phase modulating layer and propagating in free space.

which shows that both signals are almost identical in terms of PSD.

To close the discussion, we refer to the plot at the bottom of Figure 3.15 to show that the PSD of the phase disturbance and the one of the intensity scintillation are closely related by a Fresnel filter function [18, 23]

$$\Phi_I(\vec{\kappa}_\perp) = 4 \cdot \sin^2\left(\vec{\kappa}_\perp^2 \cdot \frac{\lambda \cdot d_\mathrm{R}}{4 \cdot \pi}\right) \cdot \Phi_\phi(\vec{\kappa}_\perp)\,, \tag{3.28}$$

where $\vec{\kappa}_\perp$ is the transversal wavenumber vector, d_R is the range from the layer to the ground and $\Phi_\phi(\vec{\kappa}_\perp)$ is the PSD of the phase modulation. For the 2-D case, $\Phi_\phi(\vec{\kappa}_\perp)$ is given by (3.3). Further analysis of the implications regarding SAR remote sensing will be done in Chapters 4 and 7.

3.4 Correction Approaches and Opportunity to Extract Information

Extensive work has been done to mitigate most of the effects mentioned above to ensure image calibration, improve the quality of the products, and facilitate the interpretability of the data. Ionospheric correction requires an intermediate *imaging* step, where the premise is that the impact in the images will be somehow an effect of the $STEC$, wavelength and bandwidth. In this sense, low-frequency SAR plays an important role (even more with future mis-

Effect on image	Correction method	References
Range defocusing	Range autofocusing	[10]
Azimuth defocusing	MapDrift Autofocus (MDA)	[44] and Section 5.2
Azimuth defocusing	Phase Gradient Autofocus (PGA)	[67, 52]
Faraday rotation	Bickel and Bates	[62] and Section 5.1
Relative phase error	Split-spectrum	[16, 40, 42]
Azimuth shifts	Cross-correlation	[43, 55]
Interferometric phase errors	Semi-focusing with azimuth shifts	[38]

Table 3.2: Summary of relevant ionospheric correction methods with selected references. The interferometric methods are shaded in blue.

sions like Biomass) because no other ionospheric sensing technology allows high-resolution ionospheric 2-D mapping with frequent coverage.

Table 3.2 highlights some relevant methods either used in current operational missions or proposed for future ones. The recovery potential will depend on the system, the state of the ionosphere and the correction approach. Due to limitations in the resolution, some approaches are suited for the recovery of the absolute background component, while the methods that attempt azimuth defocusing correction specifically deal with the turbulent ionosphere. It is also possible to correct differential ionosphere in InSAR and Polarimetric Interferometric SAR (PolInSAR) applications to separate the ionospheric phase screens from other phase contributions. Since all the effects are proportional to the $STEC$, in some cases it will be convenient to bypass the FR for phase correction [62] or to combine different approaches to benefit from the different sensitivities and obtain better estimators [42, 44].

Unless stated otherwise, in this work we will assume that the background component has been properly calibrated so the focus is put on the calibration and imaging of the challenging ionospheric irregularities.

4

Simulation

In Section 3.3, we explored the various ionospheric disturbances that can impact the performance of SAR remote sensing, with a specific focus on those caused by small-scale irregularities. In this chapter, we introduce a novel simulation method. This method not only accurately introduces all types of ionospheric disturbances into simulated SAR images but also allows for efficient parallel implementation. The process can account for irregularities smaller than the synthetic aperture projected on the ionospheric irregularity plane and the squint angle from the center of the beam. By using a sub-aperture operation, we can introduce the ionospheric effects at each satellite position, eliminating many of the assumptions made in other approaches that use the beam-center approximation. This innovative tool will be used in the following chapters to deepen our understanding of the effects of the ionosphere in SAR data and the investigation of calibration algorithms.

This chapter serves as a comprehensive summary of the main ideas presented in Pub1, which can be found in Appendix A. Pub1 primarily focuses on the injection of phase errors and the related intensity scintillation into simulated data. It shows that an aperture-dependent ionospheric injection is preferred for a better accommodation of irregularities of a scale size comparable to or smaller than the synthetic aperture. In this chapter, we extend this discussion to include the injection of FR into simulated data, taking into account the LOS variation inside the beam. We conclude by emphasizing the importance of our aperture-dependent method compared to the beam-center approximation and provide further application examples.

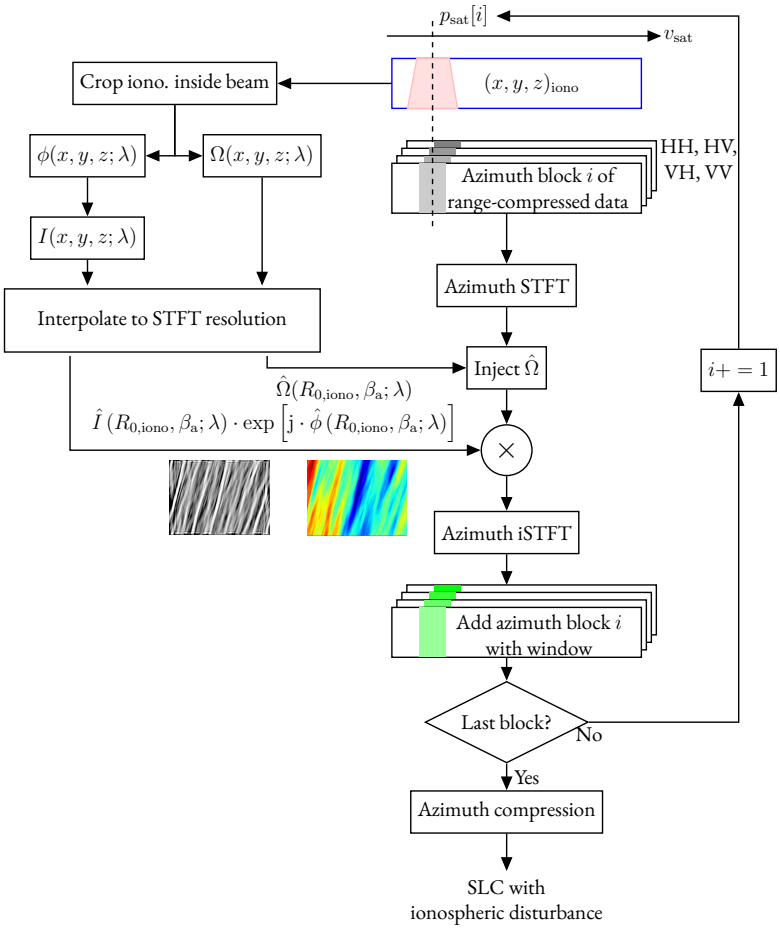

Figure 4.1: SADI block diagram.

4.1 Aperture-Dependent Ionospheric Injection Into SAR Simulations

The principle of Sub-Apertures for Disturbance Injection (SADI) was introduced in Pub1. It was shown that it allows to accommodate the look angle variability inside the radar beam efficiently for an accurate injection of the ionospheric disturbances into the range-compressed data. The block diagram for the simulation of the disturbances in a fully polarimetric dataset is shown in Figure 4.1. The inputs are the range-compressed data of the four polarizations, the ionospheric irregularity map, the location of the ionospheric piercing points and the satellite orbit. Under the thin layer approximation, the piercing points are the coordinates where the radar beam goes through the imaginative layer on the way to the ground. In general, the piercing points can be found on a shell of variable height. For each satellite position, the section of the ionosphere that is seen by the radar beam is extracted so that the corresponding phase, FR and amplitude modulation (scintillation) are calculated.

One of SADI's most significant benefits is that it allows the injection of a time-varying

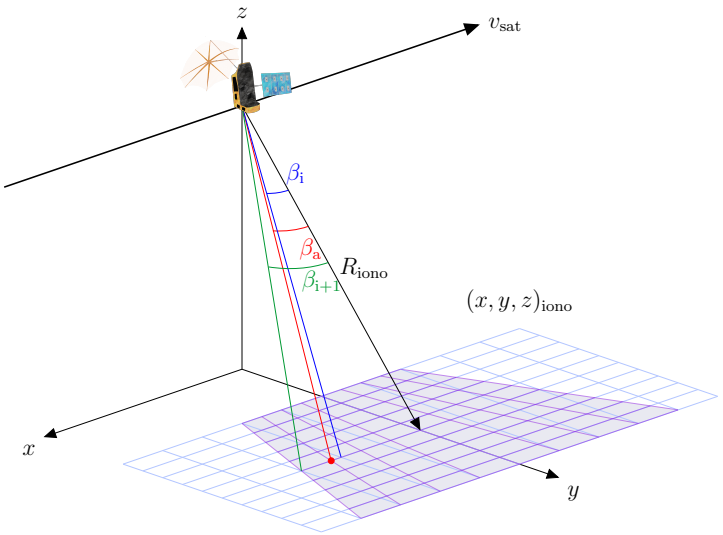

Figure 4.2: SADI geometry. The blue grid corresponds to the ionosphere, and the angular purple grid corresponds to the STFT of an azimuth sub-aperture. To obtain the unknown disturbance at the red piercing point in the direction of β_{a} (not known), a linear angle interpolation between β_{i} and $\beta_{\mathrm{i+1}}$ is necessary.

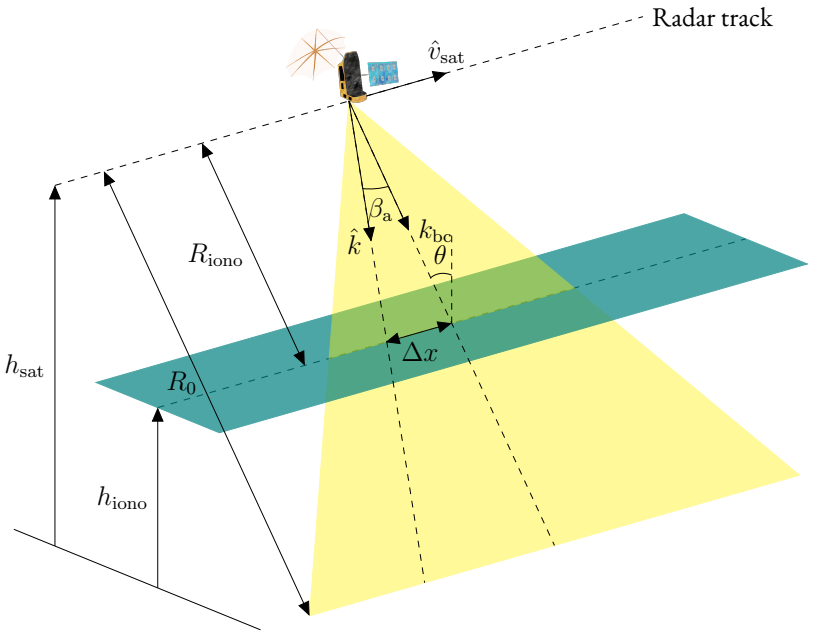

Figure 4.3: Aperture-dependent FR geometry. The pointing direction inside the radar beam $\hat{k}$ is derived from the pointing vector of the center of the beam $\hat{k}_{\mathrm{bc}}$.

and drifting ionosphere. The azimuth Short-Time Fourier Transform (STFT) of a small range-compressed sub-aperture (around the satellite position $p_{\mathrm{sat}}[i]$) facilitates an angular separation of the locally processed ionosphere in squinted views. Then, the disturbance seen at each satellite position with a given squint angle can be introduced for each sub-aperture in the frequency domain, with the geometry given in Figure 4.2. The local illuminated ionosphere must be downsampled to the STFT resolution (at the corresponding squint angles β_{a}) with an angular interpolation between the β_{i} and $\beta_{\mathrm{i}+1}$ angles for each range bin. After the frequency domain injection and an inverse Short-Time Fourier Transform (iSTFT), windowed sub-aperture re-colocation gives the range-compressed data with the ionospheric screen disturbance. Finally, regular azimuth compression provides the SLC image with ionospheric disturbances.

In Pub1, SADI was compared to the state-of-the-art method for ionospheric injection of *semi-focusing* the image at the location of the thin layer h_{iono} [62], which follows the beam-center approximation: The disturbance injection is approximated to the convolution of the ionosphere seen by the synthetic aperture projected at h_{iono} but in the LOS at the center of the beam neglecting the angular view inside the radar beam. As discussed in Pub1, this approximation can introduce non-negligible errors when the ionospheric irregularities have spatial scales comparable to or smaller than the beam projected on the ionospheric layer or in wide-beam high-resolution systems. In Pub1, the injection of phase advance and amplitude modulation was introduced. The FR needs some further consideration, which will be discussed in the following.

The geometry used for the FR injection is shown in Figure 4.3. At a given time, the satellite platform moves at an altitude h_{sat} in the $\hat{v}_{\mathrm{sat}}$ direction, illuminating the ground and the ionosphere (consider a thin layer at an altitude h_{iono} in blue) with the beam shown in yellow. The range to the ground is R_0, and the range to the ionospheric layer is R_{iono} (note that this is a simplified representation with a rectilinear trajectory where only the middle range bin is highlighted). A squinted view of the ionosphere at R_{iono} is taken from the platform displaced by an along-track distance Δx. The unit pointing vector at the center of the beam is called $\hat{k}_{bc}$, and the general *aperture-dependent* pointing vector is $\hat{k}$. This unit vector includes the squint angle and an added horizontal component along $\hat{v}_{\mathrm{sat}}$ [60]

$$\hat{k} = \hat{k}_{bc} \cdot \cos\beta_{\mathrm{a}} + \hat{v}_{\mathrm{sat}} \cdot \sin\beta_{\mathrm{a}} \,. \tag{4.1}$$

As it will be discussed in Section 5.1.1, this change of LOS with respect to the center of the beam introduces non-negligible and asymmetric changes in the FR due to the $\vec{B} \cdot \hat{k}$ product in (3.23). The change can be more than 10% towards the geomagnetic equator for the beam corresponding to a f_0 of 435 MHz and 12-m antenna aperture as in Biomass.

Similar to Pub1, in the following, a simulation is used to present the differences with respect to the semi-focusing method. The simulation is done with the parameters in Table 4.1 [1]. The satellite and scene coordinates are extracted from the Biomass simulated orbit. A mid-

[1] MSFR stands for Multi-Squint FR, for details refer to Section 5.1.

Parameter	Units	Value
Scene center (lon, lat)	[deg, deg]	[107, 21]
Ionospheric screen center (lon, lat)	[deg, deg]	[108.5, 21.5]
Ionospheric height, h_{iono}	km	350
Local geomagnetic field, $\vec{B}$ (N, E, D)	[nT, nT, nT]	[32419.675, -978.814, 19730.05]
Line of sight, $\hat{k}_{\mathrm{bc,ECEF}}$	-	[0.6417, -0.6423, -0.4189]
Satellite velocity (vector), $\hat{v}_{\mathrm{sat,ECEF}}$	-	[0.3225, -0.2695, 0.9073]
Satellite velocity (value), v_{sat}	km/s	7.610
Range to the ionosphere, R_{iono}	km	351
Outer scale of irregularity, l_o	m	20000
Anisotropy, $a:b$	-	5:1
Strength of irregularity, $C_k L$	-	10^{33}
Power-law index, p	-	2.6
Carrier wavelength, λ	m	0.69
Azimuth antenna length, L_{a}	m	12
Mean incidence angle, θ_{inc}	deg	25
Azimuth bandwidth, B_{a}	Hz	1268.3595
Pulse Repetition Frequency, PRF	Hz	1522.0314

Table 4.1: Input parameters for SADI and MSFR simulation. Note that the geomagnetic field vector and the unitary LOS and velocity vectors are calculated in the middle of the scene.

latitude location was chosen to emphasize the impact of the change in $\vec{B} \cdot \hat{k}$ across the beam. In the low and mid-latitudes, the geomagnetic field vector has a strong horizontal component pointing towards the geomagnetic North, similar to the $\hat{v}_{\mathrm{sat}}$ in the polar orbit of Biomass. The FR injection was simulated in a set of complex clutter images (note that in the absence of the ionosphere $M_{\mathrm{HV}} = M_{\mathrm{VH}}$). The results are summarized in Figure 4.4: The top panel shows the integrated electron density irregularity field generated from the phase screen with the parameters in Table 4.1, the middle panel shows the single-look FR measured with Bickel and Bates from the semi-focused images (beam-center approximation) and the bottom panel shows the difference with respect to the semi-focusing injection. The middle panel indicates that (as expected from the literature) the beam-center approximation can be used to measure FR with high spatial resolution (even if the disturbance was injected with SADI); however, the difference due to the $\vec{B} \cdot \hat{k}$ variability is more appreciated in the bottom panel. The low-pass component of the difference map is related to the improvement in the accuracy of the current method. It shows the type of simulation and calibration errors that result from the beam-center approximation. These errors become more pronounced for larger beamwidths.

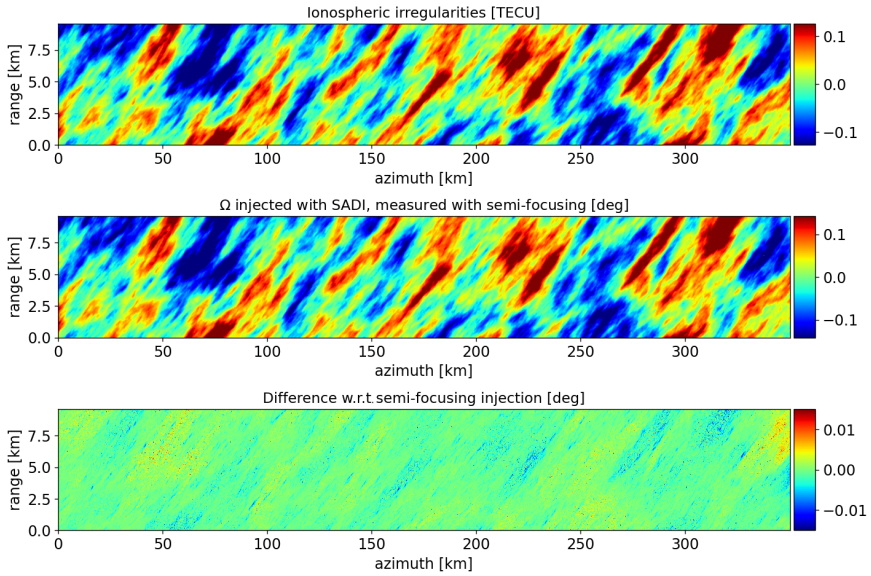

Figure 4.4: FR injected with SADI. The simulated irregularity field (top), FR measured with semi-focusing and beam-center approximation (middle) and difference with respect to beam-center FR (bottom).

4.2 Final Remarks

Simulations are used to develop and tune the proposed calibration algorithms for the operational part of the mission. At the simulation stage, with an accurate ionospheric injection, it is possible to estimate the suitability of the calibration algorithms in terms of performance and analyze the limitations. This is also the case of the ionospheric calibration, where an accurate injection of the ionospheric disturbances was needed to develop the algorithms presented in Chapter 5 or to understand the scintillation phenomenon in Chapter 7. In Section 5.1, it will be proven that the LOS variability is needed for a correct application of the FR for the mapping of the ionosphere.

The focus of this thesis is the simulation and the recovery of high-frequency ionospheric irregularities. However, the algorithm presented in this section is also generic for the background component. Direct uses are the ionospheric parallax [62] for the estimation of h_{iono} based on FR signatures, the estimation of TEC (background component) and h_{iono} from azimuth sub-apertures and multi-squint [60] or other ionospheric mapping approaches that use sub-looks [63, 91]. The use of all these techniques will still be considered for Biomass.

Finally, from any calibration approach, such as the ones presented in Chapter 5, an $STEC$ map can be obtained. A reverse application of SADI can then be applied to correct the ionospheric distortions accurately.

5 Calibration

This chapter describes the different ionospheric calibration approaches for the turbulent ionosphere investigated in the frame of this thesis. Given that the calibration involves an estimation of the ionospheric disturbance, we also refer to the visualization or imaging of the ionospheric irregularities. Then, parallel to the image correction, we focus on the quality of the recovery of the ionospheric irregularity maps. The starting point of all the methodologies is the exploitation of the azimuth synthetic aperture used to obtain high-resolution images in terms of azimuth sub-looks looking at different parts of the antenna beam utilizing Doppler frequency sub-bands. In other works, this approach to exploit different Doppler bands is also referred to as multi-squint [99, 68, 48]. This powerful principle will be used in Section 5.1 to undo the convolution of the FR disturbance in the data described in Section 3.3 while exploiting the change in $\vec{B} \cdot \hat{k}$ inside the radar beam, similar as in Section 4.1. This way, it is possible to transform squinted FR estimations in an accurate phase advance or TEC screen. This Multi-Squint Faraday Rotation (MSFR) method contributes to the calibration of quad-pol systems such as Biomass.

Sensitivity and geographic location (among other factors) limit the performance of FR-based calibration approaches (refer to Pub4 for more details). In addition, we shall consider that quad-pol systems are complex and limit the swath width [66]. For these reasons, we are interested in measuring the phase errors (that directly translate into TEC) and seeking solutions that work on images with a single polarization. An autofocus based on phase error estimates can help in this matter. In Section 5.2, we discuss the state-of-the-art and present advances in the development of a MapDrift Autofocus (MDA) algorithm. Again, the principle is based on the use of azimuth sub-looks to estimate the local azimuth variation of the phase screen error and to recover ionospheric realizations that will be used for data correction.

The implementation of the MDA in the framework of this thesis was first introduced in Pub2 in Appendix B and Section 5.2 provides a more thorough description of the principle, latest development and challenges.

In Section 5.3, we use the azimuth sub-looks again to estimate differential phase screens between single-image pairs in an interferometric stack. Interferometric methods, in general, give better ionospheric resolution. However, they can only recover the differential ionosphere, and even though they allow for interferometric coherence recovery, they are not helpful for the enhancement of individual products. In this work, we also introduce a method for the combination of interferometric results with the output of single-pass calibration approaches. We will show that the single-pass residuals are indeed inconsistencies that cancel out, leading to better single-pass solutions when interferometric information is employed. This work was introduced in Pub3 in Appendix C; Section 5.3 shows the latest developments and opens the possibility of future work in this field.

5.1 Quad-pol Calibration

As introduced in Section 3.3, propagation through an ionized medium in the presence of a magnetic field introduces a rotation in the polarization vector of linearly polarized waves. This phenomenon is widely known in low-frequency SAR systems such as the L-band ALOS-PALSAR [35, 69] and different estimators have been presented, with the Bickel and Bates estimator giving the best performance [59]. In [62], it is shown how *semi-focusing* the SAR images at h_{iono} can be used for FR estimation and correction. In addition, the FR angle can be converted into phase advance for phase correction and it has become a standard approach for ionospheric calibration in systems like Biomass [79]. When semi-focusing the image at ionospheric height, the available FR screen resolution is only limited by the SAR resolution and the filters applied in the estimation. This methodology follows the beam-center approximation: It assumes the estimation can be done based on the pointing at the center of the beam and neglects the pointing variability within the aperture.

In the following, a new way to look at the retrieval of ionospheric irregularities for calibration will be presented, overcoming the beam-center approximation. It will be shown that by accounting for the variation of the pointing inside the beam, low-pass errors in the conversion from estimated FR to phase advance can be avoided. In addition, looking at the FR variability inside the beam can also be used to detect and disregard inconsistencies in the geomagnetic field model.

5.1.1 Faraday Rotation Variation Inside the Beam

A Multi-Squint Faraday Rotation (MSFR) estimation scheme is proposed in this work. MSFR is a preferred approach that can efficiently accommodate the geometry, considering the changes in the pointing vector inside the radar beam. The principle is based on the Doppler frequency f_{a} to squint angle relation [80]

$$\sin \beta_{\mathrm{a}} = \frac{\lambda \cdot f_{\mathrm{a}}}{2 \cdot v} \,. \tag{5.1}$$

This means that a given Doppler frequency represents one of the squinted views of the radar acquisition during the aperture synthesis. Note that if the entire azimuth bandwidth B_{a} is processed, the range of squint angles was given in (2.1) and smaller antenna lengths or larger wavelengths lead to larger aperture angles.

For the problem geometry, refer to Section 4.1. From Figure 4.3, a squinted view of the ionosphere at R_{iono} is taken from the platform displaced an along-track distance Δx. Going back to (3.23) and (3.17), the conversion between the estimated FR angle Ω and ϕ depends on the $\vec{B} \cdot \hat{k}$ product with

$$\phi = -\frac{4 \cdot \pi \cdot \mathrm{m_e} \cdot f}{\mathrm{q_e} \cdot (\vec{B} \cdot \hat{k})} \cdot \Omega \,. \tag{5.2}$$

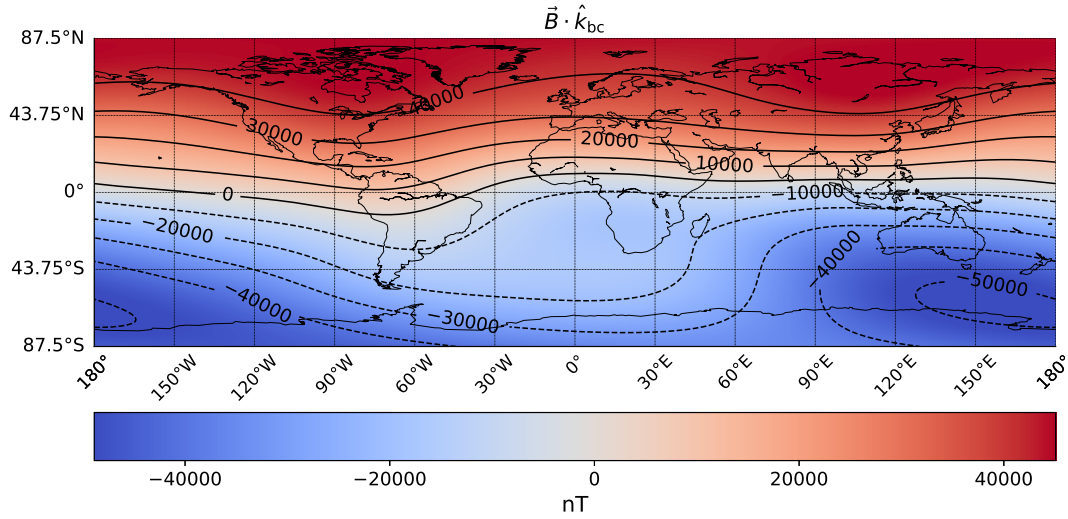

Figure 5.1: Global $\vec{B} \cdot \hat{k}_{\mathrm{bc}}$ measured by Biomass at the center of the beam, in a polar orbit with left-looking geometry. The geomagnetic field is calculated at 350 km altitude.

Figure 5.1 shows the value of $\vec{B} \cdot \hat{k}_{\mathrm{bc}}$ for the center for the beam with the Biomass geometry: Consider a polar orbit with a left-looking geometry and a 25° incidence angle onto the ionospheric plane, and the components of $\vec{B}$ are calculated at 350 km altitude. Note that the distribution strongly depends on the geomagnetic field vector and that at the geomagnetic Equator, $\vec{B}$ and $\hat{k}$ are almost perpendicular; this means that there will not be FR sensitivity there, a phenomenon known as *equatorial gap*. With a multi-squinted approach, it is possible to exploit the variation in LOS, reflected as a change in $\vec{B} \cdot \hat{k}$ [60], for an appropriate conversion to phase as in (5.2). The top map in Figure 5.2 shows the global change of

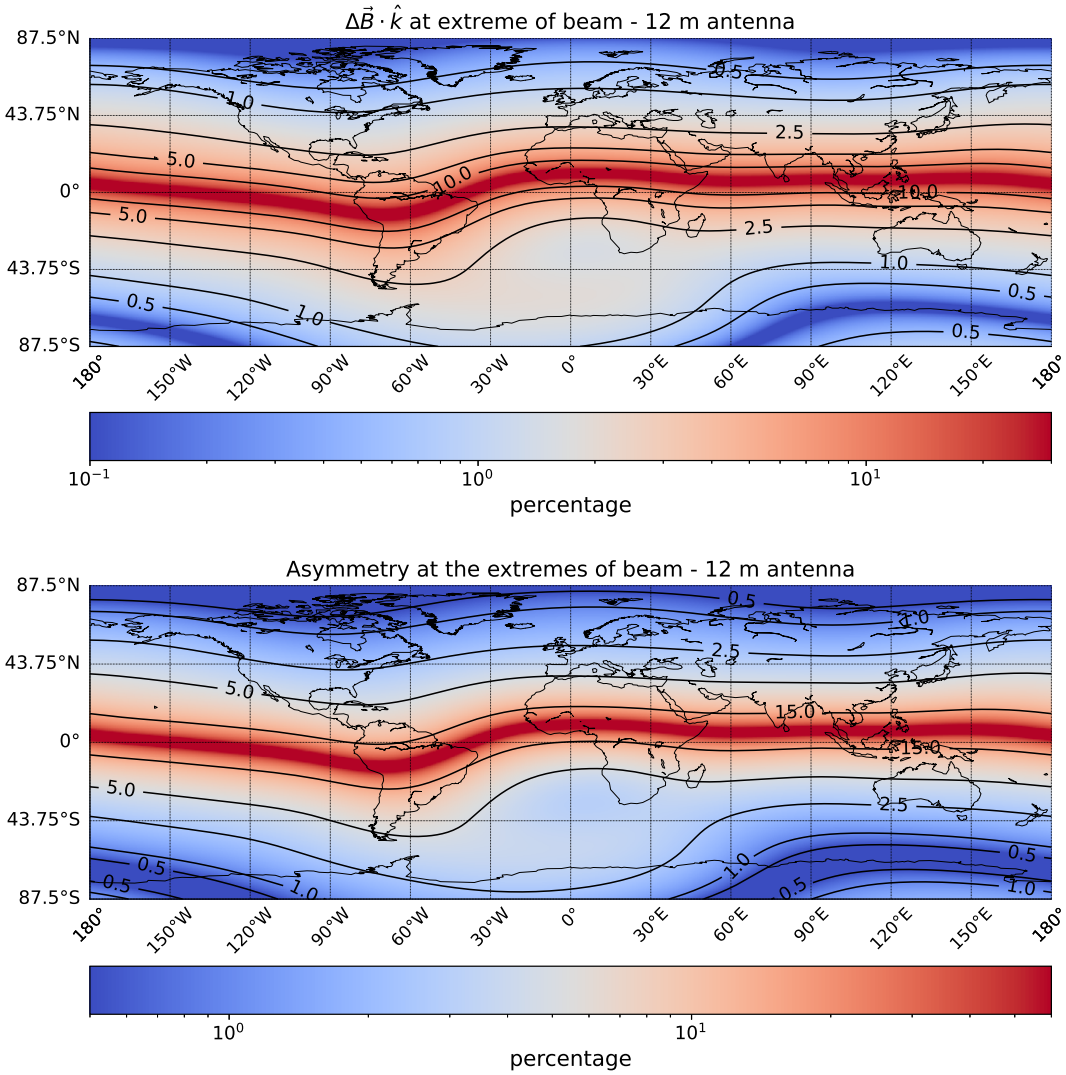

Figure 5.2: Change of $\vec{B}\cdot\hat{k}$ inside beam for a 12-m antenna. Percentage of variation from one beam extreme to the center (top) and asymmetry between the two beam extremes (bottom).

$\vec{B} \cdot \hat{k}$ in percentage with respect to the local value at the center of the beam $\vec{B} \cdot \hat{k}_{\mathrm{bc}}$, for the 12-m Biomass antenna. The first thing to notice is that the variation gets larger at mid and low latitudes; the reason for this is that the geomagnetic field vector has a stronger horizontal component that is amplified with $\hat{v}_{\mathrm{sat}}$ in (4.1). In addition, the variation is nearly zero at the locations where the geomagnetic dipole points perpendicular to $\hat{v}_{\mathrm{sat}}$, where the squint angle does not add to the $\vec{B} \cdot \hat{k}$ product.

The horizontal component of the geomagnetic field vector is, in general, not parallel to $\hat{v}_{\mathrm{sat}}$, even in a polar orbit, due to the geomagnetic dipole inclination and the SAA. For this reason, in general, the variation in the fore and aft halves of the azimuth antenna pattern is not symmetrical and does not cancel out (invalidating the beam-center approximation). In one half of the beam, the variation is positive and in the other negative; however, the difference in absolute percentage might not be negligible as it is shown in the bottom map in Figure 5.2, even at mid-latitudes. The wider the beam, the more significant the variation, and the beamwidth can be enlarged either by reducing the antenna size or by increasing the wavelength. The variations will be negligible neither in high-resolution systems where the synthetic aperture is increased with the antenna length nor in lower-frequency systems. A low-frequency system can be a radar sounder, which in some particular cases can go down to a central frequency of just 45 MHz [34].

5.1.2 Algorithm

Figure 5.3 describes the MSFR algorithm proposed in this work. The starting point is the full polarimetric set of range-compressed images (with the required geometry adjustments, the problem can also be solved with the focused SLC data). A set of Doppler frequencies for the generation of azimuth sub-looks with a given sub-look filter bandwidth is defined, and the sub-looks are generated by bandpass filtering in the range-Doppler domain. The central frequency is used to determine the corresponding squint angle with (5.1), which will be used for the calculation of the aperture-dependent LOS with (4.1) and corresponding $\vec{B} \cdot \hat{k}$. This will be used to transform from the measured squinted FR angle to phase advance. With the squint angle β_{a}, it is possible to approximate the displacement Δx with

$$\Delta x \approx R_{\mathrm{iono}} \cdot \tan \beta_{\mathrm{a}} \tag{5.3}$$

to coregister the estimated phase screens. The loop is repeated for all Doppler frequencies, and after averaging to combine the sub-looks and remove noise, a phase screen map that is usable for image calibration is obtained. Note that it is assumed that h_{iono} and R_{iono} are known, either from models or data-driven estimations (refer to Pub5 and Chapter 7 for a more thorough discussion on such methods).

To analyze the results, the phase screen in Figure 5.4 together with the corresponding FR screen are injected into a fully polarimetric complex speckle realization (for the details of the injection process, refer to Chapter 4 and Pub1). For this simulation, only the retrieval of the

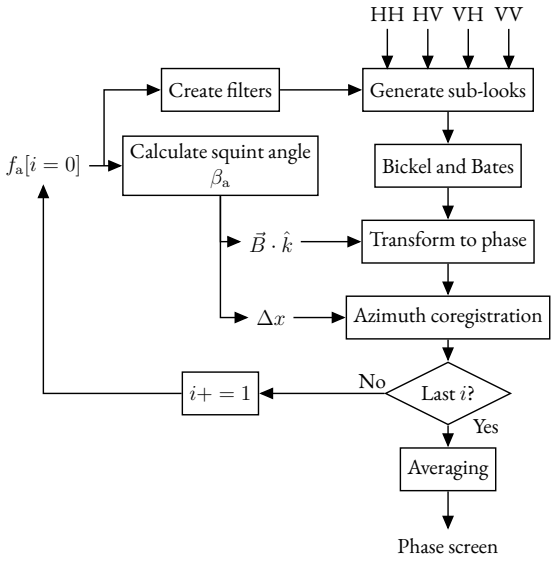

Figure 5.3: Multi-Squint Faraday Rotation block diagram.

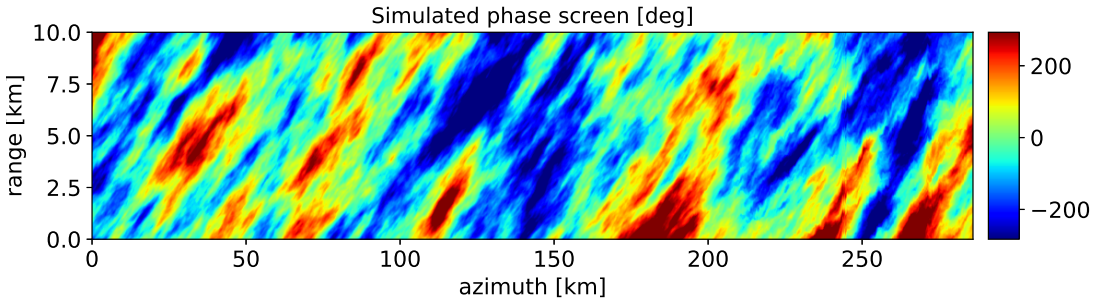

Figure 5.4: Simulated phase screen for MSFR experiment.

turbulent component of the ionosphere is considered (assuming the background ionosphere can be compensated entirely). The parameters used for the simulation are summarized in Table 4.1. The results presented here are with 70 non-overlapping sub-looks. Note that the exact geometry and orbit are used. For this simulation, a mid-latitude location was chosen to highlight the impact of the squint angle variability.

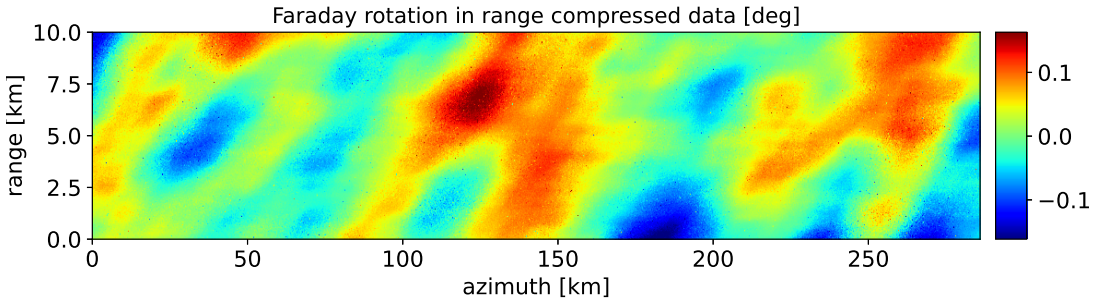

Figure 5.5: FR estimated with the Bickel and Bates algorithm in the range-compressed data.

The IGRF model provides the geomagnetic field coordinates in a local NED coordinate system, while the observation geometry is given in the Earth-Centered Earth-Fixed ($ECEF$) one. The following coordinate transformation to change from NED to $ECEF$ is used:

$$\mathbf{R}_{NED}^{ECEF} = \begin{pmatrix} -\sin\Lambda\cdot\cos\Theta & -\sin\Theta & -\cos\Lambda\cdot\cos\Theta \\ -\sin\Lambda\cdot\sin\Theta & \cos\Theta & -\cos\Lambda\cdot\sin\Theta \\ \cos\Lambda & 0 & -\sin\Lambda \end{pmatrix}, \tag{5.4}$$

with Λ and Θ being the geographic latitue and longitude, respectively.

As described in Section 3.3, either in the range-compressed or in the focused data, the ionospheric signature is smeared in azimuth due to the convolution inside the synthetic aperture. This effect is seen in Figure 5.5, which shows the FR estimated with the Bickel and Bates algorithm applied to the range-compressed data. Note that the direct signature is a low-pass version of the turbulent FR screen. State-of-the-art methods such as semi-focusing the image at h_{iono} undo this convolution, allowing the Bickle and Bates estimation at full spatial resolution [62]. The MSFR proposed in this thesis also does it by separating the spectral components of the data and an accurate geometric accommodation. Figure 5.6 shows two of the FR maps measured by sub-looking the range-compressed data; note the gain in resolution and the displacement associated with the squinted view. The extension at the edges of the maps is a result of the azimuth extension of the raw data; it was decided to be kept and cropped at the final stage to avoid data wrapping in the Fourier transforms.

Figure 5.7 shows the recovered phase screen map with the proposed approach together with the error map with respect to Figure 5.4. From the top map, note the good agreement with the injected phase distortion and the noise reduction compared to the single maps in Figure 5.6. From the residual map, we observe a high-frequency structure with the same

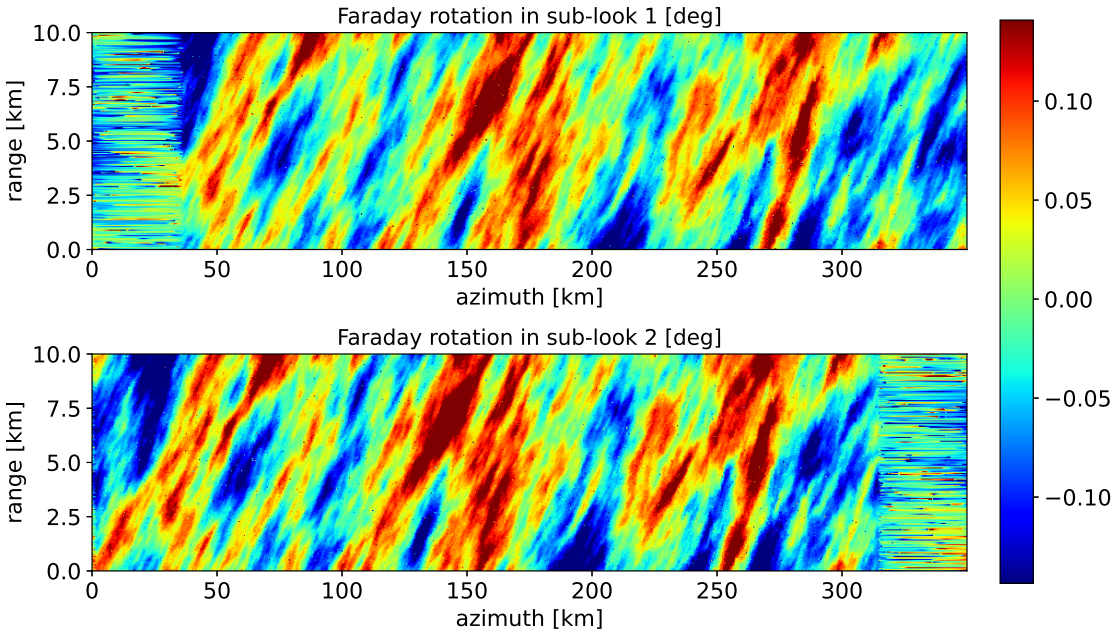

Figure 5.6: Two FR azimuth sub-looks.

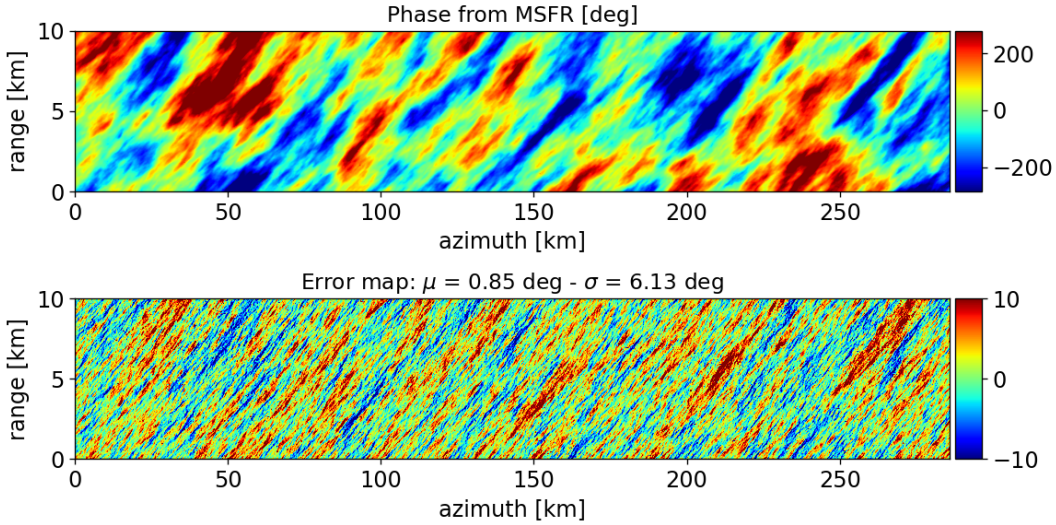

Figure 5.7: Phase screen recovered with MSFR (top) and residual error map (bottom).

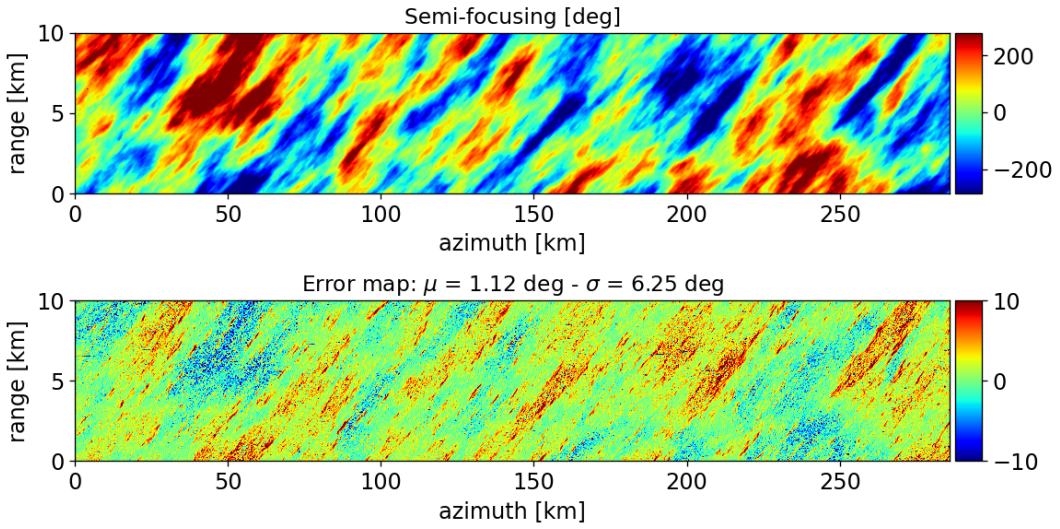

Figure 5.8: Phase screen recovered by semi-focusing (beam-center approximation) from FR (top) and residual error map (bottom).

orientation as the phase irregularities in the original map. As is discussed in Pub4, this is a result of the azimuth bandpass filtering step, which is responsible for a loss in sensitivity of the high-frequency components of the ionospheric signal. For comparison with another state-of-the-art method, Figure 5.8 shows the retrieved phase and residual map after estimating the FR in the semi-focused image at ionospheric height [62]: The omission of the squint angle variability results in additional low-pass errors reflected in the structure of the residual map. A quantitative comparison to the results in Figure 5.7 is the standard deviation of the residuals. For a fair comparison, the estimated phase screen in Figure 5.8 was bandpass filtered in azimuth to the same bandwidth as the MSFR sub-looks. Without this operation, the semi-focusing solution is, in addition, contaminated with high-frequency noise in the LR-RL interferogram.

5.1.3 Error Sources

The MSFR can better accommodate the geometry of the ionospheric retrieval based on FR while allowing for an efficient implementation. The accommodation of the $\vec{B} \cdot \hat{k}$ inside the beam allows for a more accurate conversion from the FR angle to phase advance by dropping the beam-center approximation. The performance of the estimation is limited by the noise in the FR estimation, uncertainties in the geomagnetic field, inaccuracies in the geometry (pointing errors and ionospheric height) and residuals from previous calibration steps (such as the antenna pattern compensation), to name a few. In this section, we will discuss separately the impact of noise, the geomagnetic field and the uncertainty in the ionospheric irregularity height h_{iono} in the thin-layer approximation.

Noise

The Bickel and Bates principle is based on the estimation of the interferometric phase between the two circularly polarized channels derived from the four linear polarizations. The performance is driven by the SNR that affects the polarimetric coherence with [47]

$$\gamma_{SNR} = \frac{SNR}{1 + SNR} \,. \tag{5.5}$$

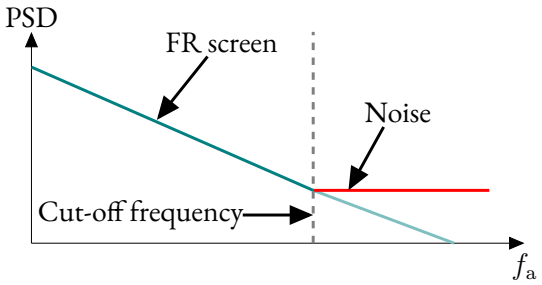

Figure 5.9: Cut-off frequency for MSFR based on noise. The filter bandwidth is given by the frequency where the additive white noise in red cuts the PSD of the FR signal.

Polarimetric decorrelation due to noise is seen as additive noise in the FR angle with single-look variance [47]

$$\sigma_\Omega^2 = \frac{1}{16}\left(\frac{\pi^2}{3} - \pi \cdot \sin^{-1}\gamma_{SNR} + \left(\sin^{-1}\gamma_{SNR}\right)^2 - \frac{\mathrm{Li}_2\left(\gamma_{SNR}^2\right)}{2}\right) \,, \tag{5.6}$$

where Li_2 is the Euler dilogarithm. The PSD of the FR screen is directly related to the one of the phase screen given in (3.3) through (5.2), so it also follows a power law as sketched in Figure 5.9. If the additive noise is modeled as Gaussian and white, its spectral representation is a constant at the variance value. The extension of the bandpass filters is chosen such that the filter covers most of the Doppler frequency components of the signal while rejecting the noise. Based on this, the SNR will move the red line in Figure 5.9 up and down, allowing for wider or narrower filters determining the frequency extent that can be estimated with a limited noise contribution. The purpose of this section is the geometrical justification of the method. The reader can refer to Pub4 for a more detailed discussion and representative figures of the noise contributions.

Geomagnetic field

In this thesis, the IGRF model is used for the determination of $\vec{B}$ and the conversion from FR angle to TEC and phase advance. In [9], an analysis of the geomagnetic field components uncertainty was carried out. It was found that, as a global average, the users shall count on a

standard deviation of 144 nT, 136 nT and 293 nT in the North, East and Down components of the geomagnetic field uncertainty vector $\vec{\sigma}_B|_{NED}$. If the geomagnetic field components in $ECEF$ are given by

$$\begin{pmatrix} B_x \\ B_y \\ B_z \end{pmatrix} = \mathbf{R}_{NED}^{ECEF} \cdot \begin{pmatrix} B_N \\ B_E \\ B_D \end{pmatrix} \ , \tag{5.7}$$

it is possible to use the error propagation algorithm described in [65, 69] to define an expression for the variance of the components in $ECEF$

$$\vec{\sigma}_B^2\big|_{ECEF} = \begin{pmatrix} \sigma_{B_x}^2 \\ \sigma_{B_y}^2 \\ \sigma_{B_z}^2 \end{pmatrix} = \left(\mathbf{R}_{NED}^{ECEF}\right)^{\circ 2} \cdot \left(\vec{\sigma}_B|_{NED}\right)^{\circ 2} \ , \tag{5.8}$$

where $\circ 2$ is the Hadamard elementwise product to indicate that the components in $\mathbf{R}_{NED}^{ECEF}$ and $\vec{\sigma}_B|_{NED}$ are squared independently before the matrix multiplication. At this point, it is assumed that the uncertainties $\vec{\sigma}_B|_{NED}$ are uncorrelated.

With the same principle, it is possible to prove that the variance of the $\vec{B} \cdot \hat{k}$ product is given by

$$\begin{aligned} \sigma_{\vec{B}\cdot\hat{k}}^2 = \sum_{i=\{x,y,z\}} \left(\left(\frac{\partial\left(\vec{B}\cdot\hat{k}\right)}{\partial B_i} \right)^2 \cdot \sigma_{B_i}^2 \right) + 2 \cdot \frac{\partial\left(\vec{B}\cdot\hat{k}\right)}{\partial B_x} \frac{\partial\left(\vec{B}\cdot\hat{k}\right)}{\partial B_y} \cdot \sigma_{B_{xy}}^2 + \\ 2 \cdot \frac{\partial\left(\vec{B}\cdot\hat{k}\right)}{\partial B_x} \frac{\partial\left(\vec{B}\cdot\hat{k}\right)}{\partial B_z} \cdot \sigma_{B_{xz}}^2 + 2 \cdot \frac{\partial\left(\vec{B}\cdot\hat{k}\right)}{\partial B_y} \frac{\partial\left(\vec{B}\cdot\hat{k}\right)}{\partial B_z} \cdot \sigma_{B_{yz}}^2 \ , \end{aligned} \tag{5.9}$$

which simplifies to

$$\sigma_{\vec{B}\cdot\hat{k}}^2 = \hat{k}^{\circ 2} \cdot \vec{\sigma}_B^2\big|_{ECEF} + 2 \cdot \left(k_x \cdot k_y \cdot \sigma_{B_{xy}}^2 + k_x \cdot k_z \cdot \sigma_{B_{xz}}^2 + k_y \cdot k_z \cdot \sigma_{B_{yz}}^2 \right) \ . \tag{5.10}$$

Note that, even if the components of $\vec{\sigma}_B|_{NED}$ are independent, the covariance terms

$$\sigma_{ij}^2 = \left(\sigma_{B_{xy}}^2, \sigma_{B_{xz}}^2, \sigma_{B_{yz}}^2 \right)^{\mathrm{T}}$$

in the second part of (5.10) cannot be neglected due to the coordinate transformation in (5.8).

Figure 5.10 shows a Monte-Carlo simulation for the current location to visualize the numerical impact of this uncertainty. The left plot shows the $\vec{B} \cdot \hat{k}$ values extracted at the center of the beam and one of the extremes. In the boxes, the analytical standard deviation values derived from (5.10) are displayed, and the vertical lines show the value of $\vec{B} \cdot \hat{k}$ if IGRF

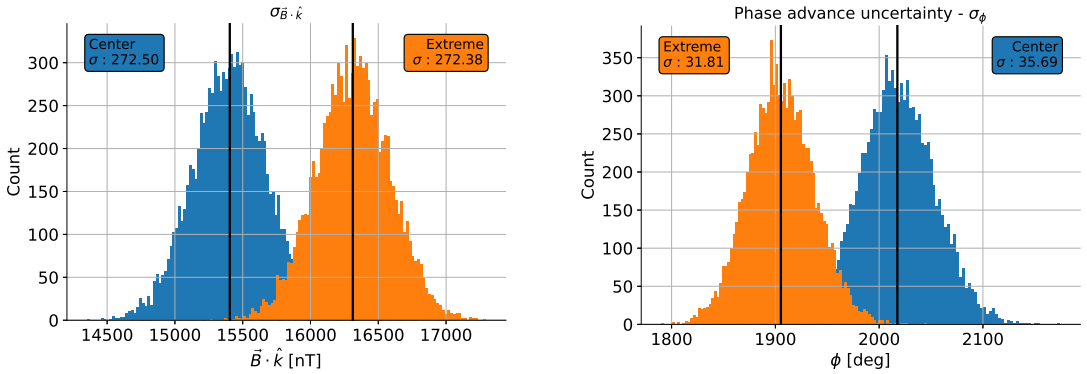

Figure 5.10: Uncertainty due to $\vec{\sigma}_B$ in the simulated scenario with parameters in Table 4.1 at the center and one extreme of the beam. Monte-Carlo simulation values for $\sigma_{\vec{B}\cdot\hat{k}}$ (left) and estimated phase advance that corresponds to $\Omega = 1°$ (right). The analytical standard deviations are highlighted in the boxes. The vertical lines show the values if IGRF would give the exact $\vec{B}$.

would provide the exact $\vec{B}$. The shift between the histograms and the slight variation in the analytical values correspond to the change in LOS (due to the subtle variation unless stated otherwise, we will keep referring to the $\sigma_{\vec{B}\cdot\hat{k}}$ at the center of the beam). The right plot shows the same realization, transforming $1°$ of FR into phase advance. Again, applying error propagation, the analytical expression for the variance of the phase advance given Ω is given by

$$\sigma^2_{\phi(\Omega)} = \left(\frac{\partial\,\phi(\Omega)}{\partial\left(\vec{B}\cdot\hat{k}\right)}\right)^2 \cdot \sigma^2_{\vec{B}\cdot\hat{k}} = \left(\frac{4\cdot\pi\cdot \mathrm{m_e}\cdot f}{\mathrm{q_e}\cdot(\vec{B}\cdot\hat{k})^2}\cdot\Omega\right)^2 \cdot \sigma^2_{\vec{B}\cdot\hat{k}}\,. \tag{5.11}$$

The non-negligible errors in the transformation from FR to phase (assuming no other calibration inconsistencies or uncertainties) are intrinsic in the use of the IGRF. However, the multi-squint operation might unlock the possibility of correcting these inconsistencies and (under specific sensitivity considerations) detecting local geomagnetic field variability with respect to the model. Figure 5.11 shows a simulation in which the MSFR reconstruction was done multiple times: First without an error in $\vec{B}$, and then with different error realizations within $\vec{\sigma}_B|_{NED}$. With the correct $\vec{B}\cdot\hat{k}$ variability inside the beam, there should not be any linear trend in the coregistered phase maps across the different sub-looks. The blue line shows the mean values of the maps across the sub-looks after coregistration, and the black line shows the linear fit. The light gray lines show the mean values of the sub-look phase maps for different geomagnetic field error realizations, and the green, orange and red lines show their linear fits. Green corresponds to a total error in the geomagnetic field below 4%, orange in the range $4-7\%$ and red above 7%. In the case of no geomagnetic field error, the residual slope is at least one order of magnitude lower than all the others. Here, for a better estimation of the fit with more samples, partially overlapped sub-looks are used.

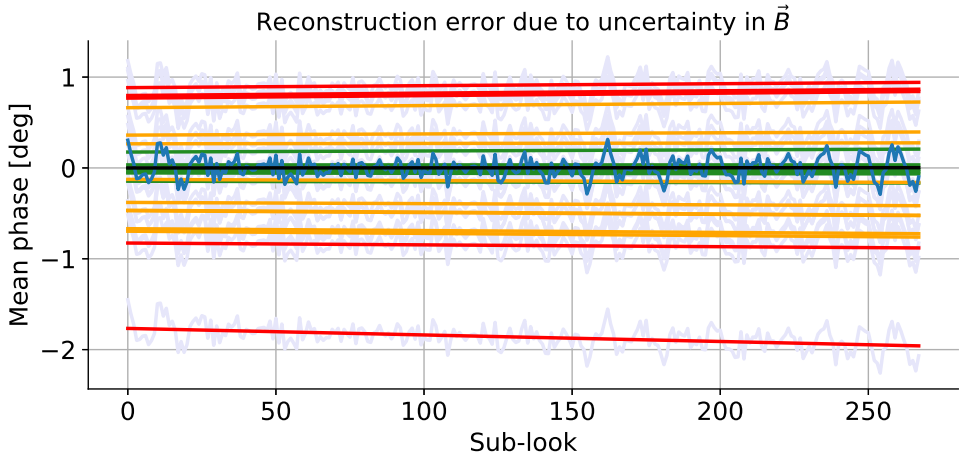

Figure 5.11: Error in phase reconstruction due to geomagnetic field uncertainty. The mean reconstructed phases for each sub-look without error in $\vec{B} \cdot \hat{k}$ (dark blue) and linear fit (black). Realizations with an error in $\vec{B} \cdot \hat{k}$ are shown in light gray with their linear fits in green (error below 4%), orange (error in the range $4 - 7\%$) and red (error above 7%).

The findings after analyzing Figure 5.11 show another way to exploit the FR estimations from a multi-squint perspective. The case was made with the uncertainty intrinsic in the IGRF model; however, the same principle can be used to detect anomalies in the geomagnetic field due to, for example, intense solar activity. The sensitivity and coupling with other residual calibration errors (such as in the antenna pattern compensation) are out of the scope of this thesis and left for further calibration performance analysis.

Ionospheric irregularity height

Errors in the geometry come from uncertainties in platform pointing and location and the knowledge of the ionospheric irregularity height h_{iono} when applying the thin layer approximation. h_{iono} determines the locations of the ionospheric piercing points, which define the local $\vec{B}$ and R_{iono}. The uncertainty in R_{iono} produces errors in the coregistration step. The reader can refer to Pub4 for a deeper discussion of h_{iono} estimation. To have a first feeling of the magnitude of the sensitivity, consider a planar geometry with

$$R_{\text{iono}} \approx \frac{h_{\text{sat}} - h_{\text{iono}}}{\cos\theta} \,. \tag{5.12}$$

Applying error propagation again on (5.3), the coregistration has a standard deviation

$$\sigma_{\Delta x} = \tan\beta_{\text{a}} \cdot \frac{\sigma_{h_{\text{iono}}}}{\cos\theta} \,. \tag{5.13}$$

Figure 5.12 shows the coregistration accuracy based on $\sigma_{h_{\text{iono}}}$, which has not been studied but is assumed small. From the results in Pub4, the azimuth resolution of the recovered

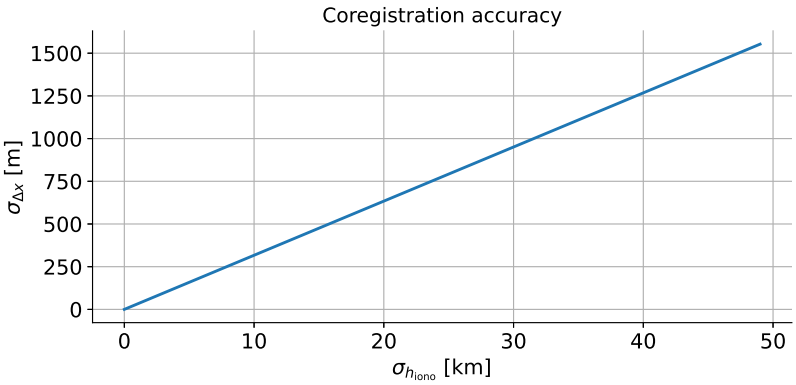

Figure 5.12: Coregistration accuracy based on $\sigma_{h_{\text{iono}}}$.

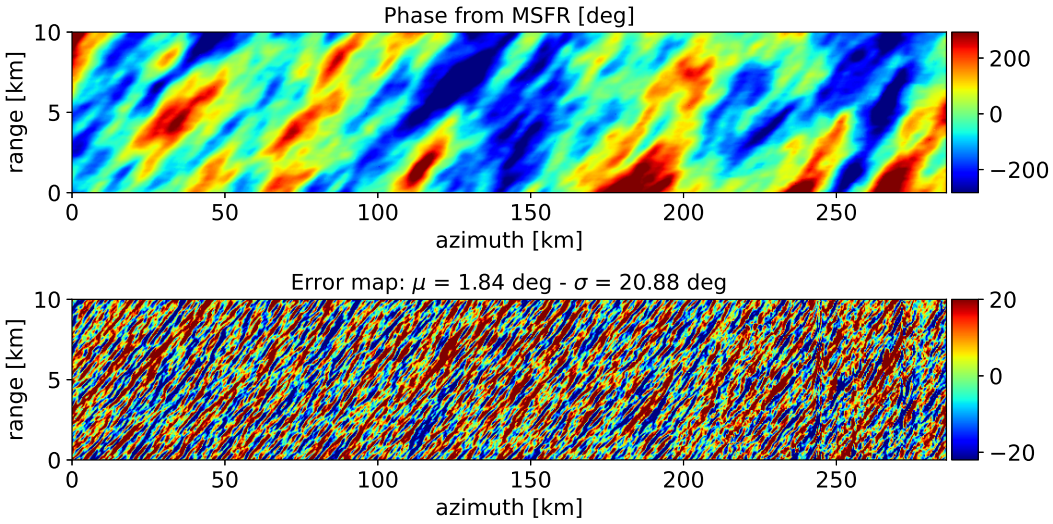

Figure 5.13: Phase advance from MSFR with 50-km error in h_{iono}.

irregularities is in the kilometer scale. To show an extreme example, an error of 50 km in the estimation of h_{iono} is shown in Figure 5.13: Here, the recovered phase advance map is defocused as compared to Figure 5.7. This is reflected in the disappearance of small features in the solution and the increased granularity of the error map (as well as the standard deviation of the error). However, for moderate errors in h_{iono}, this does not seem to be a critical point.

5.2 Single-Image Calibration

An estimation of the FR can be used to correct the polarimetric distortions in quad-pol datasets. Given that, like the phase advance, the FR derives directly from the TEC, it can also be used to correct phase errors. In Section 5.1, it was shown that Bickel and Bates could be used for the correction of small-scale ionospheric irregularities based on the estimation of a phase screen from squinted FR measurements. It was also seen that this approach poses several difficulties:

- From Figure 5.1 and (3.23) it is possible to deduce that even in the presence of an ionized plasma in the ionosphere, the FR disturbance gets lower towards the geomagnetic Equator due to the $\vec{B} \cdot \hat{k}$ product. For this reason, despite being a region with high scintillation activity expectancy, low FR sensitivity is expected at low latitudes.
- From (5.2), it is also possible to deduce that due to the inverse proportionality to the $\vec{B} \cdot \hat{k}$ product, small errors in the FR can translate into large errors in the phase advance used in the correction (more strongly at mid and low latitudes). As a consequence, the estimation of the FR at mid and low latitudes implies the use of large averaging windows that are insensitive to the high-frequency spatial variations. For this reason, the FR is instead used for the estimation of the ionospheric background component, approximating the ionosphere to a shell.
- Even though it is not the purpose of this thesis, it is essential to keep in mind that errors in the system calibration and antenna pattern compensation can also be reflected as polarimetric cross-talk, which adds to the phase advance estimation masked as FR.
- The impact of residuals in the IGRF model was studied and a method for the detection was proposed; however, the compensation of such uncertainty will depend on the sensitivity (which is still to be studied). It is hard to tell whether these residuals will be noticeable after single pass correction, but they are likely to impact the quality of the interferometric products.
- The SNR can highly limit the spatial frequency bandwidth for the FR measurement. Directional filtering for the recovery of smaller-scale irregularities is also implemented in the processor prototype; however, its parametrization depends on the IGRF (with its uncertainties). The scale of the filter is defined from scintillation models and the local SNR.

- Approaches based on the FR are limited to quad-pol systems, such as Biomass, but might be undesired in other low-frequency yet simpler mission concepts. Full polarimetry adds complexity to the system and reduces the swath width due to the incremented PRF.

For all these reasons, part of this thesis defines a prototype of a parallel approach that complements the ionospheric calibration based on FR. What is proposed here is an autofocus that directly measures the phase disturbance and bypasses the conversion from FR. The performance of such autofocus is latitude-independent and can be used at latitudes with low FR sensitivity as the equatorial gap. Since it measures ionospheric errors only, it is also independent of residuals in previous polarimetric calibration steps. It is possible to see the problem the other way around and attempt to correct for FR disturbances from phase advance with the benefit that from (5.2) the $\vec{B} \cdot \hat{k}$ product would then be multiplying and reducing the noise scaling of errors in the phase screen estimation. Last but not least, the phase screens obtained using autofocus can be used to separate the ionospheric contribution to the estimated FR from other polarimetric calibration errors.

Compared to the phase ramps expected by the slowly varying background component of the ionosphere, the turbulent part introduces high-frequency phase errors in the images. The irregularities that shall be taken into account here are the ones with a size comparable to or smaller than the synthetic aperture projected at h_{iono}. A quadratic (or of higher order) phase error along the azimuth direction introduces azimuth defocusing. Therefore, autofocus techniques are insensitive to phase advance biases and phase ramps, which are expected to be calibrated separately. Figure 5.14 shows the impact of the turbulent ionosphere in terms of phase advance after the injection in a TerraSAR-X reflectivity image with multiplicative complex speckle. Azimuth is the horizontal and range is the vertical axis. The defocusing in different regions of a simulated image is highlighted in the squares: In a green frame, the image block without ionospheric disturbance and in a red frame, the block with high-frequency phase advance error. Note the loss of contrast and defocusing in the azimuth direction. The second map from the bottom shows the coherence loss after the ionospheric phase injection, and the last map shows the interferometric phase. Note that this is not the injected phase screen used but a low-pass version due to the synthetic aperture averaging. Also, the higher coherence loss is found in the regions of larger phase differences. For details in the disturbance injection step, the reader can refer to Chapter 4.

Recovering equation (3.20)

$$s_{\text{rc}}(t_{\text{a}}; R_0) = \int a\left(t'_{\text{a}}\right) \cdot \text{rect}\left(\frac{t'_{\text{a}} - t_{\text{a}}}{L_{\text{a}}}\right) \cdot \exp\left(-\frac{4 \cdot j \cdot \pi}{\lambda} \cdot R_0\right) \cdot \exp\left(j \cdot \pi \cdot K_{\text{a}} \cdot \left(t'_{\text{a}} - t_{\text{a}}\right)^2\right) \cdot \exp\left(j \cdot \phi_{\text{iono}}\left(\frac{R_{\text{iono}}}{R_0}\left(t'_{\text{a}} - t_{\text{a}}\right)\right)\right) \text{d}t'_{\text{a}}\,,$$

the ionosphere adds a phase disturbance component to the phase history of the raw data.

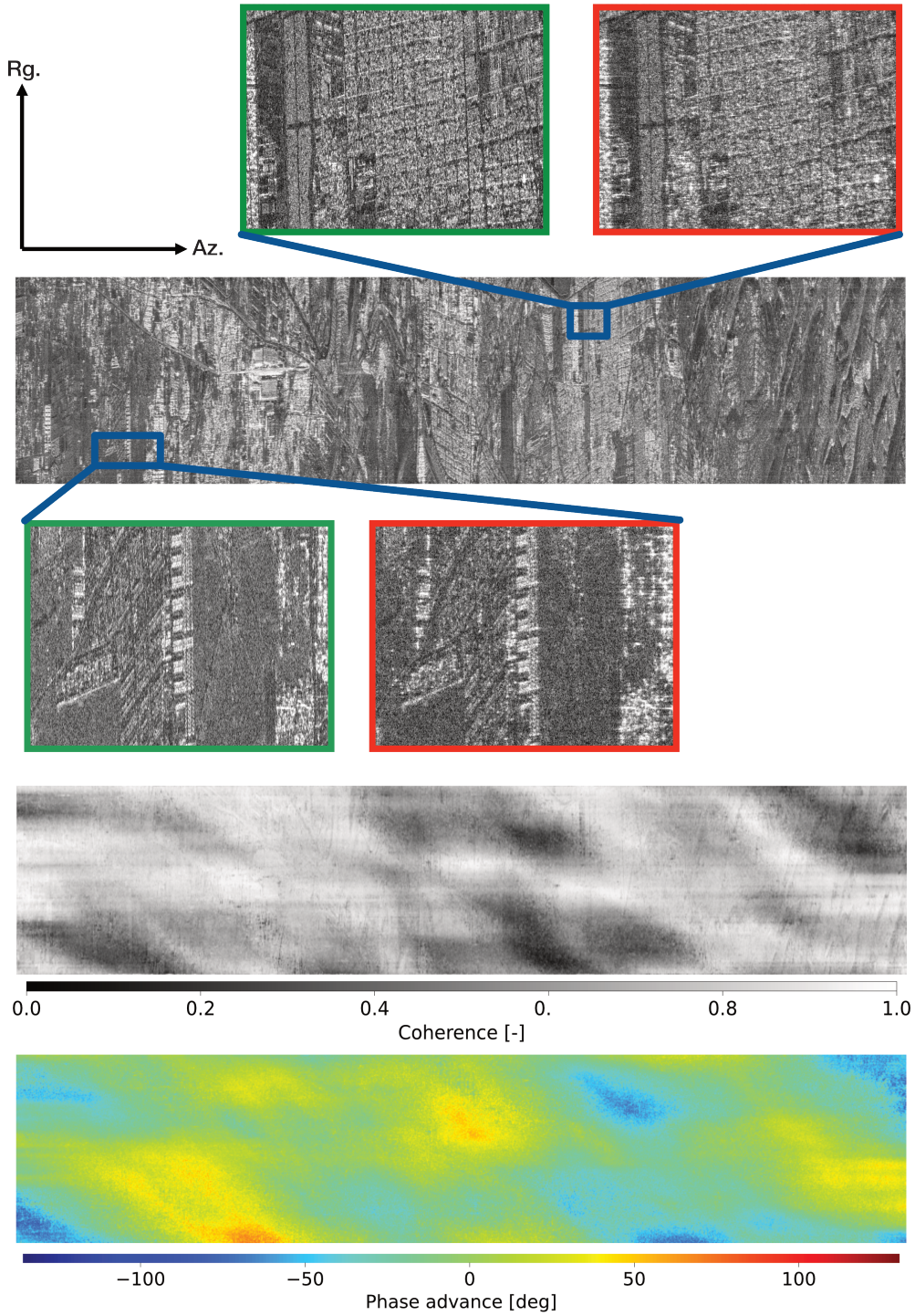

Figure 5.14: High-frequency phase errors in a TerraSAR-X image (example). Image blocks without defocusing (green frame) and with defocusing (red frame). Coherence loss (second from the bottom) and interferometric phase (bottom) between the ionosphere-free and the ionosphere-affected images.

This additional phase history is not compensated by the matched filter with Doppler rate K_a and remains as defocusing. The most obvious is a Quadratic Phase Error (QPE), which has a form similar to the second exponential in (3.20) and across the synthetic aperture is seen as an error in the Doppler rate δK_a. The problem is well known in airborne SAR interferometry where, due to the unstable aircraft trajectory, range errors comparable to the wavelength are visible in the interferograms even after Motion Compensation (MoCo) despite the use of advanced navigation systems [29]. This problem has led to the development of data-driven algorithms such as autofocus. An autofocus estimates the defocusing directly from the data, models the corresponding compensation and iteratively applies a correction. Metrics such as contrast or entropy are used to analyze the convergence.

The Phase Gradient Autofocus (PGA) [31, 106] was developed for spotlight acquisitions and estimates the derivative of phase errors in range-compressed prominent targets. After a first-order integration, the absolute phase errors can be recovered (except for an integration constant). The Phase Curvature Autofocus (PCA) adapts the PGA to be used with stripmap data [107]. These approaches attempt to resolve 1-D phase errors around the point targets by averaging across the range bins, but, as was discussed so far, the interest relies on resolving 2-D ionospheric irregularity structures. PGA or PCA requires the presence of prominent targets to be used and a sparse implementation of the PGA was presented in [52]; however, the performance is strongly limited by the presence of enough point targets, a condition that, in general, is not warranted (especially in low-frequency radar).

During the development of this work, the focus was put on the development of a Map-Drift Autofocus (MDA) [50] prototype for the correction of phase errors to be used in synergy with the calibration based on the FR estimation. The MDA proposed in this work is able to recover 2-D phase advance errors from single images, and it is preferred to the PCA because it does not require the presence of prominent point targets, therefore making it suitable for distributed scenes. In addition, Weighted Least Squares (WLS) can be used to combine the information retrieved from different polarimetric channels and (optionally) the phase screen recovered from the FR step. Under the assumption that the errors given by different measurements are independent, the WLS optimization sees them as inconsistencies and cancels them out [44]. This approach can be extended to incorporate alternative estimations extracted from a range-autofocus that exploits chirp dispersion or from PCA.

5.2.1 Principle and Methodology

The MDA principle is based on the estimation of the absolute phase error from the measurement of local second derivatives by means of sub-look coregistration of image blocks. Figure 5.15 shows the effects of a QPE injected at h_iono in a point target with the parameters in Table 5.1. The left panel shows the azimuth impulse response of a point target with and without a QPE. Note that even with the small δK_a, the point target looks quite defocused, with an decreased PSLR. The right panel shows two azimuth sub-looks of the defocused point target generated by band-pass filtering in the frequency domain (one sub-look taking

the positive and the other taking the negative Doppler frequencies); note that the orange impulse response in the left panel is the sum of the two sub-looks in the right panel. The shift in pixels between the sub-looks Δa is related to δK_{a} as

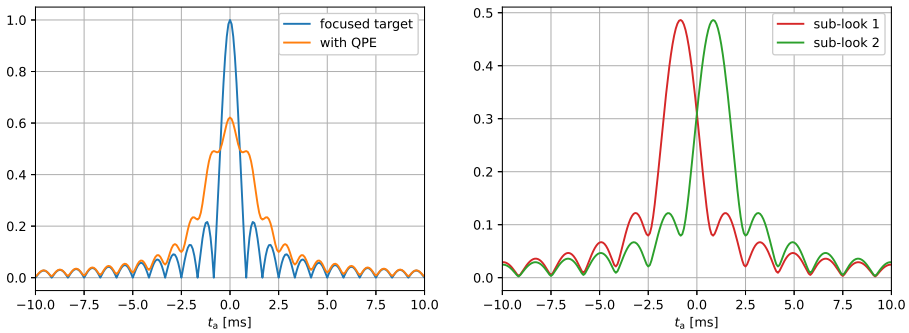

Figure 5.15: Simulated phase error in point targets. The impulse response of a point target under a QPE (left). Two azimuth sub-looks after spectral separation (right).

$$\delta K_{\mathrm{a}} = \frac{2 \cdot \Delta a}{B_{\mathrm{a}}^2 \cdot \mathrm{osf}} \cdot K_{\mathrm{a}}^2 \,, \tag{5.14}$$

where osf is the oversampling factor in azimuth. Since the phase disturbance is injected in the target semi-focused at h_{iono}, the position vector x_{a} must be scaled to

$$x_{\mathrm{a,iono}} = x_{\mathrm{a}} \cdot \frac{L_{\mathrm{sa}}}{L_{\mathrm{sa,iono}}} \,,$$

where L_{sa} is the synthetic aperture and $L_{\mathrm{sa,iono}}$ is the synthetic aperture projected at h_{iono}. $L_{\mathrm{sa,iono}}$ is approximately

$$L_{\mathrm{sa,iono}} \approx \frac{(R_0 - R_{\mathrm{iono}}) \cdot \lambda}{L_{\mathrm{a}}} \tag{5.15}$$

according to Figure 5.16.

This is the same as saying that δK_{a} is scaled to

$$\delta K_{\mathrm{a,iono}} = \frac{2 \cdot \Delta a}{B_{\mathrm{a}}^2 \cdot \mathrm{osf}} \cdot K_{\mathrm{a}}^2 \cdot \left(\frac{L_{\mathrm{sa}}}{L_{\mathrm{sa,iono}}} \right)^2 \,. \tag{5.16}$$

Measuring the coregistration error between the two sub-looks by cross-correlation gives Δa, and with (5.16), $\delta K_{\mathrm{a,iono}}$ can be estimated. This is used to estimate the quadratic phase history error that caused the defocusing

$$\phi_{\mathrm{Q}}\left(t_{\mathrm{a}}\right) = \pi \cdot \delta K_{\mathrm{a,iono}} \cdot t_{\mathrm{a}}^2 \,, \tag{5.17}$$

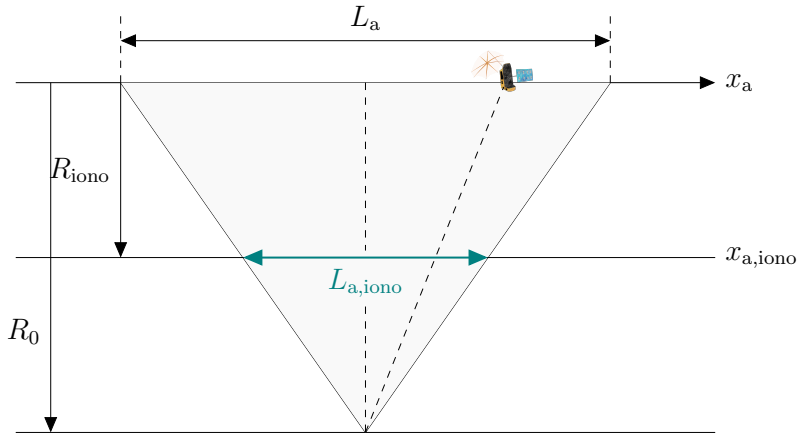

Figure 5.16: Simplified slant geometry from focused point target.

Parameter	Unit	Value
Frequency, f_0	MHz	435
Antenna length, L_{a}	m	12
Closest range, R_0	km	728.229
Range to iono., R_{iono}	km	342.047
Doppler rate, K_{a}	s^{-2}	-206.58
Doppler rate error, $\delta K_{\mathrm{a,iono}}$	s^{-2}	0.4264
Doppler bandwidth, B_{a}	s^{-1}	1200

Table 5.1: Parameters for QPE simulation in Biomass point target.

and its second derivative is

$$\ddot{\phi} = 2 \cdot \pi \cdot \delta K_{\mathrm{a,iono}}. \tag{5.18}$$

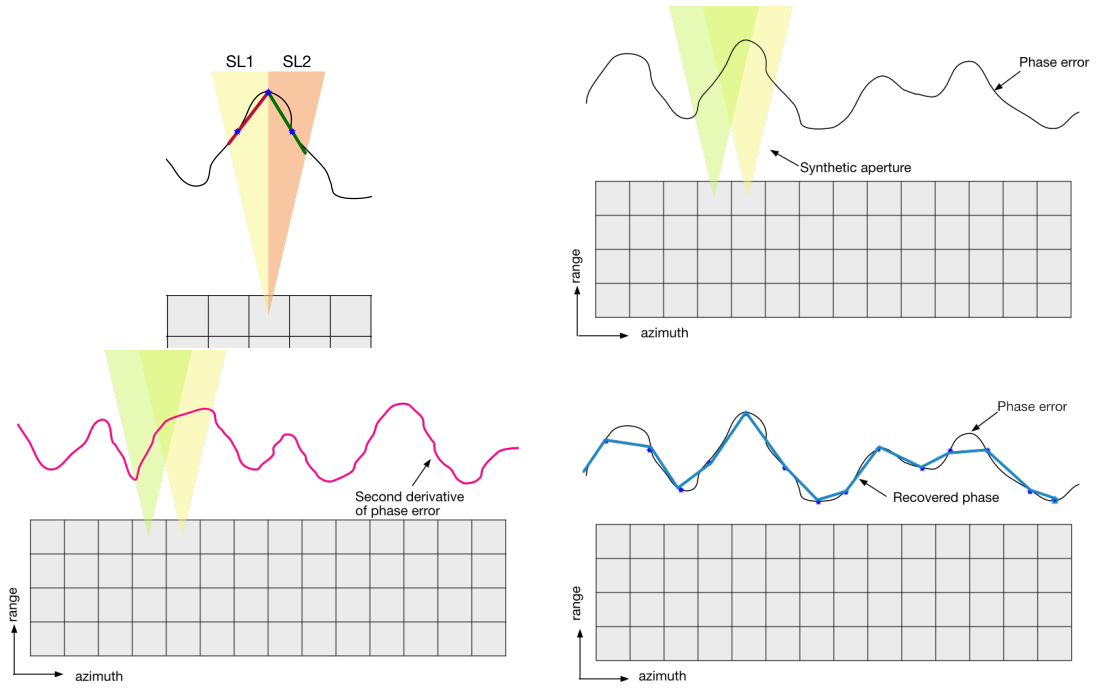

Figure 5.17: MDA principle. Local estimation of second derivative from azimuth sub-looks (top-left), phase error (top-right) over an image range bin, estimated second derivative (bottom-left) and integrated phase (bottom-right).

Similar to the MSFR principle in Section 5.1, taking azimuth sub-looks from an SLC image block gives squinted views of the locally processed ionosphere. This allows us to locally estimate $\phi_{\mathrm{Q}}(t_{\mathrm{a}})$ along azimuth as sketched in the top-left panel of Figure 5.17. Here, the phase error curve seen by an image block in black is approximated by a quadratic function using the shift estimated from the two block sub-looks. The red and green lines approximate the QPE with two linear phases (one in each half of synthetic aperture) that *push* the sub-looks in opposite directions (as seen in the right panel in Figure 5.15). The second derivative estimated by the MDA is the difference between these two slopes. The top-right panel in Figure 5.17 shows that if the SLC is divided into blocks, the phase error in each of them will concentrate on what is seen by the local synthetic aperture. For each block, an approximation of the second derivative of the phase advance error (bottom-left panel) is estimated, which has to be double-integrated to a downsampled version of the phase error (sampled at the block centers). This way, it is possible to reconstruct higher-order errors by utilizing second derivatives. The phase error compensation is applied to the image at full resolution. In this case, a linear interpolation was used for upsampling (bottom-right panel). A higher order interpo-

lation (3rd degree) was also considered and will be kept in mind, even thoguh a first analysis showed little improvement.

The double integration provides an estimate of the 2-D phase advance error map without two integration constants in each range bin; therefore, it is assumed that the constant and linear terms have been previously calibrated. This is the most critical part of the MDA. In the integration step, errors in the local $\delta K_{\mathrm{a,iono}}$ estimation integrate into random walks that not only affect the corresponding range bin but add undesired discontinuities in the range direction. For this reason, the integration is made globally in a Least-Squares (LS) framework to *force* each integrated phase in azimuth to be consistent with the neighboring range bins.

The LS relates the observed second derivatives along a range bin $\ddot{\phi}$ (measurements) to the absolute phase ϕ with the double differential operator $\mathbf{L}$

$$\ddot{\phi} = \mathbf{L} \cdot \phi + n \,, \tag{5.19}$$

where n denotes independent errors in the measurement of $\ddot{\phi}$. If the first derivative operator is

$$\mathbf{L}^{(1)} = \frac{1}{\mathrm{d}t} \cdot \begin{pmatrix} -1 & 1 & 0 & 0 \\ 0 & -1 & 1 & 0 \\ 0 & 0 & -1 & \ddots \\ 0 & 0 & 0 & \ddots \end{pmatrix} , \tag{5.20}$$

then

$$\mathbf{L} = \mathbf{L}^{(1)} \cdot \mathbf{L}^{(1)} \,, \tag{5.21}$$

where $\mathrm{d}t$ is the time step between the samples (the block centers). The pseudo-inverse of $\mathbf{L}$ is used to solve for a best estimate of ϕ, that we call $\hat{\phi}$, minimizing the impact of n (optimally, canceling the random walks). The system is easily expandable in the range direction to integrate all the range bins at once into a 2-D solution. During the development of this work, it was found that it is a good practice to *tight* the different range bins at the ends to minimize discontinuities. The quality of the recovered map depends on the LS solution of (5.19), which is limited by the quality of the second derivative estimates. If available, the system can be extended to a WLS with an estimate of the $\ddot{\phi}$ uncertainty (directly from the uncertainty in Δa). The solution is then given by

$$\hat{\phi} = \left(\mathbf{L}^{\mathrm{T}} \cdot \mathbf{W} \cdot \mathbf{L}\right)^{-1} \cdot \mathbf{W} \cdot \mathbf{L}^{\mathrm{T}} \cdot \ddot{\phi} \,, \tag{5.22}$$

where $\mathbf{W}$ is a diagonal matrix made of the inverse of the variance of each $\ddot{\phi}$ measurement. The WLS gives less weight to the Δa with higher uncertainty. A more thorough discussion is given in Section 5.2.3, but a first good approach to reject the outliers is to use, for each block, the variance of the Δa measured in a 3x3 surrounding window.

ϕ is common to all channels and the information is redundant in a polarimetric system such as Biomass. In addition, the transformation matrix can be adapted to combine independent estimates of the phase advance, such as the one extracted from the FR ϕ_{FR} (refer to Section 5.1). Then, (5.19) can be transformed into

$$\begin{pmatrix} \ddot{\phi}_{\mathrm{HH}} \\ \ddot{\phi}_{\mathrm{HV}} \\ \ddot{\phi}_{\mathrm{VH}} \\ \ddot{\phi}_{\mathrm{VV}} \\ \phi_{\mathrm{FR}} \end{pmatrix} = \begin{pmatrix} \mathbf{L} \\ \mathbf{L} \\ \mathbf{L} \\ \mathbf{L} \\ \mathbf{I} \end{pmatrix} \cdot \phi + \begin{pmatrix} n_{\mathrm{HH}} \\ n_{\mathrm{HV}} \\ n_{\mathrm{VH}} \\ n_{\mathrm{VV}} \\ n_{\mathrm{FR}} \end{pmatrix}, \tag{5.23}$$

where $\ddot{\phi}_{\mathrm{ij}}$ are the second derivative measurements from each of the polarimetric channels, $\mathbf{I}$ is the identity matrix (the FR gives a direct estimate of the absolute phase advance), n_{ij} are the errors in the second derivative measurements for each channel and n_{FR} is the error in the phase advance recovered by the FR. Solving for (5.23) with a weighted solution as in (5.22) can efficiently be done with a sparse Lower-Upper (LU) decomposition [75]. The weights used for the uncertainty in phase advance derived from the FR can be extracted from the polarimetric decorrelation due to the noise γ_{SNR} and (5.6) [44]. In addition, the geomagnetic field uncertainty described in Section 5.1.3 should be taken into account (even though it has so far been neglected in this prototype).

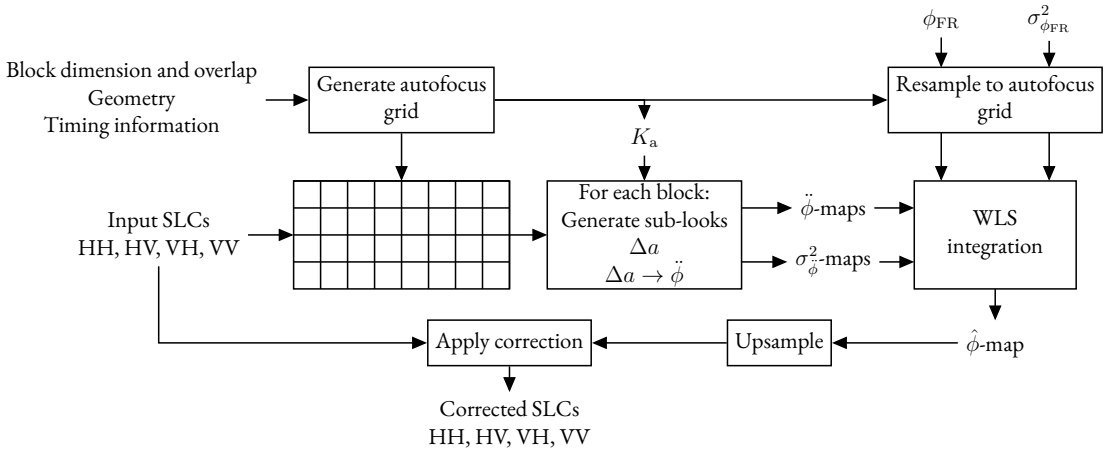

Figure 5.18: MDA block diagram.

The block diagram in Figure 5.18 summarizes the MDA steps. The inputs are the SLCs from the polarimetric channels, as well as the acquisition geometry and timing. The block size to be used is an input parameter chosen to balance the performance of the cross-correlation for sub-look shift estimation with the spatial averaging of the solution. The block centers give the autofocus grid, which is where the second derivatives and the integrated phase advance

will be sampled. For each block, two sub-looks are generated with Doppler frequency filtering and from Δa, the local second derivative $\ddot{\phi}$ is estimated after scaling to $\delta K_{\mathrm{a,iono}}$. Since the effective velocity varies across the scene, the local K_{a} at each block center is used for the scaling. Once a second derivative map is obtained, the uncertainty of each estimate is calculated. If the phase advance map extracted from the FR is to be used, first, it must be resampled to the same grid as the one given by the block centers (same with its uncertainty). Now, all observables can be put into a WLS system like (5.23) to obtain a downsampled version of the absolute phase advance map. Before using it for correction, it is upsampled to the SLC size with a linear interpolation. In this prototype, the correction of the data is done by semi-focusing. The algorithm is iterative: In each iteration, the phase advance is estimated on the accumulated Δa, and the initial images are the ones to be corrected to avoid additional defocusing from random walks in earlier iterations.

The method could be extended to the estimation of higher-order components as in the Multi-Aperture MapDrift (MAM) [21]; however, this practice involves the division into multiple sub-apertures, lowering the resolution and effective energy in each sub-image [2]. This practice could be applied in a high-resolution system with a large Doppler bandwidth, and its operational use in Biomass will be studied in the future.

5.2.2 Results

In the following, an example of a phase recovery with the MDA is presented. The simulation is run with the Biomass-looking geometry and, in the absence of satellite P-band images, the reflectivity of the X-band acquisition in Fig. 5.14 is used. The algorithm is iterated five times and the phase from the FR map measured by the GPP is shown in Figure 5.19; note that the GPP does not estimate the phase from FR as in Section 5.1 but it uses a directional Gaussian filter instead. Figure 5.20 shows the shifts Δa measured in the first and the last iteration for all four polarimetric channels in the case in which the FR was not used in the top and middle panels and where the FR was used in the bottom panel. Note that the value of the shifts decreases, but they do not vanish entirely due to the inconsistencies introduced by the sampling, averaging and integration steps. Note also that in this case, the use of the FR leaves some larger shifts, the reason for which is that using the weights of the FR dominates the WLS solution and somehow limits the MDA resolution.

Figure 5.21 shows the parameters used to analyze the convergence of the MDA in the GPP. The left panel shows the evolution of the Shannon entropy [96] as a contrast metric of the image after each correction for the case in which the FR was used. The first iteration gives a significant jump in entropy. Another metric used to analyze the convergence of the solution is the standard deviation of the recovered phase screens in each iteration, which is expected to increase with the cumulative Δa slowly. During the development of the MDA in the GPP, discontinuities and jumps in this curve also hinted at non-convergence.

Figure 5.22 shows the phase screen used in the simulation and the ones recovered with the MDA after five iterations. The top panel corresponds to the case in which the integration

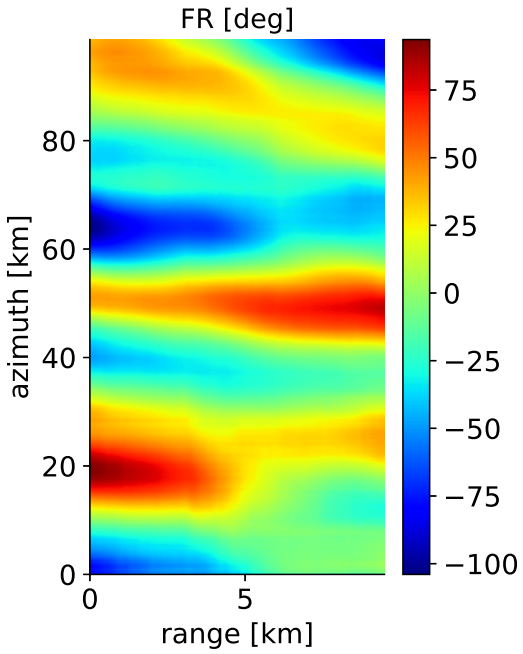

Figure 5.19: Phase map derived from estimated FR used in MDA simulation.

was done with the measured Δa only, and the bottom panel shows the case in which the integration was aided with the FR. The right plots in both panels show the residual maps. The structure of the error maps is characteristic of the resolution limitation given by the sub-look aperture and the approximation of high-frequency irregularities by their quadratic components only. Note that two sub-looks in a projected synthetic aperture of 20 km give around 10-km resolution. Even though it was shown that the solution with the FR leaves some larger shifts in this case, in general, it *guides* the integration to avoid jumps and discontinuities. During the development of the MDA in the GPP, this was beneficial in challenging scenarios that would not converge otherwise. However, it is clear that by using the Δa measurements alone, a higher resolution in the regions with quick variabilities can be obtained if, for example, due to the SNR, the FR to be used only gives a coarse resolution.

As commented earlier, during the development of this prototype, it was also seen that for scenarios in which σ^2_{FR} is much smaller than $\sigma^2_{\dot{\phi}}$, the FR solution will dominate (even when its spatial resolution is not smaller than the one of the MDA) and the combined WLS does not bring any improvement. In conclusion, the combined framework has its benefits, but further tuning is required for a robust and reliable scheme that would work in a good number of scenarios. Different metrics of the weights in the WLS and ways to gain resolution will have to be explored in the commissioning and operational phases of the mission when the P-band data are available. Finally, the coherence gain with respect to the original image without any phase disturbance is shown in Figure 5.23.

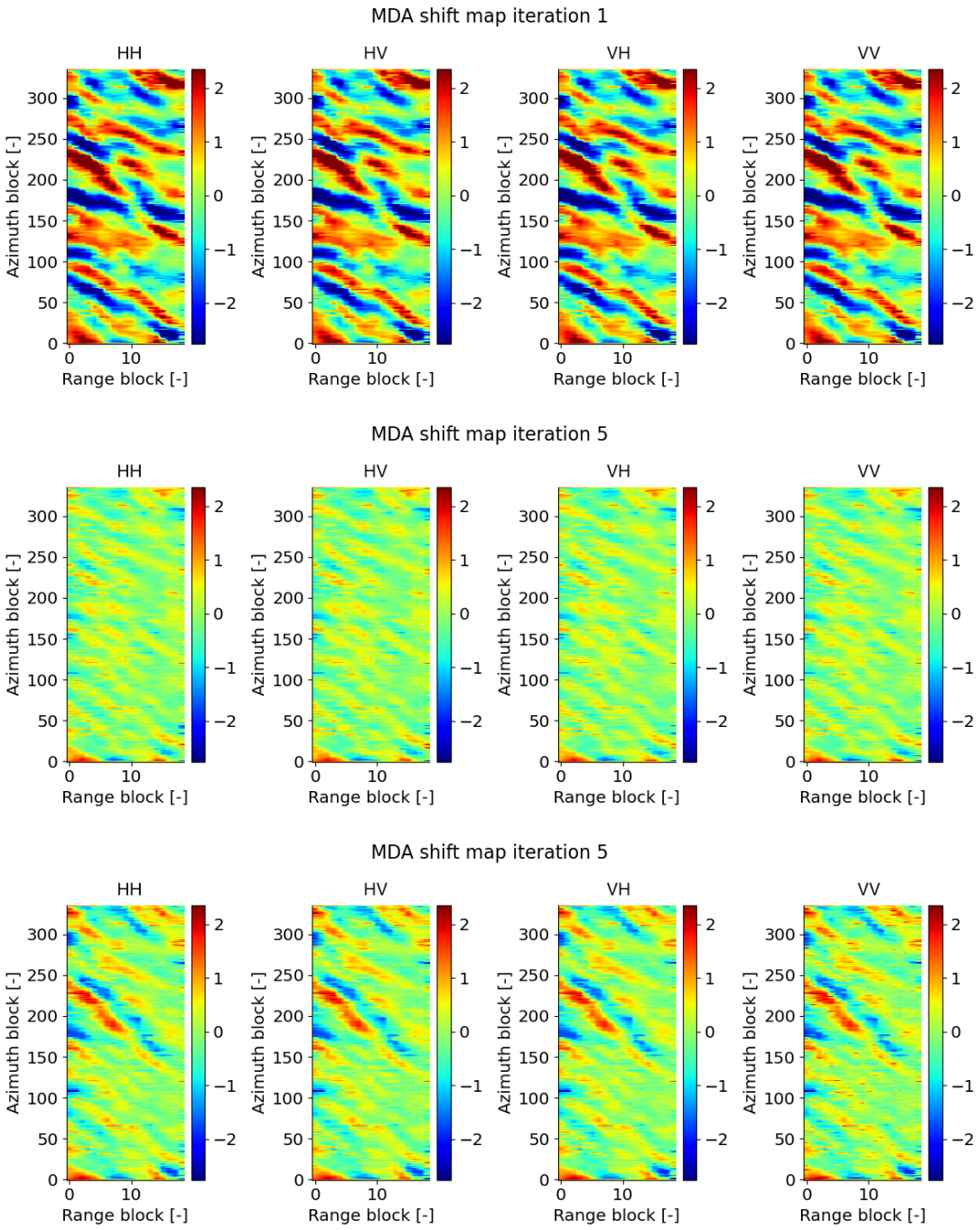

Figure 5.20: Iterative MDA shift maps. The top and middle panels correspond to the case in which the integration was done without the aid of the FR. The bottom panel shows the 5th iteration of the case in which the FR was used.

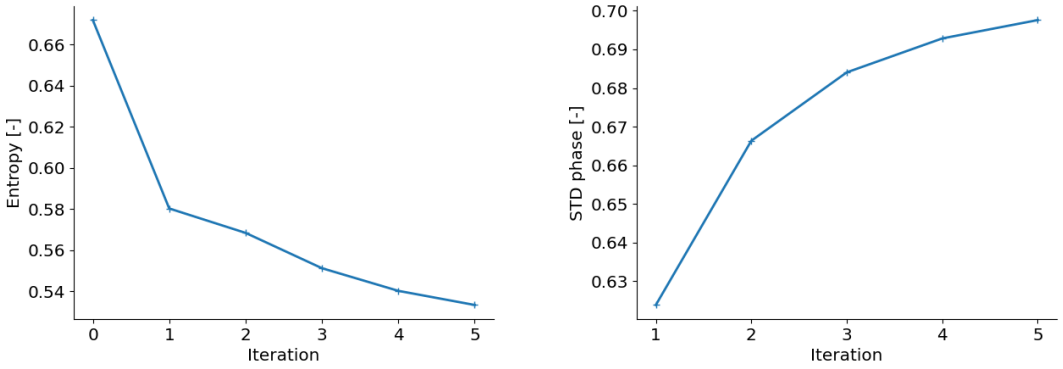

Figure 5.21: MDA convergence. Entropy evolution (left) and STD of the phase (right).

5.2.3 Sources of Uncertainty

The primary sources of uncertainty in the estimation of $\hat{\phi}$ in the MDA are the errors introduced by the single steps in the algorithm and the integration of random walks that result from errors in the measurement of the sub-look coregistration error Δa. A good $\ddot{\phi}$ relies on the accurate sub-pixel measurement of Δa, which in turn depends on the *quality* of the cross-correlation peak. This strongly depends on the content of the image block itself and the contrast. The top panels in Figure 5.24 show blocks of the reflectivity of a TerraSAR-X image, where no phase error was simulated. The bottom panels show the different shapes of the cross-correlations used for sub-look coregistration; the sub-pixel location of the cross-correlation peak maximum gives Δa. *A* shows the case in which elongated structures stretch the cross-correlation peak, lowering its sharpness and limiting the possibility of sub-pixel location. *B* shows a case in which the block has barely any contrast (a block with mostly clutter is typical in agricultural and forest scenes) and the cross-correlation peak is immersed in considerable clutter. *C* shows that periodic structures in the block lead to multiple cross-correlation peaks. Finally, *D* shows that periodic prominent targets also lead to the appearance of multiple scattered peaks. These are just some examples of bad-quality cross-correlations that lead to uncertainty in the determination of $\delta K_{\mathrm{a,iono}}$, and identifying them is a big challenge.

Different criteria for the identification of low-quality blocks were studied in this work, such as the identification of multiple cross-correlation peaks, outliers with large Δa with respect to the neighboring blocks and blocks whose cross-correlation maximum appears to be displaced in range (if the sub-looks are done in azimuth, no range shift is expected). As shown in Figure 5.25, identifying these blocks and doubling their size before repeating the measurement of Δa reduces the number of outliers efficiently. In addition, works like [114] analyze the uncertainty of the peak maximum location based on the cross-correlation sharpness. The operational implementation of these methods for the identification and mitigation of outliers in the GPP is left for future work.

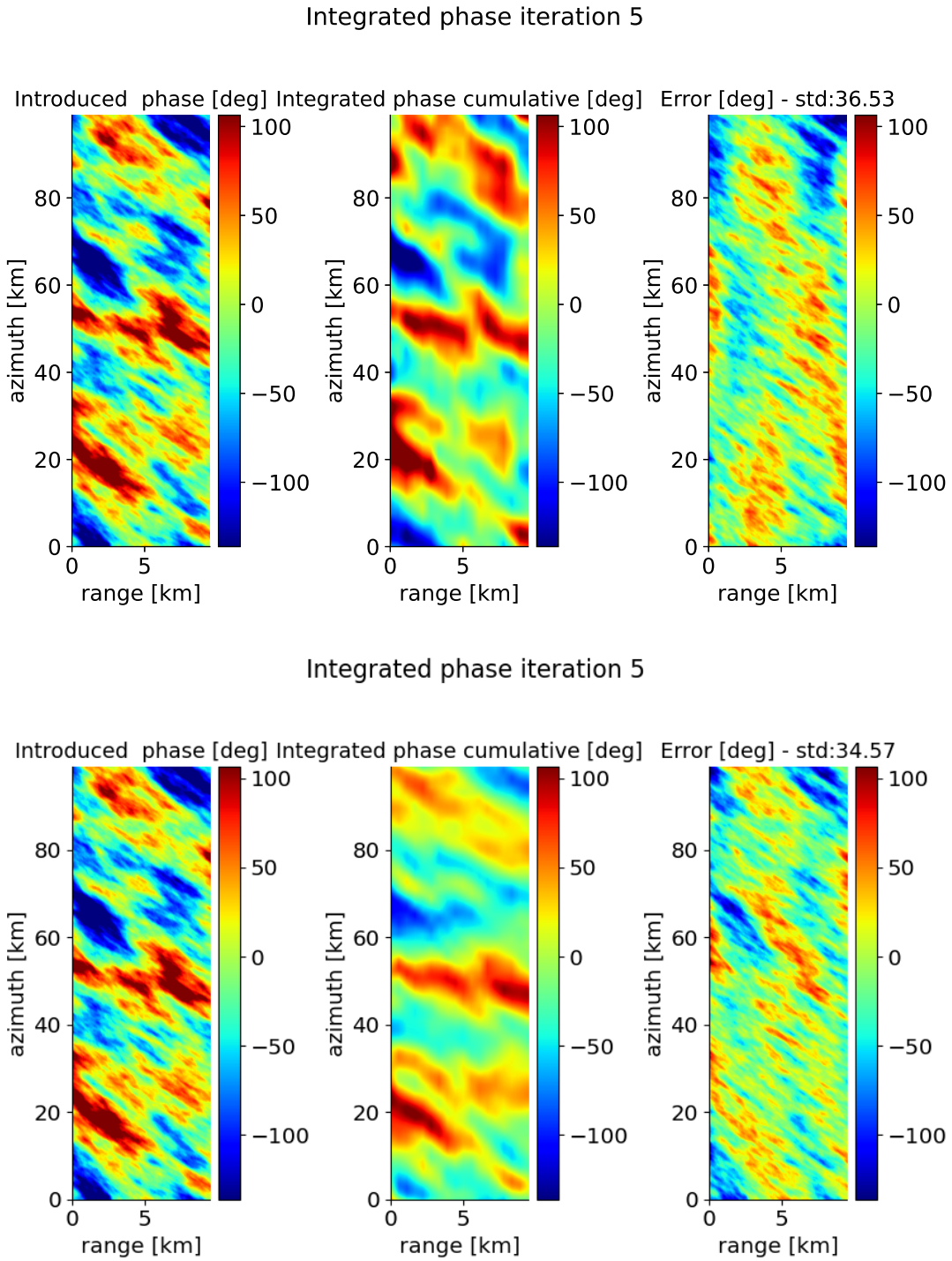

Figure 5.22: Phase screens recovered with the MDA after five iterations. Without the FR (top) and with the FR (bottom).

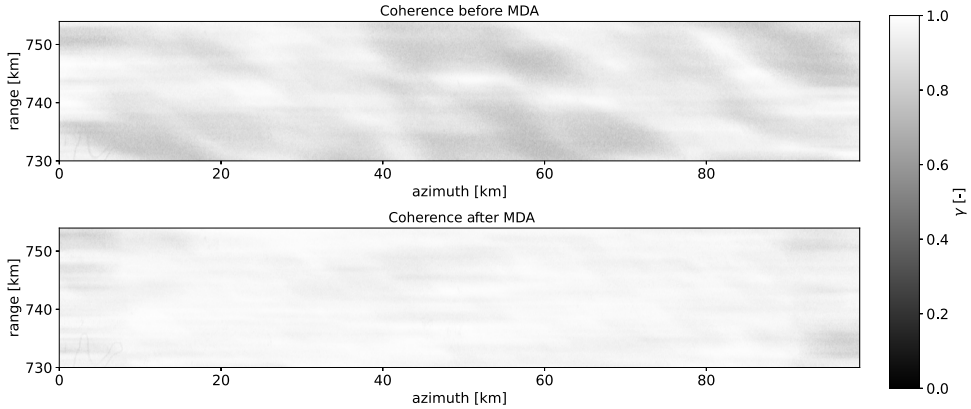

Figure 5.23: Coherence before (top) and after (bottom) MDA.

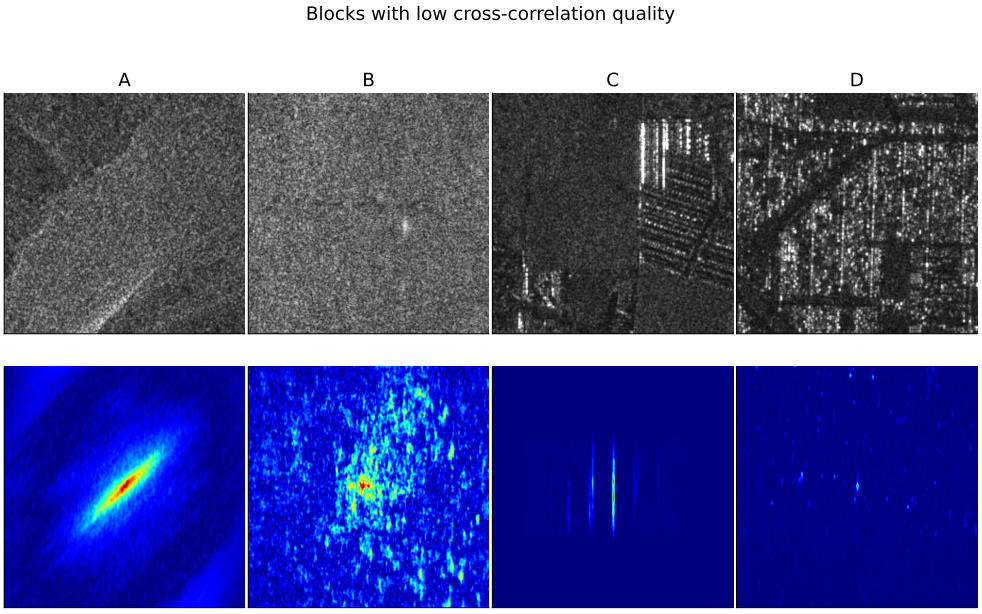

Figure 5.24: Examples of cross-correlation peaks in blocks of a TerraSAR-X image. No phase error was introduced in the SLC.

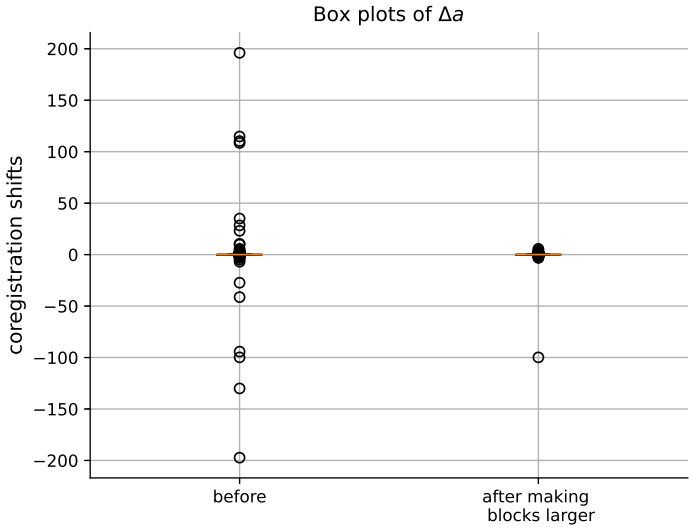

Figure 5.25: Outliers boxplot before and after doubling the size of low-quality blocks.

In addition, errors were introduced by the MDA itself. The $\hat{\phi}$ used for the correction of the images is an estimation of ϕ. Following the impulse response in the frequency domain of each calibration step, it is possible to see the impact on the performance of the phase advance recovery and image correction. In Section 3.1.2, it was shown that the turbulent component of the ionosphere can spatially be described by a power law, which is not bandlimited. The block-wise operation of the MDA represents a low-frequency sampling that makes the solution aliased with replicas (both in azimuth and range) with the block center spacing. In addition, there are two types of averaging taking place in the process: The one given by the block size and the one given by the sub-look aperture. Going back to Figure 5.17, it is possible to see that the quadratic approximation is only valid for ionospheric irregularities that change slowly enough through the synthetic aperture projected at h_{iono} (around 20 km in the case of Biomass). A simple $\delta K_{\mathrm{a,iono}}$ is not representative of too fast variations unless smaller bandwidths are chosen (at the cost of lowering the quality of the cross-correlation peaks). Finally, interpolation errors are introduced during the upsampling. The reader might refer to Pub4 for a detailed explanation of the impulse response of each calibration step and the impact on the final result.

5.3 Interferometric Stack Calibration

The differential ionosphere between satellite passes also leaves a signature in the interferometric stacks. Low-order phase errors introduced by the ionosphere (azimuth phase ramps) do not introduce defocusing but azimuth shifts, which are seen as coregistration errors in the processing of the stacks. Higher-order errors introduce defocusing in the single images,

which adds decorrelation between image pairs. In addition, the turbulent ionosphere leaves phase screens that lead to a wrong interpretation of the interferograms. Efforts have been made for the differential ionosphere estimation and compensation [40, 39, 42], which results in the removal of phase screens and regain of coherence. Two common approaches for the inversion of the differential ionosphere are the use of azimuth shifts and range dispersion (split-spectrum).

In general, an interferometric calibration achieves better performance than the single-pass calibration approaches (such as the ones presented in the preceding sections). On the other hand, interferometric calibration techniques estimate the differential error affecting the interferogram and not the individual errors affecting each single SLC image. For example, the estimation of the azimuth shifts [43] requires block cross-correlation between full-resolution image patches, compared to the sub-band cross-correlation involved in the MDA. In addition, azimuth shift phase estimation requires a first-order integration compared to the second-order integration necessary in the MDA. In the framework of Biomass, a two-step calibration scheme is defined: First, a single-pass calibration based on FR and autofocus, and second, the use of an interferometric calibration to correct for differential residuals.

The differential calibration improves the interpretability of the interferograms but does not improve the quality of the single-pass images. This could be attempted with large enough image stacks (similar to what is done in persistent scatterer interferometry techniques, where the atmospheric phase screen of each individual image can be estimated [32]); however, this possibility is limited by the number of passes available in the Biomass mission plan (up to 7 in the tomographic phase of the mission). In the following, a data combination approach introduced in Pub3 is presented. The proposed method combines the single-pass solutions and the interferometric solutions to separate the inconsistencies between both kinds of solutions and obtain better single-pass corrections by exploiting the interferometric results. The improved single-pass solutions are used to correct the data in an *interferometric autofocus*.

5.3.1 Methodology

Figure 5.26 shows a data combination scheme that aims to combine the single-pass and interferometric solutions. Single-pass and interferometric pair methods for the estimation of phase screens and differential phase screens are used for the n images in an interferometric stack. Note that these are not made sequentially. Each calibration approach has a solution made of the (differential) phase screens, ϕ_{n} and ϕ_{nm}, and different kinds of errors, ϵ_{n} and ϵ_{nm}. The reader might refer to Pub4 for a deeper analysis of the error composition. All solutions are put into a system that *forces* the single-pass solutions to be compatible with the interferometric solutions. Under the assumption that the calibration errors (ϵ_1 to ϵ_{n} and ϵ_{12} to ϵ_{nm}) are independent, they cancel out when using an LS system for data combination. The system for the combination of a stack of three images is given by

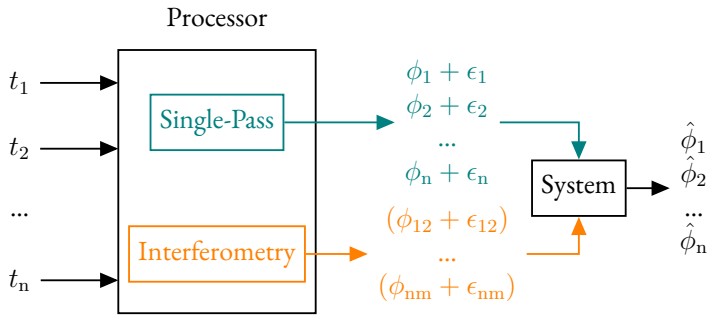

Figure 5.26: Block diagram for interferometric data combination.

$$\underbrace{\begin{bmatrix} 1 & 0 & 0 \\ 0 & 1 & 0 \\ 0 & 0 & 1 \\ 1 & -1 & 0 \\ 1 & 0 & -1 \\ 0 & 1 & -1 \end{bmatrix}}_{\text{System}} \underbrace{\begin{bmatrix} \hat{\phi}_1 \\ \hat{\phi}_2 \\ \hat{\phi}_3 \end{bmatrix}}_{\text{combined estimation}} = \underbrace{\begin{bmatrix} \phi_1 + \epsilon_1 \\ \phi_2 + \epsilon_2 \\ \phi_3 + \epsilon_3 \\ \phi_{12} + \epsilon_{12} \\ \phi_{13} + \epsilon_{13} \\ \phi_{23} + \epsilon_{23} \end{bmatrix}}_{\text{calibration output}}, \tag{5.24}$$

that can be solved pixel-wise with the pseudoinverse of the system matrix. If available, based on the accuracy of every single estimation, it is possible to add weights to the system to make it a WLS and improve the quality of the result by telling the system what solutions are more valuable.

In the following, the scheme used for the interferometric estimation is the one given by multi-squint, similar to the case presented in [99], assuming that the ionosphere gives the only phase signature between an image pair. However, the system of equations is directly expandable to incorporate multiple calibration approaches, such as the FR for the single-pass contribution or azimuth shifts and split-spectrum for the interferometric one. Indeed, one of the challenges detected during the development of this algorithm is the separation of the ionospheric phase contribution from other interferometric phases, such as those given by deformation, topography and the troposphere as well as the volume contribution in the tomographic phase of the mission. In addition, errors in δK_a due to the uncertainties in the geometry (e.g., the topographic variability and orbit determination errors) contribute to the azimuth defocusing measured by the MDA. For this reason, it is encouraged to combine estimations that only reflect the ionospheric component so that the combination system sees the other contributions as inconsistent. Dispersion and the use of split-bandwidth might not be very relevant in the case of Biomass; however, the estimation is interesting in larger bandwidth systems such as the L-band systems NISAR and ROSE-L. The same principle

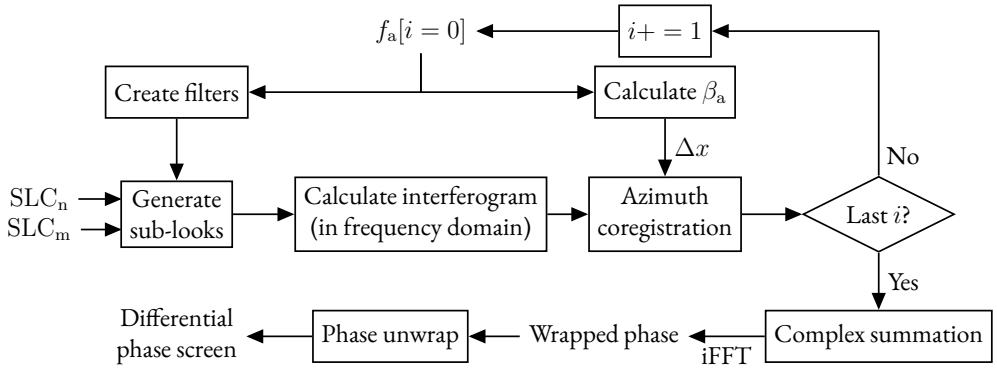

Figure 5.27: Multi-squint interferometry, block diagram. The horizontal features correspond to the extended sidelobes of simulated point targets.

can be used to incorporate boundary conditions, e.g., if the ionospheric signal is temporally uncorrelated, it is expected that the mean value of the all interferometric phase combinations in a stack is zero [5].

5.3.2 Differential Phase Estimation by Multi-Squint

In this work, the differential ionospheric phase screen in an interferometric pair is estimated with a multi-squint approach. Similarly to the MSFR described in Section 5.1, the method undoes the convolution of the phase disturbance into the data by separating the different squinted acquisitions utilizing azimuth sub-looks. The block diagram is shown in Figure 5.27: For a Doppler frequency value from a set, the bandpass filter is defined, and the corresponding squint angle β_a is calculated. The azimuth sub-looks are generated in the frequency domain from the SLCs; same as the MSFR, the problem could also be solved with the range compressed data with the appropriate geometry adjustments. Before bringing the sub-looks back to the spatial domain, their interferogram is multiplied by a phase ramp with Δx for time domain coregistration. Once the looks have been coregistered, they are added (still in the frequency domain). This efficient implementation saves three Fourier transforms per sub-look. After an inverse Fourier transform, it is possible to obtain a high-resolution realization of the differential phase. A final phase unwrapping step might be necessary for large turbulent strengths. Note that if the inputs are the SLCs, $R_0 - R_{\text{iono}}$ must be used instead of R_{iono}. In this case, the differential phase is estimated directly, and there is no dependence on β_a.

With the Sun-synchronous orbit, the height of the F2 layer is expected to be similar for the different acquisitions, so the coregistration is not expected to be a problem more than what was discussed in Section 5.1.3. The limitations of this approach are, again, the noise that will limit the size of the bandpass filter, determining the spatial resolution, and the decorrelation between the images. In the case of Biomass, the temporal decorrelation is expected to stay low due to the long wavelength.

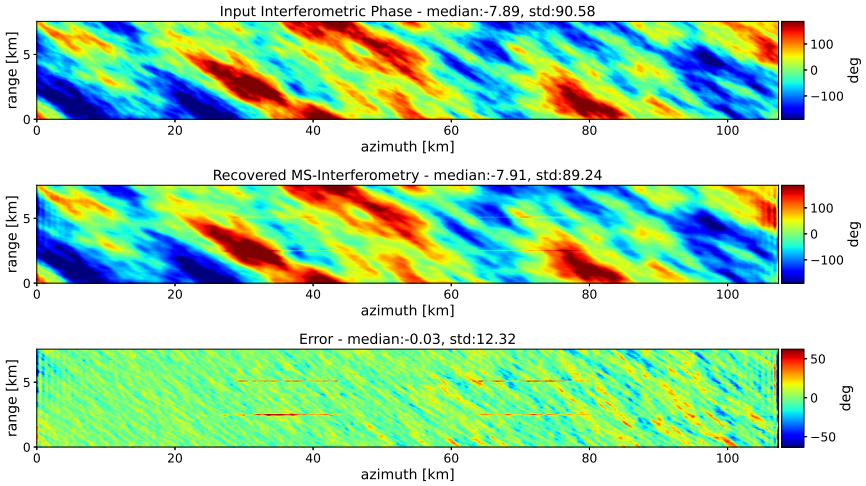

Figure 5.28: Interferometric phase recovered with multi-squint. The simulated phase difference between two satellite passes (top), estimated (middle) and error map (bottom).

Figure 5.28 shows the differential ionosphere recovered for a simulated interferometric pair and the error map. This section shows the principle, and the performance can be analyzed similarly to the case of the MSFR (see Section 5.1 and Pub4). Note that, again, the error map shows a directional residual related to the high spatial frequency components, which stay insensitive due to the filter bandwidth.

5.3.3 Results

Figure 5.29 summarizes the simulation steps to show the principle of data combination into interferometric autofocus. The simulations were carried out with the Biomass parameters and a stack of seven passes. The different phase screens were injected into the raw data with BEEPS, and image formation was performed using the GPP. The single-pass estimation of the ionosphere is extracted directly from the MDA developed in the framework of this thesis and used in the GPP. The interferometric estimation of the differential phase screens is done with the multi-squint technique described in Section 5.3.2; see the result for one of the pairs in Figure 5.28 [1]. In the absence of satellite P-band data, BEEPS offers the functionality of generating synthetic forest-non-forest maps with the reflectivity and resolution expected to be measured by Biomass. The output of the different calibrations is fed into the combination system, and the improved single-pass solutions are used to refocus the data. For the data combination, all possible interferometric pairs are taken into account.

Figure 5.30 shows the improvement of the phase screen recovery with the proposed data combination scheme compared to the phase recovered from applying the MDA alone. The

[1] The four horizontal traces in the error map correspond to the error of four prominent point targets that were present in the simulated scenario.

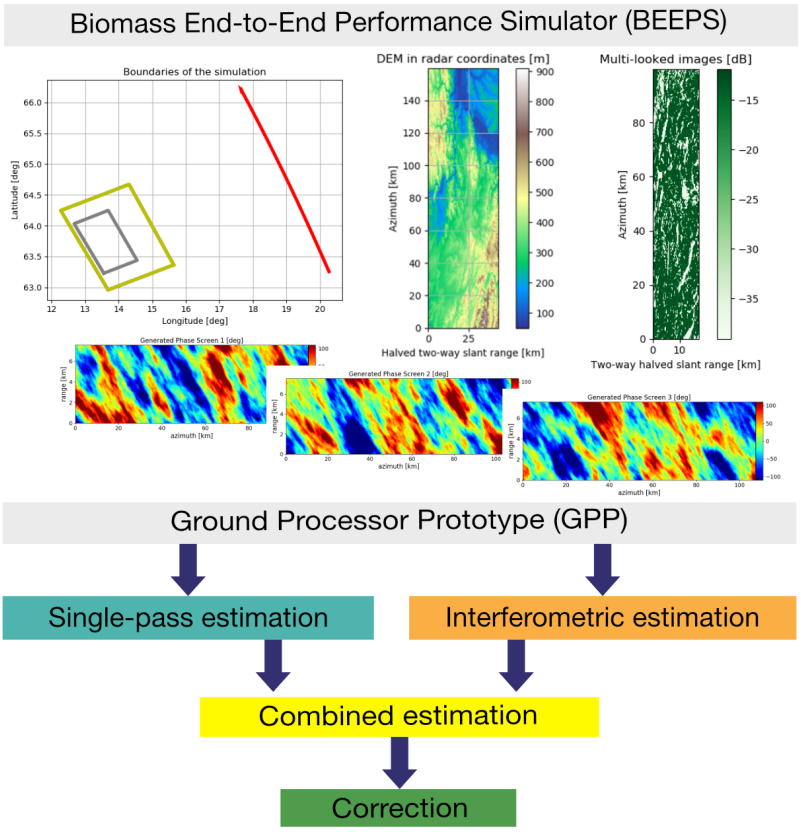

Figure 5.29: Interferometric autofocus simulation scheme.

gain in resolution is a result of the cancellation of inconsistencies in the second map with all other interferometric pairs. The MDA solution is not just a low-pass version of the map on the simulated screen; it contains aliasing and interpolation errors, as well as random walks derived from the double integration of errors in the estimation of the second derivatives. All these are inconsistencies that do not match the results observed by the interferometric calibration, and the proposed solution succeeds in mitigating them. The reader might refer to Pub4 for a deeper analysis of the error contributions present in the MDA.

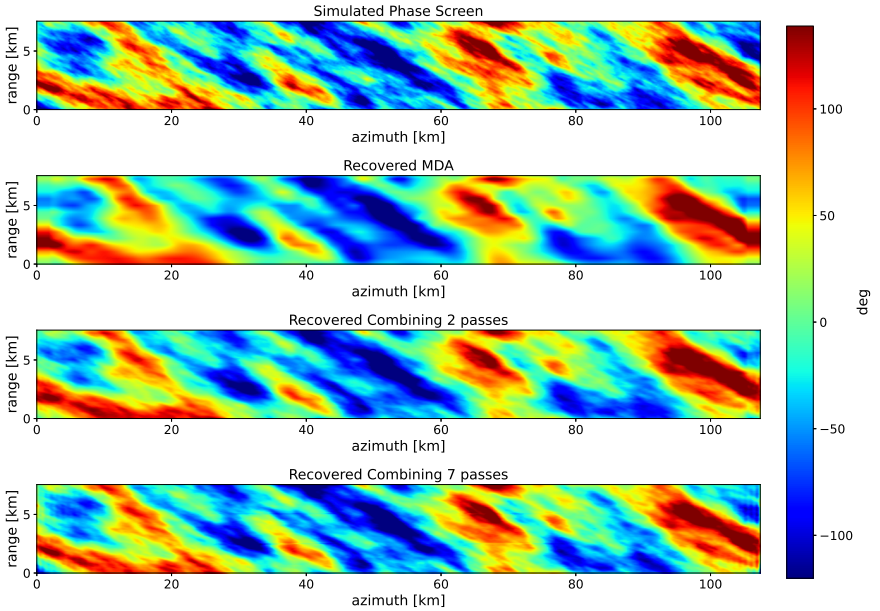

Figure 5.30: Phase screen recovered from the interferometric stack combination. From top to bottom: simulated phase screen, recovered with the MDA, after the combination of 2 passes and after the combination of 7 passes.

The improvement between just using the information of two passes and seven is better appreciated in the middle and bottom maps in Figure 5.31. Comparing the residual of the combined solutions and the one of the MDA, the structure and orientation are maintained; only the values decrease with the number of passes. This is a result of the spatial resolution provided by the MDA alone; the data combination can cancel the inconsistent alias and random walks but cannot increase the resolution. Figure 5.32 shows the Root-Mean-Square (RMS) error of the residual phase with respect to the number of passes. As expected, a larger stack leads to a better retrieval of the independent solutions. Apart from the 7-pass limitation, it is important to emphasize the limitation in the spatial resolutions provided by the independent calibrations alone. Finally, Figure 5.33 shows the improvement in interferometric coherence in an image pair after applying the single-pass MDA alone and after the interferometric autofocus compared to not applying any correction.

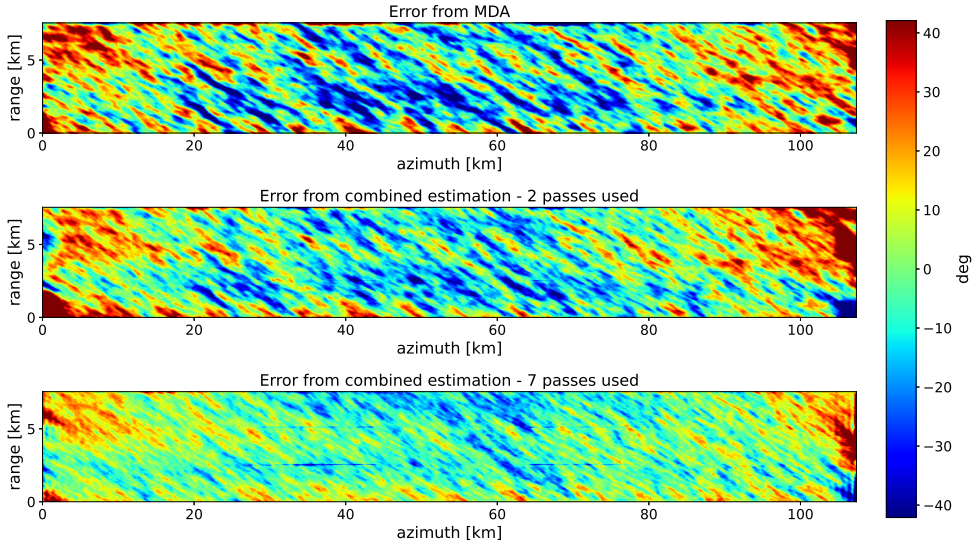

Figure 5.31: Error in the phase screen recovered from the interferometric stack combination. From top to bottom: Error from the MDA, error from after the combination of 2 passes and after the combination of 7 passes.

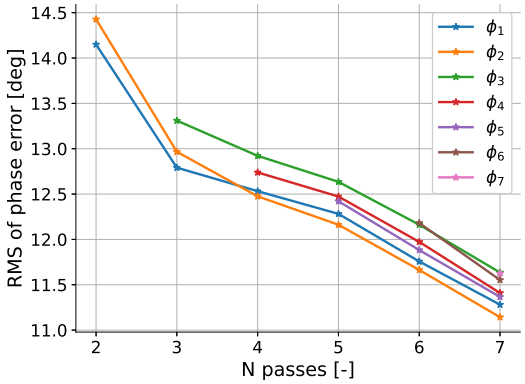

Figure 5.32: RMS of residual phase error with number of passes in the stack.

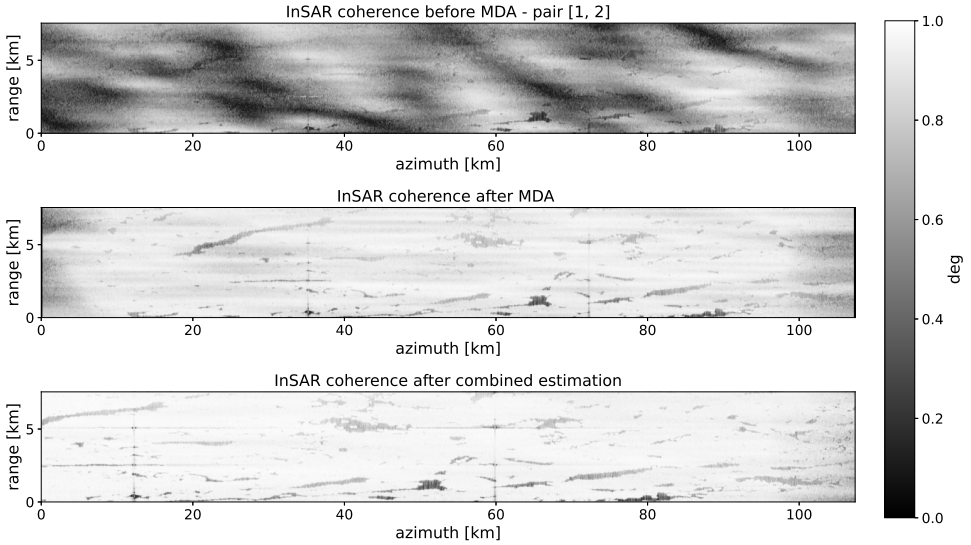

Figure 5.33: InSAR coherence. From top to bottom: before applying MDA, after applying MDA and after the correction with the combined estimation.

5.3.4 Discussion

The interferometric autofocus presented in this section exploits the differential phase screens resolved by the interferometric calibration to obtain better single-pass solutions compared to the single-pass calibration alone. The results were shown with an MDA and multi-squint interferometry. It was demonstrated that the larger the interferometric stack, the better the estimation up to a spatial resolution limited by the independent calibration algorithms themselves.

The interferometric calibration can also benefit from this combination scheme: The performance of the differential phase estimations strongly depends on the coherence between the pairs. In a two-step calibration (as the one proposed in Biomass), the interferometric calibration will be limited by the single-pass step. Solving the entire problem at once makes sure all solutions are consistent with each other. This section showed the principle within the Biomass simulation framework and the methods developed in this thesis; a prototype for an operational module is out of the scope of this work and left for future activities.

5.4 Final Remarks

Throughout this chapter, it was shown that the combination of data utilizing WLS and appropriate linear operations is beneficial for minimizing errors and uncertainties. In these data-driven methods, no assumptions about either the state of the ionosphere or the spatial description of the ionospheric irregularities are made. However, it is well known that the

availability of *a priori* information for the use of adaptive filters highly increases the performance of the turbulent ionospheric screen recovery. An adaptive rotated Gaussian can be used in the FR estimation to directionally average the looks and reduce σ^2_Ω [62]. A Wiener filter that combines the results of the FR and the MDA was presented in [44]. Similarly, [42] uses the same principle to combine the azimuth shifts and dispersion for the recovery of differential phase screens. These approaches require the parametrized knowledge of the spatial distribution of ionospheric irregularities, which, unless determined from the same data with an alternative estimate, relies on the use of look-up tables and models.

This chapter presented different approaches for the ionospheric calibration of single-pass SAR images developed during this thesis in the framework of the Biomass mission. All these are data-driven methods that recover an ionospheric disturbance or TEC map, which is used for data correction. The TEC map imaging is a by-product that is usable for further ionospheric research.

6 Error Characterization

This chapter deals with the characterization of residuals after the application of ionospheric calibration algorithms in SAR data, focusing on the FR-based and autofocus approaches presented in Chapter 5. Knowing that the spatial and statistical properties of the turbulent ionosphere can, in principle, be described in terms of a PSD, it is possible to analyze the impact of the calibration filters in the PSD of the recovered disturbance and residual maps. This helps to account for the error sources in the calibration step, to identify the limits of the algorithms, and to interpret the disturbance residuals expected in the products. This knowledge is also applicable to the interpretation of the TEC maps that can be recovered from the calibration step. Furthermore, we compare the suitability of each of the calibration approaches in different scenarios (varying the SNR and geographic location). Again, the discussions are based on simulations tailored for Biomass.

This chapter serves as a comprehensive summary of the main contributions presented in Pub4, which can be found in Appendix D.

6.1 Analysis of Calibration Errors

It is assumed that the turbulent part of the ionosphere is described by a certain PSD $\Phi_\phi\left(\vec{f}\right)$ (in this case, the power law description introduced in (3.3)) to characterize the residuals in the calibration of single-pass images by FR and MDA. Pub4 shows that during the estimation of the disturbance maps, by keeping track of the impulse response of each linear operation, it is possible to characterize the mapping residuals and the impact on the images. As long as the applied operators are linear (and most of them are), it is possible to derive the PSD of the

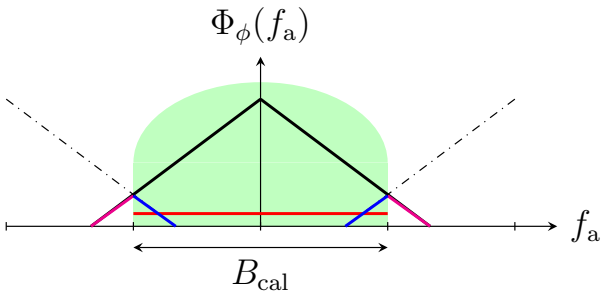

Figure 6.1: Sketch of the power spectral density of the phase advance error observed by SAR (black). The green area describes the calibration filter used in the ionospheric mitigation algorithms, which are also used for ionospheric imaging. The blue, magenta and red lines correspond to the intrinsic filtering errors caused by aliasing, limited bandwidth, and thermal noise, respectively. Aliasing replicas (dashed lines) occur by sampling the non-bandlimited ionospheric irregularity function (here described by a power law).

solution and of the residual (assuming the PSD of the disturbance is known either by models or independent estimations).

Figure 6.1 summarizes the contributions to the errors. The power law that describes the irregularities is not bandlimited, and any bandpass filter will reject the high-frequency components in the estimation. Also, sampling a non-bandlimited function introduces replicas $\mathcal{A}$

$$\mathcal{A} = \sum_{i=1}^{+\infty} \left(\Phi_\phi\left(f_\mathrm{a} + i \cdot f_\mathrm{samp}\right) + \Phi_\phi\left(f_\mathrm{a} - i \cdot f_\mathrm{samp}\right)\right)$$

which cause aliasing in the final estimation. The summation represents the replicas that occur at the sampling frequency f_samp. This aliasing might be negligible in the MSFR but should be taken into account in the MDA solution. If the system noise is modeled as white, it is represented by a flat PSD Φ_N at its variance value. Finally, the solution is also affected by the spectral shape and operations of the calibration filters. These contributions are added to the PSD of the error

$$\Phi_{\Delta\phi}(f_\mathrm{a}) = \begin{cases} \Phi_\phi\left(f_\mathrm{a}\right) + \mathcal{A} & f_\mathrm{a} > \frac{B_\mathrm{cal}}{2} \\ B \cdot \left(\Phi_\mathrm{N}\left(f_\mathrm{a}\right) + \mathcal{A}\right) & f_\mathrm{a} \leq \frac{B_\mathrm{cal}}{2} \end{cases}, \tag{6.1}$$

where the first component represents what falls outside of the calibration bandwidth B_cal and the second all inside-of-the-band contributions. B is the spectral shape of the calibration filter.

If all contributions in the problem remain stationary, the variance of the error is given by the integral of (6.1). The contributions are shown in the azimuth direction, but in range the problem is analogous. The scenario simulated with BEEPS for this analysis is shown in Figure 6.2 with the parameters in Table 6.1.

Parameter	Units	Value
Scene center	(deg, deg)	(65.5, 11.0)
$C_k L$	-	10^{32}
Outer scale, l_0	km	20
Anisotropy, $a : b$	-	5:1
Spectral index, p	-	2.65
Irregularity height, h_{iono}	km	351

Table 6.1: Parameters used in the simulation for performance estimation.

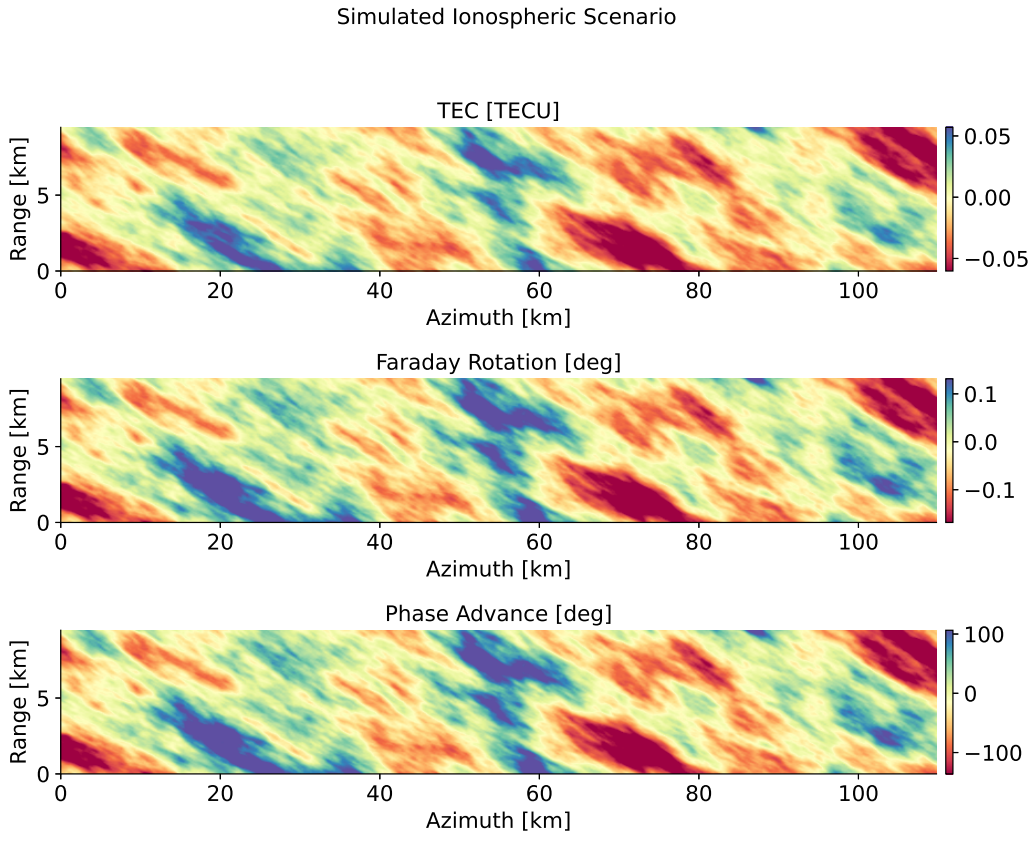

Figure 6.2: Ionospheric irregularity realization generated with the parameters in Table 6.1. The FR (middle) and phase (bottom) maps are derived from the TEC map (top).

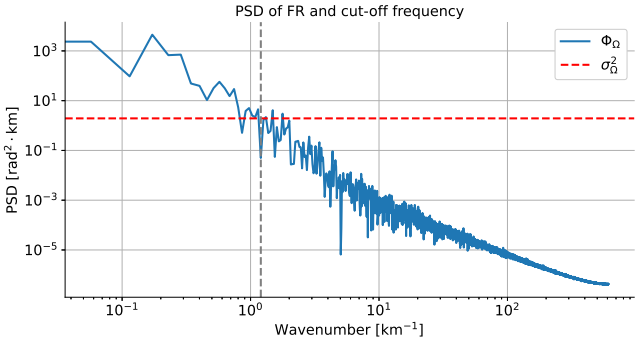

Figure 6.3: Azimuth profile of the PSD of the simulated phase scaled to FR. The red horizontal line represents the noise power corresponding to the simulation assuming an $SNR = 25\,\mathrm{dB}$. The vertical dashed line represents half the bandwidth of one of the 476 sub-looks used in this simulation.

6.1.1 Faraday Rotation

Figure 6.3 shows the FR PSD Φ_Ω of the simulated scenario and the noise power that corresponds to a $SNR = 25\,\mathrm{dB}$. For the MSFR, the bandwidth of the bandpass filters is given by the dashed vertical line: The bandwidth is chosen so that the spatial resolution is kept maximum while minimizing the noise in the measurement. Note that the scenario is chosen at boreal latitudes, where good FR sensitivity is expected with low variability with the change in LOS. In Pub4, the beam-center approximation is applied and the following results are not transformed into phase advance with the $\vec{B} \cdot \hat{k}$ variability. However, the focus here is on the spatial resolution and the structure of the error maps and the results. Figure 6.4 shows the recovered FR map and the corresponding residual map after MSFR reconstruction. Averaging was applied in range with a filter whose bandwidth was chosen similarly as in Figure 6.3. In this analysis, the interest is put in the structure of the error map: It presents a high-frequency structure in the same direction as the original map, which corresponds to the $f_\mathrm{a} > B_\mathrm{cal}/2$ component of (6.1).

The integral of (6.1) gives the variance of the stationary residual field

$$\sigma^2_{\Delta\Omega} = \overbrace{\iint_{S_\mathrm{cbw}} B \cdot \left(\Phi_\mathrm{N} + \sum_{i=-\infty}^{+\infty} \sum_{j=-\infty}^{\infty} \Phi_\Omega[i,j] \right) \mathrm{d}f_\mathrm{r}\, \mathrm{d}f_\mathrm{a}}^{\text{inside of band}} + \overbrace{\iint_{S^\mathrm{c}_\mathrm{cbw}} \Phi_\Omega \, \mathrm{d}f_\mathrm{r}\, \mathrm{d}f_\mathrm{a}}^{\text{outside of band}}, \quad (6.2)$$

where S_cbw is the area of the calibration bandwidth (defined in the azimuth and range frequencies f_a and f_r) and $S^\mathrm{c}_\mathrm{cbw}$ its complement. The summations are the aliasing contributions; note that $i, j \in \setminus\{0\}$. Knowing that the aliasing contribution is very small due to the high sampling frequency of SAR, the Monte Carlo experiment for different SNR in Figure 6.5 shows that the out-of-band component has a more significant influence in the total error

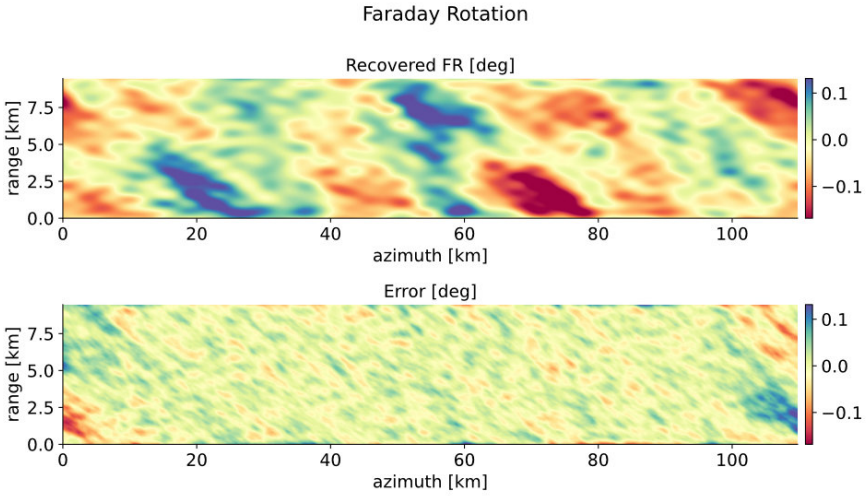

Figure 6.4: Recovered FR map (top) and the corresponding error map (bottom).

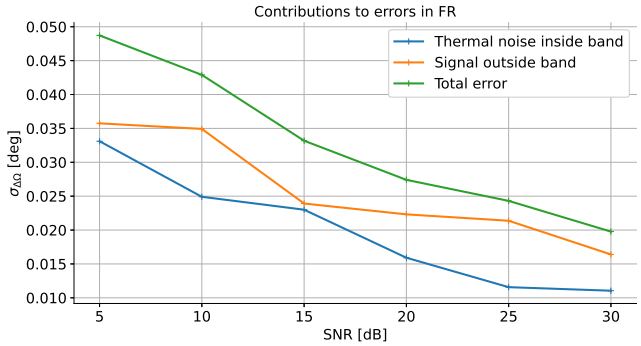

Figure 6.5: Standard deviation of the different error components (thermal noise inside of the band and signal outside) and the sum.

than the noise inside the band. For the presented scenario, Figure 6.6 shows the expected azimuth and range spatial resolutions. Note that in the boreal scenario, azimuth resolution in Biomass is expected to stay around a few kilometers in azimuth and around 1 km in range.

Impact of geomagnetic field uncertainty

Pub4 gives a qualitative and quantitative description of the residual maps, both from the image calibration point of view and the one of the scientific community that will work with the ionospheric products. Similar to Section 5.1.3, uncertainty propagation can be used to estimate the TEC uncertainty due to FR at a global scale due to the IGRF uncertainty. Following Pub4, the standard deviation of TEC, σ_{TEC}, is as a function of the $\vec{B} \cdot \hat{k}$ uncertainty,

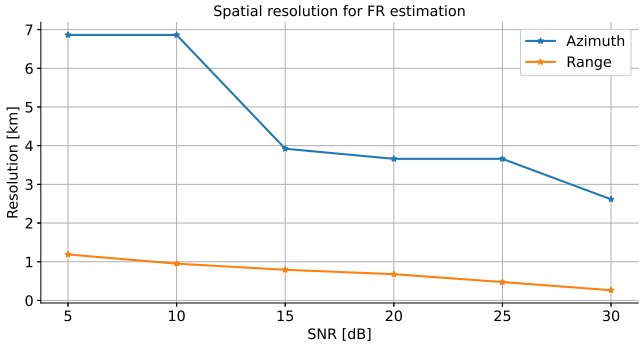

Figure 6.6: For the simulated scenario, the resolutions in range and azimuth of the retrieved FR with multi-squint for different SNRs after a Monte Carlo simulation. The cut-off frequencies in range and azimuth correspond to the first -3 dB cut of the corresponding Wiener filter.

$\sigma_{\vec{B}\cdot\hat{k}}$, and the local TEC itself

$$\sigma_{TEC}(TEC) = \frac{TEC}{\left|\vec{B}\cdot\hat{k}\right|}\cdot\sigma_{\vec{B}\cdot\hat{k}}\,. \tag{6.3}$$

Figure 6.7 shows two examples of the background global TEC that Biomass is expected to measure in a time of solar maximum and a time of solar minimum. The values at 6 a.m. were taken for the entire globe from the IONEX database. The small-scale TEC modulations that do not seem to have a physical explanation are a product of the interpolations between very low-resolution IONEX maps. These TEC values are injected into (6.3) to give Figure 6.8. Note that the contours strongly depend on the global geomagnetic field and the observation geometry. As expected, the equatorial gap also introduces noise scaling amplifying σ_{TEC}.

6.1.2 MapDrift Autofocus

As described in Section 5.2, the operations on the simulated phase screen that take place in the recovery are:

- Second order differentiation $(j\cdot\omega_1)$: The MDA measures second derivatives of the along-track variation.
- Averaging M: In the block-wise operation, it is assumed that the same $\delta K_{\mathrm{a,iono}}$ affects an entire image block. In addition, the averaging in the aperture sub-look must be taken into account.
- Sampling: Again, due to the block-wise operation. This low-frequency sampling introduces non-negligible aliasing in this case.

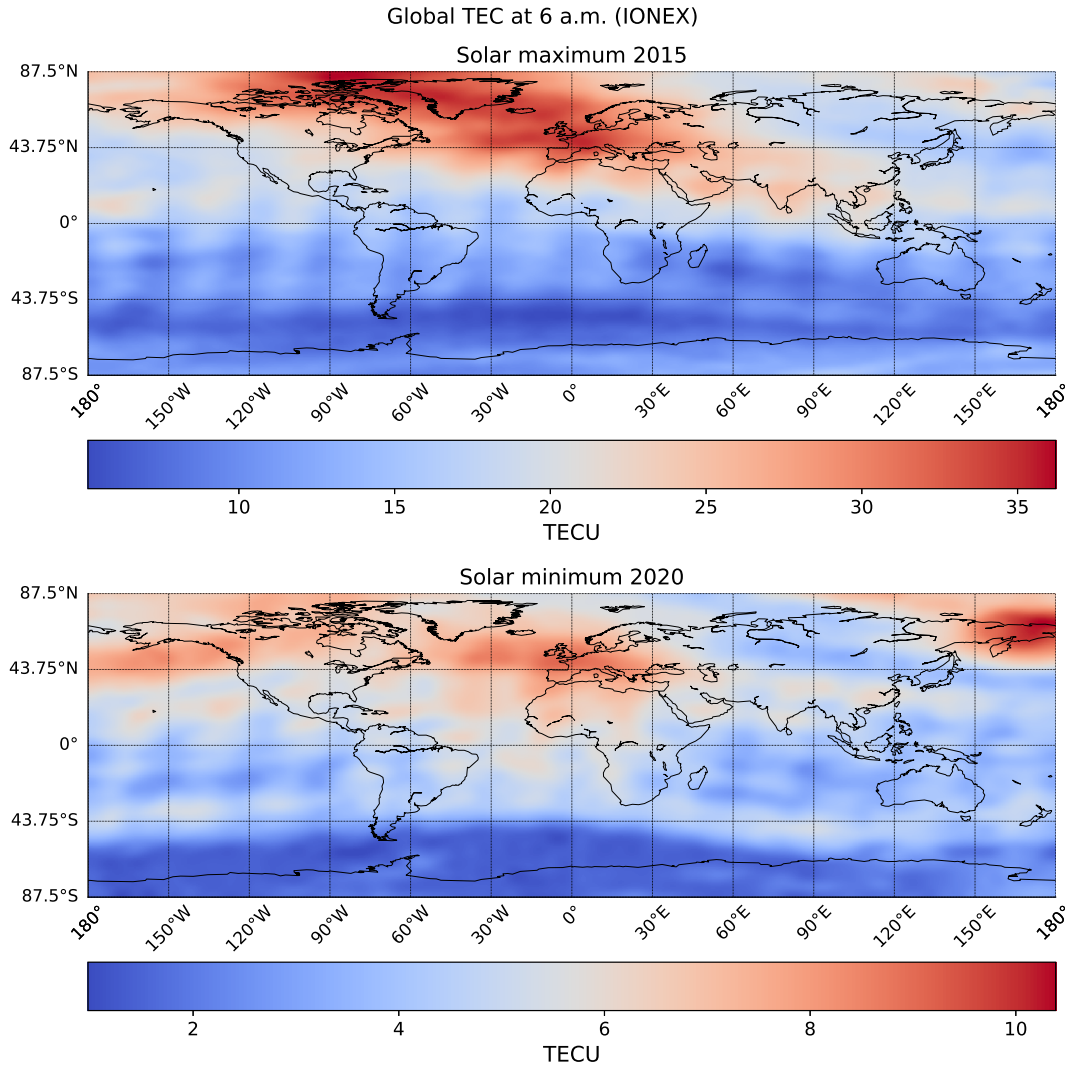

Figure 6.7: Global TEC maps at 6 a.m. extracted from the IONEX database for the 40th DoY 2015 (solar maximum, top) and 2020 (solar minimum, bottom).

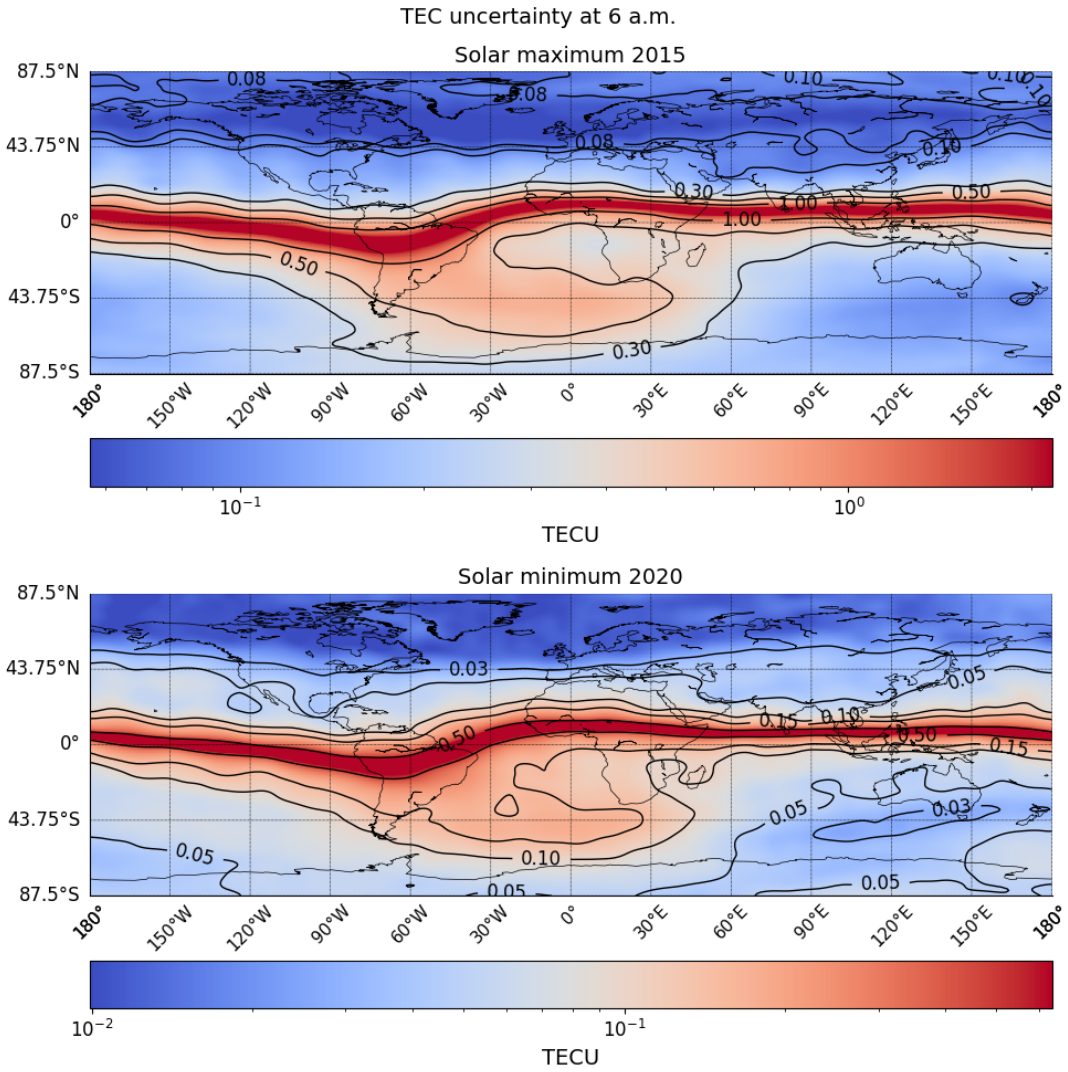

Figure 6.8: Global uncertainty in estimating the background TEC from FR. Consider the ascending node of a polar Sun-synchronous orbit with the Biomass left-looking geometry at a time of solar maximum (top) and solar minimum (bottom).

- Integration $\left(\frac{1}{j\cdot\omega_2}\right)$: A high-order phase error reconstruction is made by integrating local second derivatives.
- Interpolation L: A linear interpolation is used to up-sample the integrated solution into the image resolution for correction. A linear interpolation has the form of a sinc^2 in the frequency domain.

Note that ω_1 and ω_2 are different since one represents the derivative with a step corresponding to the two sub-look centers, and the other corresponds to the displacement of the block centers in azimuth. The aliasing due to the low-frequency sampling is reflected in the summations, again with $i, k \in \backslash\{0\}$. All these contributions add to the PSD of the phase screen recovered by the MDA

$$\Phi_{\phi,\mathrm{AF}} = \overbrace{L^2}^{\text{interpolation}} \cdot \overbrace{\frac{1}{(j\cdot\omega_2)^4}}^{\text{integration}} \overbrace{\left(\sum_{i=-\infty}^{\infty}\sum_{k=-\infty}^{\infty}\left(\underbrace{M^2}_{\text{averaging}} \cdot \underbrace{(j\cdot\omega_1)^4\,\Phi_\phi[i,k]}_{\text{differentiation}}\right)\right)}^{\text{sampling}} . \quad (6.4)$$

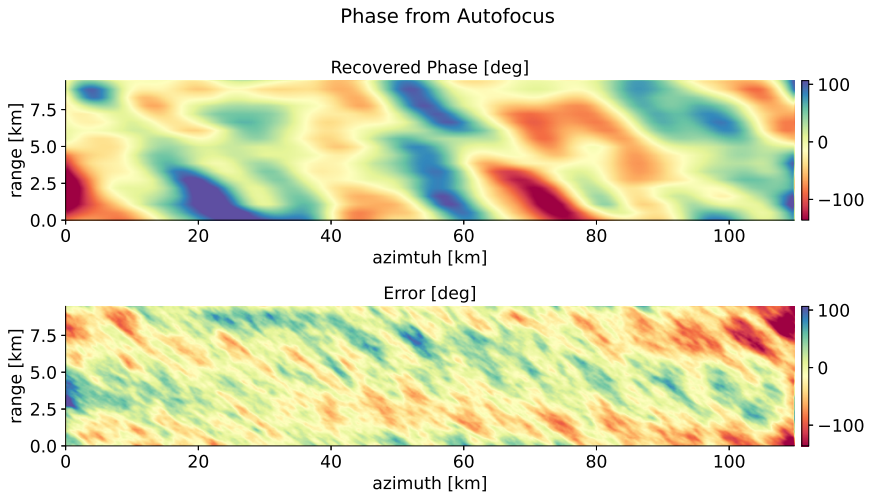

Figure 6.9: Recovered phase after applying MDA (top) and corresponding error map (bottom).

The recovered map and residual are shown in Figure 6.9 when the phase disturbance was injected into the L-band ALOS-2/PALSAR-2 acquisition in Figure 6.10. Figure 6.11 shows the good agreement between the PSD of the MDA solution and a simulation in which the series of operations in (6.4) are applied to the PSD of the simulated phase screen. Refer to Pub4 for a more detailed discussion. At this point, the most relevant finding to highlight is that even if the intuition might tell that the block averaging drives the quality of the MDA,

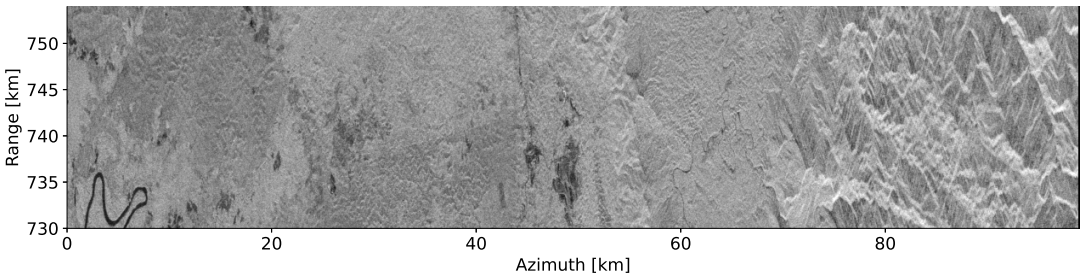

Figure 6.10: ALOS-2/PALSAR-2 image used for MDA simulation.

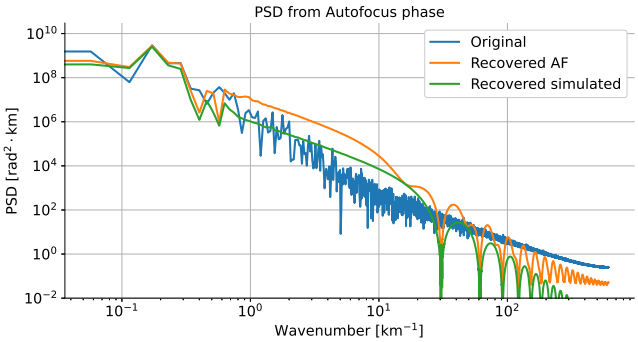

Figure 6.11: Azimuth profile of the PSD of the simulated phase map (blue), the recovered after MDA (orange), and the result of applying the equivalent transfer functions to the simulated PSD (green).

there is much more hidden in the retrieved ionospheric signal. Specifically, the spectral extension of the MDA solution and the energy increment in the low-frequency regime is a result of the aliasing introduced by the block-wise operation. Also, the high-frequency sinc-like behavior is a result of the aliased signal with the linear interpolator. All these characteristic inconsistencies drove the development of the interferometric autofocus in Section 5.3: The phase advance solution is covered by the inconsistencies natural of the MDA operation and it was necessary to find a way to separate them apart.

6.2 Discussion About the Convenience of the Different Calibration Algorithms

The biggest drawback of using the FR for ionospheric calibration is its latitude-dependent performance. In Pub4, the $\vec{B} \cdot \hat{k}$ product is used to estimate the approximated latitude at which the same field in Figure 6.2 is expected to be better recovered with the MDA than with the FR. The results are summarized in Figure 6.12 in terms of the standard deviation of the residual maps after scaling the FR to phase advance. The curves represent the FR performance, which is $\vec{B} \cdot \hat{k}$-dependent; note that it rapidly decreases towards the Equator. The

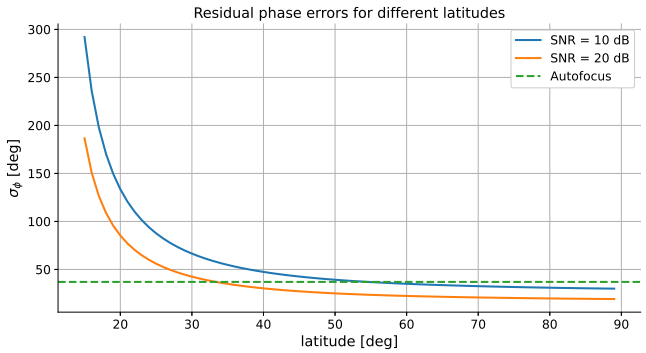

Figure 6.12: Comparison of the expected performance estimating the phase screen in Figure 6.2 using the FR and the MDA, for two different SNRs and different latitudes.

green horizontal dashed line shows the performance of the MDA (latitude independent). Below around 50 degrees latitude for an $SNR = 10\,\mathrm{dB}$ and 30 degrees for $SNR = 20\,\mathrm{dB}$, the MDA is expected to perform better despite its complications. This and the points discussed in Sections 5.1 and 5.2 is another justification for why a direct phase estimation is preferred over the FR only, and both calibration approaches should work in a complementary manner.

Pub4 helps the scientific community understand the potential of ionospheric imaging as a calibration step in low-frequency SAR, and it introduces a description of the residual maps and their components. All of this is to help interpret the features and quality of the ionospheric maps. The ionospheric products extracted by Biomass can work in synergy with any other ionospheric sensing technique and their correct use requires a proper characterization of their limitations.

7

Extraction of Ionospheric Parameters

This chapter shows a practical case that puts together the scintillation theory introduced in Section 3.3, the simulation presented in Section 4.1 and Pub1, and the processing presented in Sections 5.1 through 5.3. It describes two methodologies for high-resolution imaging and the extraction of geophysical information from intensity scintillation patterns in low-frequency SAR images. In particular, it discusses the height at which the ionospheric irregularities that mainly disturb the data are located. Intensity scintillations aligned to the geomagnetic field in the equatorial regions, also called *stripes*, are known to L-band SAR, such as in ALOS/PALSAR. It is known that they might appear in the intensity of the SLCs under certain circumstances if they have a specific size or are oriented along the satellite trajectory. Scintillation stripes also appear in the intensity of azimuth sub-looked images. With an ALOS-2/PALSAR-2 dataset, we show that a maximum contrast autofocus can be used to estimate the location of the irregularities by semi-focusing the image at different heights. The experimental results are compared to the ones obtained by estimating the height of irregularity with feature tracking in azimuth sub-looks. This information is highly valuable, not only from the scientific point of view but also for the proper application of the calibration algorithms.

This chapter summarizes the main contributions presented in Pub5, which can be found in Appendix E.

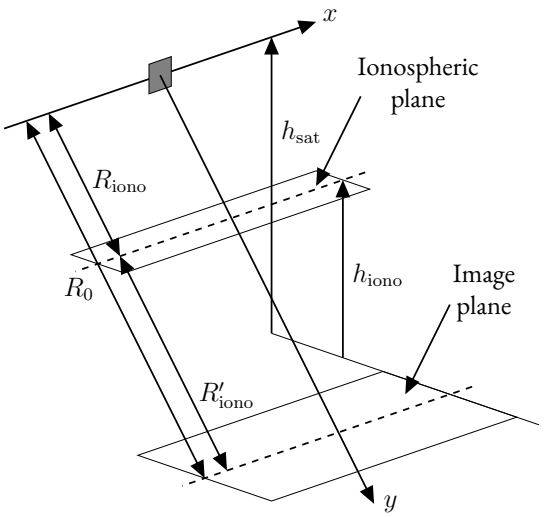

Figure 7.1: Geometry for the estimation of h_{iono} from scintillation stripes.

7.1 Estimation of Ionospheric Irregularity Height from Intensity Scintillation

The geometry of the problem is presented in Figure 7.1. By the estimation of R_{iono} (first method) or R'_{iono} (second method), h_{iono} can be derived. Note that in this study, the exact geometry with the orbit and Earth's ellipsoid is used. The principle is based on the observation of the intensity scintillation patterns that might appear in SAR images at low latitudes. Around the Equator, the ionospheric irregularities take elongated rod-like shapes that produce high-frequency phase variations. Further diffraction in free-space [18] provokes changes in the RCS of the imaged targets [97, 12]. As discussed in [61] and presented in Pub1, the change in intensity *smears* in the focused images due to the synthetic-aperture averaging. This phenomenon is less visible when the irregularities are aligned to the trajectory of the satellite. Then, there are two ways to visualize them: Either by separating the amplitude modulation from the scattering signal or by processing a smaller synthetic aperture and reducing the averaging.

Estimation by semi-focusing

The first approach is similar to what was introduced in [41]. Semi-focusing an image decouples the convolution in the synthetic aperture processing from the data. This way, it is possible to visualize the impact of the ionosphere on the data without the convolution of the azimuth compression. In this case, it is possible to observe the fast changes in the RCS due to intensity scintillation, even when they are not aligned in the along-track direction. Figure 7.2 shows the steps of the maximum contrast autofocus proposed for this task. The SLC is semi-focused at different heights, normalized to remove the background component and

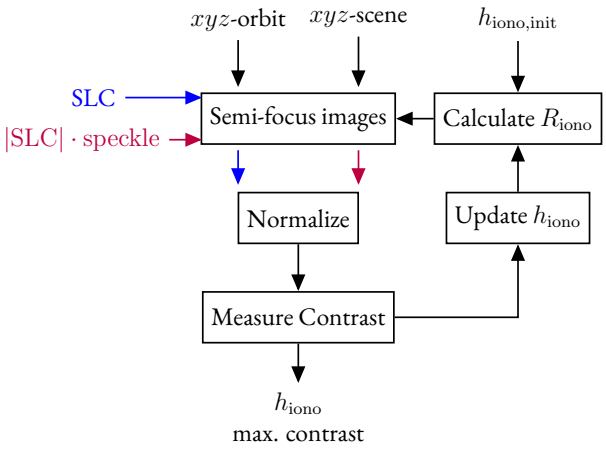

Figure 7.2: Block diagram of the contrast autofocus for the estimation of h_{iono}.

better visualize the scintillation component only. The R_{iono} related to h_{iono} is found with the variance of the intensity as a contrast indicator. For the semi-focusing step, from the range-compressed data, the image is focused by adapting the R_{iono} and effective velocity v in the compression filter

$$H_{\text{ac}}(f_{\text{a}}, R_{\text{iono}}) = \exp\left[-j \cdot \frac{4 \cdot \pi \cdot R_{\text{iono}}}{\lambda}\left(\sqrt{1 - \left(\frac{f_{\text{a}} \cdot \lambda}{2 \cdot v}\right)^2} - 1\right)\right] . \tag{7.1}$$

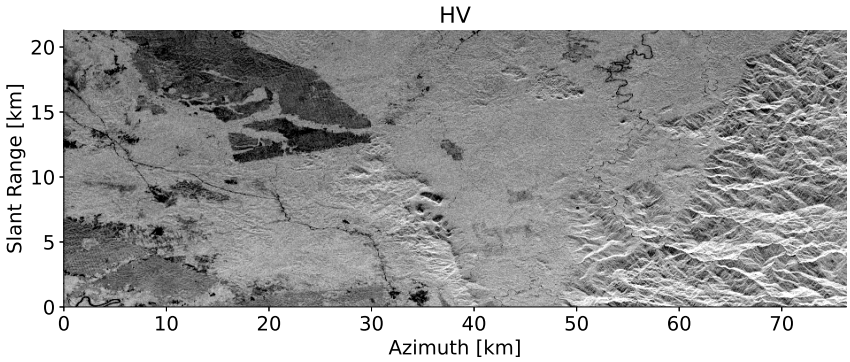

Figure 7.3: SLC intensity of the HV channel of the ALOS-2/PALSAR-2 image (ALOS2050060000). The forest scene is located in Indonesia, very close to the geomagnetic Equator.

For a step-by-step explanation and details of the normalization, the reader might refer to Pub5. Figure 7.3 shows the HV channel of the dataset used in this investigation and Table 7.1 the acquisition parameters. Figure 7.4 shows the image semi-focused at the height of 330

Parameter	Unit	Value
Coordinates center image (lon, lat)	(deg, deg)	(116, 0.63)
Date	YYYY/MM/DD	2015/04/27
Time	hh:mm:ss	16:26:33
Pulse repetition frequency (PRF)	Hz	2320.8627
Incidence angle (θ_{inc})	deg	31.086
Azimuth oversampling (aosf)	-	0.3888
Satellite height (h_{sat})	km	634.285
Range to ground (R_0)	km	728.84
Doppler rate (K_{t})	Hz/s	-607.08432
Central frequency (f_0)	GHz	1.2575

Table 7.1: Observation parameters of the ALOS2050060000 dataset.

km before the normalization step. Note that the scintillation pattern appears superimposed on the scattering data and that the stripes follow the geomagnetic field line (highlighted in white). It is necessary to remove the background component so that features like the darker agricultural field on the top-left corner of the figure do not affect the estimation of the stripe contrast.

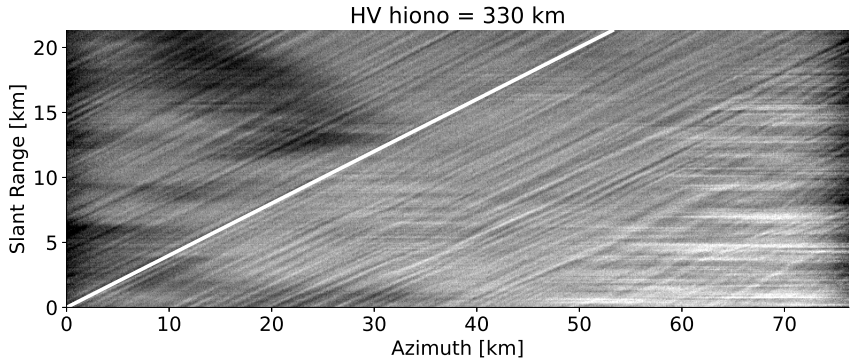

Figure 7.4: Non-normalized SLC image semi-focused at 330 km. The white line shows the geomagnetic field projected on the image plane.

Finally, Figure 7.5 shows the contrast of the normalized scintillation pattern for all polarizations in the dataset after semi-focusing at different heights using (7.1). This data-driven approach estimates a height of 330 km. For comparison, the hmF2 height (the height of maximum electron density) of the IRI model is plotted with a dashed vertical.

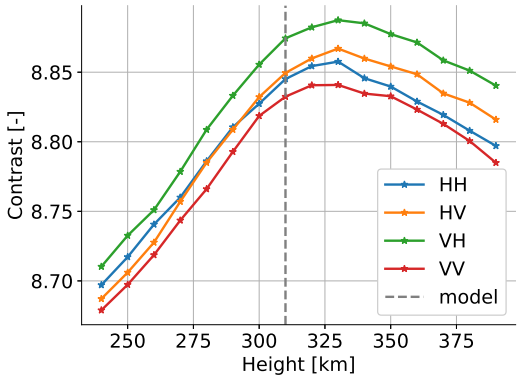

Figure 7.5: Stripe contrast change with ionospheric height. As a reference, the height of maximum ionization of the F2 layer, as taken from the IRI model, is indicated by a vertical dashed line.

Estimation by sub-look feature tracking

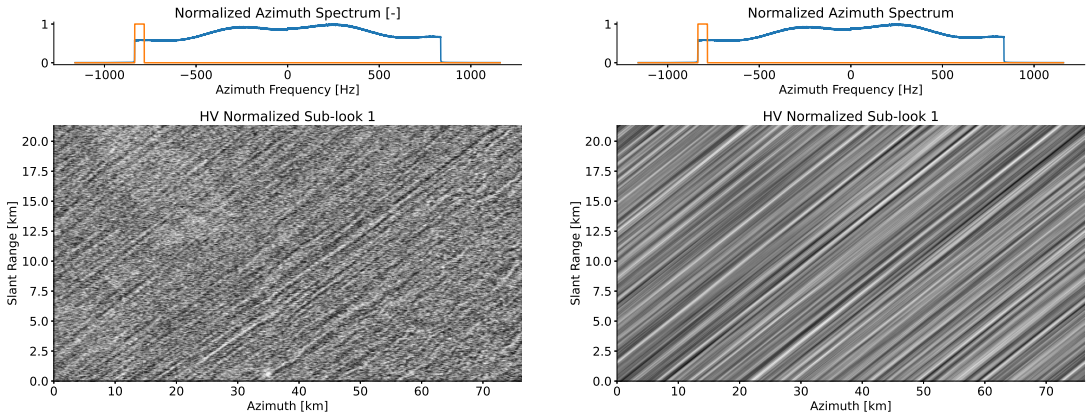

Figure 7.6: Stripe pattern in an amplitude image of a normalized sub-look, 1/32-th of azimuth bandwidth (left). Normalized sub-look after a 10-pixel directional averaging along the geomagnetic field line (right).

The same principle presented in Section 5.1 can be used as an alternative for ionospheric height estimation from the intensity scintillation patterns. At this low latitude, the FR sensitivity is too low to detect irregularities, but the change in intensity is polarization-independent. Similar to the visualization of irregularities utilizing the FR in Section 5.1, Figure 7.6 shows the appearance of the scintillation stripes on the amplitude of an image sub-look. The sub-look is normalized with the average of all other sub-looks to remove the background component; see the left panel. On the right panel, a directional filter was applied in the direction of the geomagnetic field. Note that the stripe feature is highlighted with respect to the background clutter. The stripe pattern also drifts in the azimuth direction for the different central Doppler frequencies of the sub-looks.

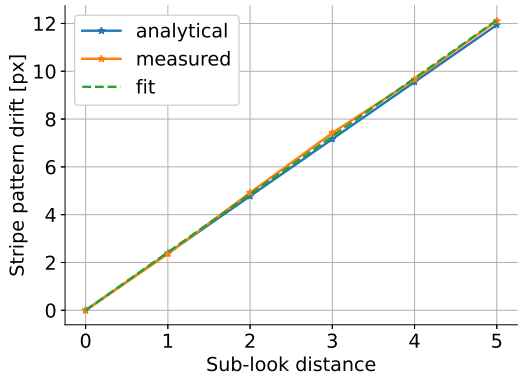

Figure 7.7: Scintillation pattern drift estimated from azimuth sub-looks that are separated up to five consecutive non-overlapping sub-looks. The analytical drift is calculated for $h_{\mathrm{iono}} = 330\,\mathrm{km}$

In the MSFR, the idea is that knowing h_{iono}, it was possible to corregister the sub-looked FR realizations into a high-resolution phase disturbance map. Here, the principle is the opposite: Cross-correlation is used to estimate the azimuth drift of the stripe pattern across sub-looks and the result can be used to invert R'_{iono}, which again gives h_{iono}. Refer to Pub5 for the details. Figure 7.7 shows the analytical and measured shift between consecutive sub-looks. The forward problem (analytical solution) is calculating the straight line knowing h_{iono}; the backward problem is estimating h_{iono} from the slope of the fit.

7.2 Discussion

The ionospheric injection and correction approach presented in Section 4.1 and the calibration algorithms presented in Sections 5.1 and 5.2 require the knowledge of the range between the satellite and the ionosphere R_{iono} which is related to the ionospheric irregularity height h_{iono}. In the literature that uses the thin layer approximation, there is the common assumption that this height is the one where the free electron density reaches its maximum in the F-layer. In this work, we separate them apart and refer to h_{iono} as the height where the irregularities that cause scintillation are found.

Pub5 shows two approaches to exploit the intensity scintillation common in low-frequency SAR acquisitions at low latitudes for the estimation of h_{iono}, which is needed for the application of the calibration algorithms. The algorithms were tested with an ALOS-2/PALSAR-2 dataset, and the principles can be applied directly to the case of Biomass. In the absence of an h_{iono} estimation, the Biomass processor would use the height of maximum ionization extracted from independent models such as IRI and NeQuick.

The results presented in this chapter work in complete synergy with any other approach for the estimation of h_{iono} at low latitudes, such as the sub-apertures method presented in [60]; however, similar to the autofocus case, an approach based on FR seems to be very error-

prone, especially towards the equatorial gap. Under the static single-thin-layer assumption, the application of these methodologies is straightforward. In this thesis work, we favor data-driven approaches over models because of the required accuracies to warrant performance. Figure 7.5 shows a significant discrepancy between the estimated h_{iono} and the hmF2 of the IRI model of around 20 km, which, in turn, translates into FR and phase advance residuals after ionospheric correction. We can also consider the effect of a drifting ionosphere as a source or error. Considering that velocity adds a Doppler error component, it can bias the estimation of h_{iono}. For completeness, the quantification of this effect and its sensitivity will be considered in further studies.Finally, visualizing the intensity scintillations alone by semi-focusing and normalizing (first method) allows us to study them at very high resolution, compared to other approaches that use sub-looks where the azimuth resolution is reduced with the bandwidth reduction.

8 Summary and Conclusions

This thesis showed the complete life cycle of the ionospheric signal in low-frequency SAR data. After the description of the relevant characteristics of the ionosphere and its impact on SAR remote sensing, the contributions of this cumulative thesis extend through publications 1 to 5. From Chapters 4 to 7, the content of the publications was discussed and extended to the latest developments highlighting their interactions. The work was developed in the framework of the Biomass mission, developing simulation and calibration tools for BEEPS and the GPP. The life cycle of the ionospheric signal in the data starts at the simulation step, with an accurate injection of the ionospheric disturbances. Then, the calibration step uses some kind of ionospheric imaging to correct for those disturbances. An error characterization is needed to quantify the reliability of the retrieved data and the characteristics of the residuals. Finally, the imaging of the ionosphere through different techniques allows the extraction of geophysical parameters. In the following sections, the contributions in each of the steps will be highlighted and an outook of future work based on these contributions will be discussed.

8.1 Contributions

Simulation

An accurate simulation method that uses Sub-Apertures for Disturbance Injection (SADI) was proposed in Pub1. With STFT in azimuth sub-apertures of the range-compressed data, it is possible to obtain an angular view of the portion of the ionosphere that falls inside the radar beam for the satellite position at the center of the sub-aperture. This allows us to add

the disturbance contributions, accounting for different squint angles from the center of the beam. Being able to account for the angle dependency accurately reduces the simulation errors when considering wide-beam low-frequency systems.

The resolution obtained by SADI is much higher than the beam-centered approaches described in the literature, like semi-focusing or using an ionospheric transfer function. Semi-focusing smoothens the ionosphere with sort of an averaging filter the size of the synthetic aperture ($\sim$ 20 km for Biomass with an ionospheric irregularity height of 350 km). In contrast, the ionospheric transfer function applies the same ionosphere to all targets in the image (making it only valid for short extended scenes). With SADI, the resolution is limited only by the number of azimuth samples of the sub-aperture, which can be matched to the satellite displacement (this way, the resolution increases to a few hundred meters).

In addition, SADI allows us to drop the following assumptions:

- Static ionosphere: SADI injects the ionospheric disturbances that affect each satellite position. Compared to the other beam-centered methods, SADI allows us to account for an ionosphere that drifts or changes during the acquisition.
- Constant ionospheric irregularity height: The semi-focusing method focuses the image at a given height, which is assumed constant across the entire acquisition. SADI allows us to accommodate the ionospheric irregularity surface and the elliptical orbit easily.

In addition to all the benefits mentioned so far, SADI is meant to introduce all kinds of disturbances into the data. In Pub1, the focus is put on the injection of phase disturbances and intensity scintillation. However, the operation can be extended to the injection of FR as it was shown in Section 4.1, dispersion (utilizing range sub-bands) and time delays. Indeed, it was proven that the LOS variability introduces non-negligible low-pass errors in the injection of the FR with respect to the beam-center approximation. Finally, this new method has a block-wise implementation that permits efficient parallelization.

Calibration

During the development of this thesis, much effort was put into investigating state-of-the-art and new algorithms for the ionospheric calibration of Biomass products. The research was carried out in three directions: *Quad-pol images*, *single-polarization images* and *interferometric stacks*. A thorough description of the methods, together with a discussion on their operational applicability in the framework of the Biomass mission, is presented in Chapter 5.

The calibration of quad-pol images is based on the use of Bickel and Bates estimator of the FR. This is used as a proxy for phase advance corrections and ionospheric imaging in terms of TEC. Section 5.1 contributes with a new way to apply the FR estimation accounting for LOS changes inside the azimuth beam; the algorithm is called Multi-Squint Faraday

Rotation (MSFR). The principle is based on the squint angle accommodation for the FR injection presented in Section 4.1, which can be achieved with azimuth sub-looks and the Doppler frequency to squint angle relation. It is shown that for the antenna beamwidth of Biomass, there is up to 10% change in the measured FR angle due to the LOS variability alone at mid-latitudes. Compared to the MSFR solution, the state-of-the-art semi-focusing method that uses the beam-center approximation leaves low-pass residual structures in the recovery of phase screens. The analysis was done with simulated data.

Section 5.1 also analyzes the factors affecting the performance of the MSFR. These factors are (among others) the SNR, uncertainties in the geomagnetic field model, the geometry and other system or calibration errors such as the antenna pattern compensation. It was shown that error propagation can be used to determine the uncertainty in the recovery of the phase advance. Finally, it was shown that the MSFR can be used to detect errors in the local geomagnetic field with respect to the IGRF model. The methods were simulated in a mid-latitude scenario, and their operational prototyping will be carried out in the future.

The biggest drawbacks of relying on the FR are the fact that its sensitivity is latitude-dependent and that it requires a full-polarimetric operation. In addition, the $\vec{B} \cdot \hat{k}$ product introduces significant noise-scaling errors towards the equatorial gap. For these reasons, it is interesting to define a method for the direct estimation and correction of phase advance errors. In this work, a MapDrift Autofocus (MDA) was proposed as it was first introduced in Pub2 in the Biomass framework. Section 5.2 discusses the latest developments to the contribution and challenges analyzed during the development of a prototype for the Biomass processor. Compared to other autofocus approaches, such as PGA, the MDA is meant to resolve 2-D phase error maps even in the absence of point targets and it works in single-polarization images. The MDA works block-wise and locally estimates the Doppler rate error introduced by quadratic components of the phase advance. The local quadratic phase parameters can be used to integrate larger-order errors along azimuth. It was shown that a WLS system can be used to solve the integration problem and combine the redundant information of the different polarimetric channels or external estimations such as the ones provided by the FR.

Apart from the challenging integration step, Section 5.2 also presents some of the most relevant sources of uncertainties in the solution. First, there is a discussion on the uncertainty of the Doppler rate estimation based on the quality of the cross-correlation peaks. It was shown that the performance in the sub-look coregistration error measurement strongly depends on the contrast and content of the block. However, there are different ways to identify low-quality blocks, and making the blocks larger reduces the number of outliers. In addition, there are errors in the solution given by the MDA steps themselves. These were first introduced in Section 5.2 and further discussed in Pub4.

During the development of this work, an interferometric data combination scheme for the improvement of the single-pass solutions was also investigated. The concept was first introduced in Pub3, and the contributions are summarized in Section 5.3. In current operational processors like the one of Biomass, a two-step calibration applies a single-pass correc-

tion before an interferometric correction of the residuals. This interferometric step recovers the coherence and corrects the ionospheric phase screens but does not improve the quality of the single-pass products. In addition, its performance is limited by the previous calibration steps. In this work, a data combination framework that combines single-pass and interferometric estimations is presented. An LS system cancels inconsistencies between the different solutions and recovers higher-resolution phase advance maps to be used in the correction. The method was tested using simulated data, and an operational prototype will be developed in the future.

Error Characterization

There are two different approaches for the ionospheric calibration of the Biomass data and ionospheric imaging, one based on the FR estimation and the other on an MDA. In the ionospheric calibration step, 2-D irregularity distortion (and TEC) maps are obtained, the quality of which determines the performance of the calibration. Assuming that the irregularities are found in a very narrow and continuous region of the ionosphere (thin layer approximation) and that their spatial structure and statistics are described by their PSD, it is possible to calculate the performance of the calibration algorithms and structure of the error maps. With the principle that the calibration filters can be expressed as combinations of linear operations, it is possible to keep track of the calibration bandwidths and the operations performed on the ionospheric PSD to determine the expected calibration performance.

In Pub4, it was shown that the calibration bandwidth for the FR is limited by the shape of the irregularity PSD (given by the outer scale, anisotropy and scintillation parameters), the SNR and geomagnetic latitude. On the one hand, the error map that corresponds to the FR is mainly made of the high-frequency component of the irregularity map that falls outside the calibration filter. On the other hand, the performance of the MDA is determined by the sequence of operations that occur in the estimation of the phase disturbance: second derivative, sub-look and block averaging, sampling, double integration and interpolation. All this assumes that non-stationary effects like the integration of random walks are adequately canceled by the filtering used in the integration step. It was shown that aliasing because of the block sampling and the sub-look averaging are the main limitations of MDA performance.

Pub4 also compares the performance of both approaches at different geographic locations. Apart from the disturbance spectral shape and the SNR, it is known that the $\vec{B} \cdot \hat{k}$ product limits the FR sensitivity. As a consequence, the FR has proven to be useful for ionospheric correction in the polar regions but not in the low latitudes. The performance of the MDA is latitude-independent, and it was shown that in the mid to low latitudes, it is preferred for ionospheric estimation. A last point to take into account is that the scaling factor between FR and phase disturbance is larger as we approach the Equator, making the FR not applicable for the correction of phase disturbances.

Extraction of Parameters

One of the effects that has been observed in L-band satellite data from ALOS/PALSAR and ALOS-2/PALSAR-2 is the intensity scintillation, a result of the (almost) free space propagation of the radar waves after irregular phase modulation within the ionosphere. The scintillation signature left by the ionospheric irregularities in the SAR images is an undesired effect that affects the quality and interpretability of the products. At the same time, this signature can be used to extract geophysical parameters that characterize the ionosphere at the time of acquisition. The elongated rod-like irregularities typical at the geomagnetic Equator produce intensity scintillation, often called *stripes*, visible in the images under certain conditions. The stripes smear in the synthetic aperture when they are not aligned to azimuth, but are visible when semi-focusing the data to the height at which the ionospheric irregularities are located. Pub5 contributes with a maximum contrast autofocus of the stripe pattern used to estimate the height at which the ionospheric irregularities are located h_{iono}. The result is compared to the height of maximum ionization estimated by the IRI model.

Another contribution is a method for the estimation of h_{iono} based on feature tracking in azimuth sub-looks, which is also proposed and tested on the same dataset. When taking an azimuth sub-look, a smaller synthetic aperture is processed, and the intensity scintillations can be recovered at higher resolution. With a geometric relation and cross-correlation of the stripe pattern in different sub-looks, it is also possible to invert for h_{iono}. Ionospheric models focus on the height of maximum ionization, which is not necessarily the one where the ionospheric irregularities are located. It is also possible to estimate this from the FR with a parallax, but the performance towards the geomagnetic Equator decreases. The methods presented in Pub5 allow the estimation directly from the data (which is more accurate from the ionospheric calibration point of view); they have proven to work well at low latitudes because they are not FR-dependent. Another benefit is that they are applied to single-channel images.

The vertical electron density profiles and the irregularity height are typically observed with ionosonde or GNSS techniques, but their coverage and resolution are limited. Our research, as presented in Pub5, offers a practical solution to this limitation. Thanks to the high resolution, wide coverage, and repeat-pass temporal resolution of SAR, the scientific community can benefit from our contributions. The high-resolution imaging of the stripes allows us to extract scintillation parameters, such as the power law coefficients and the irregularity height, which enables further investigation of spread-F and bubbles. This practical application of our research opens up new possibilities for the study of ionospheric irregularities.

8.2 Outlook

The contributions of this thesis are targeted at the simulation and processing of the ionospheric disturbances that are expected to impact the Biomass products. The research goes

in two directions: the development of algorithms for disturbance correction and the extraction of parameters from the ionospheric maps retrieved in the calibration process. The first is meant to enhance the quality and interpretability of the scientific data retrieved by Biomass. The second is meant to facilitate valuable and reliable data to the scientific community for further research. All techniques studied in this work exploited the angle variability and the squinted view separation inside Biomass synthetic aperture. The algorithms presented in Chapter 5 are at different levels of maturity; however, they are implemented or tested in the end-to-end simulator or the processor prototype and ready for further development. In the preparation for the launch and commissioning phase of the mission, the algorithms have to be tuned for real data.

The most challenging is the MDA and, even though a prototype is available, further tuning is needed to resolve the difficulties presented in Section 5.2: the handling of outliers before the integration step and finding ways to minimize the impact of the uncertainties which are inherent in the processing. The diversity in the outliers makes it very difficult to define a single robust metric or characteristic to tell them apart; however, if the focus is put on analyzing the properties of the cross-correlation peaks and the contrast or Signal-to-Clutter ratio in the image block, uncertainty weights can be obtained for the integrating WLS system. On the other hand, it was also seen that each step in the MDA (second derivative, sampling, averaging, integration and interpolation) has an impact on the final solution. The first thing to further analyze is the feasibility of using more sub-looks in the blocks to extract higher-order derivative components or minimize the sub-look aperture averaging. It is known that this process reduces the sub-look resolution, affecting the performance of the cross-correlation step, but the possibility must be investigated even if it is only valid in discrete scenarios. We also believe that changing the location of the block centers during the iterative operation of the MDA might be beneficial for the cancelation of inconsistencies in the integration.

The calibration based on the FR proposed in this work also needs further analysis. It was proven that dropping the beam-center approximation in the estimation of phase advance maps makes a difference and MSFR can be used to detect uncertainties in the geomagnetic field. A deeper sensitivity analysis is needed at different locations and with complex scenes (with future real data) to propose it in an updated operational processor. It is also known that the FR is strongly affected by other system uncertainties and residuals in previous calibration steps; this coupling has been considered but its research was out of the scope of this work. We believe that the squint angle variability can also be exploited to separate the different uncertainties within the processed signal. This is a matter of further research.

The data combination approach presented in Pub3 also needs further implementation. The results shown in this thesis use multi-squint interferometry for the recovery of the differential phase. The next step is the use of all other interferometric calibration algorithms for a weighted combination, such as the one proposed in the MDA. After that, it is necessary to make sure that the ionospheric phase screens are not contaminated with other phase contributions natural from the interferometry (i.e., baselines, troposphere, topography or de-

formation). For that, the use of measurements that are only sensitive to the dispersive nature of the ionosphere will be beneficial.

In general, the publications that compose this thesis refer to the impact and the retrieval of the turbulent part of the ionosphere. These contributions are fully complementary to the established methodologies found in the literature. The high resolution and coverage of a SAR mission like Biomass unlocks the path towards the evaluation of scintillation models and the determination of further geophysical parameters, to name a few applications. These are out of the scope of this work but in the next steps of research.

Finally, this thesis was focused on the visualization and correction of the ionosphere effects on low-frequency SAR. These principles also apply to other remote sensing systems, such as the nadir-looking radar sounder and a distributed version of it. The principle has worked in interplanetary missions [95, 54] and there have been proposals for Earth observation [19, 24]. So it is a matter of time before such a mission is on the table. The radar sounders work closer to the critical frequency limit and all the aspects described in this thesis will have to be revisited. In the case of a Very High Frequency (VHF) sounder with a carrier frequency of 40-50 MHz, the disturbances are multiplied almost by 10 with respect to the Biomass case. Then, every aspect of this thesis will have to be revisited, starting with the scattering and scintillation modeling. However, the good understanding of the phenomena and the signal life cycle worked out during this thesis leaves us in a good position to further develop the algorithms towards low-frequency SAR and sounder missions while extracting the most of the ionosphere.

A

Aperture-Dependent Injection of Ionospheric Perturbations into Simulated SAR Data.

Aperture-Dependent Injection of Ionospheric Perturbations Into Simulated SAR Data

Felipe Betancourt-Payan, Marc Rodriguez-Cassola, Pau Prats-Iraola, *Fellow, IEEE*, and Gerhard Krieger, *Fellow, IEEE*

***Abstract*— This letter presents an algorithm for the introduction of ionospheric disturbances into synthetic aperture radar (SAR) simulations in an aperture-dependent manner using subapertures. Its suitability is compared with other methods that follow the beam-center approximation. The method can be generalized to the injection of all kinds of disturbances, and its two main benefits are the accuracy of the squint angle accommodation inside the synthetic aperture and the possibility of neglecting the static ionosphere assumption. For example, realistic ionospheric disturbance maps (phase and intensity scintillation) are introduced into clutter images simulated for the Biomass mission. In this case, with a typical ionospheric irregularity height of 350 km, the limiting azimuth resolution of the irregularities to be injected is around 337 m.**

***Index Terms*— Ionosphere, ionospheric simulation, scintillation, synthetic aperture radar (SAR).**

I. Introduction

THE performance of low-frequency synthetic aperture radar (SAR) is affected by the dispersive nature of the ionosphere, which introduces time delay, phase advance, and Faraday rotation (FR) in the radar echoes, degrading the quality of the products [1], [2]. All these effects are related to the total electron content (TEC) experienced by the radar waves on their two-way propagation through the ionosphere [3], and the impact will also depend on the structure of the ionospheric irregularities. Turbulent plasma irregularities are responsible for fast phase and amplitude variations in radio signals (scintillation) and are mainly found at the F-layer of the ionosphere (with a peak altitude between 250 and 400 km) [4]. Observations have found ionospheric irregularities with outer scales starting at 5 km [5], [6], [7], [8]. Regarding the drift velocity, it has been reported, for example, that close to the Equator, the ionosphere drifts eastward at significant velocities at around 100–200 but also up to 400 m/s [9]. At the poles, the irregularities spiral around the magnetic field lines.

Simulations that account for the trans-ionospheric interaction must be conducted to study its impact on the SAR products and assess ionospheric mitigation algorithms. This can be done with the application of an Ionospheric Transfer Function (ITF) as described in [10] using a *beam-center* approximation: assuming that during the azimuth integration, the phase history of each pixel is only affected by the disturbance at the piercing point located at zero Doppler. Note that the ITF method is meant only to introduce disturbance in the phase history and intensity modulation of the raw data while the injection of the FR is missing. Different approaches to apply the ITF were found [11], [12]. However, the studies focused on the statistics of amplitude modulations rather than the accuracy of the injection of phase disturbances or the inclusion of FR.

It is also possible to introduce the effects on SAR data, which are *semi-focused* at ionospheric height [13] by adjusting the distances of closest approach and effective velocities in the azimuth matched filter. This operation accounts for the spatial variations in the ionospheric irregularities. However, it is still beam-centered as it acts as an averaging window equal to the size of the synthetic aperture (neglecting small structure perturbations) instead of allocating the disturbance as seen at each azimuth frequency for each position. The semi-focused approach also neglects propagation in the oblique directions, which introduces notable errors in wide-beam systems. In addition, both the beam-centered methods assume that the ionospheric scenario does not change (frozen ionosphere) or drift during the time of acquisition, and a fixed ionospheric height also constrains them.

Inspired by the knowledge of aperture-dependent motion compensation [14], [15], we present in this letter a new algorithm for the injection of ionospheric effects into simulated SAR images. It works with subapertures along the azimuth direction, allowing it to accommodate the distortion corresponding to the ionosphere portion that falls into the antenna beam for every satellite position. This way, one accounts for the angle variability and oblique propagation through the ionosphere and can also drop the frozen ionosphere and fixed ionospheric height assumptions. The performance of this method will be contrasted with the one of the semi-focusing, and simulation examples for the Biomass mission [16] will be presented. Compared with the beam-center approaches, this new algorithm can better accommodate the impact of irregularities that are of the order or smaller than the synthetic aperture at the ionospheric height (that for the case of Biomass is of ∼19 km). Because of blockwise implementation, the algorithm can be efficiently implemented and parallelized.

In Section II, the aperture-dependent principle and implementation will be presented. Section III shows a series of

Manuscript received 28 March 2024; revised 21 May 2024; accepted 23 May 2024. Date of publication 11 June 2024; date of current version 18 June 2024. This work was supported in part by the IEEE Publication Technology Department and in part by the German Academic Exchange Service (DAAD) under Grant 57478193. *(Corresponding author: Felipe Betancourt-Payan.)*

The authors are with the Microwaves and Radar Institute, German Aerospace Center (DLR), 82234 Wessling, Germany (e-mail: felipe.betancourtpayan@dlr.de).

Digital Object Identifier 10.1109/LGRS.2024.3411064

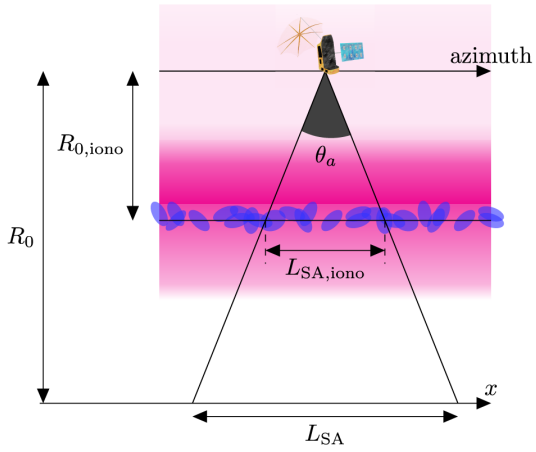

Fig. 1. Slant geometry of an SAR system through the ionosphere. The altitude-varying free electron density distribution is illustrated in pink, and the irregularities that can cause scintillation are shown in blue.

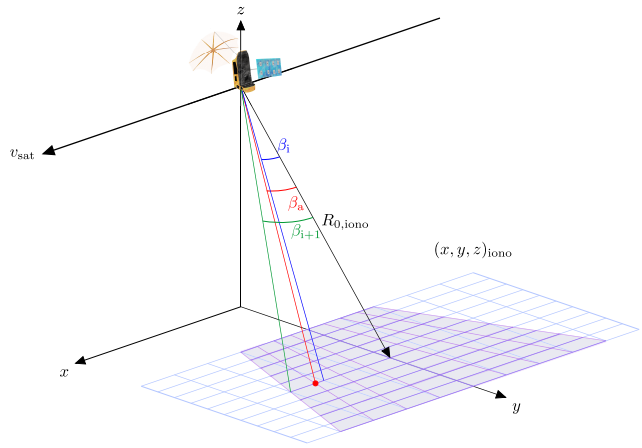

Fig. 2. Geometry at the ionospheric plane. The blue grid corresponds to the ionosphere, and the angular purple grid corresponds to the STFT of an azimuth subaperture. To obtain the unknown disturbance at the red piercing point in the direction of β_a (not known), a linear angle interpolation between β_i and β_{i+1} is necessary.

experimental results, and Section IV summarizes the results and draws conclusions.

II. Injection of Ionospheric Perturbations by Subapertures

In this section, we present an algorithm to incorporate high-frequency ionospheric perturbations into the simulation of SAR data. Fig. 1 shows the slant observation geometry of an SAR system through the ionosphere. For illustration purposes, a vertical free electron density distribution has been color-coded with shades of pink (darker means higher density at the altitude of the F-layer), and electron density irregularities are depicted around the area of maximum ionization. The slant range to the targets on the ground is R_0, θ_a is the azimuth angular aperture of the beam, and L_{SA} is the length of the synthetic aperture on the ground. For engineering and scientific applications of the scintillation theory, it has been proven that a phase screen model located at the height of maximum ionization, h_{iono}, well approximates more elaborated computations that include scattering across the vertical region [17], [18]. We will assume that the irregularities that cause scintillation are concentrated on a surface whose height might vary continuously, $h_{\text{iono}}(x)$, so that the variations are in general not negligible in high-resolution wide-beam systems and long acquisitions; therefore, the slant distance to the surface $R_{0,\text{iono}}$ and the approximate length of the synthetic aperture on the ionospheric surface $L_{\text{SA,iono}}$ can vary for each satellite position. A more complex scenario can be simulated with propagation through multiple phase screens [19], but that does not invalidate the method proposed in this letter.

Subapertures for Disturbance Injection: Based on available knowledge on aperture-dependent motion compensation [14], we propose an algorithm that uses subapertures for disturbance injection (SADI) to introduce ionospheric perturbations into SAR simulated images precisely. The principle is based on applying short-time Fourier transforms (STFTs) on partially overlapping blocks in the range-compressed data to exploit the relationship between azimuth frequency and squint angle

$$\sin(\beta_a[n]) = \frac{\lambda \cdot f_a[n]}{2 \cdot v_{\text{sat}}} \tag{1}$$

in small azimuth subapertures. This way, it is possible to accurately introduce the perturbations of the corresponding ionosphere portion that the beam sees for each satellite position (at the center of each subaperture). In (1), β_a is the azimuth squint angle from the beam center, λ is the wavelength, f_a is the azimuth frequency, and v_{sat} is the satellite velocity. n is the azimuth index in the STFT of each subaperture block.

Fig. 2 sketches the geometry of the ionospheric plane for one satellite position as seen at the center of a subaperture after an STFT (purple), together with the regular grid of the simulated ionosphere with coordinates $(x, y, z)_{\text{iono}}$ in blue. Without loss of generality, both the ionospheric perturbation and the radar beam can be sampled for a surface of changing altitude, and the satellite moves in an elliptical orbit. The angular purple grid illustrates the angular view of the beam with the polar coordinates $R_{0,\text{iono}}$ and β_a. The red dot along the red line denotes a piercing point, where the disturbance is not necessarily known but can be approximated by interpolation from the values at the known positions at the piercing points that correspond to β_i and β_{i+1}. A low-order angle interpolation is adequate to generalize the problem for nonflat surfaces with varying heights and downsample the ionosphere grid to the STFT resolution. The result will be referred as $\hat{\phi}(R_{0,\text{iono}}(h_{\text{iono}}), \beta_a; \lambda)$ for the phase and $\hat{\Omega}(R_{0,\text{iono}}(h_{\text{iono}}), \beta_a; \lambda)$ for the FR. Note that we highlight the dependency on λ to indicate that the method can be generalized to a nonmonochromatic wavefront, and on h_{iono} to indicate the variation in the layer inside the beam and along the acquisition. This way, it is possible to add for each frequency $f_a[n]$ (or each look angle $\beta_a[n]$ according to (1)) the disturbance that corresponds to the piercing point.

Fig. 3 shows a block diagram of the algorithm: For each satellite position, $p_{\text{sat}}[i]$, with the ionospheric surface

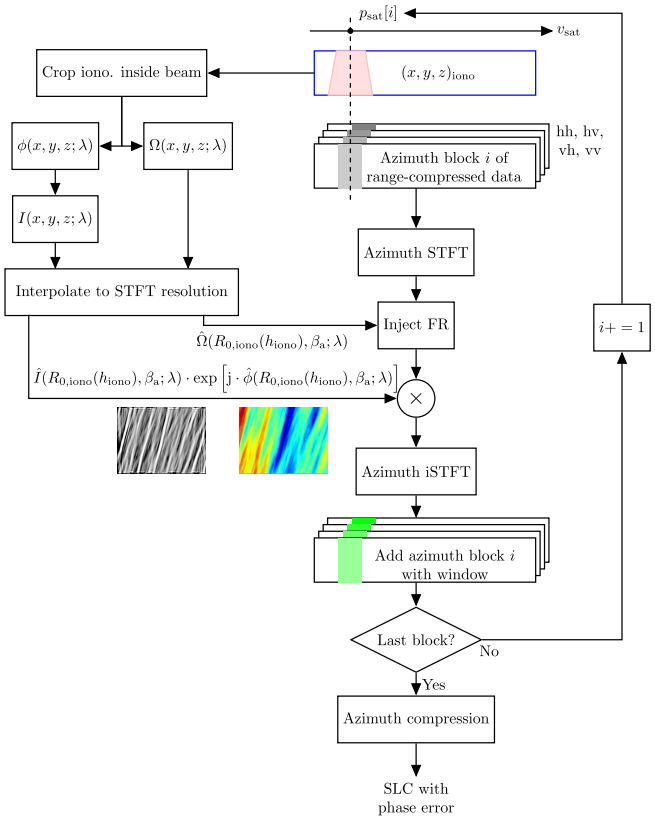

Fig. 3. Block diagram of the proposed aperture-dependent ionospheric injection algorithm.

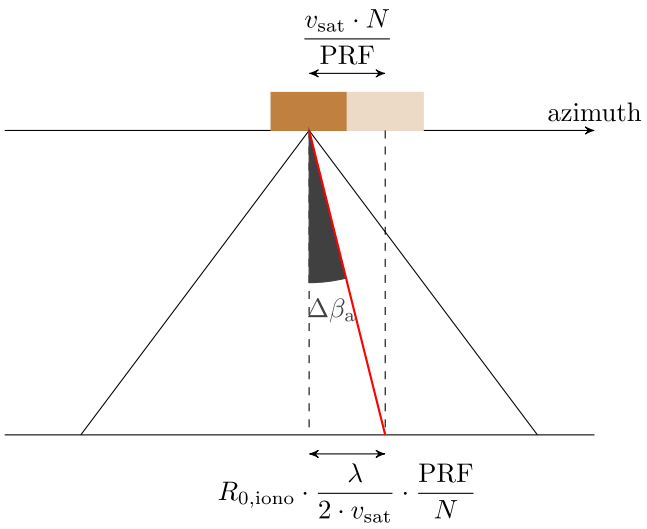

Fig. 4. Ionospheric irregularity resolution with azimuth subaperture size. Flight track (top) with the platform displacement across a subaperture and ionospheric irregularity plane (bottom). The differential squint angle $\Delta\beta_{\text{a}}$, which is given by the subaperture size N, determines the spatial resolution of the ionospheric plane.

coordinates, the part of the ionosphere that falls inside the beam is calculated. Before the downsampling step, from the local phase disturbance seen by the beam, it is possible to simulate the corresponding double-pass amplitude modulation approximating it to the absolute value of the split-step solution of a monochromatic wave that goes through a phase disturbance as described in [12]. Similar to [10], it is assumed that the ionosphere modulation can be pulled out of the summation over all the targets that make the range-compressed data, but given the subaperture operation proposed in this letter, without the small target assumption.

On the left side of Fig. 3, an example of the phase and intensity scintillation component corresponding to one subaperture is shown. Now, the local FR, phase, and intensity *screens* are downsampled and interpolated to the STFT resolution before injection. Around the corresponding satellite azimuth position index in the range-compressed image, an STFT is done (in this case, for the data from all the polarimetric channels). First, the local FR disturbance and then the phase and intensity are injected before using an inverse STFT to bring the subaperture back to the time domain. The range-compressed solution with ionospheric disturbances is built up by adding all subapertures, each with a window to maintain the power of the data. The steps are repeated in a loop to the last azimuth position. After building a range-compressed image, the data are compressed with a matched filter in azimuth to obtain single-look complex (SLC) images with the ionospheric disturbances.

The last thing to discuss is the number of pulses N in the subaperture, which is related to the azimuth frequency resolution, (PRF/N), and ultimately to the differential squint angle $\Delta\beta_{\text{a}}$ in Fig. 4 (note that we are making use of $\sin\beta_{\text{a}} \approx \beta_{\text{a}}$ approximation for small angles in (1)). To ensure consistency, the spatial sampling $(v_{\text{sat}} \cdot N)/\text{PRF}$, locally increased by the block operation, shall be matched to the reduced spatial frequency resolution at which the ionospheric coordinates are sampled, which is also driven by the distance to the ionospheric plane, $R_{0,\text{iono}} \cdot (\lambda \cdot \text{PRF})/(2 \cdot v_{\text{sat}} \cdot N)$, i.e.,

$$N = \sqrt{\frac{R_{0,\text{iono}} \cdot \lambda}{2}} \cdot \frac{\text{PRF}}{v_{\text{sat}}}. \tag{2}$$

The corresponding resolution, the scale of the smallest irregularities that can be detected, is given by the following equation:

$$\delta_x = \sqrt{\frac{R_{0,\text{iono}} \cdot \lambda}{2}}. \tag{3}$$

The Biomass mission parameters described in Table I give an azimuth block size N of approximately 70 pixels. These correspond to an azimuth resolution of 337.92 m at an ionospheric height of 350 km.

III. Experimental Results

In this section, the performance of the beam-center approach described in [13] for the injection of ionospheric disturbances will be compared with the aperture-dependent one proposed in this letter. For the simulations, a complex clutter scenario is used. With the thin-layer approximation, phase advance maps that follow a power spectral density (PSD) function can be generated as described in [10] and [20]. Two representative maps at two different geographic locations are shown in Fig. 5 generated with the parameters in Table II. $C_k L$ and p are

TABLE I

SYSTEMS PARAMETERS

Parameter	Units	Biomass
Carrier frequency f_0	Hz	$435 \cdot 10^6$
Carrier wavelength λ	m	0.69
Satellite height h_{sat}	km	650
Ionospheric height h_{iono}	km	350
Satellite velocity v_{sat}	km/s	7.534
Antenna azimuth length L_{a}	m	12
Incidence angle θ_{inc}	deg	25
Range to ionosphere $R_{0,\text{iono}}$	km	331
Pulse repetition frequency PRF	Hz	1581.03
Azimuth bandwidth B_{a}	Hz	1255.79
Synthetic aperture L_{SA}	km	41.19
Synthetic aperture at ionosphere $L_{\text{SA,iono}}$	km	19.01

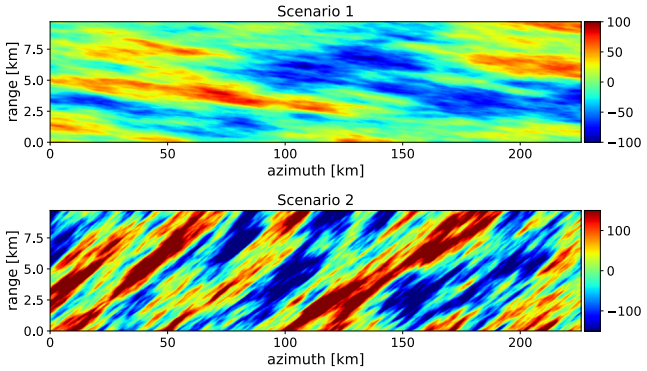

Fig. 5. Phase maps used in the simulations. Generated with Rino's method and the parameters in Table II.

TABLE II

PHASE MAP PARAMETERS

Parameter	Units	Scenario 1	Scenario 2
Geographic location (lat, lon)	(deg, deg)	14.5, 10.5	-25.5, -22
Outer scale L_0	km	10	8
Strength of turbulence $C_k L$	-	10^{32}	10^{33}
Anisotropy parameter a	-	10	10
Anisotropy parameter b	-	1	1
Spectral index p	-	2.65	2.65

related to the strength and granularity of the irregularities, a and b to the anisotropy, and the outer scale L_0 is the scale size of the bigger irregularities. Note that despite the size of the outer scale, there would be plenty of smaller scale irregularities up to the order of a few meters. The scenarios and the exact geometry have been defined using the Biomass End-to-End Performance Simulator (BEEPS) [21].

The first step in comparing the beam-centered approach and SADI is to show that both the methods give similar results when the irregularities are much larger in the azimuth dimension than the synthetic aperture projected on the ionosphere. For that, we use the phase map in Scenario 1 (Fig. 5), where irregularities change slowly due to the high anisotropy compared with the synthetic aperture. Fig. 6 shows two interferograms that compare the unperturbed image for the beam-center approach (top) and the SADI approach. Note that in both the cases, the output is a smoothed version of Scenario 1 due to the synthetic aperture convolution, and the interferograms look identical, so the improvement in resolution is not perceived. This is better appreciated in Fig. 7 where the phase difference is shown (nearly 0 everywhere).

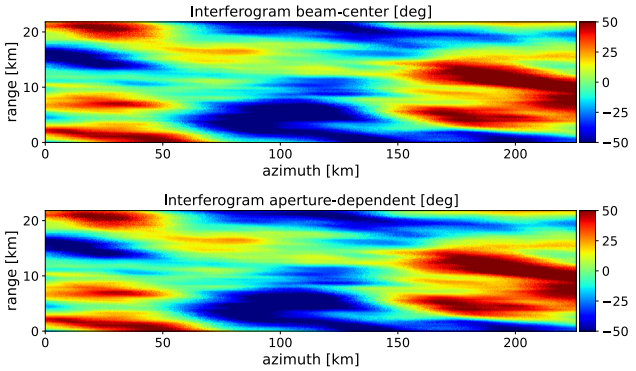

Fig. 6. Interferograms between images before and after the injection of the phase map in Scenario 1 with the beam-center method (top) and SADI (bottom).

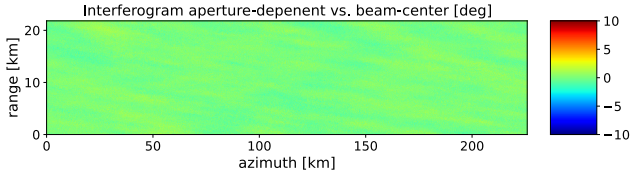

Fig. 7. Phase difference between the output of both the methods in Scenario 1.

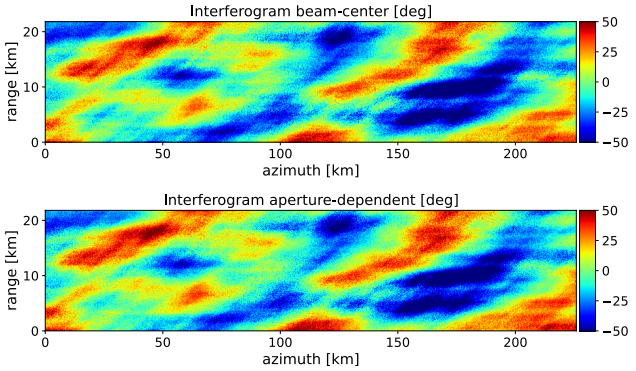

Fig. 8. Interferograms between images before and after the injection of the phase map in Scenario 2 with the beam-center method (top) and SADI (bottom).

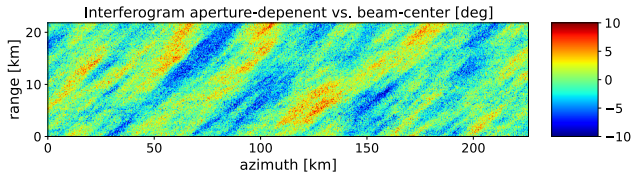

Fig. 9. Phase difference between the output of both the methods in Scenario 2.

We compare the results when the phase map in Scenario 2 (Fig. 5) is used. Here, despite the large anisotropy, due to the geomagnetic field orientation, the size of the irregularities in the azimuth direction is small compared with the synthetic aperture. The resolution increment is not visible in Fig. 8 but in Fig. 9, which shows the phase difference between both the interferograms. Here, one can see that the difference between both the methods is the high-frequency component of the phase, which was averaged by the beam-center approximation but not by the SADI technique.

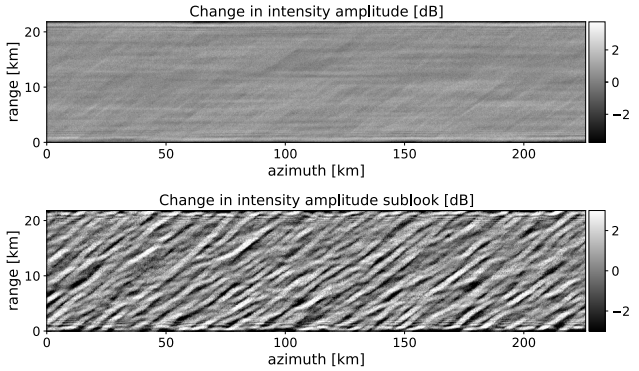

Fig. 10. Intensity scintillation in focused image with ionospheric disturbance (top), 1/10 bandwidth sublook (bottom).

The results in Fig. 10 show the intensity scintillation corresponding to Scenario 2, the focused image, and the intensity of one sublook. Note the appearance of the stripes in the sublooked image and that the orientation is maintained with respect to the phase screen with a higher frequency variation as expected.

IV. Conclusion

This letter has presented a method for incorporating ionospheric disturbances into SAR simulations in an aperture-dependent manner. This approach is preferred over other beam-center methods like applying an ITF or semi-focusing at ionospheric height previously discussed in the literature because it allows to accommodate ionospheric realizations with a varying height or which are quickly changing with time. It works with subapertures and introduces the ionospheric disturbance for each satellite position that, at the instant, falls inside the antenna beam while it adapts the geometry. It also takes into account the oblique propagation out of the beam center. This makes it possible to gain resolution when ionospheric irregularities smaller than the synthetic aperture projected on the ionosphere are present, making it fit for wide-beam systems. This was shown in realistic simulation scenarios in the framework of the Biomass mission. Injection of intensity scintillations was also proved possible. This approach can be generalized to inject all kinds of disturbances. Here, we commented on the possibility of injecting FR, but it would be possible to inject dispersion and time delays, too.

References

[1] N. C. Rogers, S. Quegan, J. S. Kim, and K. P. Papathanassiou, "Impacts of ionospheric scintillation on the BIOMASS P-band satellite SAR," *IEEE Trans. Geosci. Remote Sens.*, vol. 52, no. 3, pp. 1856–1868, Mar. 2014.

[2] F. J. Meyer and J. Nicoll, "The impact of the ionosphere on interferometric SAR processing," in *Proc. IEEE Int. Geosci. Remote Sens. Symp. (IGARSS)*, vol. 2, Jul. 2008, p. 391.

[3] Z.-W. Xu, J. Wu, and Z.-S. Wu, "A survey of ionospheric effects on space-based radar," *Waves Random Media*, vol. 14, no. 2, pp. S189–S273, Apr. 2004.

[4] J. Aarons, "Global morphology of ionospheric scintillations," *Proc. IEEE*, vol. 70, no. 4, pp. 360–378, Apr. 1982.

[5] Y.-H. Liu, C.-H. Liu, and S.-Y. Su, "Global and seasonal scintillation morphology in the equatorial region derived from ROCSAT-1 in-situ data," *Terr., Atmos. Ocean. Sci.*, vol. 23, no. 1, p. 95, 2012.

[6] S. Basu, S. Basu, and B. K. Khan, "Model of equatorial scintillations from in-situ measurements," *Radio Sci.*, vol. 11, no. 10, pp. 821–832, Oct. 1976.

[7] K. C. Yeh and C. H. Liu, "Diagnosis of the turbulent state of ionospheric plasma by propagation methods," *Radio Sci.*, vol. 12, no. 6, pp. 1031–1034, Nov. 1977.

[8] C. L. Rino and J. Owen, "Numerical simulations of intensity scintillation using the power law phase screen model," *Radio Sci.*, vol. 19, no. 3, pp. 891–908, May 1984.

[9] S. Ji, W. Chen, X. Ding, and C. Zhao, "Equatorial ionospheric zonal drift by monitoring local GPS reference networks," *J. Geophys. Res.*, vol. 116, 2011, Art. no. A08310, doi: 10.1029/2010JA015993.

[10] C. S. Carrano, K. M. Groves, and R. G. Caton, "Simulating the impacts of ionospheric scintillation on L band SAR image formation," *Radio Sci.*, vol. 47, no. 4, pp. 1–14, Aug. 2012.

[11] N. Rogers and P. Cannon, "The synthetic aperture radar trans-ionospheric radio propagation simulator (SAR-TIRPS)," in *Proc. IRST*, Apr. 2009, pp. 1–5.

[12] F. J. Meyer, K. Chotoo, S. D. Chotoo, B. D. Huxtable, and C. S. Carrano, "The influence of equatorial scintillation on L-band SAR image quality and phase," *IEEE Trans. Geosci. Remote Sens.*, vol. 54, no. 2, pp. 869–880, Feb. 2016.

[13] J. S. Kim, K. P. Papathanassiou, R. Scheiber, and S. Quegan, "Correcting distortion of polarimetric SAR data induced by ionospheric scintillation," *IEEE Trans. Geosci. Remote Sens.*, vol. 53, no. 12, pp. 6319–6335, Dec. 2015.

[14] P. Prats, A. Reigber, and J. J. Mallorqui, "Topography-dependent motion compensation for repeat-pass interferometric SAR systems," *IEEE Geosci. Remote Sens. Lett.*, vol. 2, no. 2, pp. 206–210, Apr. 2005.

[15] M. Rodriguez-Cassola et al., "Doppler-related distortions in Tops SAR images," *IEEE Trans. Geosci. Remote Sens.*, vol. 53, no. 1, pp. 25–35, Jan. 2015.

[16] *Report for Mission Selection: Biomass*, document ESA SP-13214/1, European Space Agency (ESA), Noordwijk, The Netherlands, Nov. 2012.

[17] C. L. Rino, "On the application of phase screen models to the interpretation of ionospheric scintillation data," *Radio Sci.*, vol. 17, no. 4, pp. 855–867, Jul. 1982.

[18] E. N. Bramley, "The accuracy of computing ionospheric radio-wave scintillation by the thin-phase-screen approximation," *J. Atmos. Terr. Phys.*, vol. 39, no. 3, pp. 367–373, Mar. 1977.

[19] D. L. Knepp, "Multiple phase screen calculation of two-way spherical wave propagation in the ionosphere," *Radio Sci.*, vol. 51, no. 4, pp. 259–270, Apr. 2016.

[20] C. L. Rino, "A power law phase screen model for ionospheric scintillation: 1. Weak scatter," *Radio Sci.*, vol. 14, no. 6, pp. 1135–1145, Nov. 1979.

[21] M. J. Sanjuan-Ferrer et al., "End-to-end performance simulator for the BIOMASS mission," in *Proc. 12th Eur. Conf. Synth. Aperture Radar (EUSAR)*, Jun. 2018, pp. 1–5.

B

An Autofocus Algorithm for the Recovery of Ionospheric Phase Signatures in the Biomass Mission.

An Autofocus Algorithm for the Recovery of Ionospheric Phase Signatures in the Biomass Mission

Felipe Betancourt-Payan[a], Marc Rodriguez-Cassola[a], Andreas Benedikter[a], Pau Prats-Iraola[a], and Gerhard Krieger[a]
[a]Microwaves and Radar Institute, DLR, Muenchnerstrasse 20, Wessling, Germany

Abstract

We present in this paper an autofocus algorithm for the recovery of ionospheric phase signatures in data from the Biomass mission. The algorithm is currently being integrated in the end-to-end simulation chain of Biomass and will be part of its ground prototype processor. The paper discusses both the pertinence and accuracy of the simulation of the ionospheric perturbations and the autofocus itself.

1 Introduction

As a response to the challenges of monitoring the above-ground biomass of Earth's forests and framed within the ESA Earth Explorer program, the Biomass mission was approved for full implementation [1]. With its main objective being the determination of the quantity and structure of forests world wide, as well as their dynamic evolution due to land use, Biomass will serve as a key input for calculation of carbon stocks and fluxes. All this data is needed for the assessment of the present and projection of the future of the global carbon cycle.

Biomass will carry onboard a fully polarimetric P-band SAR (with a frequency of 435 MHz) which has exceptional capabilities for forest observation. These include high sensitivity and temporal coherence over repeated passes when observing forested areas, allowing for the application of SAR interferometry and tomography for the determination of the vertical distribution of forests scatterers. Propagation of low frequency electromagnetic waves through the ionospheric plasma translates into time delay, phase advance and Faraday rotation that will deteriorate the quality of the radar measurements [2, 3, 4]. The irregularities introduced by the ionosphere propagate as phase errors into the focussed images which may cause relevant geolocation errors, interferometric phase errors, depolarisation of the polarimetric channels, and range and azimuth defocussing, significantly degrading the quality of the acquired images [5].

As a part of the end-to-end simulation tool and the ground prototype processor for the Biomass mission, an autofocus algorithm analogous to [6] but based on the mapdrift technique is currently under development. We present in this paper the suggested algorithm and the simulation chain supporting the development and its validation. We also provide in the paper an assessment of the approximations in the simulation and the processing of the data.

The paper is distributed as follows. Section 2 discusses the simulation of the data including an analysis of the approximations conducted in the injection of the ionospheric perturbations into the data. Section 3 describes succinctly the autofocus algorithm suggested in the paper. Section 4 presents experimental results obtained with the prototype end-to-end simulation chain. Section 5 concludes the paper with a discussion.

2 Data Simulation

This section discusses the simulation of the ionospheric perturbations, the selected data to support the development of the autofocus algorithm, and the incorporation of the perturbations into the data.

2.1 Simulation of the Ionosphere

The ionospheric perturbations are simulated as the superposition of a background and a turbulent component [7]. The background component is based on electron density profiles provided by the NeQuick2 model [9], and converted into slant total electron content (TEC) by mapping an integrated vertical profile according to the Biomass observation geometry. The turbulent component is modelled using a Rino power spectral law [12], in which the anisotropy parameters are computed according to the orientation of the magnetic field and the spacecraft observation geometry. The magnetic field reference is read from the International Geomagnetic Reference Field (IGRF) [11].

The turbulent component is directly generated as a phase advance map using the following expression [12, 13]

$$\Phi_\phi(\vec{\kappa}) = \frac{\lambda^2 \cdot r_\mathrm{e}^2 \cdot \sec^2\theta \cdot a \cdot b \cdot \left(\frac{2\pi}{1000}\right)^{p+1} \cdot C_k L}{\left(\kappa_0^2 + A \cdot \kappa_r^2 + B \cdot \kappa_r \cdot \kappa_x + C \cdot \kappa_x^2\right)^{\frac{p+1}{2}}}, \quad (1)$$

where the Φ_ϕ corresponds to the power spectral density of

ISBN 978-3-8007-5823-4 / ISSN 2197-4403

the turbulent phase advance, $\vec{\kappa}$ is the vector of the spatial wavenumber in range and azimuth (κ_r, κ_x), respectively, λ is the carrier wavelength, r_e is the classical electron radius, θ is the incident angle of the radar wave onto the ionospheric screen at the center of the block, a and b are the anisotropy coefficients, p is the spectral index, $C_k L$ is the vertically integrated strength of the turbulence at 1 km scale, κ_0 is the wavenumber of the outer scale of the irregularities L_0, A, B, and C are geometric factors that depend on the propagation geometry compared to the direction of the magnetic field [14]. From the simulated phase advance maps, we estimate an equivalent slant TEC according to the expression [12]

$$\mathrm{TEC} \approx -\frac{\mathrm{c}_0 \cdot f_0}{2\pi \cdot \zeta} \cdot \phi \quad , \tag{2}$$

where $\zeta = 40.31\ \mathrm{m}^3/\mathrm{s}^2$ is a scaling constant, c_0 is the velocity of light, f_0 is the carrier frequency. The turbulent TEC estimated with the expression above is added to the background TEC, and the Faraday rotation experienced by the data are computed according to [12, 7]

$$\Omega = \zeta \cdot \frac{q_\mathrm{e} \cdot \vec{B} \cdot \vec{k}}{\mathrm{c}_0 \cdot m_\mathrm{e} \cdot f_0^2} \cdot \mathrm{TEC} \quad , \tag{3}$$

where q_e is the electron charge, $\vec{B}$ is the magnetic field vector map drawn from the IGRF model, $\vec{k}$ is the line of sight vector, m_e is the electron mass. Table 1 shows the parameters used for the ionospheric simulations presented in this subsection.

Table 1 Ionospheric simulation parameters

Parameter	Units	Value
Center of the scene (lon, lat)	deg	(-20, -25)
Carrier frequency	MHz	435
Carrier wavelength λ	m	0.68
Classical electron radius r_e	m	$2.817 \cdot 10^{-15}$
Incidence angle onto ionosphere θ	deg	25
Anisotropy parameter a	-	10.0
Anisotropy parameter b	-	1.0
Spectral index p	-	2.65
Turbulence strength $C_k L$	-	$7.5 \cdot 10^{32}$
Outer scale L_0	m	30000
A	-	1.0073
B	-	0.0746
C	-	1.197
Electron charge q_e	C	$1.602 \cdot 10^{-19}$
Electron mass m_e	kg	$9.109 \cdot 10^{-31}$

Fig. 1 shows a realization of the phase advance map conducted with the parameters listed in Table 1.

Note the variation of the background component is from far range to near range within 350 deg for the simulated acquisition. The turbulent perturbations show a standard deviation of about 122.10 deg. The group delay map is generated by scaling the phase advance map as discussed in [7].

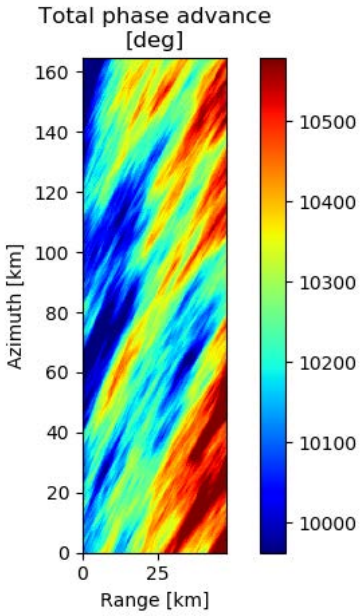

Figure 1 Phase advance map (background + turbulence) simulated using the parameters in Table 1.

Fig. 2 shows a realization of the Faraday rotation consistent with the parameters listed in Table 1.

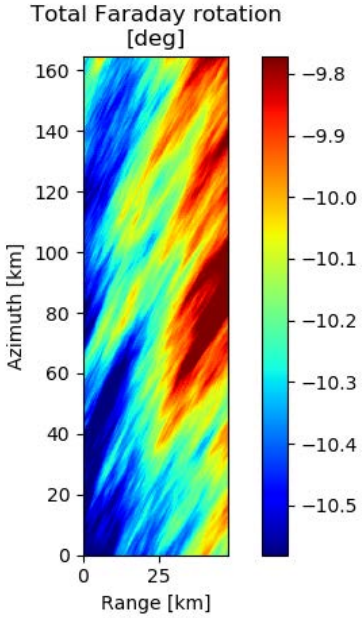

Figure 2 Faraday rotation map (background + turbulence) consistent with Fig. 1.

The total variation of the background contribution to the Faraday rotation is 0.6 deg, and the standard deviation of the turbulent contribution is of 0.204 deg.

Note the value of the turbulent contribution to the Faraday rotation is small because the scene is located around the Equator, where the line of sight vector and the magnetic field vectors are close to perpendicular. The components of the magnetic field vector in north-east-down coordinates

are shown in Fig. 3

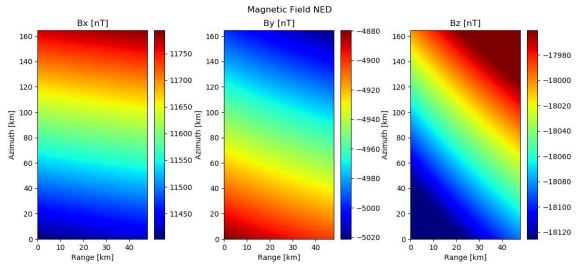

Figure 3 Components of the magnetic field vector in north-east-down coordinates used for the simulation parameters of Table 1.

Note the large proportionality factor between the phase and Faraday rotation values. Correcting ionospheric-induced phase perturbations based on Faraday rotation estimates might result in significant noise scaling, which can only be avoided by using large averaging windows in the Bickel and Bates algorithm as described in [8]. By doing so, the finer structures in the ionosphere may not be captured, leaving non-negligible phase errors - and probably defocussing - in the calibrated images, which speaks in favour of considering the use of an autofocus algorithm within the processing chain. This further justifies the need of an autofocus in the processing chain.

2.2 Simulation Data

For the development of an autofocus algorithm, the selection of the reference data to be used is essential. Since the quality of the estimates provided by the algorithm are based on the contrast within the image, the use of images with realistic contrast is mandatory. Now in the case of Biomass this poses a real challenge, since only airborne images in P band are available. The ones of the F-SAR we have access to [15], have swaths well below that of Biomass and may also be affected by focussing errors due to residual calibration errors. The other alternative is to use spaceborne data, e.g., TerraSAR-X or Sentinel-1, which provide comparable swaths, but different backscattering and crontrast in the images. The image used for generating the results of this paper (shown in Fig. 4) is a Sentinel-1 in the Munich area, to which no radiometric correction has been appllied to simulate for changes between P-band and C-band reflectivity.

2.3 Perturbation of the Raw Data

We incorporated the previous two modules -one to simulate the ionosphere, and one to ingest Sentinel-1 reflectivity images- into the End-to-End simulator currently being developed for Biomass [16].

The followed approach is similar to the one described in [13, 8], and is based on the incorporation of the group delay and the Faraday rotation on the focused image, and the

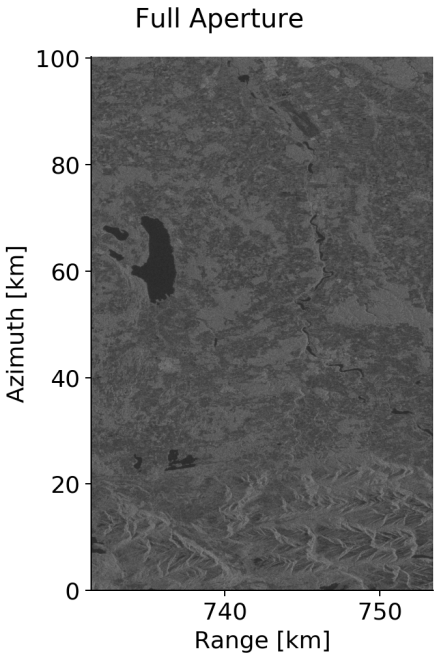

Figure 4 Sentinel-1 image used to produce results in this paper showing different backscattering aread and distictive features.

phase advances after defocussing in azimuth at the ionospheric height.

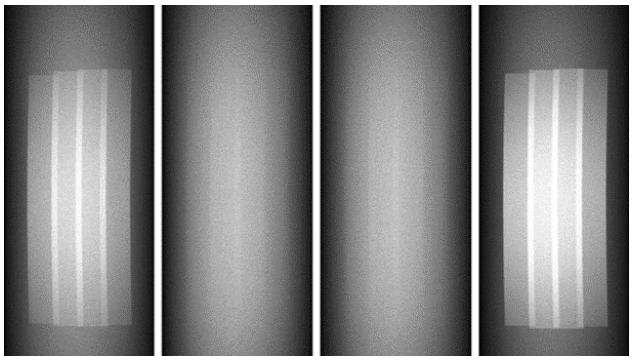

Figure 5 Simulated raw data for the four polarimetric channels according to the Biomass geometry and acquisition timeline.

Fig. 5 shows an example of simulated raw data for the four polarisations. Note the four blocks in the middle of the image correspond to four point targets introduced for the assessment of the quality of the processed data. Note the middle images correspond to the cross-pol channels, in which the response of the point targets is only perceived via the cross-pol patterns.

3 Autofocus Algorithm

As hinted above, a rapidly changing ionosphere adds phase errors within the synthetic aperture that deteriorate the im-

ISBN 978-3-8007-5823-4 / ISSN 2197-4403

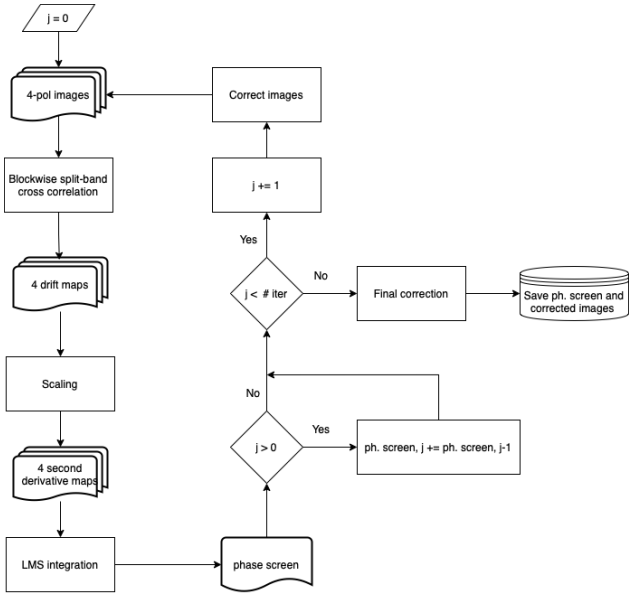

Figure 6 Autofocus workflow.

pulse response of the targets during image formation. This degradation is seen as azimuth defocussing and loss of contrast of the focussed images. Due to its development for the ground prototype processor of Biomass, we base our solution in a map-drift kernel [17]. Unlike the phase gradient kernel, the map-drift can be applied over extended areas even in the absence of point-like structures.

Fig. 6 shows the blcok diagram of the proposed algorithm. The autofocus wotks on all four polatimetric images simultanously. The images are divided into blocks and the local defocusing is estimated by measuring the drifts between two or more sub-look images. The measured drifts are proportional local estimates of the second derivatives of the phase screen along the azimuth direction as follows,

$$\frac{\mathrm{d}^2\phi(t)}{\mathrm{d}t^2} = \frac{4 \cdot \pi \cdot K_t^2}{B_\mathrm{a}^2 \cdot (1+\alpha)} \cdot \Delta_a \quad , \tag{4}$$

where K_t is the Doppler rate at the centers of the blocks projected at ionospheric height, B_a is the processing azimuth bandwidth, α is the oversampling factor in azimuth and Δ_a is the shift measure between sub-looks in pixels. For this simulation B_a is 846 Hz and α is 0.7379. The integration of all four second derivative maps into a single phase screen is put as a Least Means Squares (LMS) problem to average the errors in the estimation of the defocussing contributions.

The obtained phase screen is used for correcting the images, applying the correction at ionospheric height. To avoid introducing inconsistencies during the iterative corrections, during the iterations the retrieves phase screens are accumulated and only the original images are corrected. At the end, the final phase screen and corrected images are retrieved.

4 Experimental Results

In this section, the phase screen shown in Fig. 7 is introduced int he data generated from the reflectivity map shown in Fig. 4. Note the level of anisotropy in the scintillations is significantly smaller thatn the maps shown in Fig. 2, which simplifies the computation of the local drifts.

The autofocus is run after removing the background component of the ionosphere so that there are no relevvant trends in the result and only the small scale irregularities are left to be corrected.

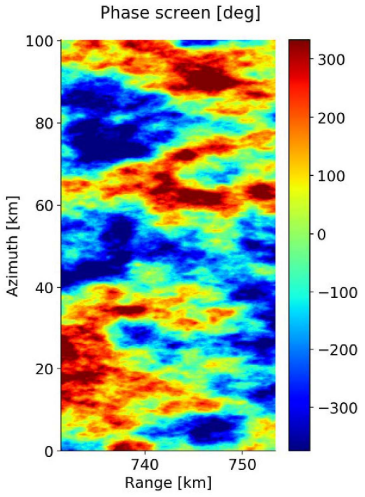

Figure 7 Phase screen used for the simulation, turbulent component only.

Fig. 8 shows the result of the phase screen recovered after the first and second iterations. Blocks the size approximately a quarter of the outer scale were used for the first iteration and an eight for the second to extend the bandwidth of the estimated solution.The result is a low pass version of the desired phase screen because the block-wise operation of the MDA. The blocks size and locations were modified for the second iteration to add more diversity to the integration and obtain a more robust solution. Note the averaging in Fig. 8 shows a strong boxcar signture, and the texture of the solution is expected to improve significantly once adaptive windows are incorporatd into the LMS solution [18, 19].

5 Conclusions

An autofocus algorithm for the recovery of ionospheric phase signatures from P-band data of the Biomass mission is currently under development at DLR. The algorithm is to be incorporated into the ground processor prototype of the mission.

An End-to-End simulation environment has been upgraded to ingest Sentinel-1 images to provide scenarios with real contrast that help tune the capabilities of the autofocus.

ISBN 978-3-8007-5823-4 / ISSN 2197-4403

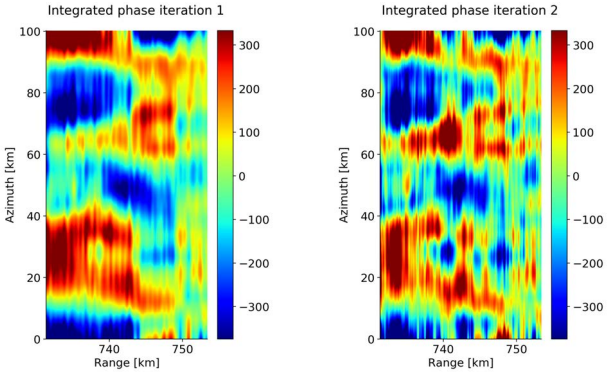

Figure 8 Integrated phases for two iterations.

Experiments have been presented where it is shown that the algorithm is capable to measure smaller scale ionospheric irregularities (of the order of 30 km outer scale). The approach has been proven to work in a realistic mission scenario with complex image features where different levels of contrast are found.

6 Literature

[1] Report for Mission Selection: Biomass (ESA SP-1324/1, May 2012), European Space Agency, The Netherlands.

[2] Belcher, D. P., and N. C. Rogers. "Theory and simulation of ionospheric effects on synthetic aperture radar." IET radar, sonar & navigation 3.5 (2009): 541-551.

[3] Belcher, D. P. "Theoretical limits on SAR imposed by the ionosphere." IET Radar, Sonar & Navigation 2.6 (2008): 435-448.

[4] Wright, Patricia A., et al. "Faraday rotation effects on L-band spaceborne SAR data." IEEE Transactions on Geoscience and Remote Sensing 41.12 (2003): 2735-2744.

[5] Quegan, Shaun, et al. "Quantifying and correcting ionospheric effects on P-band SAR images." IGARSS 2008-2008 IEEE International Geoscience and Remote Sensing Symposium. Vol. 2. IEEE, 2008.

[6] Li, Zhuo, et al. "Performance analysis of phase gradient autofocus for compensating ionospheric phase scintillation in BIOMASS P-band SAR data." IEEE Geoscience and Remote Sensing Letters 12.6 (2015): 1367-1371.

[7] Kim, Jun Su. Development of ionosphere estimation techniques for the correction of SAR data. Diss. ETH Zurich, 2013.

[8] Kim, Jun Su, et al. "Correcting distortion of polarimetric SAR data induced by ionospheric scintillation." IEEE Transactions on Geoscience and Remote Sensing 53.12 (2015): 6319-6335.

[9] Nava, B., P. Coisson, and S. M. Radicella. "A new version of the NeQuick ionosphere electron density model." Journal of Atmospheric and Solar-Terrestrial Physics 70.15 (2008): 1856-1862.

[10] Rino, C. L. "A power law phase screen model for ionospheric scintillation: 1. Weak scatter." Radio Science 14.6 (1979): 1135-1145.

[11] Alken, Patrick, et al. "International geomagnetic reference field: the thirteenth generation." Earth, Planets and Space 73.1 (2021): 1-25.

[12] Rino, C. L. "A power law phase screen model for ionospheric scintillation: 1. Weak scatter." Radio Science 14.6 (1979): 1135-1145.

[13] Carrano, Charles S., Keith M. Groves, and Ronald G. Caton. "Simulating the impacts of ionospheric scintillation on L band SAR image formation." Radio Science 47.04 (2012): 1-14.

[14] Rino, C. L., and E. J. Fremouw. "The angle dependence of singly scattered wavefields." Journal of Atmospheric and Terrestrial Physics 39.8 (1977): 859-868.

[15] M. Pardini *et al.,* 3-D Structure Observation of African Tropical Forests with Multibaseline SAR: Results from the AfriSAR Campaign, Proc IGARSS 2017.

[16] Sanjuan-Ferrer, Maria Jose, et al. "End-to-end performance simulator for the BIOMASS mission." EUSAR 2018; 12th European Conference on Synthetic Aperture Radar. VDE, 2018.

[17] Carrara, Walter G., R. S. Goodman, and Rd M. Majewski. "Spotlight synthetic radar: signal processing algorithms." Artech House (1995).

[18] Gracheva, Valeria and Kim, Jun Su and Prats-Iraola, Pau and Scheiber, Rolf and Rodriguez-Cassola, Marc. "Combined Estimation of Ionospheric Effects in SAR Images Exploiting Faraday Rotation and Autofocus"

[19] Gomba, Giorgio, and Francesco De Zan. "Bayesian data combination for the estimation of ionospheric effects in SAR interferograms." IEEE Transactions on Geoscience and Remote Sensing 55.11 (2017): 6582-6593.

C

Towards an Interferometric Autofocus for the Estimation of Ionospheric Signatures in Biomass.

Towards an Interferometric Autofocus for the Estimation of Ionospheric Signatures in Biomass

Betancourt-Payan, Felipe[a], Rodriguez-Cassola, Marc[a], Prats-Iraola, Pau[a], and Krieger, Gerhard[a]
[a]Deutsches Zentrum fuer Luft- und Raumfahrt (DLR), Muenchener Str. 20, 82234 Wessling, Germany

Abstract

This paper presents the workflow towards an improved estimation and correction of phase errors due to trans-ionospheric propagation in low-frequency Synthetic Aperture Radar (SAR) images when interferometric stacks are available. The method consists of estimating the absolute ionospheric phase delays in each of the images with traditional methods like autofocus. These setimations will later be combined with what is obtained during the correction of the differential ionosphere in interferometric pairs. By running the algorithms on simulated data, it is shown that it is possible to resolve faster changing phase errors than with the autofocus alone for a more accurate correction.

1 Introduction

The use of lower frequencies in Synthetic Aperture Radar (SAR) is motivated by the penetration capability of the radar waves into volumetric scatterers like forests and ice. The achieved lower temporal decorrelation is also desired in the processing of interferometric products and motivated the development of new systems like the P-band SAR Biomass (435 MHz) [1]. These low-frequency radio waves are also significantly affected by the double passage through the ionosphere [2, 3], which leaves a footprint in the images that must be corrected to improve the quality and interpretation of the data. On the other hand, since to calibrate the ionosphere effects, we first need to *see it*, it also offers the potential of high resolution 2D ionospheric imaging [4].

The refractive index experienced by the radar waves changes with the concentration of free electrons and frequency. In the presence of the ionosphere, the lower the frequency, the larger the phase errors introduced into the SAR images [5]. The phase errors that occur due to small ionospheric irregularities are particularly interesting. They produce defocussing in the azimuth dimension, lowering the contrast and resolution of the images. In the interferograms, this irregular part of the ionosphere introduces azimuth shifts between the image pairs and phase screens. For the imaging and calibration of ionospheric effects in the Biomass framework, there are different approaches, based on the estimation of the Faraday rotation [6], one Map-Drift Autofocus (MDA) [7, 8] or the combination of both [9]. In this paper, we will focus on using the MDA calibration only. There are also different methods for the correction of phase errors in the interferograms, such as range split-spectrum, azimuth shifts, or a combination of both too [10].

In this paper, we present a method that attempts to regain resolution in the estimation of the single-pass solutions by using the results obtained by the interferometric calibration. These last estimations have higher resolutions, and the combination is possible via a system of linear transformations. Section 2 explains the methodology, Section 3 describes the scenario used for the simulations carried out and that lead to the results in Section 4. Section 5 presents a summary and conclusions.

2 Methodology

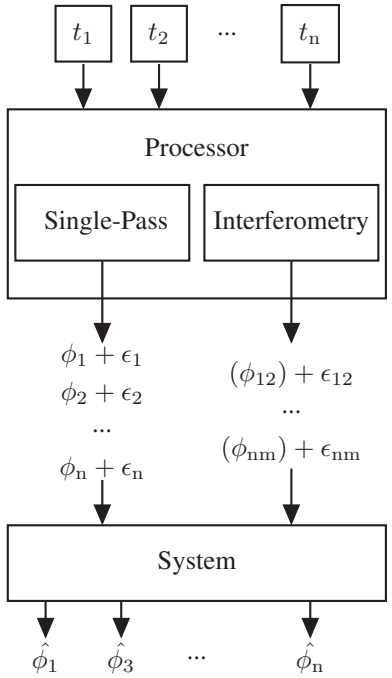

Figure 1 Block diagram for data combination.

Figure 1 shows the block diagram of the scheme that we propose for the updated estimation of the ionospheric phase errors. First, the image stacks for all available times,

ISBN 978-3-8007-6286-6 / ISSN 2197-4403

t_1 to t_n, must be processed separately in a single pass calibration step. For this paper, we consider the case in which an MDA is applied, but in a more refined approach, a combination with the Faraday rotation can also be used. The output would be a first set of estimations of the absolute phases (ϕ_1, ϕ_2 to ϕ_n) with the associated errors (ϵ_1, ϵ_2 to ϵ_n) that are determined by the performance of the calibration algorithms.

At the same time, interferometric combinations of all possible pairs are used to estimate the interferometric phase screen that corresponds to the differential ionosphere, ϕ_{nm}, again with the errors ϵ_{nm} that correspond to the performance of the calibration algorithm. More sensitivity and resolution are expected in the interferometric calibration but will only produce differential phase variations.

Finally, all this information is fed into a Least Squares (LS) system that makes the single-pass estimations compatible with the interferometric estimations. Under the assumption that calibration errors (ϵ_1, ϵ_2 to ϵ_n) are independent of each other, an LS tries to cancel them out, leading to single-pass solutions with improved resolution ($\hat{\phi}_1$, $\hat{\phi}_2$ to $\hat{\phi}_n$). An LS system was chosen because it has proven to integrate different estimations when (as in this case) the data combination can be expressed as a set of linear operations. A system for a stack of three images is shown in (1).

$$\underbrace{\begin{bmatrix} 1 & 0 & 0 \\ 0 & 1 & 0 \\ 0 & 0 & 1 \\ 1 & -1 & 0 \\ 1 & 0 & -1 \\ 0 & 1 & -1 \end{bmatrix}}_{\text{LT}} \underbrace{\begin{bmatrix} \hat{\phi}_1 \\ \hat{\phi}_2 \\ \hat{\phi}_3 \end{bmatrix}}_{\text{combined estimation}} = \underbrace{\begin{bmatrix} \phi_1 + \epsilon_1 \\ \phi_2 + \epsilon_2 \\ \phi_3 + \epsilon_3 \\ \phi_{12} + \epsilon_{12} \\ \phi_{13} + \epsilon_{13} \\ \phi_{23} + \epsilon_{23} \end{bmatrix}}_{\text{calibration output}} \quad (1)$$

As inputs to the system, there are all phases recovered from the MDA in this case ($\phi_n + \epsilon_n$) and all the differential phases extracted from interferometric methods [10] ($\phi_{nm} + \epsilon_{nm}$). The system is over-determined since the number of unknowns is just the number of images in the stack, and the number of equations is the stack length plus the number of interferometric pairs. It will be shown that adding weights to the system can make the solution more robust.

3 Simulation Scenario

Due to the lack of Biomass data, for this work, it was decided to inject simulated 1D ionospheric phase errors into a TerraSAR-X reflectivity image (Figure 2) by partially focusing at the height of maximum ionization, h_{iono} [6]. To the detected reflectivity, partially correlated realizations of multiplicative speckles were added (simulating temporal decorrelation). This was done up to seven times since it is the number of passes defined for Biomass' tomographic phase.

The spatial distribution of the ionospheric irregularities, responsible for quickly changing phase errors, which are smaller than the outer scale l_0 (that range starting from $\sim$ 5 km [12], well below the synthetic aperture length) is described by a power law spectrum [13]

$$\Phi_\phi(\kappa) = \frac{\lambda^2 \cdot r_e \cdot \sec^2\theta \cdot ab \cdot (2\pi/1000)^{p+1} \cdot C_k L}{(\kappa_0^2 + \kappa^2)^{(p+1)/2}}, \quad (2)$$

where κ is the spatial wave number, λ is the wavelength that corresponds to the carrier frequency f_0, r_e is the classical electron radius, θ is the incidence angle onto the ionosphere, ab is the anisotropy ratio, p is the spectral index, $C_k L$ is the vertically integrated turbulent strength at 1km scale and $k_0 = 2\pi/l_0$ is the outer scale wave number.

For this study, we are also focusing on the single-pass calibration case where only the MDA was applied. Running the experiments over an actual reflectivity image is necessary to assess the performance of the MDA in retrieving the quickly varying ionospheric irregularities. The simulation parameters are summarized in Table 1.

Parameter	Units	Value
Wavelength λ	m	0.69
Incidence angle θ	deg	25
Anisotropy $a:b$	-	5:1
Spectral index p	-	2.65
Turbulent strength $C_k L$	-	10^{33}
Outer scale l_0	km	20
Satellite height h_{sat}	km	660
Ionospheric height h_{iono}	km	350

Table 1 Simulation parameters.

4 Results

In this results section, we are going to focus on two main points: first, we will focus on the output of the ionospheric recovery with the MDA for one case, then the discussion can be extrapolated to all other cases; second, we will show the results obtained from the combination framework.

4.1 Single-Pass Solution

The MDA performance is affected by (i) the block-wise operation, (ii) the limited resolution in the estimation of second derivatives due to the averaging of the synthetic aperture, and (iii) the limitation of the bounding the random walks errors in the integration. The block operation also produces a down-sampled estimate of the phase error that we up-sample again with a linear interpolation. With all this, the single-pass inconsistencies are made of aliasing, low-pass filtering, and interpolation errors.

Figure 3 shows the profiles of the recovered phase after five iterations, and one can see the limitation of retrieving very fast varying phases. Another way to see it is in Figure 4, which shows the interferometric phase error contribution from the ionosphere between the images before and after applying MDA with respect to the same image with no ionosphere for one of the scenarios. This is what we will refer to as single-pass solutions. Note that after applying

ISBN 978-3-8007-6286-6 / ISSN 2197-4403

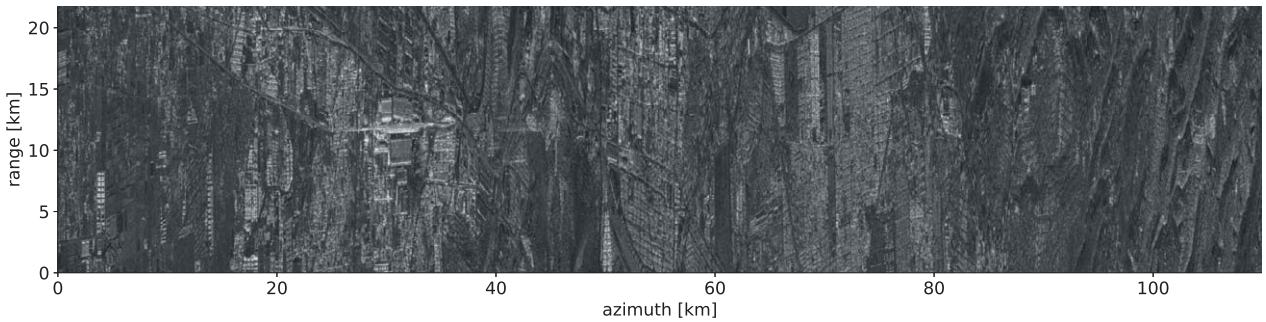

Figure 2 Reflectivity of TerraSAR-X image over Mexico used in the simulations.

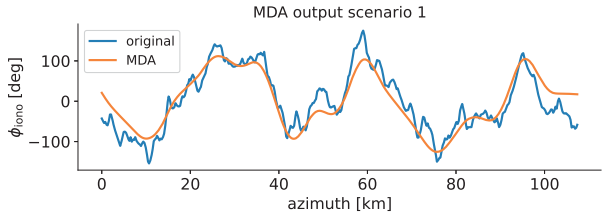

Figure 3 Recovered phase profile with MDA.

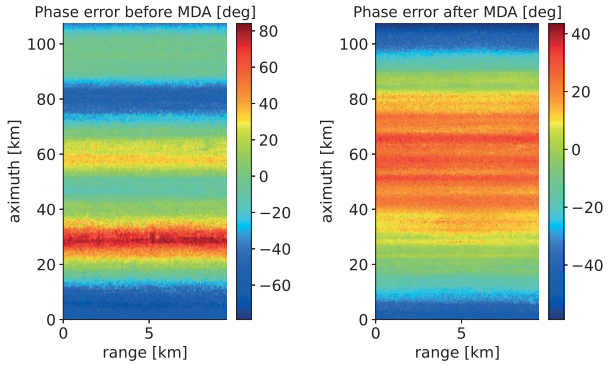

(a) Phase error before applying MDA.

(b) Phase error after applying MDA.

Figure 4 Interferometric phase with respect to the image with no ionosphere for one of the scenarios. Note the different color scales.

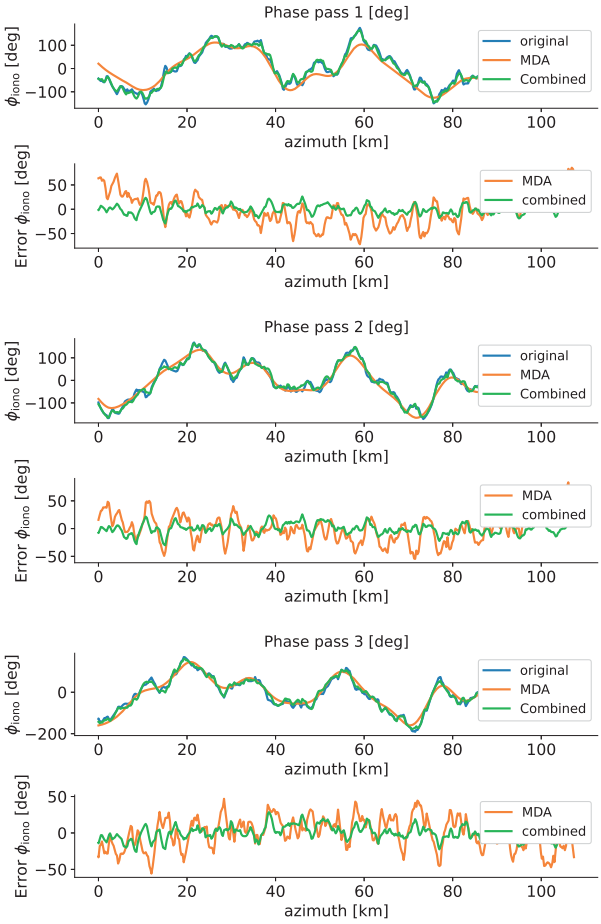

Figure 5 Phase profiles recovered by combining the information of seven different passes with the single pass solutions.

the MDA, there is a high-frequency phase component left behind that will not only contaminate the interferometric product but also leave residual defocusing.

4.2 Combined solution

As an example for the simulation of seven passes, Figure 5 compares three of the single-pass phases obtained with the MDA only separately in each image, with the combined solution after combining with the interferometry of all possible pairs. Note that in the error curves, it is possible to see how residual trends are canceled out and the magnitude of the errors is reduced, which translates into a gain in resolution.

Figure 6 shows the root mean square (RMS) residual error for all ionospheric phases as a function of the stack length. If the errors are uncorrelated, in principle, the more information put in the estimator, the better. In this case, this is not what is seen after five passes. The performance of the MDA depends on the structure of the phase error itself, and in the fifth image ϵ_5 was remarkably larger. The system in (1) can be extended to a Weighted Least Squares (WLS) to compensate for this (here case using the covariance of the error). Figure 7 shows the result of using a weighted system.

ISBN 978-3-8007-6286-6 / ISSN 2197-4403

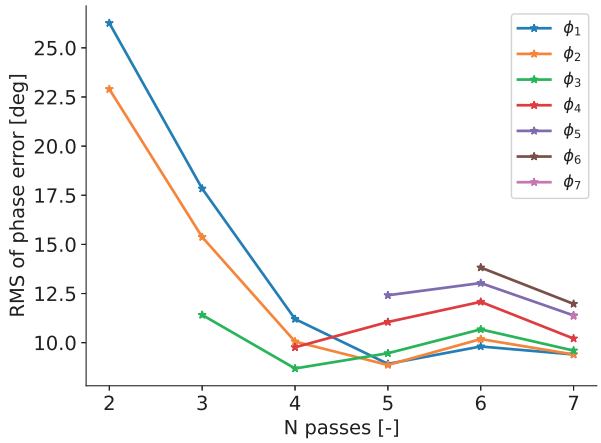

Figure 6 RMS of error with number of passes that are being used for the estimation.

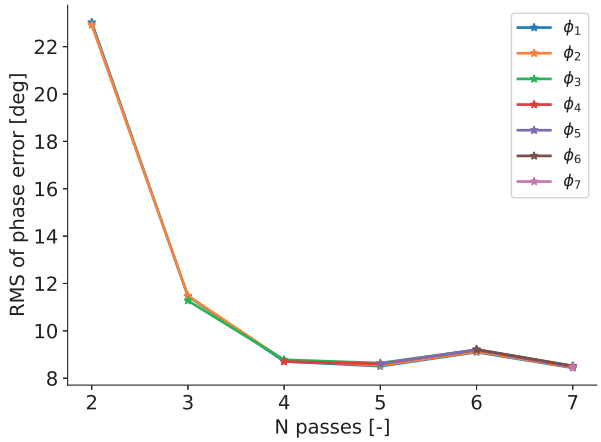

Figure 7 RMS of error with number of passes that are being used for the estimation in a weighted system.

Finally, after obtaining the new ionospheric estimation ($\hat{\phi}_1$, $\hat{\phi}_2$ to $\hat{\phi}_n$), they can be fed back into the calibration chain to obtain single images with even smaller phase errors. Figure 8 shows a histogram of the residual phase in the image before and after applying the MDA (the map in Figure 4) and after correcting with the phase recovered in the top panel in Figure 5.

5 Conclusions

The ionospheric calibration of Biomass products has two steps: first, at a single image level, and later, an interferometric calibration. The interferometric calibration provides high sensitivities but of the differential ionosphere only. On the other hand, ionospheric imaging and calibration with single images are limited by the performance of the calibration algorithm (in this paper we focused on the MDA). We presented a method that can be used to gain resolution in the absolute ionospheric realizations through a Least-Squares filter that cancels out inconsistencies in the

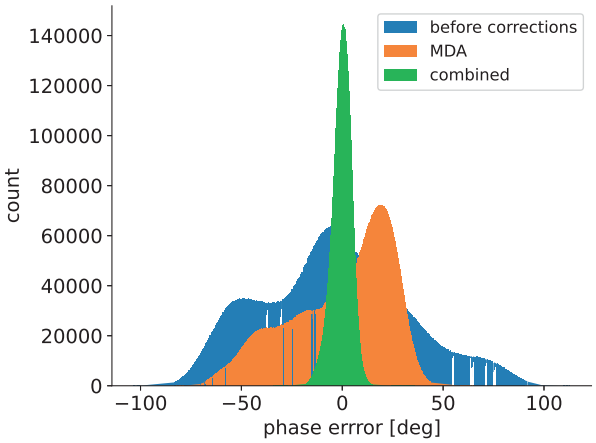

Figure 8 Histograms of interferometric phase errors with respect of the image without ionosphere.

single-pass products by utilizing what is measured in the interferometric calibration step.

By injecting different simulated phase errors into a reflectivity image with the Biomass's parameters, it was possible to test that this approach can cancel residual trends in the estimation of the phase errors compared to the MDA solution and that higher-frequency errors could be resolved. It was also shown that the RMS of the solution decreases with the number of images available to input into the system.

This framework can be extended to add other effects in the processing, like errors in the interferograms due to noise and decorrelation. It can also be adapted to separate the dispersive ionospheric component to the interferogram from other geophysical signals (such as the motion of surfaces and topography) by adding more equations (from other measurements if available) to keep the system determined.

6 Literature

[1] "Report for mission selection: Biomass," Tech. Rep. (ESA SP-13214/1), European Space Agency (ESA), Noordwijk, The Netherlands, November 2012.

[2] F. J. Meyer and J. Nicoll, "The impact of the ionosphere on interferometric sar processing," in *IGARSS 2008-2008 IEEE International Geoscience and Remote Sensing Symposium*, vol. 2, pp. II–391, IEEE, 2008.

[3] Z.-W. Xu, J. Wu, and Z.-S. Wu, "A survey of ionospheric effects on space-based radar," *Waves in Random media*, vol. 14, no. 2, p. S189, 2004.

[4] F. Meyer, R. Bamler, N. Jakowski, and T. Fritz, "The potential of low-frequency sar systems for mapping ionospheric tec distributions," *IEEE Geoscience and Remote Sensing Letters*, vol. 3, no. 4, pp. 560–564, 2006.

[5] D. Belcher, "Theoretical limits on sar imposed by the

ISBN 978-3-8007-6286-6 / ISSN 2197-4403

ionosphere," *IET Radar, Sonar & Navigation*, vol. 2, no. 6, pp. 435–448, 2008.

[6] J. S. Kim, K. P. Papathanassiou, R. Scheiber, and S. Quegan, "Correcting distortion of polarimetric sar data induced by ionospheric scintillation," *IEEE Transactions on Geoscience and Remote Sensing*, vol. 53, no. 12, pp. 6319–6335, 2015.

[7] C. V. Jakowatz, D. E. Wahl, P. H. Eichel, D. C. Ghiglia, and P. A. Thompson, *Spotlight-mode synthetic aperture radar: a signal processing approach: a signal processing approach*. Springer Science & Business Media, 2012.

[8] F. Betancourt-Payan, M. Rodriguez-Cassola, A. Benedikter, P. Prats-Iraola, and G. Krieger, "An autofocus algorithm for the recovery of ionospheric phase signatures in the biomass mission," in *EUSAR 2022; 14th European Conference on Synthetic Aperture Radar*, pp. 1–5, VDE, 2022.

[9] V. Gracheva, J. S. Kim, P. Prats-Iraola, R. Scheiber, and M. Rodriguez-Cassola, "Combined estimation of ionospheric effects in sar images exploiting faraday rotation and autofocus," *IEEE Geoscience and Remote Sensing Letters*, vol. 19, pp. 1–5, 2021.

[10] G. Gomba and F. De Zan, "Bayesian data combination for the estimation of ionospheric effects in sar interferograms," *IEEE Transactions on Geoscience and Remote Sensing*, vol. 55, no. 11, pp. 6582–6593, 2017.

[11] S. Tebaldini, A. M. Guarnieri, and F. Rocca, "Recovering time and space varying phase screens through sar multi-squint differential interferometry," in *EUSAR 2012; 9th European Conference on Synthetic Aperture Radar*, pp. 16–19, VDE, 2012.

[12] J. Aarons, "Global morphology of ionospheric scintillations," *Proceedings of the IEEE*, vol. 70, no. 4, pp. 360–378, 1982.

[13] D. Belcher and N. Rogers, "Theory and simulation of ionospheric effects on synthetic aperture radar," *IET radar, sonar & navigation*, vol. 3, no. 5, pp. 541–551, 2009.

ISBN 978-3-8007-6286-6 / ISSN 2197-4403

D

Analysis of the Retrieval Performance of 2-D Ionospheric Irregularity Maps in the Biomass Mission.

Analysis of the Retrieval Performance of 2-D Ionospheric Irregularity Maps in the Biomass Mission

Felipe Betancourt-Payan, *Graduate Student Member, IEEE*, Marc Rodriguez-Cassola, Pau Prats-Iraola, *Fellow, IEEE*, and Gerhard Krieger, *Fellow, IEEE*

***Abstract*— Low-frequency synthetic aperture radar (SAR) images are affected by trans-ionospheric propagation of the radar waves. The 2-D total electron content (TEC) maps can be obtained as a product of the ionospheric corrections, allowing for imaging of ionospheric irregularities at very high resolution and broader coverage compared to other sensing technologies (such as Global Navigation Satellite Systems (GNSS) and ionosondes). We analyze, in this article, the case of the Biomass mission and characterize the errors in the imaging of the ionosphere resulting from the calibration algorithms foreseen for its ground processor prototype: a Faraday rotation (FR)-based and an autofocus (AF) approach. The analysis relies on a turbulent power law Rino model for the perturbation of the ionosphere and the spectral behavior of the calibration algorithms. We also discuss the suitability of both approaches for image correction in different scenarios (varying signal-to-noise ratio (SNR) and geographic location).**

***Index Terms*— Autofocus (AF), Biomass, Faraday rotation (FR), ionosphere, synthetic aperture radar (SAR).**

I. Introduction

THE ionosphere is a region of the atmosphere that extends from ∼50 to 1000 km of altitude and consists of ionized plasma. It is a dispersive and dynamic medium for which the level of ionization and orientation of plasma depends on its interaction with the Earth's magnetic field and other factors like solar activity. Its state can be described by the free electron density. In most satellite applications, this electron density is measured as the integrated total electron content (TEC) between the platform and the ground. Several mechanisms have been developed over the years for sensing the ionosphere. Ionosonde techniques, for example, can provide vertical (or oblique, if operated in a bistatic mode) electron density profiles. This approach alone cannot provide global coverage despite increasing stations. On the other hand, Global Navigation Satellite Systems (GNSS) signals can be used for monitoring the spatially slow-changing ionosphere (background component) and, to some extent, continuous monitoring of ionospheric irregularities using the rate of TEC index (ROTI) [1], [2], able to provide average values to characterize the scintillation strength (e.g., using the S4 parameter) [3]. Even some approaches to imaging and tomography have been proposed [4]; however, they require large interpolations and smoothing (which lowers the resolution), and their capabilities are limited by the number and nonuniform distribution of the GNSS receivers that can be hundreds of kilometers apart.

The images of synthetic aperture radar (SAR) satellites are also affected by trans-ionospheric propagation, especially when operating at lower frequencies, and allow for sensing the ionosphere not with constant-global temporal coverage but with very high 2-D resolution. An example is the new SAR mission, Biomass from the European Space Agency (ESA), to be launched in 2024. Its main goal is quantifying the global forest Biomass, thus contributing to monitoring carbon fluxes and stocks. To reach this objective, it will be the first spaceborne SAR mission operating in P-band (435 MHz, ∼69-cm wavelength) with full polarimetry, allowing for both deep penetration into the forest canopies and good coherence for repeat-pass interferometry [5]. With a 12-m antenna, the SAR image resolution in azimuth for the single-look case is 6 m [6]. The ionosphere will leave its footprint in the images by introducing amplitude modulations, time delay, and phase advance in the radar echos (seen as geolocation and phase errors), as well as crosstalk among the polarimetric channels induced by Faraday rotation (FR). Of particular interest are the effects caused by ionospheric irregularities that change rapidly compared to the synthetic aperture (the synthetic aperture length of Biomass projected at the ionospheric height is about 20 km), inducing defocusing (seen as a loss of contrast) and intensity scintillation (patterns in the intensity images) that degrade the quality of the radiometric products. These distortions occur predominantly in the regions close to the geomagnetic equator [7] in the very early morning and evening times due to the characteristic appearance of instabilities of ionospheric plasma in these regions, as well as near the poles.

From the signal processing point of view, one can benefit from these adverse effects by retrieving information about the current state of the ionosphere while correcting the images. The ionospheric calibration of the images itself will allow the generation of 2-D TEC maps with the very high resolution that SAR provides. We will exploit the proportionality relationship between FR, phase advance, and TEC. Biomass will have a

Manuscript received 26 March 2024; revised 30 June 2024; accepted 2 August 2024. Date of publication 8 August 2024; date of current version 30 August 2024. This work was supported by the German Academic Exchange Service (DAAD) under Grant 57478193. *(Corresponding author: Felipe Betancourt-Payan.)*

The authors are with the Microwaves and Radar Institute, German Aerospace Center (DLR), 82234 Weßling, Germany (e-mail: felipe.betancourtpayan@dlr.de).

Digital Object Identifier 10.1109/TGRS.2024.3440628

Sun-synchronous polar low Earth orbit (average altitude of 660 km) with an orbital period of around 1.5 h. Beyond the calibration of the SAR images, the high-resolution TEC products over large areas unlock important scientific research opportunities, such as improving ionospheric equatorial irregularity models or the effect of space weather events in the polar regions.

There exist several calibration proposals for this challenging aspect of the mission. These exploit the FR [8], refocusing with an autofocus (AF) algorithm or a combination of both [9]. This article aims to characterize the residual errors expected after these calibration approaches. This article is structured as follows. Section II introduces the methodology and assumptions to solve this problem. We show that the error standard deviation can be expressed as the sum of different error sources. Section III discusses the residual errors after a multisquinted version of the Bickel and Bates algorithm for the estimation of FR; it also analyzes the impact of geomagnetic field uncertainty in TEC retrieval when using the FR. Section IV analyzes the remaining errors for a phase-based estimation with an AF. Section V discusses and compares the suitability of the two methods, and Section VI concludes this article with a summary.

II. Problem Statement

The propagation of radar waves through the ionosphere results in a perturbation of the amplitude, phase, and polarization of the signals [10]. We will use in our analysis the two following assumptions: 1) the perturbations show a specific consistency when observed from different positions along the satellite track, which allows us to model the impact as coming from a single surface (not necessarily spherical or ellipsoidal) and 2) the perturbations at spatial scales larger than the extension of the projection of the radar beam on the ionospheric surface have been successfully calibrated at previous processing stages. The former assumption is frequently found in the literature and justified by the continuity in the models of the ionospheric height [11], as well as supported by data collected from previous missions [12]. The latter assumption is justified by the dense sampling used in SAR, which allows the estimation of large-scale perturbations with large averaging windows. Following the previous discussion, we can approximate the impact on the radar waves by using a turbulent, stationary, dispersive, Doppler-dependent, and elevation-dependent perturbation field. The field consists of irregularities in the electron density, which directly translate into a phase and polarization distortion of the signals [13]. The spatial statistics of the stationary phase distortion field are often described by the Rino power law expression [14],

$$\Phi_\phi(\kappa_x,\kappa_y)=\frac{\lambda^2\cdot r_e^2\cdot \sec^2\theta_{\text{inc}}\cdot ab\cdot(2\cdot\pi/1000)^{p+1}\cdot C_kL}{\left(\kappa_0^2+A\cdot\kappa_x^2+B\cdot\kappa_x\cdot\kappa_y+C\cdot\kappa_y^2\right)^{(p+1)/2}} \tag{1}$$

where ϕ refers to the phase advance, κ_x and κ_y describe the orthogonal spatial frequencies in the reference geometry of the ionosphere, in this case, the geomagnetic North and East directions, λ is the carrier wavelength, r_e is the classical electron radius, θ_{inc} is the incident angle onto the ionospheric surface, p is the ionospheric spectral index, C_kL is the vertically integrated strength of turbulence at 1-km scale, and $\kappa_o=2\pi/l_o$ is the outer scale wavenumber. The A, B, and C parameters relate the magnetic field and anisotropy factors to the direction of propagation of the radar waves [15]. The relationship between the two-way phase advance ϕ, TEC, and FR Ω can be expressed as

$$\phi=\frac{\zeta\cdot 4\cdot\pi}{c_0\cdot f}\cdot\text{TEC} \tag{2}$$

and

$$\Omega=\zeta\cdot\frac{q_e\cdot\vec{B}\cdot\hat{k}}{c_0\cdot m_e\cdot f^2}\cdot\text{TEC} \tag{3}$$

where $\zeta\approx 40.31\,m^3/s^2$ is a constant, c_0 is the velocity of propagation in vacuum, f is the frequency, q_e is the electron charge, $\vec{B}$ is the Earth's electromagnetic field vector, $\hat{k}$ is the direction of propagation of the radar waves in the same reference frame, and m_e is the electron mass. The power spectral density (PSD) of the FR can be related to (1) as follows:

$$\Phi_\Omega(\kappa_x,\kappa_y)=\left(\frac{q_e\cdot\vec{B}\cdot\hat{k}}{m_e\cdot f\cdot 4\cdot\pi}\right)^2\cdot\Phi_\phi(\kappa_x,\kappa_y). \tag{4}$$

The statistical characterization of the errors in estimating the turbulent component of the ionosphere will result from filtering these PSD functions with the frequency response of the calibration algorithms. For this approach to yield representative results for a SAR acquisition, we need to make the additional assumption that this PSD is known (e.g., via models such as wideband model (WBMOD) for ionospheric scintillation [16]) or can be estimated from the data. The direct estimation from the data can be carried out by fitting the PSD of the observed ionosphere to the parameters of (1) or an approximation of it. For example, in [17], where the fitting is done based on what is retrieved in the interferometric correction, or [18], where the equatorial scintillation stripe signature is used. However, the correctness of the methodology and the illustrative power of the presented results are not affected.

For example, Fig. 1 shows one ionospheric realization in the Biomass observation geometry (satellite flying along the horizontal axis) according to the model described above for a region close to the North pole. The parameters of the simulation are listed in Table I. The Biomass End-to-End Performance Simulator (BEEPS) [19] is used to incorporate the ionospheric perturbations (phase and change in polarization) in the simulated SAR raw data.

TABLE I
Parameters Used for the Ionospheric Realization

Location Polar ROI (lat, lon)	(65.5, 11.0) [deg, deg]
C_kL	10^{32}
Outer scale l_0	20 km
Anisotropy $a:b$	5:1
Spectral index p	2.65
Ionospheric height h_{iono}	351 km

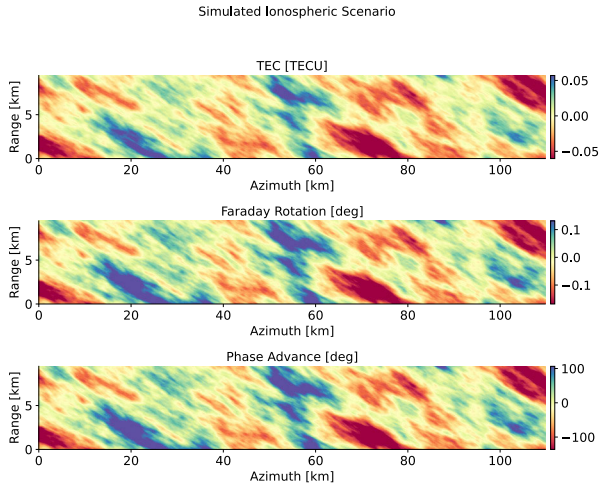

Fig. 1. Ionospheric irregularity realization generated with the parameters in Table I. From the TEC map (top), FR (middle) and phase (bottom) maps are obtained from (2) and (3).

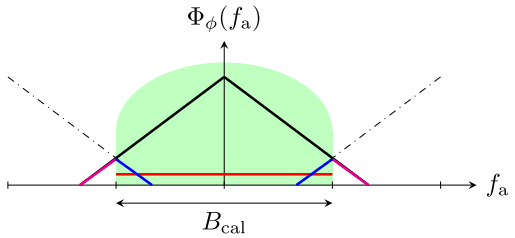

Fig. 2. Sketch of the PSD of the phase advance error observed by the SAR (black). The green area describes the calibration filter used in the ionospheric mitigation algorithms also used for ionospheric imaging. The blue, magenta, and red lines correspond to the intrinsic filtering errors caused by aliasing, limited bandwidth, and thermal noise, respectively. Aliasing replicas (dashed lines) occur by sampling the nonbandlimited ionospheric irregularity (here described by a power-law) function.

Fig. 2 sketches the errors (in blue, red, and magenta) in the ionospheric signal when reconstructing the phase field from the data. For simplicity, Fig. 2 refers to the azimuth dimension of the survey (f_a refers to azimuth or Doppler frequency), but the situation in the range is analogous. The green area corresponds to the filter that defines the calibration operations and extends to what we define as calibration bandwidth, B_{cal}. The blue lines within the filter correspond to the aliased power coming from the tails of the first spectral replicas. Replicas occur because of the sampling of a nonbandlimited field. The magenta solid lines outside the filter correspond to the power outside the calibration bandwidth, whereas the red line represents the power of thermal noise.

The one-sided PSD of the error when reconstructing the irregularity field (in our case, either using the FR or the phase signature that it leaves in the image) can be approximated as the sum of the contributions within and outside the calibration bandwidth, $f_a \leq B_{cal}/2$ and $f_a > B_{cal}/2$, respectively, as described in (5), as shown at the bottom of the next page. $\Phi_N(f_a)$ is the PSD of the thermal noise, assumed constant for white noise. The variance of the phase error (or the FR) is given in (6), as shown at the bottom of the next page: the first integral corresponds to the error within the band, composed by the noise plus the tails of the aliased replicas (that as we will see, might or might not be neglected). Here, i is the index of the aliasing replicas that occur every sampling frequency f_{samp}. The calibration filter B modulates these two components. The second integral shows the high frequency of the original perturbation lost because it falls outside the calibration window.

TABLE II
SIMULATION PARAMETERS

Satellite altitude h_{sat}	660 km
Incidence angle θ_{inc}	25 deg
Antenna diameter	12 m
Carrier frequency f_0	435 MHz
Pulse Repetition Frequency (PRF)	1475.506 Hz
Azimuth Bandwidth (B_a)	1229.588 Hz
Range Sampling Frequency (RSF)	7565217.4 Hz
Range bandwidth (B_r)	6877470.363 Hz

For the characterization of the errors, i.e., the residual disturbances in the imaging of the ionospheric irregularities, we will consider the two ionospheric calibration algorithms available in the Biomass Ground Processor Prototype (GPP) [20]. They should provide exemplary ionospheric recovery maps and the residual errors expected in Biomass images. The baseline for ionospheric correction in Biomass uses the estimation of the FR using the Bickel and Bates algorithm [8]. The estimation of the FR has proven to be a robust and effective method for ionospheric imaging in quad-pol systems. Still, the accuracy of the Bickel and Bates algorithm is latitude and signal-to-noise ratio (SNR)-dependent. From (3), one can see that the sensitivity depends on the value of the dot product $\vec{B} \cdot \hat{k}$. Close to the geomagnetic equator, these two vectors are almost perpendicular, which makes FR-based calibration algorithms insensitive to the ionosphere. Fig. 3 shows a global map of the error in the TEC estimation for a 1° error in the FR measurement. The geographic variations come from the geomagnetic field distribution. Note that from (3), errors in the FR scale to errors in TEC with the inverse of $\vec{B} \cdot \hat{k}$, and since at low latitudes the dot product is very small in practice it not possible carry out ionospheric inversion at the so-called *equatorial gap*. This region is depicted in red in Fig. 3.

For tracking fast ionospheric variations within the synthetic aperture, which might degrade the performance of the FR estimation, the GPP also incorporates a map-drift autofocus (MDA) algorithm [9], [21], [22]. This method takes observations of local defocusing across the image and transforms them into second derivatives of the phase variation along azimuth, which can also be integrated into TEC estimates. The AF performance depends on the image contrast and content, where a lack of contrast significantly reduces its robustness (and attractiveness); therefore, the MDA is kept as a backup solution in the processing flow. The fact that the MDA reconstructs higher order errors from second derivative measurements makes it insensitive to zeroth- and first-order errors (this is the reason for the previous assumption that any slowly varying background component is assumed to be removed). Errors in the measurements integrate into random walks during the double integration step. Sections III and IV will present the error characterization for the two suggested algorithms. Table II summarizes the main parameters for the simulations on the L-band image in Fig. 4 (in the absence of satellite P-band data, we used an actual ALOS-2 image).

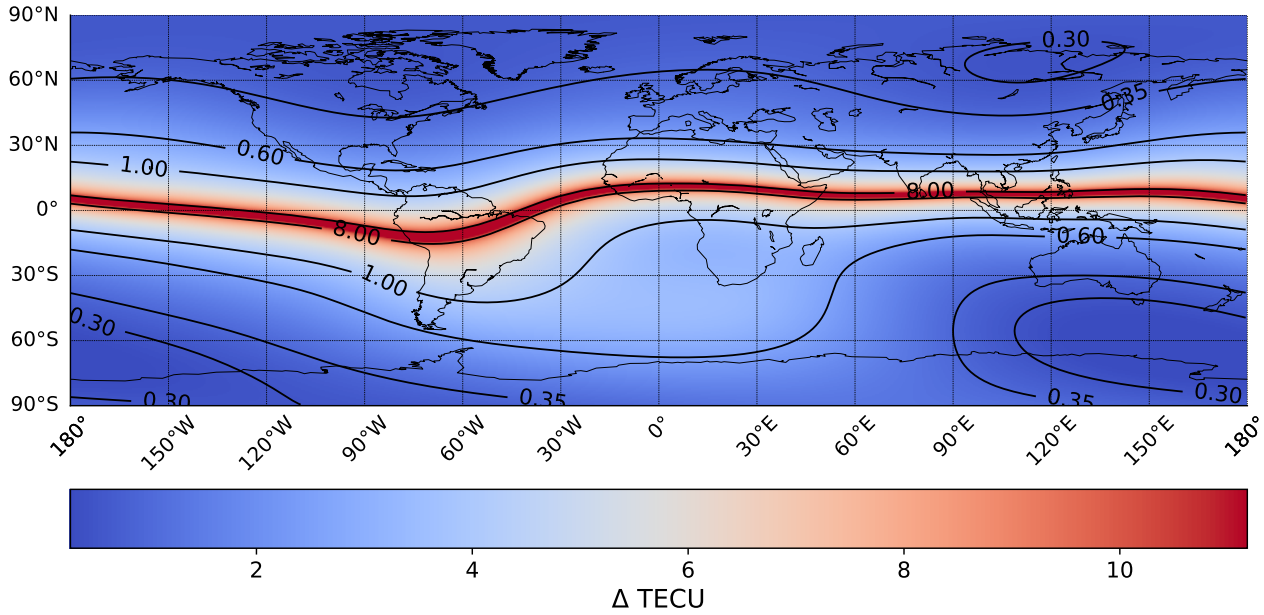

Fig. 3. Error in TEC estimation for 1° error in the FR measurement. The geometry is an ascending polar orbit with a 25° incidence angle onto the horizontal ionospheric layer. The red area shows the equatorial gap, where $\vec{B} \cdot \hat{k}$ tends to zero and there is no FR sensitivity.

For this article, we ingested the reflectivity image into the BEEPS/GPP processing chain to investigate the ionospheric effects and realistically process the data, demonstrating the capability of the MDA in a realistic scenario.

III. Bickel and Bates-Based Estimation

The examples in this section will be generated using a multi-squinted version, based on azimuth sublooks, of the Bickel and Bates estimator to estimate the FR. For a detailed description of the fundamentals, the reader should refer to [8], [23], and [24]. The calibration bandwidth is estimated from the PSD of the data. Fig. 5 shows that the azimuth cutoff frequency (gray) can be chosen where the PSD of the simulated FR field in the middle of Fig. 1 (blue) cuts the noise floor of the simulation (red). The noise floor depends on the SNR and the polarimetric coherence as discussed in [8] and [25]. The polarimetric coherence is related to the SNR as follows:

$$\gamma_{\mathrm{SNR}} = \frac{\mathrm{SNR}}{1+\mathrm{SNR}}. \tag{7}$$

The variance of the additive noise to FR (depicted with the red dashed line in Fig. 5) is given by (8), as shown at the bottom of page 6, where Li_2 is the Euler dilogarithm. An SNR of 25 dB leads to 0.996484 polarimetric coherence, and the corresponding filter azimuth bandwidth allows 476 nonoverlapping sublooks to cover the entire SAR azimuth bandwidth in the multisquint processing.

The calibration filter can be extended to the range dimension to improve noise suppression. For this analysis, we give it a rectangular shape in range, with a cutoff frequency that limits the noise inside the calibration bandwidth. Similar to (6), the final expression for the error variance is given in (9), as shown at the bottom of page 6. Here, B represents the spectral shape of the averaging window, S_{cbw} is the area of the calibration bandwidth, and S^c_{cbw} is its complement. $\mathrm{d}f_r$ is the frequency in the slant range direction, and i and k are the indexes of the replicas both in azimuth and range. Note that $i, k \in \mathbb{Z} \setminus \{0\}$. In the following, we only consider 2-D rectangular bandpass filters, but we can also use more elaborate filters oriented along the geomagnetic field for better performance.

$$\Phi_{\Delta\phi}(f_{\mathrm{a}}) = \begin{cases} \Phi_\phi(f_{\mathrm{a}}) & \text{for } f_{\mathrm{a}} > B_{\mathrm{cal}}/2 \\ B \cdot \left(\Phi_{\mathrm{N}}(f_{\mathrm{a}}) + \sum_{i=1}^{+\infty} \left(\Phi_\phi\left(f_{\mathrm{a}} + i \cdot f_{\mathrm{samp}}\right) + \Phi_\phi\left(f_{\mathrm{a}} - i \cdot f_{\mathrm{samp}}\right) \right) \right) & \text{for } f_{\mathrm{a}} \le B_{\mathrm{cal}}/2 \end{cases} \tag{5}$$

$$\sigma^2_{\Delta\phi} = 2 \cdot \left(\overbrace{\int_0^{B_{\mathrm{cal}}/2} \underbrace{B}_{\text{cal. filter}} \cdot \left(\underbrace{\Phi_{\mathrm{N}}(f_{\mathrm{a}})}_{\text{noise}} + \underbrace{\sum_{i=1}^{+\infty} \left(\Phi_\phi\left(f_{\mathrm{a}} + i \cdot f_{\mathrm{samp}}\right) + \Phi_\phi\left(f_{\mathrm{a}} - i \cdot f_{\mathrm{samp}}\right) \right)}_{\text{aliasing}} \right) \mathrm{d}f_{\mathrm{a}}}^{\text{inside of band}} + \overbrace{\int_{B_{\mathrm{cal}}/2}^{\infty} \Phi_\phi(f_{\mathrm{a}})\, \mathrm{d}f_{\mathrm{a}}}^{\text{outside of band}} \right). \tag{6}$$

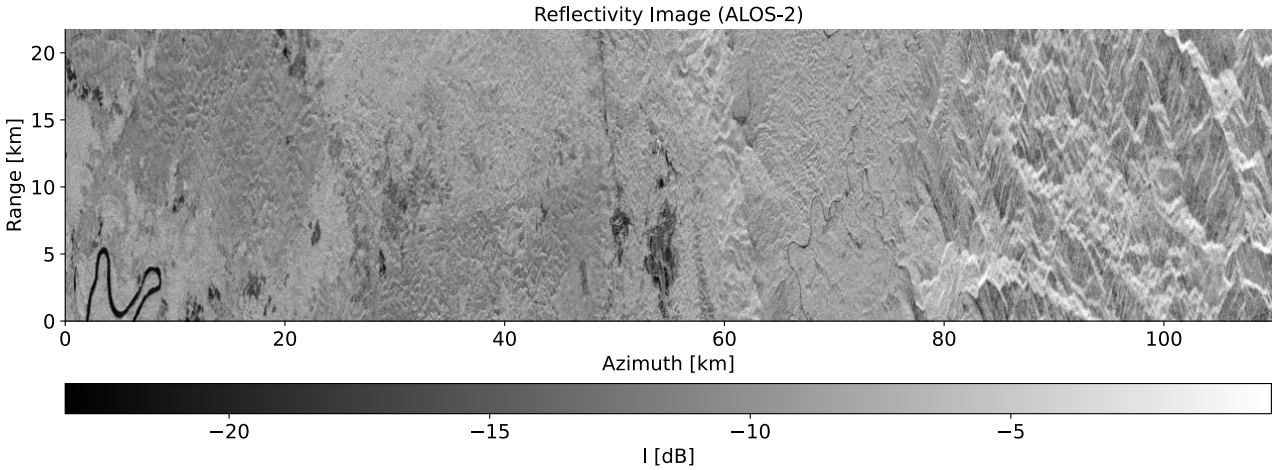

Fig. 4. Reflectivity image used in the simulations. The scene shows a forested and mountainous area with the L-band sensor ALOS-2 over Indonesia. An L-band acquisition is used in the absence of spaceborne P-band data.

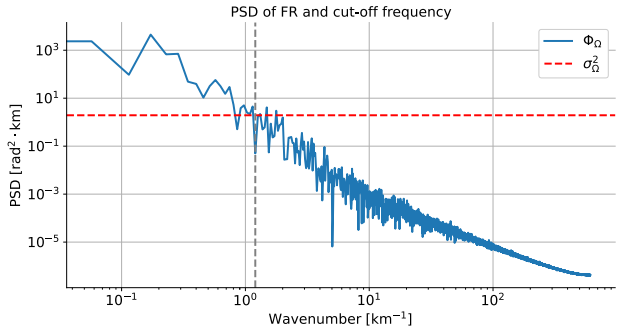

Fig. 5. Azimuth profile PSD of the simulated phase scaled to FR. The red horizontal line represents the noise power corresponding to the simulated with an SNR = 25 dB and $\gamma = 0.996484$. The vertical dashed line represents half the bandwidth of one of the 476 sublooks used in this simulation.

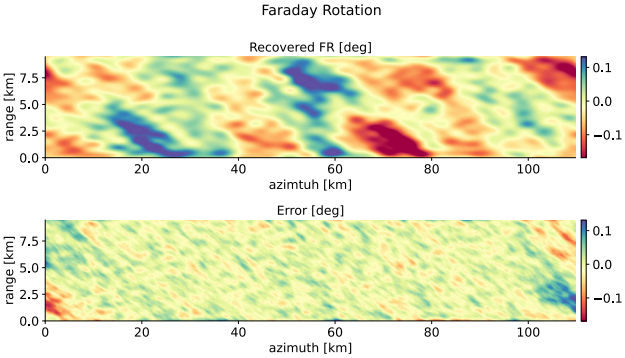

Fig. 6. (Top) Recovered FR map using Bickel and Bates and (bottom) corresponding error map for the simulated FR field in Fig. 1.

Fig. 6 shows the FR map recovered with this technique. Note the agreement in the structure with respect to the middle map in Fig. 1 and range of values (with a slight variability). Any discrepancy is better visualized in the error map below. This error contains mainly the high-frequency component of the original field that is not seen by the calibration bandwidth (note that the small structure still preserves the orientation). We can better validate this claim by looking at Fig. 7, where we compare the PSD of the recovered FR field (orange) to the PSD of the original one (blue). For reference, the PSD of the error is shown in green. Here, one can see that, as expected, the frequency coverage of the recovered FR only extends to

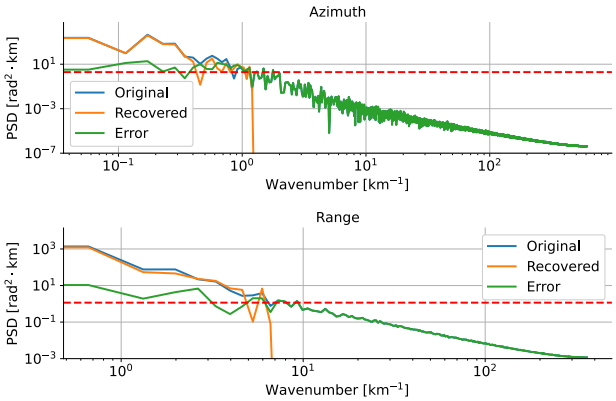

Fig. 7. (Top) Azimuth and (bottom) range PSD of the simulated FR field (blue), the recovered FR field using the multisquint approach (orange), and errors (green). Note that the frequency coverage of the recovered FR field only extends to the cutoff frequencies.

the cutoff frequency, so the error outside of the band is just the part of the spectrum not seen by it. Inside the band, there is a part of the noise spectrum and a smaller contribution coming from possible interpolation errors in the processing. Note that this error is still more than two orders of magnitude smaller than the original signal. The aliasing contribution depends on the sampling and the transfer function of the calibration filter, which, for the FR, is narrow compared to the high SAR sampling, making it negligible.

Fig. 8 shows the apparent azimuth and range resolution corresponding to the simulated ionospheric scenario for different SNRs. Here, a Monte Carlo simulation was carried out, generating various additive noise realizations for the FR field and choosing the cutoff frequency by looking at the magnitude of the corresponding Wiener filter (maintaining only the part before its magnitude reached −3 dB). The noise floor decreases for higher SNR, and a larger apparent bandwidth can improve the resolution to the kilometer scale in azimuth and subkilometer scale in range. Because the irregularity field is described as stationary, the variance of the error field is also stationary, and it is reasonable to characterize it with the standard deviation, $\sigma_{\Delta\Omega}$. Disregarding aliasing and interpolation errors, Fig. 9 shows the change in FR standard deviation for different SNRs. According to this, the main

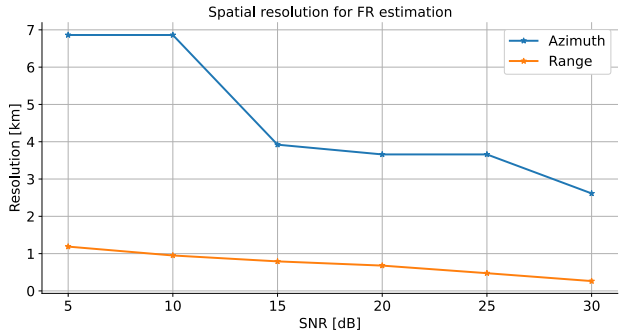

Fig. 8. For the simulated scenario, the resolutions in range and azimuth of the retrieved FR with the multisquint approach for different SNRs after a Monte Carlo simulation. The cutoff frequencies in range and azimuth correspond to the first −3-dB cut of the corresponding Wiener filter.

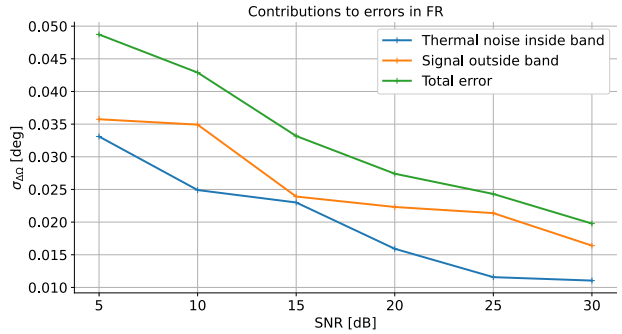

Fig. 9. Standard deviation of different error components (thermal noise inside of the band and signal outside) and the sum. Note that the main contribution comes from the signal part, which is not seen by the calibration bandwidth.

contribution to the error comes from the part of the spectrum that falls outside of the calibration bandwidth.

As described in [8], the estimated FR can be scaled to phase and used to correct phase errors. We can assess the impact of the residual errors in the quality of the image by looking at the radiometry. With remaining phase errors after the calibration, apart from the defocusing, the interpretation of the images will be distorted by discrepancies in the radiometry. We refer to the change power Δ_{P} with respect to the image without any distortion $|A|$ over an averaging window, i.e.,

$$\Delta_{\mathrm{P}} = \frac{\mathbb{E}\left[|A'|^2\right]}{\mathbb{E}\left[|A|^2\right]} \tag{10}$$

where $|A'|$ is the amplitude of the image with the residual errors after calibration. Errors in the radiometry distort the measured radar cross section of the imaged targets and mislead the interpretation of the data. Fig. 10 shows the radiometric error after the FR scaled to dB. The FR-based approach gives a good result in a polar scenario with a standard deviation of ≈0.068 dB.

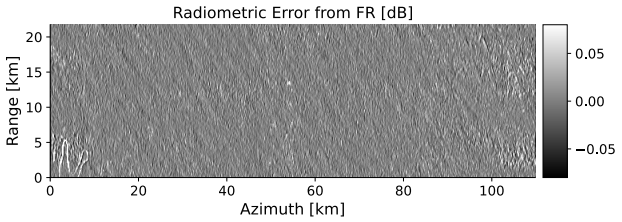

Fig. 10. Radiometric error after correction based on the FR field recovered in Fig. 6 scaled to phase.

A. Global Uncertainty Due To Geomagnetic Field

In addition to the calibration residuals presented so far, other error sources come from system uncertainties or model variability. We shall consider geometry errors that affect the line-of-sight (LOS), uncertainties introduced by the thin layer approximation and ionospheric height estimation, and residuals in the antenna pattern compensation, which are seen as polarimetric crosstalk contaminating the FR estimation, to mention a few. Assuming that these variables are controlled to a certain extent, we will shortly comment on the effect of the geomagnetic field uncertainty.

From [26], average values for the geomagnetic field vector uncertainty $\vec{\sigma}_B$ associated with the International Geomagnetic Reference Field (IGRF) model are 144 nT for the North (X), 136 nT for the East (Y), and 293 nT for Down (Z) components. The geomagnetic field vector, together with the LOS, is used for converting from FR into TEC and phase advance; as we will see in the following, this uncertainty introduces nonnegligible errors in the ionospheric retrieval with the Biomass system. Following the error propagation method described in [27] and assuming that the single uncertainties are independent and the orbit is polar, the uncertainty in $\vec{B}\cdot\hat{k}$ is given by (11), as shown at the bottom of the next page, which simplifies to

$$\sigma_{\vec{B}\cdot\hat{k}} = \sqrt{\hat{k}^2\cdot\vec{\sigma}_B^2}. \tag{12}$$

Considering that Biomass has a polar orbit with a left-looking geometry and a mean incidence angle onto the ionospheric horizontal plane of 25°, this uncertainty is 271.70 nT, constant everywhere on Earth. Different values are obtained with orbit inclinations or incidence angles, reflected in $\hat{k}$. Similarly, when estimating TEC (background or turbulent component) from FR, the uncertainty $\sigma_{\mathrm{TEC}}(\Omega)$ depends on $\sigma_{\vec{B}\cdot\hat{k}}$ and the local $\vec{B}\cdot\hat{k}$

$$\sigma_{\mathrm{TEC}}(\Omega) = \sqrt{\left(\frac{\partial \mathrm{TEC}}{\partial\left(\vec{B}\cdot\hat{k}\right)}\right)^2\cdot\sigma^2_{\vec{B}\cdot\hat{k}}} \tag{13}$$

$$\sigma_{\Omega}^2 = \frac{1}{16}\left(\frac{\pi^2}{3} - \pi\cdot\sin^{-1}\gamma_{\mathrm{SNR}} + \left(\sin^{-1}\gamma_{\mathrm{SNR}}\right)^2 - \frac{\mathrm{Li}_2\left(\gamma^2_{\mathrm{SNR}}\right)}{2}\right) \tag{8}$$

$$\sigma^2_{\Delta\Omega} = \overbrace{\int\int_{S_{\mathrm{cbw}}} B\cdot\left(\Phi_{\mathrm{N}} + \sum_{i=-\infty}^{+\infty}\sum_{k=-\infty}^{\infty}\Phi_{\Omega}[i,k]\right)\mathrm{d}f_r\,\mathrm{d}f_{\mathrm{a}}}^{\text{inside of band}} + \overbrace{\int\int_{S^c_{\mathrm{cbw}}}\Phi_{\Omega}\,\mathrm{d}f_r\,\mathrm{d}f_{\mathrm{a}}}^{\text{outside of band}} \tag{9}$$

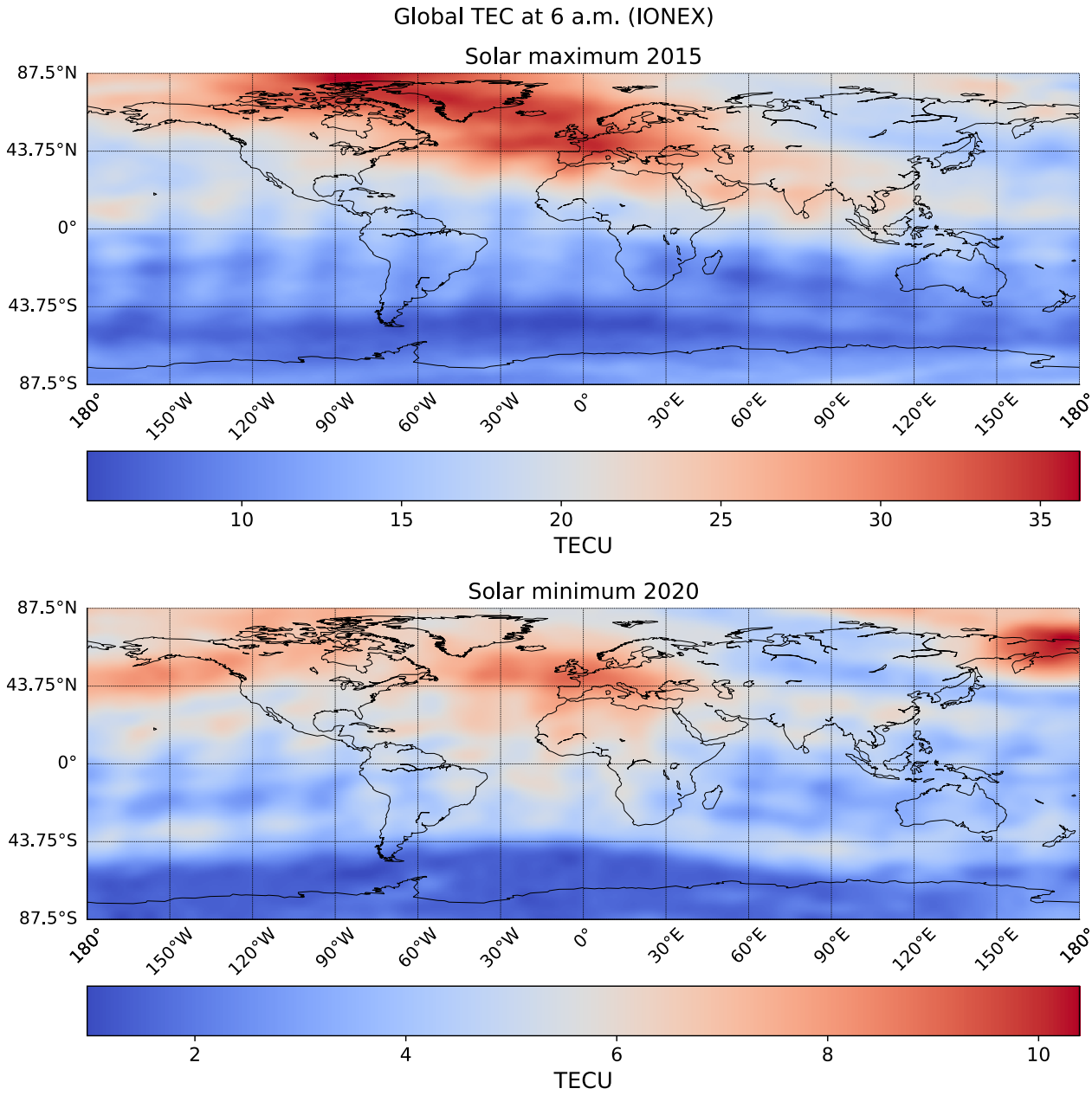

Fig. 11. Global TEC maps at 6 A.M. extracted from IONEX database for the 40th DoY 2015 (solar maximum, top) and 2020 (solar minimum, bottom).

with

$$\frac{\partial \mathrm{TEC}}{\partial\left(\vec{B}\cdot\hat{k}\right)} = -\frac{c_0 \cdot m_\mathrm{e} \cdot f^2}{\zeta \cdot q_\mathrm{e}} \cdot \frac{1}{\left(\vec{B}\cdot\hat{k}\right)^2} \cdot \Omega(\mathrm{TEC}). \tag{14}$$

Note that in (14), we highlight that the uncertainty in TEC depends on the local FR angle that is given by the value of TEC itself. Plugging $\Omega(\mathrm{TEC})$ from (3), we come to the following expression for the uncertainty in TEC based on the local TEC and $\vec{B}\cdot\hat{k}$:

$$\sigma_{\mathrm{TEC}}(\mathrm{TEC}) = \frac{\mathrm{TEC}}{|\vec{B}\cdot\hat{k}|} \cdot \sigma_{\vec{B}\cdot\hat{k}}. \tag{15}$$

Now, we proceed to give some representative numbers. For that, Fig. 11 shows the global TEC maps from the ionosphere map exchange (IONEX) database [28] at 6 A.M. that corresponds to what Biomass will observe (with the Sun-synchronous orbit, the same can be done for 6 P.M.), and

$$\sigma_{\vec{B}\cdot\hat{k}} = \sqrt{\left(\frac{\partial \vec{B}\cdot\hat{k}}{\partial B_X}\right)^2 \cdot \sigma_{B_X}^2 + \left(\frac{\partial \vec{B}\cdot\hat{k}}{\partial B_Y}\right)^2 \cdot \sigma_{B_Y}^2 + \left(\frac{\partial \vec{B}\cdot\hat{k}}{\partial B_Z}\right)^2 \cdot \sigma_{B_Z}^2} \tag{11}$$

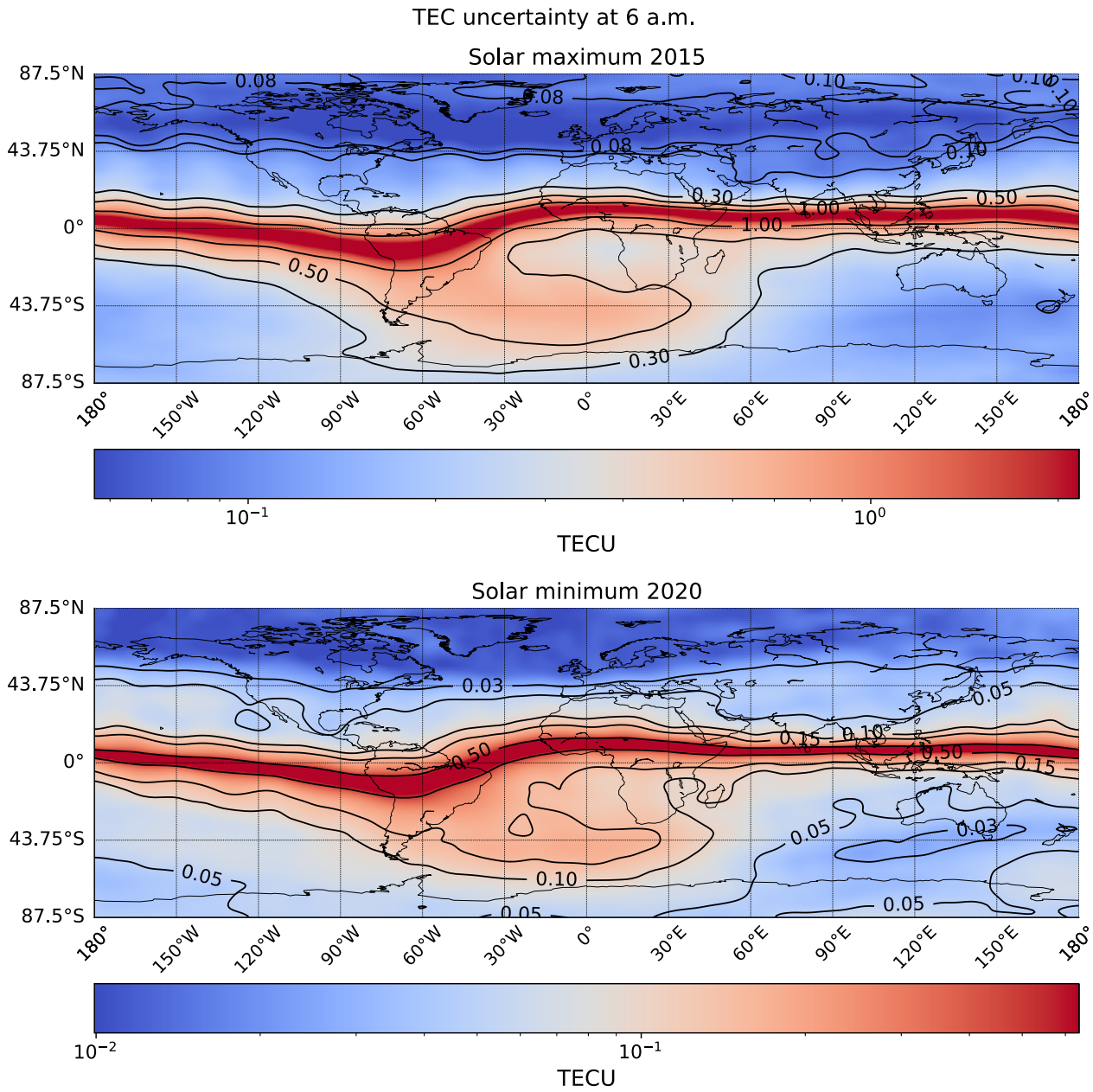

Fig. 12. Global uncertainty in estimating the background TEC from FR. Consider the ascending node of a polar Sun-synchronous orbit with the Biomass left-looking geometry at a time of solar maximum (top) and solar minimum (bottom).

we do this for two dates: the 40th day of the year (DoY) 2015 (solar maximum) and 2020 (solar minimum). The color bars show that in the solar maximum times, the TEC values triple the solar minimum values. Note that the irregularities in the map potentially come from the interpolations over the low resolution of the IONEX products; however, it does not invalidate our analysis since the purpose of this article is to have a sense of the global sensitivity variation. Putting these values in (15) with the local $\vec{B}\cdot\hat{k}$ leads to Fig. 12. Here, we see the uncertainty in TEC estimation from FR for the Biomass geometric configuration at a time of solar maximum and a time of solar minimum. Note that the uncertainty distribution strongly depends on the geomagnetic field dipole and its anomalies and that the higher uncertainty is found around the geomagnetic equator.

IV. Map-Drift Autofocus

An essential factor to consider when assessing the performance of the MDA is that it works with partially overlapped blocks across the image. Because of this, the measurements constitute a map of second derivatives (of the variation of the phase in the azimuth direction) that represents the difference between the average slopes across the two corresponding nonoverlapping synthetic aperture sublooks. In Fig. 13, they are illustrated by the two slopes in red and green in the sublooks shaded in yellow and orange. Because of the block operation and the assumption that the second derivative is constant across the block, some averaging happens in range and azimuth, too. Note that the second derivative map is subsampled to the block center spacing in both directions, leading to significant aliasing in the solution, as we will see.

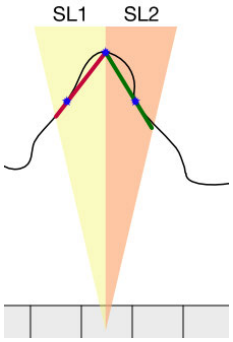

Fig. 13. Second derivative of azimuth variation across the synthetic aperture as seen by splitting the azimuth spectrum in the MDA.

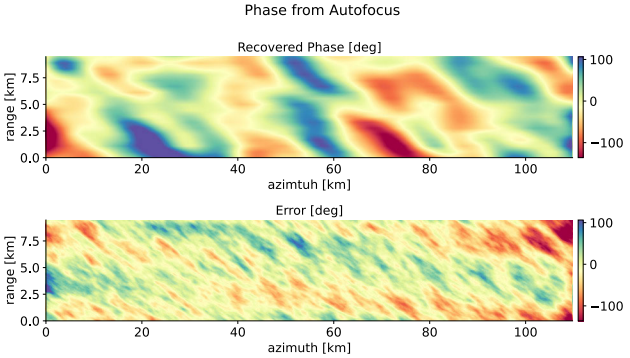

Fig. 14. (Top) Recovered phase after applying MDA and (bottom) corresponding error map.

The integration of this second derivative map into a TEC map can be done, for example, with a Wiener filter [9] or with a weighted least-squares (WLS) approach [21]. Either method will minimize the effect of the integrated random walks that derive from integrating errors in the second-derivative measurement. Even though random walks fail to be stationary, complicating the spectral analysis, an iterative MDA with a WLS integration has shown to dampen them to a reasonable extent. The MDA is an iterative method, and in each iteration, a phase map of the original size is obtained using a linear interpolation.

Fig. 14 shows the phase field recovered by the MDA with a WLS integration. In this simulation, we use a 128×128 pixel window (644×1106 m in azimuth and range) with shifts of 40 and 64 pixels in azimuth and range. Compared to the simulated field in Fig. 1, the MDA outputs a smoothed solution due to the averaging of the second derivative across the synthetic aperture, block averaging, aliasing due to sampling, integration, and linear interpolation reconstruction. Similar to the previous case, the error map presents structures aligned with the simulated field, but not only is the high-frequency component appreciated, as in the last case. This is better seen in the PSD azimuth profiles shown in Fig. 15: the PSD of the recovered phase field (orange) extends to the

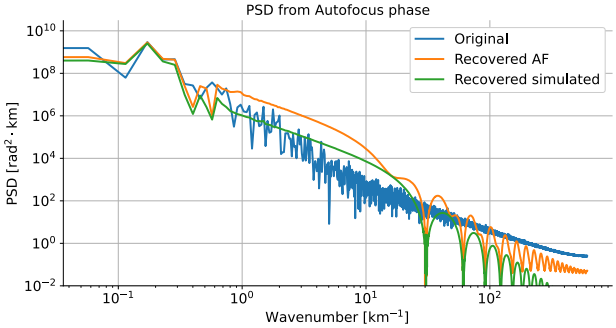

Fig. 15. Azimuth profile of the PSD of the simulated phase map (blue), the recovered after MDA (orange), and the result of applying the equivalent transfer functions to the simulated PSD (green).

TABLE III
PARAMETERS USED FOR EQUATORIAL SIMULATION

Location Equator ROI (lat, lon)	(19.0, 9.5) [deg, deg]
$C_k L$	$10^{3.2}$
Outer scale l_0	20 km
Anisotropy $a : b$	2:1
Spectral index p	2.65
Ionospheric height h_{iono}	351 km

end of the frequency coverage. This can be shown to be an effect of the corresponding aliasing (also responsible for the higher energy at the beginning of the PSD) and modulation of the frequency response of the MDA operations (green) as described in (16), as shown at the bottom of the page. Here, L is the frequency response of the linear interpolation operation (a sinc^2), $j \cdot \omega_1$ represents the differentiation in the frequency domain, $\frac{1}{j \cdot \omega_2}$ is the integration, M represents the block averaging, and again the summations with $i, k \in \mathbb{Z} \setminus \{0\}$ correspond to the aliasing that now plays a role because of the much lower sampling rate. Note that ω_1 and ω_2 are different since one represents the derivative with a step corresponding to two sublook centers, and the other corresponds to the displacement of the block centers in azimuth. The development of random walks has not been included in (16), but the results shown in Fig. 15 are still consistent. This shows that the iterative WLS integrator can cancel them appropriately.

As in Section III, we also use the residual radiometric error to assess the calibration performance (see Fig. 16). As shown in Fig. 14, the error map has larger granularity, also seen in the radiometric error map. In this case, the AF performs worse than the FR-based approach with radiometric errors with a standard deviation of 0.107 dB.

V. CONVENIENCE OF DIFFERENT CALIBRATION ALGORITHMS

So far, we have discussed a method for characterizing errors in two calibration approaches. Now, it is interesting to discuss their suitability in the ionospheric correction and imaging process. Regarding the Bickel and Bates measurement, for

$$\Phi_{\phi,\text{AF}} = \overbrace{L^2}^{\text{interpolation}} \cdot \overbrace{\frac{1}{(j \cdot \omega_2)^4}}^{\text{integration}} \overbrace{\left(\sum_{i=-\infty}^{\infty} \sum_{k=-\infty}^{\infty} \left(\underbrace{M^2}_{\text{averaging}} \cdot \underbrace{(j \cdot \omega_1)^4 \Phi_\phi[i,k]}_{\text{differentiation}} \right) \right)}^{\text{sampling}} \tag{16}$$

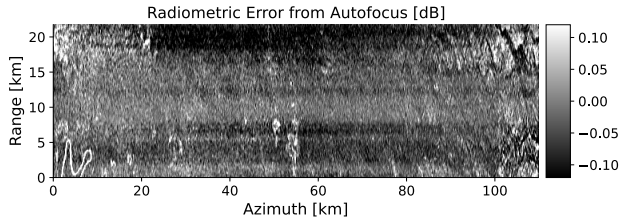

Fig. 16. Radiometric error after correction based on the phase field recovered in Fig. 14.

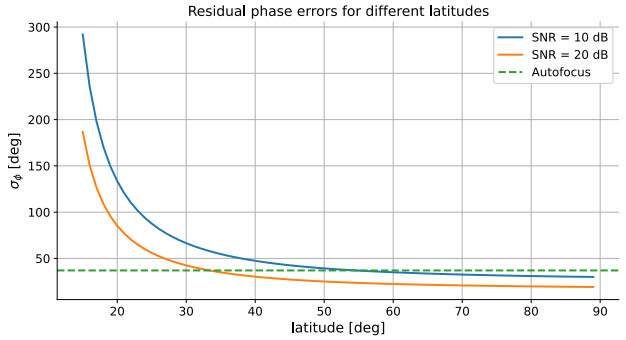

Fig. 17. Comparison of the expected performance estimating the phase screen in Fig. 1 using the FR and AF for two different SNRs and different latitudes along the prime meridian. The curves represent the FR performance that will change with latitude due to the variation in the $\vec{B} \cdot \hat{k}$ and SNR. The green horizontal dashed line shows the performance of the AF on the image in Fig. 4.

a fixed spectral index, the performance will be defined by $\vec{B} \cdot \hat{k}$, $C_k L$, the outer scale, and the noise floor, which will move up or down depending on the SNR, thus increasing or decreasing the cutoff frequency (Fig. 5). Conversely, for a fixed SNR, the cutoff frequency will also be determined by the PSD of the signal that would move up and down with $C_k L$ and $\vec{B} \cdot \hat{k}$, worsening the performance of this approach for smaller irregularity strength and when the FR sensitivity decreases compared to the SNR (toward the equatorial gap). Irregularities with larger outer scales focus the bigger portion of their energy in the low frequencies, so they can be resolved in higher SNR scenarios with a narrower filter. Due to the $\vec{B} \cdot \hat{k}$ latitude dependence, using the FR to correct for phase errors or directly measure TEC also leads to considerable errors due to the noise scaling toward the equator.

The performance of the phase estimation using the MDA is limited by the block sizes and overlapping factors (that define the new sampling grid and the aliasing introduced in the spectrum of the solution). The contrast and content of the image play an essential role in the accuracy of the estimation of the shift between sublooks, which, as discussed for the case of split-band interferometry [29], is better estimated with larger block sizes at the expense of a loss in resolution due to block averaging. In addition, the fact that the measurements are not of absolute phase but of a second derivative map that has to be integrated imposes that the performance of the MDA also depends on the capability of the integrator (e.g., the WLS discussed in this article) to disregard outliers and dampen random walks. The errors in the estimation of the second derivative cannot be globally characterized since they depend on the contrast and content of each block. Moreover, the statistics of the developed random walks cannot be described with notions of stationary fields.

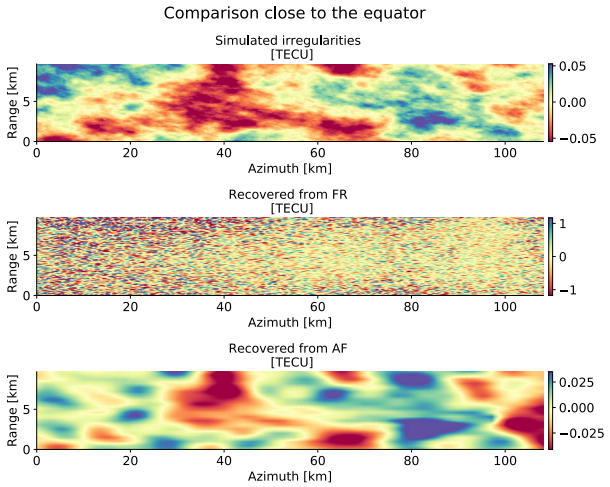

Fig. 18. Recovery of ionospheric irregularity maps closer to the equator. TEC map (top), recovered from FR (middle) and AF (bottom).

To compare the performance of both methods, we focus on the phase screen recovery (take the scenario in Fig. 1 as an example). The errors in the estimation of the FR discussed in Section III (for the 10- and 20-dB SNR cases) are scaled to phase with the corresponding $\vec{B} \cdot \hat{k}$ for different latitudes along the prime meridian. The curves in Fig. 17 show the standard deviation of the residual phase error after scaling from FR. Note that the performance rapidly decreases toward the equator. The green dashed line shows the standard deviation of the residual phase after applying the AF algorithm on Fig. 4, which is not latitude-dependent. Below around 50° for an SNR = 10 dB and 30° for an SNR = 20 dB the AF is expected to perform better.

For example, Fig. 18 shows the result for the simulation parameters in Table III and moving the simulation closer to the equator. Here, the irregularities are more aligned to the azimuth direction, and the AF can still recover their structure, opposite to when the estimation is based on the FR. Based on the FR, applying any phase correction would not be possible in such a case, so image restoration is only possible with the AF.

VI. Conclusion

Low-frequency SARs offer an exceptional possibility to obtain ionospheric maps with spatial resolutions significantly better than other systems (such as GNSS receivers). As part of the ionospheric calibration, Biomass produces ionospheric irregularity maps with resolutions of hundreds of meters or a couple of kilometers, depending on the algorithm used and its sensitivity. In addition, these maps can be generated covering similar latitudes within less than two hours. Despite its limitations, due to its sensitivity, the ionospheric Biomass products are expected to reinforce current areas of research and work in synergy with any other ionospheric sensing approach. At this point, we highlight the importance of small-scale irregularity sensitivity, which poses a challenge in terms of calibration but is highly valuable for the scientific community.

In this study, we have provided an analytical description of the errors expected in Biomass ionospheric images. These

were then compared to the results obtained using data simulated and processed with the Biomass simulator and prototype processors. We focused on two calibration approaches: one based on the estimation of the FR and one with an MDA. The errors from the FR approach come mainly from the high-frequency component of the ionospheric irregularities that are not captured by the calibration bandwidth. We demonstrated that the spatial resolution can be maintained to a few kilometers depending on the sensitivity. The errors from the MDA calibration approach, on the other hand, are mainly due to block averaging, sampling (which introduces aliasing in the frequency domain), and interpolation operations. We also addressed the issue with the random walks during the double integration and showed that they can be significantly reduced with a WLS integrator.

The scenario studied close to the pole shows a better performance of the FR than the MDA; however, one needs to account for the fact that good FR sensitivity is not always warranted. For this reason, the calibration of Biomass products shall be complemented by an AF algorithm when required. Sample cases arise when approaching the equatorial gap or when the strength of the irregularities is low compared to the SNR. The method described in this article can be extended to provide a global sensitivity analysis and characterization of Biomass ionospheric images, which will be the subject of subsequent research.

This article mainly focused on the filtering operations that make the calibration algorithms. In addition, one needs to account for error in other calibration steps (such as the antenna pattern compensation), and other system and model uncertainties. To complement this aspect, we carried out a sensitivity analysis when estimating the TEC from the FR based on the uncertainties in the geomagnetic field present in the IGRF. The uncertainty in the geomagnetic field vector introduces errors in the transformation from FR to TEC and phase, which are nonnegligible and the spatial structure of the uncertainly at a global scale depends on the Earth's magnetic field. The approach is based on error propagation with partial derivatives to analyze the contribution of each variable, and it can be extended to the rest of the variables in the system. This part of the discussion showed yet another factor to take into account when using the FR as a proxy for ionospheric estimation as its geographical limitations. Methods based on the phase error estimation have other difficulties but are not dependent on the $\vec{B} \cdot \hat{k}$ product. For this reason, we emphasize that both approaches should be complementary.

All this contributes to the understanding of error characteristics in terms of standard deviation and puts focus on the structure. This article is intended for the user to interpret different ionospheric calibrations and retrieval error sources. This knowledge will be relevant when using the provided ionospheric maps for applications such as ionospheric state characterization or scintillation model validation.

REFERENCES

[1] X. Pi, A. J. Mannucci, U. J. Lindqwister, and C. M. Ho, "Monitoring of global ionospheric irregularities using the worldwide GPS network," *Geophys. Res. Lett.*, vol. 24, no. 18, pp. 2283–2286, Sep. 1997, doi: 10.1029/97gl02273.

[2] C. T. Nguyen, S. T. Oluwadare, N. T. Le, M. Alizadeh, J. Wickert, and H. Schuh, "Spatial and temporal distributions of ionospheric irregularities derived from regional and global ROTI maps," *Remote Sens.*, vol. 14, no. 1, p. 10, Dec. 2021, doi: 10.3390/rs14010010.

[3] S. Basu, K. M. Groves, J. M. Quinn, and P. Doherty, "A comparison of TEC fluctuations and scintillations at ascension island," *J. Atmos. Solar-Terr. Phys.*, vol. 61, no. 16, pp. 1219–1226, Nov. 1999, doi: 10.1016/S1364-6826(99)00052-8.

[4] G. S. Bust and C. N. Mitchell, "History, current state, and future directions of ionospheric imaging," *Rev. Geophys.*, vol. 46, no. 1, pp. 1–23, Mar. 2008, doi: 10.1029/2006rg000212.

[5] ESA, "Report for mission selection: Biomass," European Space Agency (ESA), Noordwijk, The Netherlands, Tech. Rep. ESA SP-13214/1), Nov. 2012. [Online]. Available: https://earth.esa.int/eogateway/documents/20142/37627/BIOMASSReport-for-Mission-Selection-An-Earth-Explorer-to-observe-forestbiomass.pdf

[6] A. Moreira, P. Prats-Iraola, M. Younis, G. Krieger, I. Hajnsek, and K. P. Papathanassiou, "A tutorial on synthetic aperture radar," *IEEE Geosci. Remote Sens. Mag.*, vol. 1, no. 1, pp. 6–43, Mar. 2013, doi: 10.1109/MGRS.2013.2248301.

[7] L. Alfonsi et al., "Analysis of the regional ionosphere at low latitudes in support of the biomass ESA mission," *IEEE Trans. Geosci. Remote Sens.*, vol. 56, no. 11, pp. 6412–6424, Nov. 2018, doi: 10.1109/TGRS.2018.2838321.

[8] J. S. Kim, K. P. Papathanassiou, R. Scheiber, and S. Quegan, "Correcting distortion of polarimetric SAR data induced by ionospheric scintillation," *IEEE Trans. Geosci. Remote Sens.*, vol. 53, no. 12, pp. 6319–6335, Dec. 2015, doi: 10.1109/TGRS.2015.2431856.

[9] V. Gracheva, J. S. Kim, P. Prats-Iraola, R. Scheiber, and M. Rodriguez-Cassola, "Combined estimation of ionospheric effects in SAR images exploiting Faraday rotation and autofocus," *IEEE Geosci. Remote Sens. Lett.*, vol. 19, pp. 1–5, 2022, doi: 10.1109/LGRS.2021.3102597.

[10] M. I. Skolnik, "Introduction to radar," in *Radar Handbook*, vol. 2. New York, NY, USA: McGraw-Hill, 1962, p. 21.

[11] C. L. Rino, "On the application of phase screen models to the interpretation of ionospheric scintillation data," *Radio Sci.*, vol. 17, no. 4, pp. 855–867, Jul. 1982, doi: 10.1029/RS017i004p00855.

[12] G. Gomba, F. Rodríguez González, and F. De Zan, "Ionospheric phase screen compensation for the Sentinel-1 Tops and ALOS-2 ScanSAR modes," *IEEE Trans. Geosci. Remote Sens.*, vol. 55, no. 1, pp. 223–235, Jan. 2017, doi: 10.1109/TGRS.2016.2604461.

[13] C. L. Rino, "A power law phase screen model for ionospheric scintillation: 1. weak scatter," *Radio Sci.*, vol. 14, no. 6, pp. 1135–1145, Nov. 1979, doi: 10.1029/RS014i006p01135.

[14] C. S. Carrano, K. M. Groves, and R. G. Caton, "Simulating the impacts of ionospheric scintillation on l band SAR image formation," *Radio Sci.*, vol. 47, no. 4, pp. 1–14, Aug. 2012, doi: 10.1029/2011RS004956.

[15] C. Rino, *The Theory of Scintillation With Applications in Remote Sensing*. Hoboken, NJ, USA: Wiley, 2011, doi: 10.1002/9781118010211.

[16] J. A. Secan, R. M. Bussey, E. J. Fremouw, and S. Basu, "An improved model of equatorial scintillation," *Radio Sci.*, vol. 30, no. 3, pp. 607–617, May 1995, doi: 10.1029/94RS03172.

[17] G. Gomba and F. De Zan, "Bayesian data combination for the estimation of ionospheric effects in SAR interferograms," *IEEE Trans. Geosci. Remote Sens.*, vol. 55, no. 11, pp. 6582–6593, Nov. 2017.

[18] S. Ji, W. Chen, X. Ding, and C. Zhao, "Equatorial ionospheric zonal drift by monitoring local GPS reference networks," *J. Geophys. Res., Space Phys.*, vol. 116, no. A8, pp. 1–17, 2011, doi: 10.1029/2010JA015993.

[19] M. J. Sanjuan-Ferrer et al., "End-to-end performance simulator for the BIOMASS mission," in *Proc. 12th Eur. Conf. Synth. Aperture Radar (EUSAR)*, Jun. 2018, pp. 1–5. [Online]. Available: https://ieeexplore.ieee.org/abstract/document/8438196

[20] P. Prats-Iraola et al., "The BIOMASS ground processor prototype: An overview," in *Proc. 12th Eur. Conf. Synth. Aperture Radar (EUSAR)*, Jun. 2018, pp. 1–6. [Online]. Available: https://ieeexplore.ieee.org/document/8438145

[21] F. Betancourt-Payan, M. Rodriguez-Cassola, A. Benedikter, P. Prats-Iraola, and G. Krieger, "An autofocus algorithm for the recovery of ionospheric phase signatures in the biomass mission," in *Proc. 14th Eur. Conf. Synth. Aperture Radar (EUSAR)*, Jul. 2022, pp. 1–5. [Online]. Available: https://ieeexplore.ieee.org/document/9944332

[22] W. Carrara, R. Goodman, and R. Majewski, *Spotlight Synthetic Aperture Radar: Signal Processing Algorithms*. Norwood, MA, USA: Artech House, 1995. [Online]. Available: https://books.google.de/books?id=uztiQgAACAAJ

[23] S. H. Bickel and R. H. T. Bates, "Effects of magneto-ionic propagation on the polarization scattering matrix," *Proc. IEEE*, vol. 53, no. 8, pp. 1089–1091, Aug. 1965, doi: 10.1109/proc.1965.4097.

[24] A. Freeman, "Calibration of linearly polarized polarimetric SAR data subject to Faraday rotation," *IEEE Trans. Geosci. Remote Sens.*, vol. 42, no. 8, pp. 1617–1624, Aug. 2004, doi: 10.1109/TGRS.2004.830161.

[25] R. F. Hanssen, *Radar Interferometry: Data Interpretation and Error Analysis*, vol. 2. Cham, Switzerland: Springer, 2001, doi: 10.1007/0-306-47633-9.

[26] C. D. Beggan, "Evidence-based uncertainty estimates for the international geomagnetic reference field," *Earth, Planets Space*, vol. 74, no. 1, pp. 1–11, Dec. 2022, doi: 10.1186/s40623-022-01572-y.

[27] H. H. Ku, "Notes on the use of propagation of error formulas," *J. Res. Nat. Bur. Standards, Sect. C, Eng. Instrum.*, vol. 70C, no. 4, pp. 263–273, Oct. 1966, doi: 10.6028/jres.070c.025.

[28] S. Schaer, W. Gurtner, and J. Feltens, "IONEX: The ionosphere map exchange format version 1," in *Proc. IGS AC Workshop*, Darmstadt, Germany, 1998, vol. 9, no. 11. [Online]. Available: http://ftp.aiub.unibe.ch/ionex/draft/ionex11.pdf

[29] R. Bamler and M. Eineder, "Accuracy of differential shift estimation by correlation and split-bandwidth interferometry for wideband and Delta-k SAR systems," *IEEE Geosci. Remote Sens. Lett.*, vol. 2, no. 2, pp. 151–155, Apr. 2005, doi: 10.1109/LGRS.2004.843203.

Felipe Betancourt-Payan (Graduate Student Member, IEEE) was born in Armenia, Quindio, Colombia, in 1993. He received the bachelor's degree in aerospace engineering from Carlos III University, Madrid, Spain, in 2017, and the master's degree in space science and technology (SpaceMaster) from Luleå University of Technology, Luleå, Sweden, and Universite Toulouse III-Paul Sabatier, Toulouse, France, in 2019. He is currently pursuing the Ph.D. degree with the German Aerospace Center (DLR-HR), Weßling, Germany.

Since 2019, he has been with the Microwaves and Radar Institute, German Aerospace Center (DLR-HR). His research interests include using autofocus techniques for ionospheric correction and retrieving ionospheric parameters from low-frequency synthetic aperture radar (SAR) images.

Marc Rodriguez-Cassola was born in Barcelona, Spain, in 1977. He received the Ingeniero degree in telecommunication engineering from the Universidad Publica de Navarra, Pamplona, Spain, in 2000, the Licenciado (M.Sc.) degree in economics from the Universidad Nacional de Educacion a Distancia, Madrid, Spain, in 2012, and the Ph.D. degree in electrical engineering from Karlsruhe Institute of Technology, Karlsruhe, Germany, in 2012.

From 2000 to 2001, he was a Radar Hardware Engineer with the Study Center of Terrestrial and Planetary Environments (CETP)/French National Center for Scientific Research (CNRS), Saint-Maur-des-Fossés, France. From 2001 to 2003, he was a Software Engineer with Altran Consulting, Munich, Germany. Since 2003, he has been with the Microwaves and Radar Institute, German Aerospace Center, Weßling, Germany, where he is leading the SAR Missions Group. His research interests include radar signal processing, synthetic aperture radar (SAR) end-to-end simulation, SAR processing and calibration algorithms, crisis theory, and radar mission analysis and applications.

Pau Prats-Iraola (Fellow, IEEE) was born in Madrid, Spain, in 1977. He received the Ingeniero and Ph.D. degrees in telecommunications engineering from the Universitat Politècnica de Catalunya (UPC), Barcelona, Spain, in 2001 and 2006, respectively.

In 2001, he joined the Institute of Geomatics, Barcelona, as a Research Assistant. In 2002, he joined the Department of Signal Theory and Communications, UPC, where he worked in the field of airborne repeat-pass interferometry and airborne differential synthetic aperture radar (SAR) interferometry. From December 2002 to August 2006, he was an Assistant Professor with the Department of Telecommunications and Systems Engineering, Universitat Autònoma de Barcelona, Barcelona. In 2006, he joined the Microwaves and Radar Institute, German Aerospace Center (DLR), Weßling, Germany, where he has been the Head of the Multimodal Algorithms Group, since 2009. He is the responsible and a Main Developer of the TanDEM-X interferometric (TAXI) processor, an end-to-end processing chain for data acquired by the TerraSAR-X and TanDEM-X satellites, which has been used to demonstrate novel SAR acquisition modes and techniques. He is currently involved in the design and implementation of ground processor prototypes and end-to-end simulators of ESA's BIOMASS and ROSE-L missions. His research interests include high-resolution airborne/spaceborne monostatic/bistatic SAR processing, SAR interferometry, advanced interferometric acquisition modes, persistent scatterer interferometry (PSI), SAR tomography, and end-to-end SAR simulation. He has co-authored more than 60 peer-reviewed journal articles in these fields.

Gerhard Krieger (Fellow, IEEE) received the Dipl.-Ing. (M.S.) and Dr.-Ing. (Ph.D.) (Hons.) degrees in electrical and communication engineering from the Technical University of Munich, Munich, Germany, in 1992 and 1999, respectively.

From 1992 to 1999, he was with Ludwig Maximilians University, Munich, where he conducted multidisciplinary research on neuronal modeling and nonlinear information processing in biological and technical vision systems. Since 1999, he has been with the Microwaves and Radar Institute, German Aerospace Center (DLR), Weßling, Germany, where he started as a Research Associate, developing signal processing algorithms for a novel forward-looking radar system employing digital beamforming on receive. From 2001 to 2007, he led the New SAR Missions Group, Wessling, which pioneered the development of advanced bistatic and multistatic radar systems, such as TanDEM-X, as well as innovative multichannel synthetic aperture radar (SAR) techniques and algorithms for high-resolution wide-swath SAR imaging. Since 2008, he has been the Head of the Radar Concepts Department, Wessling, which hosts about 40 scientists focusing on new SAR techniques, missions, and applications. He has been serving as a Mission Engineer for TanDEM-X, and he also made major contributions to the development of the Tandem-L mission concept, where he led the Phase-0 and Phase-A studies. Since 2019, he has also been holding a professorship at Friedrich-Alexander University Erlangen–Nuremberg (FAU), Erlangen, Germany. He has authored or co-authored more than 100 peer-reviewed journal articles, nine invited book chapters, and more than 400 conference papers, and holds more than 20 patents.

Prof. Krieger has been an Associate Editor of IEEE TRANSACTIONS ON GEOSCIENCE AND REMOTE SENSING since 2012. In 2014, he served as the Technical Program Chair for the European Conference on SAR and a Guest Editor for IEEE JOURNAL OF SELECTED TOPICS IN APPLIED EARTH OBSERVATIONS AND REMOTE SENSING. He received several national and international awards, including two best paper awards at the European Conference on SAR, two transactions prize paper awards from the IEEE Geoscience and Remote Sensing Society, and the W.R.G. Baker Prize Paper Award from the IEEE Board of Directors.

E

Estimating the Ionospheric Height from Amplitude Scintillation Signatures in SAR Images.

Estimating Ionospheric Height From Amplitude Scintillation Signatures in SAR Images

Felipe Betancourt-Payan, *Graduate Student Member, IEEE*, Jun Su Kim, *Member, IEEE*, Konstantinos P. Papathanassiou, *Fellow, IEEE*, Marc Rodriguez-Cassola, and Gerhard Krieger, *Fellow, IEEE*

***Abstract*— In this letter, we discuss the estimation of the location of ionospheric irregularities exploiting the appearance of intensity scintillations in ALOS-2 images, as they are semifocused at different heights. The intensity scintillations (stripes) are not always visible in the single-look complex (SLC) images. However, they start to be visible, as the image is semifocused at different heights with a peak of contrast where electron density irregularities are found (ionospheric height). The slant range between the satellite and the ionospheric plane can be estimated and converted directly into the ionospheric height by autofocusing the stripes. The observations show good agreement with the height of maximum ionization estimated by the International Reference Ionosphere (IRI). Furthermore, we perform an alternative geometric validation based on feature tracking by comparing the shifts between azimuth sublooks. With both methods for the presented dataset, the height of the ionospheric irregularities was estimated to be 330 km.**

***Index Terms*— Intensity scintillation, ionosphere, synthetic aperture radar (SAR).**

I. Introduction

LOW-FREQUENCY synthetic aperture radar (SAR) images are affected by the two-way passage of the radar waves through the ionosphere in different ways (phase errors, delays, Faraday rotation, and scintillation) [1], [2]. All these effects are related to the total electron content (TEC) and its spatial variation. The TEC has a background component that changes slowly and a turbulent component made of electron density irregularities with outer scales as small as a few kilometers [3], [4], [5]. These irregularities are mostly found within the F2 layer of the ionosphere, the region of maximum ionization that extends approximately between 200 and 400 km. Ionospheric irregularities form in a narrow region within this layer that, in practice, will be approximated to a thin layer at the so-called ionospheric height h_{iono} [6], [7], [8]. It should be emphasized that this height is not necessarily the height of maximum background ionization.

Turbulent irregularities are typical in equatorial and polar latitudes [9]. Around the equator, the irregularities are elongated blobs or bubbles [10] that can produce scintillation. Scintillations are rapid phase variations added to the SAR data that, when not compensated, produce defocusing [2]. The diffraction experienced by the radar waves as they exit the irregular phase modulation inside the ionosphere and further propagate in nearly free space [7], [11], [12], [13] can also produce intensity scintillation patterns. These are commonly seen as elongated intensity stripes aligned to the geomagnetic field direction as found in ALOS images in equatorial regions [14], [15], [16].

The intensity scintillation will not always be visible in the focused images if the geomagnetic field is not aligned with the azimuth direction. The reason for this is that the ionosphere is between the satellite and the ground, so the stripe pattern is smeared by the processing of the synthetic aperture [17]. This letter proposes a method to estimate the height at which the ionospheric irregularities are located directly from the data based on the observation of amplitude scintillation when semifocusing the image at different heights [18]. By semifocusing, the azimuth matched filter parameters are adapted to gain resolution at different slant ranges (other than the one from the satellite to the targets on ground) and autofocus the ionospheric features. The slant range from the satellite to the ionosphere and the ionospheric height can be extracted from the derived azimuth matched filter.

The ionospheric height estimation by semifocusing is compared with the one obtained by exploring feature tracking in azimuth sublooks. When separating one sub-band of the azimuth spectrum, it is as if a smaller synthetic aperture was processed. Then, one loses resolution in the image on the ground, but it enables detection and tracking of amplitude scintillations. With a geometric inversion, one can also estimate the ionospheric height.

Estimates of the height of maximum ionization can be obtained from models, such as NeQuick [19] and International Reference Ionosphere (IRI) [20], based on the electron density profiles. The models focus on the background component of the ionosphere, and the height of maximum ionization is not exactly the height where irregularities are found. In addition, to circumvent the model limitations, it is preferred to estimate the location of the irregularities directly from the data. In the polar regions, where good Faraday rotation sensitivity is given, it is possible to estimate the ionospheric height from the fully polarimetric data using a parallax between the Faraday rotation azimuth sublooks [18]. The Faraday rotation parallax does not work well closer to the equator, where the Faraday rotation

Manuscript received 19 March 2024; revised 24 June 2024; accepted 16 July 2024. Date of publication 19 July 2024; date of current version 31 July 2024. This work was supported by German Academic Exchange Service (DAAD) under Grant 57478193. *(Corresponding author: Felipe Betancourt-Payan.)*

The authors are with the Microwaves and Radar Institute, German Aerospace Center (DLR), 82234 Weßling, Germany (e-mail: felipe.betancourtpayan@dlr.de).

Digital Object Identifier 10.1109/LGRS.2024.3431023

sensitivity is low. On the other hand, the method proposed in this letter uses the intensity scintillation signature in single images and is polarization-independent. Because of the high anisotropic nature of equatorial irregularities, this method is meant to be exploited in low latitudes.

Section II describes the observations and method used to process the data. In Section III, the height inversion method is shown to validate the observations geometrically. Finally, Section IV summarizes the findings.

II. Amplitude Scintillation in Semifocused Images

Fig. 1 shows a simplified version of the SAR observation geometry, including the ionosphere. The platform moves along the x-axis and the y-axis points in the slant range direction, with the slant range to a given range bin R_0. The platform flies at the height of h_{sat}. The plane where the irregularities form (ionospheric plane) is located between the satellite and the ground at a height h_{iono}, and the slant ranges to the satellite and ground are R_{iono} and R'_{iono}, respectively. Even if a flat Earth and rectilinear motion geometry are shown in Fig. 1, the Earth's ellipsoid and exact orbit available in the dataset are considered in the following. However, it is always straightforward to relate h_{iono} to R_{iono} or R'_{iono}.

Semifocusing SAR images at h_{iono} is a well-known practice to inject and correct for ionospheric effects, such as phase advance and Faraday rotation [8], [18], of the turbulent ionosphere. By doing so, the resolution at which the ionospheric disturbances are visible is only limited by the azimuth and range bandwidths. Semifocusing can be done by modifying the slant range either to the ground or to the ionospheric plane from the satellite orbit, R, and the corresponding effective velocity, v, in the azimuth matched filter

$$H_{\text{ac}}(f_a, R) = \exp\left[j \cdot \frac{4 \cdot \pi \cdot R}{\lambda}(\zeta(f_a) - 1)\right] \tag{1}$$

with

$$\zeta(f_a) = \sqrt{1 - \left(\frac{f_a \cdot \lambda}{2 \cdot v}\right)^2}$$

where f_a is the azimuth frequency and λ is carrier wavelength. A detailed explanation can be found in [18].

Starting from the range compressed data, when compressing at any height other than h_{iono}, the contribution of ionospheric resolution cell spreads into the neighboring image resolution cells. Consequently, if the image is focused on the ground, the ionospheric signatures of phase delay, Faraday rotation, and amplitude scintillation are smeared by an averaging along azimuth. The size of the averaging window is the one of the synthetic apertures projected on the ionospheric plane. The smearing becomes less apparent for highly anisotropic irregularities aligned to the azimuth direction [21].

Fig. 2 summarizes the processing steps. Our starting point is the full-polarimetric set of single-look complex (SLC) images of ALOS-2 (ALOS2050060000) without apparent amplitude modulation, together with the orbit and scene coordinates. We also choose an initial value for the irregularity height, which is used to calculate the slant range between the satellite orbit and the ionospheric coordinates. The parameters of the

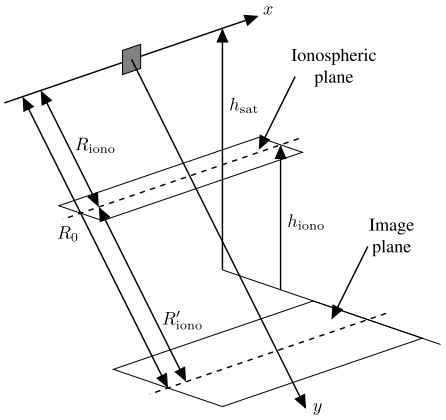

Fig. 1. Simplified SAR observation geometry.

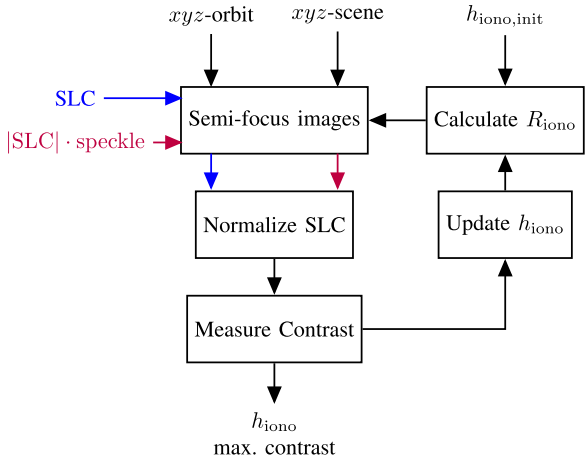

Fig. 2. Algorithm block diagram.

dataset used in our investigation are summarized in Table I. Fig. 3 shows the SLC of the HV channel (amplitude scintillation is better seen in the cross-pol channels of the current dataset, but they are indeed present in all other channels too). As the SLC images are semifocused at different ionospheric heights, stripe-like patterns start to appear, as shown in Fig. 4. Note that the stripes follow the geomagnetic field projected on the image plane (white line), which is off the azimuth direction, and the ionospheric signature appears superimposed on the azimuth defocusing of the scene.

For a better characterization of the stripes, it is necessary to normalize and remove the background scene component. A logical way to obtain semifocused images without the background component is to normalize with the amplitude of a semifocused image without phase modulation introduced by the ionosphere. This was obtained by taking the amplitude of the SLC images and adding multiplicative complex speckle. Hence, the phase modulation goes away, but the amplitude image bandwidth expands and can be decompressed with the matched filter. Fig. 5 shows the normalized HV images semifocused at different ionospheric heights. Note the different levels of contrast or sharpness of the stripes.

As shown in Fig. 6, an iterative autofocus approach can be used to update the h_{iono} value and estimate the R_{iono} for which the intensity stripes have maximum contrast and invert

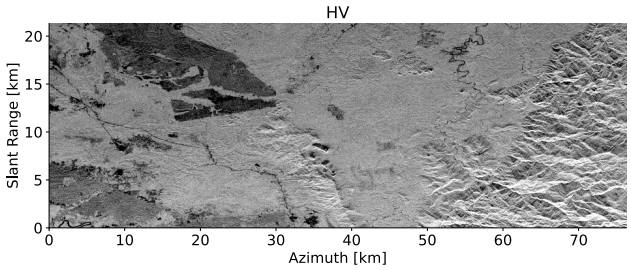

Fig. 3. SLC intensity of the HV channel of an ALOS-2 image. The forest scene is located in Indonesia, very close to the geomagnetic equator.

TABLE I
OBSERVATION PARAMETERS OF THE ALOS2050060000 DATASET

Parameter	Unit	Value
Coordinates center image (lon, lat)	(deg, deg)	(116, 0.63)
Date	YYYY/MM/DD	2015/04/27
Time	hh:mm:ss	16:26:33
Pulse repetition frequency (PRF)	Hz	2320.8627
Incidence angle (θ_{inc})	deg	31.086
Azimuth oversampling (aosf)	-	0.3888
Satellite height (h_{sat})	km	634.285
Range to ground (R_0)	km	728.84
Doppler rate (K_{t})	Hz/s	-607.08432
Central frequency (f_0)	GHz	1.2575

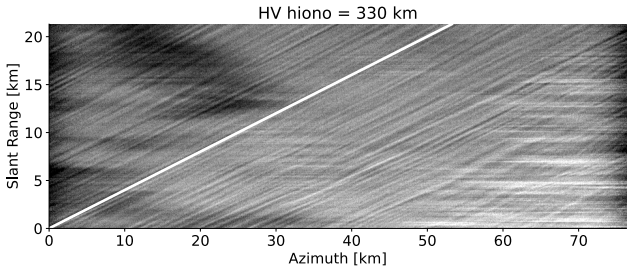

Fig. 4. Non-normalized SLC image semifocused images at 330 km. The white line shows the geomagnetic field projected on the image planes.

for h_{iono}. The best-performing contrast metric for this task was the variance of the gray level [22]. In this case, an ionospheric height of 330 km is estimated with the current method and is compared with the height of maximum ionization in the F2 layer (hmF2) according to the IRI model. Note that models like the IRI present drawbacks, such as limited precision, coarse resolution, and only focus on the background ionosphere. However, due to the high resolution of SAR, we are sensitive to lower scale variations, and even under the thin layer approximation, instead of the height of maximum ionization, we are interested in the height that better represents the location of the irregularities. For this reason, even though the models are a good starting point in practice, it is essential to rely on direct estimations.

III. GEOMETRIC VALIDATION

The ionospheric height estimation can be validated geometrically using azimuth sublooks. The principle is based on the fact that anything at a height different from the (semi-)focused image will appear to shift from the beam center while taking azimuth sub-bands. It is possible to look at it

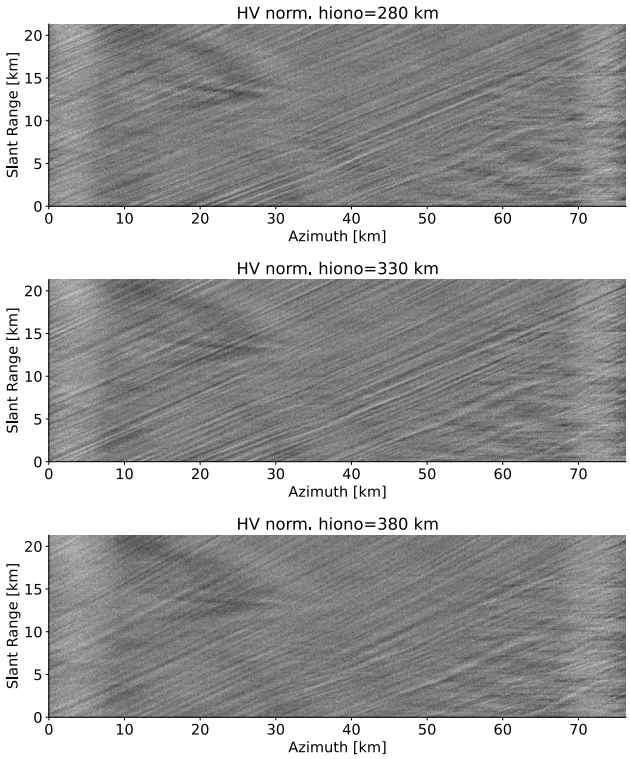

Fig. 5. Normalized SLC semifocused at different ionospheric heights: 280 km (top), 330 km (middle), and 380 km (bottom).

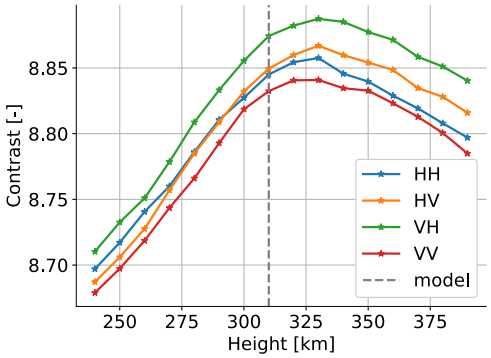

Fig. 6. Stripe contrast change with ionospheric height. As a reference, the height of maximum ionization of the F2 layer, as taken from the IRI model, is indicated by a vertical dashed line.

like this: when the image is fully focused (on ground), the ionosphere is defocused in azimuth by a quadratic phase error

$$\phi_\epsilon\left(R'_{\text{iono}};\, f_a\right) = \frac{4\cdot\pi\cdot R'_{\text{iono}}}{\lambda}\cdot\zeta(f_a) \tag{2}$$

and R'_{iono} can be inverted from azimuth-sublook cross correlation, similar to what would be done in a map-drift autofocus [23]. Here, the quadratic error across the whole image is constant, and many sublooks are taken instead of operating by blocks.

We start from the SLC images and take 32 nonoverlapping azimuth sublooks (the added sublook bandwidths extend to the image azimuth bandwidth). As an example, the amplitude of one of the sublooks is shown in Fig. 7, which has been normalized with the mean amplitude value of all other sublooks to remove the background scene component. Here, the amplitude

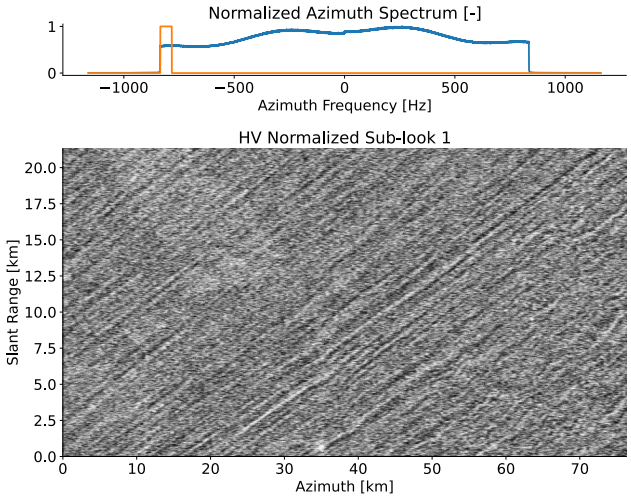

Fig. 7. Stripe pattern in an amplitude image of a normalized sublook, 1/32th of azimuth bandwidth.

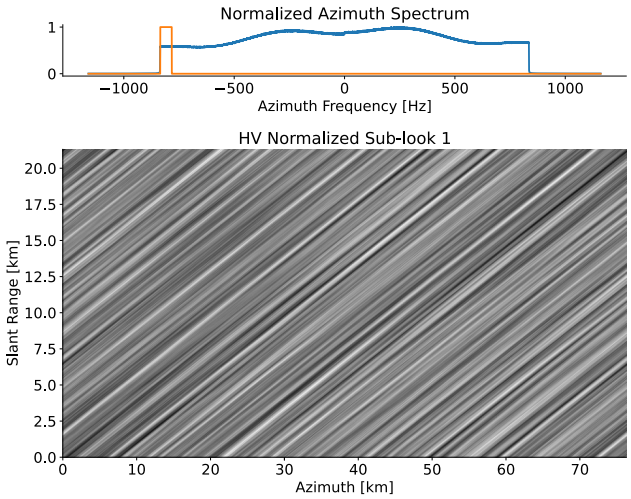

Fig. 8. Normalized sublook after a 10-pixel directional averaging along the geomagnetic field line.

stripes clearly appear, because, at the expense of lowering the resolution of the SLC image, the resolution of the ionosphere irregularities is increased by the shorter processed synthetic aperture [17]. By taking different sublooks, the feature drifts along azimuth and by tracking it, it is possible to invert for R'_{iono} and again for h_{iono}. Another method to take into consideration for the separation of the stripe pattern is the bandpass filtering in the direction of the geomagnetic field, as described in [24].

It was necessary to preprocess the data with an averaging filter oriented in the geomagnetic field to improve the accuracy in estimating along the drift between normalized sublooks. See the averaged data in Fig. 8.

It is known that due to the azimuth frequency to squint-angle relation [25], one can relate any azimuth frequency, f_a, to a corresponding squint angle off the zero Doppler, β_a

$$\sin(\beta_a) = \frac{\lambda \cdot f_a}{2 \cdot v}. \tag{3}$$

With R'_{iono} being the slant range from the ground to the ionospheric plane, the drift of the ionospheric pattern between

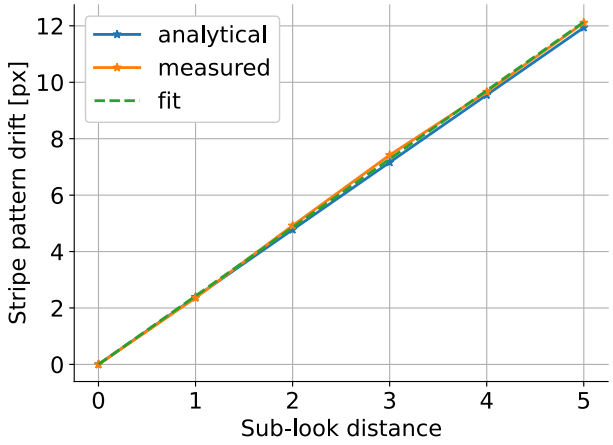

Fig. 9. Scintillation pattern drift estimated from azimuth sublooks that are separated by up to five consecutive nonoverlapping sublooks.

two consecutive sublooks with center frequencies $f_{a,1}$ and $f_{a,2}$ can be approximated to

$$\Delta x = R'_{\text{iono}} \cdot \left(\tan\left(\beta_{a,2}\right) - \tan\left(\beta_{a,1}\right)\right) \tag{4}$$

in meters. This can be translated into pixels, Δpx, as follows:

$$\Delta\text{px} = \frac{\Delta x}{v} \cdot \Delta f. \tag{5}$$

with

$$\Delta f = \frac{\text{PRF}}{N_{\text{sl}} \cdot (1 + \text{aosf})} \tag{6}$$

and aosf the azimuth oversampling factor.

Fig. 9 shows the drift of the amplitude scintillation pattern along azimuth for sublooks separated by up to five consecutive sublooks, measured by cross correlation (no drift in range was observed). In blue, there is the expected drift as given by (5), and the measurements are in orange. Including Earth's ellipsoid, for an h_{iono} of 330 km, R'_{iono} is 381.895 km, the pixel distance between consecutive sublooks is 2.42, and the slope of the fit in green is 2.38. Note the good agreement in the slope, which points out that the altitude estimation and R'_{iono} are very similar.

IV. Conclusion

This letter presents an autofocus method for estimating the height of ionospheric irregularities at equatorial latitudes based on the analysis of intensity scintillations. The methodology is tested with an ALOS-2 dataset. In this dataset, where the geomagnetic field does not align with the trajectory, the intensity scintillations smear with the synthetic aperture and are not visible in the focused image. The ionospheric irregularities start to become visible when semifocusing the image at different heights, and the contrast is maximum at the height where the irregularities are found (assumed they extend over a narrow enough region to be approximated to a thin layer), because their resolution is maximum too. This allows the estimation of the ionospheric height directly from the data based on contrast metrics. A geometric validation was made using feature tracking in azimuth sublooks. When taking nonoverlapping azimuth sublooks and normalizing to remove the background, it is possible to see that the irregularity

features drift along azimuth. By measuring the drift, it is also possible to estimate the ionospheric height, further confirming the reliability and accuracy of our method.

It is imperative to know the ionospheric height precisely to calibrate SAR images correctly. The benefits of the methods proposed in this letter are that they do not rely on models (as shown in Section II) and that they have shown to work well even at equatorial latitude (where Faraday rotation-based methods, such as the ionospheric parallax, have low sensitivity) with single images.

REFERENCES

[1] Z.-W. Xu, J. Wu, and Z.-S. Wu, "A survey of ionospheric effects on space-based radar," *Waves Random Media*, vol. 14, no. 2, pp. S189–S273, Apr. 2004.

[2] D. P. Belcher, "Theoretical limits on SAR imposed by the ionosphere," *IET Radar, Sonar Navigat.*, vol. 2, no. 6, pp. 435–448, Dec. 2008.

[3] Y.-H. Liu, C.-H. Liu, and S.-Y. Su, "Global and seasonal scintillation morphology in the equatorial region derived from ROCSAT-1 in-situ data," *Terr., Atmos. Ocean. Sci.*, vol. 23, no. 1, pp. 95–106, 2012.

[4] S. Basu, S. Basu, and B. K. Khan, "Model of equatorial scintillations from in-situ measurements," *Radio Sci.*, vol. 11, no. 10, pp. 821–832, Oct. 1976.

[5] K. C. Yeh and C. H. Liu, "Diagnosis of the turbulent state of ionospheric plasma by propagation methods," *Radio Sci.*, vol. 12, no. 6, pp. 1031–1034, Nov. 1977.

[6] C. L. Rino, "On the application of phase screen models to the interpretation of ionospheric scintillation data," *Radio Sci.*, vol. 17, no. 4, pp. 855–867, Jul. 1982.

[7] C. S. Carrano, K. M. Groves, and R. G. Caton, "Simulating the impacts of ionospheric scintillation on L band SAR image formation," *Radio Sci.*, vol. 47, no. 4, pp. 1–14, Aug. 2012.

[8] G. Gomba, M. Eineder, A. Parizzi, and R. Bamler, "High-resolution estimation of ionospheric phase screens through semi-focusing processing," in *Proc. IEEE Geosci. Remote Sens. Symp.*, Jul. 2014, pp. 17–20.

[9] J. Aarons, "Global morphology of ionospheric scintillations," *Proc. IEEE*, vol. 70, no. 4, pp. 360–378, Apr. 1982.

[10] L. Alfonsi et al., "Analysis of the regional ionosphere at low latitudes in support of the biomass ESA mission," *IEEE Trans. Geosci. Remote Sens.*, vol. 56, no. 11, pp. 6412–6424, Nov. 2018.

[11] B. H. Briggs, "Ionospheric irregularities and radio scintillations," *Contemp. Phys.*, vol. 16, no. 5, pp. 469–488, Sep. 1975.

[12] C. Rino, *The Theory of Scintillation With Applications in Remote Sensing*. Hoboken, NJ, USA: Wiley, 2011.

[13] D. L. Knepp, "Multiple phase screen calculation of two-way spherical wave propagation in the ionosphere," *Radio Sci.*, vol. 51, no. 4, pp. 259–270, Apr. 2016.

[14] M. Shimada, Y. Muraki, and Y. Otsuka, "Discovery of anoumoulous stripes over the Amazon by the PALSAR onboard ALOS satellite," in *Proc. IEEE Int. Geosci. Remote Sens. Symp.*, Jul. 2008, pp. 387–390.

[15] D. P. Belcher and P. S. Cannon, "Amplitude scintillation effects on SAR," *IET Radar, Sonar Navigat.*, vol. 8, no. 6, pp. 658–666, Jul. 2014.

[16] H. Sato, J. S. Kim, Y. Otsuka, C. M. Wrasse, E. R. de Paula, and J. R. de Souza, "L-band synthetic aperture radar observation of ionospheric density irregularities at equatorial plasma depletion region," *Geophys. Res. Lett.*, vol. 48, no. 16, p. 2021, Aug. 2021.

[17] J. S. Kim, K. P. Papathanassiou, H. Sato, and S. Quegan, "Detection and estimation of equatorial spread F scintillations using synthetic aperture radar," *IEEE Trans. Geosci. Remote Sens.*, vol. 55, no. 12, pp. 6713–6725, Dec. 2017.

[18] J. S. Kim, K. P. Papathanassiou, R. Scheiber, and S. Quegan, "Correcting distortion of polarimetric SAR data induced by ionospheric scintillation," *IEEE Trans. Geosci. Remote Sens.*, vol. 53, no. 12, pp. 6319–6335, Dec. 2015.

[19] B. Nava, P. Coïsson, and S. M. Radicella, "A new version of the NeQuick ionosphere electron density model," *J. Atmos. Sol.-Terr. Phys.*, vol. 70, no. 15, pp. 1856–1862, Dec. 2008.

[20] D. Bilitza, "IRI the international standard for the ionosphere," *Adv. Radio Sci.*, vol. 16, pp. 1–11, Sep. 2018.

[21] F. J. Meyer, K. Chotoo, S. D. Chotoo, B. D. Huxtable, and C. S. Carrano, "The influence of equatorial scintillation on L-band SAR image quality and phase," *IEEE Trans. Geosci. Remote Sens.*, vol. 54, no. 2, pp. 869–880, Feb. 2016.

[22] B. N. Anoop, P. E. Ameenudeen, and J. Joseph, "A meta-analysis of contrast measures used for the performance evaluation of histogram equalization based image enhancement techniques," in *Proc. 9th Int. Conf. Comput., Commun. Netw. Technol. (ICCCNT)*, Jul. 2018, pp. 1–6.

[23] C. V. Jakowatz, D. E. Wahl, P. H. Eichel, D. C. Ghiglia, and P. A. Thompson, "Phase errors and autofocus in SAR imagery," in *Spotlight-Mode Synthetic Aperture Radar: A Signal Processing Approach*. Boston, MA, USA: Springer, 1996, pp. 221–271.

[24] S. Ji, W. Chen, X. Ding, and C. Zhao, "Equatorial ionospheric zonal drift by monitoring local GPS reference networks," *J. Geophys. Res., Space Phys.*, vol. 116, no. A8, Aug. 2011, Art. no. A08310.

[25] P. Prats, A. Reigber, and J. J. Mallorqui, "Topography-dependent motion compensation for repeat-pass interferometric SAR systems," *IEEE Geosci. Remote Sens. Lett.*, vol. 2, no. 2, pp. 206–210, Apr. 2005.

References

[1] Aarons, J. (1982). Global morphology of ionospheric scintillations. *Proceedings of the IEEE*, 70(4), 360–378.

[2] Afroz, R., Ng, B., Abbott, D., & Scheiber, R. (2022). Combined MAM-PCA autofocus for stripmap SAR. In *23rd International Radar Symposium (IRS)* (pp. 16–20).

[3] Alfonsi, L., Povero, G., Spogli, L., Cesaroni, C., Forte, B., Mitchell, C. N., Burston, R., Veettil, S. V., Aquino, M., Klausner, V., et al. (2018). Analysis of the regional ionosphere at low latitudes in support of the Biomass ESA mission. *IEEE Transactions on Geoscience and Remote sensing*, 56(11), 6412–6424.

[4] Alken, P., Thébault, E., Beggan, C. D., Amit, H., Aubert, J., Baerenzung, J., Bondar, T. N., Brown, W. J., Califf, S., Chambodut, A., et al. (2021). International Geomagnetic Reference Field: the thirteenth generation. *Earth, Planets and Space*, 73(49).

[5] Alshawaf, F., Hinz, S., Mayer, M., & Meyer, F. J. (2015). Constructing accurate maps of atmospheric water vapor by combining interferometric synthetic aperture radar and GNSS observations. *Journal of Geophysical Research: Atmospheres*, 120(4), 1391–1403.

[6] Appleton, E. V. (1946). Two Anomalies in the Ionosphere. *Nature*, 157(3995), 691–691.

[7] Balan, N., Liu, L., & Le, H. (2018). A brief review of equatorial ionization anomaly and ionospheric irregularities. *Earth and Planetary Physics*, 2, 257–275.

[8] Bandyopadhayay, T., Guha, A., DasGupta, A., Banerjee, P., & Bose, A. (1997). Degradation of navigational accuracy with Global Positioning System during periods of scintillation at equatorial latitudes. *Electronics Letters*, 33(12), 1010–1011.

[9] Beggan, C. D. (2022). Evidence-based uncertainty estimates for the International Geomagnetic Reference Field. *Earth, Planets and Space*, 74(1).

[10] Belcher, D. (2008). Theoretical limits on SAR imposed by the ionosphere. *IET Radar, Sonar & Navigation*, 2(6), 435–448.

[11] Belcher, D. & Rogers, N. (2009). Theory and simulation of ionospheric effects on synthetic aperture radar. *IET Radar, Sonar & Navigation*, 3(5), 541.

[12] Belcher, D. P. & Cannon, P. S. (2014). Amplitude scintillation effects on SAR. *IET Radar, Sonar & Navigation*, 8, 658–666.

[13] Berardino, P., Fornaro, G., Lanari, R., & Sansosti, E. (2001). A new algorithm for surface deformation monitoring based on small baseline differential SAR interferograms. *IEEE Transactions on geoscience and remote sensing*, 40(11), 2375–2383.

[14] Bhattacharyya, A., Basu, S., Groves, K. M., Valladares, C. E., & Sheehan, R. (2001). Dynamics of equatorial F region irregularities from spaced receiver scintillation observations. *Geophysical Research Letters*, 28, 119–122.

[15] Bilitza, D. (2001). International Reference Ionosphere 2000. *Radio Science*, 36(March), 261–275.

[16] Brcic, R., Parizzi, A., Eineder, M., Bamler, R., & Meyer, F. (2010). Estimation and compensation of ionospheric delay for SAR interferometry. In *2010 IEEE International Geoscience and Remote Sensing Symposium* (pp. 2908–2911).

[17] Briggs, B. & Parkin, I. (1963). On the variation of radio star and satellite scintillations with zenith angle. *Journal of Atmospheric and Terrestrial Physics*, 25(6), 339–366.

[18] Briggs, B. H. (1975). Ionospheric irregularities and radio scintillations. *Contemporary Physics*, 16(5), 469–488.

[19] Bruzzone, L., Bovolo, F., Carrer, L., Donini, E., & Thakur, S. (2021). STRATUS: A new mission concept for monitoring the subsurface of polar and arid regions. In *2021 IEEE International Geoscience and Remote Sensing Symposium IGARSS* (pp. 661–664).

[20] Caicoya, A. T., Pardini, M., Hajnsek, I., & Papathanassiou, K. (2015). Forest aboveground biomass estimation from vertical reflectivity profiles at L-band. *IEEE Geoscience and Remote Sensing Letters*, 12(12), 2379–2383.

[21] Calloway, T. M. (1992). *Automatic focus and registration of synthetic aperture radar images*. PhD thesis, The University of New Mexico.

[22] Camps, A., Barbosa, J., Nestoras, I., Jordão, A., Sanjuan-Ferrer, M. J., Rodriguez-Cassola, M., de Almeida, V. Q., & Betancourt-Payan, F. (2023). Updated ionospheric module for ESA Biomass mission end-to-end performance simulator. In *IGARSS 2023-2023 IEEE International Geoscience and Remote Sensing Symposium* (pp. 7673–7676).

[23] Carrano, C. S., Groves, K. M., & Caton, R. G. (2012). Simulating the impacts of ionospheric scintillation on L band SAR image formation. *Radio Science*, 47, 1–14.

[24] Carrer, L., Gerekos, C., Bovolo, F., & Bruzzone, L. (2019). Distributed radar sounder: A novel concept for subsurface investigations using sensors in formation flight. *IEEE Transactions on Geoscience and Remote Sensing*, 57, 9791–9809.

[25] Cohen, O. (2023). Earth's magnetic field protects life on Earth from radiation, but it can move, and the magnetic poles can even flip.

[26] Cumming, I. G. & Wong, F. H. (2005). *Digital Processing of Synthetic Aperture Radar Data: Algorithms and Implementation*. Artech House Publishers.

[27] Davidson, M. W. & Furnell, R. (2021). ROSE-L: Copernicus L-Band SAR Mission. In *2021 IEEE international geoscience and remote sensing symposium IGARSS* (pp. 872–873).

[28] Davies, K. (1965). *Ionospheric Radio Propagation*, volume 80. US Department of Commerce, National Bureau of Standards.

[29] De Macedo, K. A. C., Scheiber, R., & Moreira, A. (2008). An autofocus approach for residual motion errors with application to airborne repeat-pass SAR interferometry. *IEEE Transactions on Geoscience and Remote Sensing*, 46(10), 3151–3162.

[30] Dubey, S., Wahi, R., & Gwal, A. (2006). Ionospheric effects on GPS positioning. *Advances in Space Research*, 38(11), 2478–2484. Middle and Upper Atmospheres, Active Experiments, and Dusty Plasmas.

[31] Eichel, P. H. & Jakowatz, C. V. (1989). Phase-gradient algorithm as an optimal estimator of the phase derivative. *Optics letters*, 14, 1101–1103.

[32] Ferretti, A., Prati, C., & Rocca, F. (2001). Permanent scatterers in SAR interferometry. *IEEE Transactions on Geoscience and Remote Sensing*, 39(1), 8–20.

[33] Fischer, G., Jäger, M., Papathanassiou, K. P., & Hajnsek, I. (2019). Modeling the vertical backscattering distribution in the percolation zone of the Greenland Ice Sheet with SAR tomography. *IEEE Journal of Selected Topics in Applied Earth Observations and Remote Sensing*, 12(11), 4389–4405.

[34] Freeman, A., Pi, X., & Heggy, E. (2017). Radar sounding through the Earth's ionosphere at 45 MHz. *IEEE Transactions on Geoscience and Remote Sensing*, 55(10), 5833–5842.

[35] Freeman, A., Saatchi, S., Kuga, Y., & Ishamaru, A. (1998). Detection, estimation and correction of Faraday rotation in linearly polarized sar backscatter signatures.

[36] Gabriel, A. K., Goldstein, R. M., & Zebker, H. A. (1989). Mapping small elevation changes over large areas: Differential radar interferometry. *Journal of Geophysical Research: Solid Earth*, 94, 9183–9191.

[37] Giraldez, A. E. (2004). SAOCOM-1 Argentina L-band SAR mission overview. *ESA Special Publication*, 565, 27.

[38] Gomba, G., Eineder, M., Parizzi, A., & Bamler, R. (2014). High-resolution estimation of ionospheric phase screens through semi-focusing processing. In *2014 IEEE Geoscience and Remote Sensing Symposium* (pp. 17–20).

[39] Gomba, G., González, F. R., & Zan, F. D. (2016a). Ionospheric phase screen compensation for the Sentinel-1 TOPS and ALOS-2 ScanSAR modes. *IEEE Transactions on Geoscience and Remote Sensing*, 55, 223–235.

[40] Gomba, G., Parizzi, A., Zan, F. D., Eineder, M., & Bamler, R. (2015). Toward operational compensation of ionospheric effects in SAR interferograms: The split-spectrum method. *IEEE Transactions on Geoscience and Remote Sensing*, 54, 1446–1461.

[41] Gomba, G. & Zan, F. D. (2015). Estimation of ionospheric height variations during an aurora event using multiple semi-focusing levels. In *2015 IEEE International Geoscience and Remote Sensing Symposium (IGARSS)* (pp. 4065–4068).

[42] Gomba, G. & Zan, F. D. (2017). Bayesian data combination for the estimation of ionospheric effects in SAR interferograms. *IEEE Transactions on Geoscience and Remote Sensing*, 55, 6582–6593.

[43] Gomba, G., Zan, F. D., & Parizzi, A. (2016b). Ionospheric phase screen and ionospheric azimuth shift estimation combining the split-spectrum and multi-squint methods. In *Proceedings of EUSAR 2016: 11th European Conference on Synthetic Aperture Radar*.

[44] Gracheva, V., Kim, J. S., Prats-Iraola, P., Scheiber, R., & Rodriguez-Cassola, M. (2021). Combined estimation of ionospheric effects in SAR images exploiting Faraday rotation and autofocus. *IEEE Geoscience and Remote Sensing Letters*, 19.

[45] Hajnsek, I. & Desnos, Y.-L. (2021). *Polarimetric Synthetic Aperture Radar: Principles and Application*. Springer International Publishing.

[46] Hajnsek, I., Kugler, F., Lee, S.-K., & Papathanassiou, K. P. (2009). Tropical-forest-parameter estimation by means of Pol-InSAR: The INDREX-II campaign. *IEEE transactions on Geoscience and Remote Sensing*, 47(2), 481–493.

[47] Hanssen, R. F. (2001). *Radar Interferometry: Data Interpretation and Error Analysis*. Springer Netherlands.

[48] Hawkins, B., Michel, T., & Hensley, S. (2020). Residual motion estimation for multi-squint airborne SAR. In *IGARSS 2020 - 2020 IEEE International Geoscience and Remote Sensing Symposium* (pp. 6162–6165).

[49] Hernández-Pajares, M., Juan, J., & Sanz, J. (1999). New approaches in global ionospheric determination using ground GPS data. *Journal of Atmospheric and Solar-Terrestrial Physics*, 61(16), 1237–1247.

[50] Jakowatz, C. V., Wahl, D. E., Eichel, P. H., Ghiglia, D. C., & Thompson, P. A. (1996). *Spotlight-mode Synthetic Aperture Radar: A Signal Processing Approach*. Kluwer Academic.

[51] Ji, Y., Dong, Z., Zhang, Y., Tang, F., Mao, W., Zhao, H., Xu, Z., Zhang, Q., Zhao, B., & Gao, H. (2024). Equatorial Ionospheric Scintillation Measurement in Advanced Land Observing Satellite (ALOS) Phased Array-Type L-Band Synthetic Aperture Radar (PALSAR) Observations. *Engineering*.

[52] Ji, Y., Dong, Z., Zhang, Y., Zhang, Q., & Yao, B. (2021). Extended scintillation phase gradient autofocus in future spaceborne P-band SAR mission. *Science China Information Sciences*, 64, 1–17.

[53] Jones, N., Strozzi, T., Rabatel, A., Ducasse, E., & Mouginot, J. (2023). Surface Instability Mapping in Alpine Paraglacial Environments Using Sentinel-1 DInSAR Techniques. *IEEE Journal of Selected Topics in Applied Earth Observations and Remote Sensing*, 16, 19–37.

[54] Jordan, R., Picardi, G., Plaut, J., Wheeler, K., Kirchner, D., Safaeinili, A., Johnson, W., Seu, R., Calabrese, D., Zampolini, E., Cicchetti, A., Huff, R., Gurnett, D., Ivanov, A., Kofman, W., Orosei, R., Thompson, T., Edenhofer, P., & Bombaci, O. (2009). The Mars express MARSIS sounder instrument. *Planetary and Space Science*, 57(14), 1975–1986.

[55] Jung, H.-S., Lee, D.-T., Lu, Z., & Won, J.-S. (2012). Ionospheric correction of SAR interferograms by multiple-aperture interferometry. *IEEE Transactions on Geoscience and Remote Sensing*, 51, 3191–3199.

[56] Kelley, M. C. (2009). *The Earth's ionosphere: Plasma physics and electrodynamics*. Academic press.

[57] Kelley, M. C., Vickrey, J. F., Carlson, C. W., & Torbert, R. (1982). On the origin and spatial extent of high-latitude F region irregularities. *Journal of Geophysical Research: Space Physics*, 87, 4469–4475.

[58] Kellogg, K., Hoffman, P., Standley, S., Shaffer, S., Rosen, P., Edelstein, W., Dunn, C., Baker, C., Barela, P., Shen, Y., et al. (2020). NASA-ISRO synthetic aperture radar (NISAR) mission. In *2020 IEEE Aerospace Conference* (pp. 1–21).

[59] Kim, J. S. & Papathanassiou, K. P. (2010). Faraday rotation estimation performance analysis. In *8th European Conference on Synthetic Aperture Radar*: VDE.

[60] Kim, J. S. & Papathanassiou, K. P. (2021). TEC and ionospheric height estimation by means of azimuth subaperture analysis in quad-polarimetric spaceborne SAR data. *IEEE Journal of Selected Topics in Applied Earth Observations and Remote Sensing*, 14, 6279–6290.

[61] Kim, J. S., Papathanassiou, K. P., Sato, H., & Quegan, S. (2017). Detection and estimation of equatorial spread F scintillations using synthetic aperture radar. *IEEE Transactions on Geoscience and Remote Sensing*, 55, 6713–6725.

[62] Kim, J. S., Papathanassiou, K. P., Scheiber, R., & Quegan, S. (2015). Correcting distortion of polarimetric SAR data induced by ionospheric scintillation. *IEEE Transactions on Geoscience and Remote Sensing*, 53, 6319–6335.

[63] Kim, J. S., Sato, H., & Papathanassiou, K. (2016). Validation of ionospheric mapping by means of SAR through ground based radar measurements. In *Proceedings of EUSAR 2016: 11th European Conference on Synthetic Aperture Radar*.

[64] Knepp, D. L. (1983). Multiple phase-screen calculation of the temporal behavior of stochastic waves. *Proceedings of the IEEE*, 71, 722–737.

[65] Ku, H. H. (1966). Notes on the use of propagation of error formulas. *Journal of Research of the National Bureau of Standards*, 70C.

[66] Lee, J.-S. & Pottier, E. (2017). *Polarimetric radar imaging: from basics to applications*. CRC press.

[67] Li, Z., Quegan, S., Chen, J., & Rogers, N. C. (2015). Performance analysis of phase gradient autofocus for compensating ionospheric phase scintillation in BIOMASS P-band SAR data. *IEEE Geoscience and Remote Sensing Letters*, 12, 1367–1371.

[68] Mancon, S., Giudici, D., & Tebaldini, S. (2018). The ionospheric effects mitigation in the BIOMASS mission exploiting multi-squint coherence supported by Faraday rotation. In *EUSAR 2018; 12th European Conference on Synthetic Aperture Radar*: VDE.

[69] Meyer, F. J. & Nicoll, J. B. (2008). Prediction, detection, and correction of Faraday rotation in full-polarimetric L-band SAR data. *IEEE Transactions on Geoscience and Remote Sensing*, 46, 3076–3086.

[70] Moreira, A. & Huang, Y. (1994). Airborne SAR processing of highly squinted data using a chirp scaling approach with integrated motion compensation. *IEEE Transactions on Geoscience and Remote Sensing*, 32(5), 1029–1040.

[71] Moreira, A., Prats-Iraola, P., Younis, M., Krieger, G., Hajnsek, I., & Papathanassiou, K. P. (2013). A tutorial on synthetic aperture rada. *IEEE Geoscience and Remote Sensing Magazine*, 1(1), 6–43.

[72] Nava, B., Coïsson, P., & Radicella, S. (2008). A new version of the NeQuick ionosphere electron density model. *Journal of Atmospheric and Solar-Terrestrial Physics*, 70(15), 1856–1862. Ionospheric Effects and Telecommunications.

[73] Oliver, C. & Quegan, S. (2004). *Understanding synthetic aperture radar images*. SciTech Publishing.

[74] Ossakow, S. L. (1981). Spread-F theories—A review. *Journal of Atmospheric and Terrestrial Physics*, 43(5), 437–452. Equatorial Aeronomy - I.

[75] Peterson, A. F., Ray, S. L., & Mittra, R. (1998). *Computational Methods for Electromagnetics*. Wiley-IEEE Press.

[76] Pi, X., Freeman, A., Chapman, B., Rosen, P., & Li, Z. (2011). Imaging ionospheric inhomogeneities using spaceborne synthetic aperture radar. *Journal of Geophysical Research: Space Physics*, 116(A4).

[77] Pi, X., Mannucci, A., Lindqwister, U., & Ho, C. (1997). Monitoring of global ionospheric irregularities using the worldwide GPS network. *Geophysical Research Letters*, 24(28), 2283–2286.

[78] Prats, P. & Mallorqui, J. J. (2003). Estimation of azimuth phase undulations with multisquint processing in airborne interferometric SAR images. *IEEE Transactions on Geoscience and Remote Sensing*, 41(6), 1530–1533.

[79] Prats-Iraola, P., Papathanassiou, K., Kim, J. S., Rodriguez-Cassola, M., D'Aria, D., Piantanida, R., Valentino, A., Giudici, D., Jaeger, M., Scheiber, R., Pinheiro, M., Yague-Martinez, N., Nannini, M., Gracheva, V., Guardabrazo, T., & Moreira, A. (2018). The BIOMASS Ground Processor Prototype: An Overview. In *EUSAR 2018; 12th European Conference on Synthetic Aperture Radar* Aachen: VDE.

[80] Prats-Iraola, P., Reigber, A., & Mallorqui, J. (2005). Topography-dependent motion compensation for repeat-pass interferometric SAR systems. *IEEE Geoscience and Remote Sensing Letters*, 2, 206–210.

[81] Rino, C. & Fremouw, E. (1977). The angle dependence of singly scattered wavefields. *Journal of Atmospheric and Terrestrial Physics*, 39(8), 859–868.

[82] Rino, C. L. (1979). A power law phase screen model for ionospheric scintillation: 1. Weak scatter. *Radio Science*, 14, 1135–1145.

[83] Rino, C. L. (1982). On the application of phase screen models to the interpretation of ionospheric scintillation data. *Radio Science*, 17, 855–867.

[84] Rino, C. L. (2011). *The Theory of Scintillation with Applications in Remote Sensing*. Wiley.

[85] Rocca, F., Prati, C., Monti Guarnieri, A., & Ferretti, A. (2000). SAR Interferometry and its Applications. *Surveys in Geophysics*, 21(2), 159–176.

[86] Rodriguez-Cassola, M., Prats-Iraola, P., Jäger, M., Reigber, A., & Moreira, A. (2013). Estimation of tropospheric delays using synthetic aperture radar and squint diversity. In *2013 IEEE International Geoscience and Remote Sensing Symposium-IGARSS* (pp. 4491–4494).

[87] Rosenqvist, A., Shimada, M., Ito, N., & Watanabe, M. (2007). ALOS PALSAR: A Pathfinder Mission for Global-Scale Monitoring of the Environment. *IEEE Transactions on Geoscience and Remote Sensing*, 45(11), 3307–3316.

[88] Roth, A. P., Huxtable, B. D., Chotoo, K., Chotoo, S. D., & Caton, R. G. (2012). Detection and mitigation of ionospheric stripes in PALSAR data. In *2012 IEEE International Geoscience and Remote Sensing Symposium* (pp. 1621–1624).

[89] Rott, H. & Nagler, T. (1995). Monitoring temporal dynamics of snowmelt with ERS-1 SAR. *1995 International Geoscience and Remote Sensing Symposium, IGARSS'95. Quantitative Remote Sensing for Science and Applications*, 3, 1747–1749.

[90] Sanjuan-Ferrer, M. J., Prats-Iraola, P., Rodriguez-Cassola, M., Zonno, M., Pinheiro, M., Nannini, M., Yague-Martinez, N., del Castillo-Mena, J., Boerner, T., Papathanassiou, K. P., et al. (2018). End-to-end performance simulator for the BIOMASS mission. In *EUSAR 2018; 12th European Conference on Synthetic Aperture Radar*: VDE.

[91] Sato, H., Kim, J. S., Jakowski, N., & Häggström, I. (2018). Imaging high-latitude plasma density irregularities resulting from particle precipitation: spaceborne L-band SAR and EISCAT observations. *Earth, Planets and Space*, 70(1).

[92] Schaer, S., Gurtner, W., & Feltens, J. (1998). IONEX: The ionosphere map exchange format version 1. In *Proceedings of the IGS AC workshop, Darmstadt, Germany*.

[93] Schneevoigt, N. J., Sund, M., Bogren, W., Kääb, A., & Weydahl, D. J. (2012). Glacier displacement on Comfortlessbreen, Svalbard, using 2-pass differential SAR interferometry (DInSAR) with a digital elevation model. *Polar Record*, 48(1), 17–25.

[94] Secan, J. A. & Bussey, R. M. (1994). *An Improved Model of High-latitude F-region Scintillation: WBMOD Version 13*. Phillips Laboratory, Directorate of Geophysics, Air Force Materiel Command.

[95] Seu, R., Biccari, D., Orosei, R., Lorenzoni, L., Phillips, R., Marinangeli, L., Picardi, G., Masdea, A., & Zampolini, E. (2004). SHARAD: The MRO 2005 shallow radar. *Planetary and Space Science*, 52(1), 157–166. Exploring Mars Surface and its Earth Analogues.

[96] Shannon, C. E. (2001). A mathematical theory of communication. *ACM SIGMOBILE Mobile Computing and Communications Review*, 5(1), 3–55.

[97] Shimada, M., Muraki, Y., & Otsuka, Y. (2008). Discovery of anoumoulous stripes over the Amazon by the PALSAR onboard ALOS satellite. In *IGARSS 2008-2008 IEEE International Geoscience and Remote Sensing Symposium*.

[98] Tatarski, V. I. (2016). *Wave propagation in a turbulent medium*. Courier Dover Publications.

[99] Tebaldini, S., Guarnieri, A. M., & Rocca, F. (2012). Recovering time and space varying phase screens through SAR multi-squint differential interferometry. In *EUSAR 2012; 9th European Conference on Synthetic Aperture Radar* (pp. 16–19).: VDE.

[100] Tebaldini, S., Nagler, T., Rott, H., & Heilig, A. (2016). Imaging the internal structure of an alpine glacier via L-band airborne SAR tomography. *IEEE Transactions on Geoscience and Remote Sensing*, 54(12), 7197–7209.

[101] Tello, M., Cazcarra-Bes, V., Pardini, M., & Papathanassiou, K. (2018). Forest structure characterization from SAR tomography at L-band. *IEEE Journal of Selected Topics in Applied Earth Observations and Remote Sensing*, 11(10), 3402 – 3414.

[102] Tesauro, M., Berardino, P., Lanari, R., Sansosti, E., Fornaro, G., & Franceschetti, G. (2000). Urban subsidence inside the city of Napoli (Italy) observed by satellite radar interferometry. *Geophysical Research Letters*, 27(13), 1961–1964.

[103] Thompson, A. R., Moran, J. M., & Swenson, G. W. (2017). *Interferometry and synthesis in radio astronomy*. Springer Nature.

[104] Touzi, R., Lopes, A., Bruniquel, J., & Vachon, P. W. (1999). Coherence estimation for SAR imagery. *IEEE transactions on geoscience and remote sensing*, 37(1), 135–149.

[105] Tsai, Y.-L. S. (2024). Monitoring Arctic permafrost coastal erosion dynamics using a multidecadal cross-mission SAR dataset along an Alaskan Beaufort Sea coastline. *Science of The Total Environment*, 917, 170389.

[106] Wahl, D. E., Eichel, P. H., Ghiglia, D. C., & Jakowatz, C. V. (1994a). Phase gradient autofocus-a robust tool for high resolution SAR phase correction. *IEEE Transactions on Aerospace and electronic systems*, 30, 827–835.

[107] Wahl, D. E., Jakowatz, C. V., Thompson, P. A., & Ghiglia, D. C. (1994b). New approach to strip-map SAR autofocus. In *Proceedings of IEEE 6th Digital Signal Processing Workshop* (pp. 53–56).

[108] Wiley, C. A. (1965). Pulsed Doppler radar methods and apparatus. *Google Patents*, (US Patent 3,196,436).

[109] Wright, P. A., Quegan, S., Wheadon, N. S., & Hall, C. D. (2003). Faraday rotation effects on L-band spaceborne SAR data. *IEEE Transactions on Geoscience and Remote Sensing*, 41, 2735–2744.

[110] Xu, Z.-W., Wu, J., & Wu, Z.-S. (2004). A survey of ionospheric effects on space-based radar. *Waves in Random media*, 14(2), S189.

[111] Yeh, K. C. & Liu, C.-H. (1982). Radio wave scintillations in the ionosphere. *Proceedings of the IEEE*, 70, 324–360.

[112] Yeh, K. C., Liu, C. H., & Seshadri, S. R. (1973). *Theory of Ionospheric Waves*. Academic Press.

[113] Zolesi, B. & Cander, L. R. (2014). *Ionospheric prediction and forecasting*. Springer.

[114] Zucker, S. (2003). Cross-correlation and maximum-likelihood analysis: A new approach to combining cross-correlation functions. *Monthly Notices of the Royal Astronomical Society*, 342.